

MULTIMODE OPTICAL WAVEGUIDES AND  
LIGHTGUIDES FOR BACKPLANE INTERCONNECTION  
AND LASER ILLUMINATED DISPLAY SYSTEMS

*Seyed Hadi Baghsiahi*

PhD Thesis

Department of Electronic and Electrical Engineering

University College London, (UCL)

August 2012

Main Supervisor:

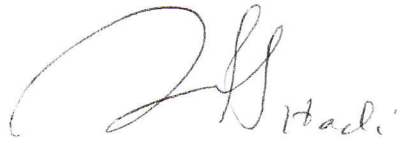
Dr. David R. Selviah

Second Supervisor:

Dr. Sally E. Day

# Declaration

I, Seyed Hadi Baghsiahi confirm that the work presented in this thesis is my own. Where information has been derived from other sources, I confirm that this has been indicated in the thesis.

A handwritten signature in black ink, consisting of a large, stylized initial 'S' followed by the name 'Hadi' in a cursive script.

# Acknowledgments

I would like to thank UCL, the Graduate school, and the Department of Electronic and Electrical Engineering for giving me the opportunity and support to pursue my research ambitions. I would like to thank the Dorothy Hodgkin Postgraduate Award, DHPA for financial support during my Ph.D which enabled me to carry out my research at UCL.

During the course of my research, I was motivated, advised and challenged by individuals who helped me in several ways, mainly my supervisor, Dr. David R. Selviah. I would like to take this opportunity to thank him with great respect for all of his advice, help and support.

I would like to thank Dr Sally E. Day and Dr F. Anibal Fernandez for all of their help and support during my Ph.D. I would also like to express my great appreciation to Dr Phil Surman, Dr Nicolae C. Panoiu, and Professor Hakan Urey for their advice and helpful suggestions. My colleagues Kai Wang, Janti Shawash, Ze Chen and Eero Willman made a pleasant environment with helpful advice and I am really grateful for the precious time we have spent together in the office, conferences, and working as a research group. I like to also thank all of the people in office 706 in the Robert's Building, Department of Electronic and Electrical Engineering, University College London who are amazing people who made the office more enjoyable in which to work. Further thanks are due to Witold Kandulski and Jonathan Calver and their colleagues at Stevenage Circuits Ltd. as well to Richard Pitwon and Dave Millward at Xyratex Technology Ltd. Great thanks are also due to all of the people involved in the IeMRC Flagship Project and the HELIUM3D project. Also thanks for the sponsors of these two projects for providing funding.

Most of all, if it were not for the encouragement of my family, I would have not been where I am or who I am now. However, I need to express my special humble gratitude to my brother, Mehdi, and my uncle, Parviz for their permanent continuing support, encouragement and life changing advice and I also send my great thanks to their family. I would also like to thank Mr Hossein Mehrabadi, and Mohammad Abdollahi for their consistent support and help. Finally, I would like to thank the individuals that made my life in London better than I would have expected. I will show my gratitude to all of my friends inside and outside UCL and will never forget the fantastic time we had together.

# Abstract

The aim of the research in this thesis was to design, model, analyse and experimentally test multimode optical waveguides and lightguides for manipulating infrared light for optical backplane interconnections and visible light for laser illuminated display systems.

Optical Input/Output Coupling loss at the entry and exit of polymer waveguides depends on optical scattering due to end facet roughness. The input/output coupling loss was measured for different end facet roughness magnitudes and the waveguide surface profiles due to different cutting methods (dicing saw and three milling routers) were compared. The effect of the number of cutting edges on the router, the rotation rate and translation (cutting) speed of the milling routers on the waveguide end facet roughness was established. A further new method for reducing the end facet roughness and so the coupling loss, by curing a layer of core material at the end of the waveguide to cover the roughness fluctuations, was proposed and successfully demonstrated giving the best results reported to date resulting in an improvement of 2.8 dB, even better than those obtained by use of index matching fluid which is impractical in commercial systems. The insertion loss due to waveguide crossing having various crossing angles was calculated using a beam propagation method and ray tracing simulations and compared to experimental measurements. Differences between the results were resolved leading to an understanding that only low order waveguide modes at no more than 6 degrees to the axis were propagating inside the waveguide. This solves a long standing problem observed by other researchers at Varioprint and gives a much deeper understanding of the physics of propagation of light in polymer waveguides.

Several different and new optical designs of multimode waveguide for the light engine of a 3D autostereoscopic laser illuminated display system were proposed. Each design performed the functions of laser beam combining, beam shaping and beam homogenizing and the best method was selected, designed, modelled, tested, and implemented in the system. The waveguide material was inspected using spectroscopy to establish the effect of high power optical density on the material performance showing an increased loss particularly in the shorter wavelengths. The effect of waveguide dimensions on the speckle pattern was investigated experimentally and the

speckle contrast was reduced to below the threshold of human perception. Speckle contrast was also recorded for the first time along the axis of the 3D display system and normal to it in the viewing area and the speckle characteristics at each stage were investigated. New algorithms for analysing speckle were used and the perceptual ability of human eyes to detect speckle size and contrast were taken into account to minimise perceived speckle patterns.

The effect of the core diameter of optical fibres on the speckle pattern was investigated and it was shown that the speckle spot diameter is reduced by increasing the fibre core diameter. Based on this experiment, it was suggested that speckle reduction is more effective if the optical fibre used in the display system has larger diameter. This is due to the reduction of speckle spot diameter below the resolution of the human eye. Therefore, a slab waveguide of 1 mm thickness and 20 m width was used for laser beam combining, homogenising and beam shaping and a uniformity of 84% was achieved with just 75 mm length. The speckle was also completely removed at the output of the waveguide.

# Table of Contents

<b>Chapter 1: Introduction.....</b>	<b>1</b>
1.1. The Aim .....	1
1.2. Motivation.....	3
1.3. Layout of the Thesis.....	7
<b>Chapter 2: Polymer Waveguide Interconnects for Optical Backplanes Review.....</b>	<b>12</b>
2.1 Introduction.....	12
2.2 Review of optical backplane systems .....	13
2.2.1 DaimlerChrysler optical backplane.....	13
2.2.2 Siemens/ C-Lab Electro-Optical Circuit board.....	14
2.2.3 IBM optical card to card demonstrator.....	15
2.2.4 Plastic Optical Fibre (POF) for short distance optical interconnections.....	17
2.2.5 High Speed on-board optical interconnection (Cambridge University) .....	19
2.3 Review of the Crossing waveguides.....	19
2.4 Review of Waveguide End Facet Roughness .....	22
<b>Chapter 3: Waveguides, Lightguides and Lightpipes in Laser-illuminated Display Systems Review.....</b>	<b>34</b>
3.1 Introduction.....	34
3.2 Review of Using Waveguides in Display Systems and Power Homogenisation .....	37
3.3 Review of the use of Waveguides for Reducing Speckle in Display Systems .....	42
<b>Chapter 4: Polymer Waveguide Optical Backplane UCL Research Review .....</b>	<b>52</b>
4.1 Introduction.....	52
4.1.1 Photolithographic Fabrication Technique.....	55
4.2 Optical Backplane Designed for 10 Gb/s Interconnection FirstLight Demonstrator ...	57

4.3 Review of Optical Loss in Polymer Waveguides.....	60
4.4 Waveguide Simulation Methods.....	63
4.4.1 Beam Propagation Method, BPM.....	64
4.5 Experimental Configuration for Optical Loss Measurements.....	67
4.6 VCSEL as the Optical Source.....	70
4.7 Conclusions.....	73
<b>Chapter 5: Multiple Viewer Laser Illuminated Autostereoscopic 3D Display System... 77</b>	
5.1 Introduction.....	77
5.2 Light Engine for the HELIUM3D System.....	81
5.3 Transfer Screen in the High Efficiency Laser-Based Multiuser Multi-modal 3D Display System.....	85
5.3.1 Intermediate Image Stage.....	86
5.3.2 Pupil Control Module.....	86
5.3.3 Front Screen.....	87
5.3.4 Pupil Tracker.....	89
5.4 Light Engine Developed at UCL .....	89
5.4.1 Low Power Laser in the HELIUM3D System (Prototype one).....	89
5.4.2 High Power Lasers in the HELIUM3D System (Prototype two).....	95
5.5 Evaluation of the NECSEL Beam Parameters.....	99
5.6 Conclusions and discussions.....	103
<b>Chapter 6: Polymer Waveguide End Facet Cutting, Smoothing, Roughness and Waveguide Input/Output Optical Coupling Efficiency..... 105</b>	
6.1 Introduction.....	105
6.2 End Facet Roughness of the Waveguide due to Various Cutting Methods.....	107
6.2.1 Waveguide End Facets Cut with a Dicing Saw.....	108

6.2.2 Waveguide End Facet Cut with a Milling Router.....	109
6.2.3 Comparing the Waveguide Surface Roughness with that of a Silicon Wafer..	123
6.3 Optical Input/Output Coupling Loss due to Roughness of Waveguide End Facets ...	124
6.4 End Facet Waveguide Roughness Reduction after Cutting.....	127
6.4.1 End Facet Waveguide polishing.....	128
6.5 End Facet Roughness Treatment Using a Layer of Polymer.....	131
6.6 Conclusions.....	133
<b>Chapter 7: Experimental Measurement and Computer Modeling of Loss and Crosstalk in Multimode Step-index Photolithographically Fabricated Polyacrylate Polymer Waveguide Crossings.....</b>	<b>137</b>
7.1 Introduction.....	137
7.2 Computer Modelling and Simulation.....	139
7.2.1 Beam Propagation Method (BPM) Using R-soft BPM Software.....	139
7.2.2 Simulating Crossings with Ray Tracing.....	145
7.3 Experiment.....	147
7.4 Discussion of the Results of Crossing Waveguide Simulation and Experiment.....	149
7.4.1 Comparison between BPM results and experiments.....	150
7.4.2 Comparison between ray tracing results and experiments.....	152
7.5 Conclusions.....	155
<b>Chapter 8: Waveguides and Lightguides for Laser Beam Combining, Homogenisation, and Beam Shaping for Display Backlighting .....</b>	<b>158</b>
8.1 Introduction.....	158
8.2 Proposal and Comparison of Various Approaches for Designing the Light Engine for HELIUM3D System.....	159
8.2.1 Free Space Method for Designing the HELIUM3D Light Engine .....	160



8.3 Laser Beam Coupling, Homogenising, and Beam Shaping using Optical Waveguides	163
8.3.1 Coupling NECSEL Laser Beams into a Waveguide using Lenses	164
8.3.2 Coupling Laser Beams into a Waveguide Using Optical Fibre	166
8.3.2.1. Fibre Ribbon	166
8.3.2.2. Multi-mode Fibre	169
8.3.2.3. Fibre Bundle	172
8.3.2.4. Multiple Fibre	174
8.3.3 Coupling Laser Beams into the Waveguide using Flexible Waveguide	175
8.4 Summary of Methods	177
8.5 Options for the Waveguide Combiner	181
8.5.1 Slab Waveguide:	181
8.5.2 Channel Waveguides	182
8.6 Summary and Conclusion of the Options for Laser–Waveguide Coupling and Waveguide Combiner	183
8.7 Polymer Micro-lens Array Material Aging Characteristics	184
8.7.1 Introduction	184
8.7.2 Spectroscopy	189
8.8 Conclusions	192
<b>Chapter 9: Design, Simulation, and Experimental Results for a Laser Beam Combining, Homogenising and Shaping Waveguide</b>	<b>196</b>
9.1 Introduction	196
9.1.1 Design of a lens system to couple the beams from NECSEL multiemitter lasers into an Optical Multimode Fibre	196
9.1.1.1 Sequential Ray Tracing for Designing a Focusing Lens System	197

9.1.1.2 The use of Non Sequential Ray Tracing for Designing a Focusing Lens System.....	201
9.2 Optical Fibre for Colour and Power Homogenisation.....	207
9.3 Waveguide Combiner Simulation.....	212
9.3.1 Simulation of a Slab Waveguide with Three Fibre Inputs.....	213
9.3.2 Simulation of the use of a Fibre Ribbon for Laser-Waveguide Coupling.....	216
9.4 Colour Balancing and Homogenising in a Slab Waveguide.....	218
9.5 Experiment Results using Slab Waveguides: .....	221
9.6 Conclusions.....	223
<b>Chapter 10: Laser Speckle Analysis Techniques.....</b>	<b>226</b>
10.1 Introduction.....	226
10.2 Speckle Contrast Measurements and Characterization.....	227
10.2.1 Real Time Speckle Analysis Software.....	230
10.2.2 Speckle Spot Diameter Measurements.....	232
10.3 Speckle contrast measurements and results.....	240
10.3.1 Speckle Contrast Measurement using NECSEL Laser as the Light Source....	241
10.3.1.1 Reducing the Speckle Contrast by Increasing the Bandwidth of the Laser.....	241
10.3.1.2 Speckle Pattern of the Laser as a Function of the Number of Emitters and Diffusers.....	243
10.3.1.2.1 The Speckle Contrast as a Function of the Number of Emitters.....	244
10.3.1.2.2 Speckle Pattern with Various Numbers of Diffusers in the System.....	245
10.3.2 Characterization of Speckle in the HELIUM3D System.....	247

10.3.2.1 Effect of the Scanning Image on the Speckle Pattern.....	248
10.3.2.2 Speckle Contrast through the System.....	252
10.3.2.3 Speckle Pattern using Simulated Eye.....	254
10.3.3 Speckle in Light Emitted from Optical Waveguides.....	256
10.3.3.1 Speckle Contrast Reduction using Multimode Waveguides.....	260
10.4 Speckle Pattern and Human Perception of Speckle.....	263
10.4.1 Contrast sensitivity of human eye.....	264
10.5 Conclusions.....	268
<b>Chapter 11: Conclusion and the Future Work .....</b>	<b>272</b>
11.1 Introduction.....	272
11.2 Multimode Optical Waveguide in High Data Rate Optical Interconnections .....	272
11.2.1 Optical Coupling Loss due to the Waveguide End Facet Roughness.....	272
11.2.2 Optical Loss due to the Waveguide Crossings.....	275
11.3 Multimode Optical Waveguide/Light guides in Laser Illuminated Display System	276
11.3.1 Various Options for Laser-Waveguide Coupling and Waveguide Combiner.	277
11.3.2 Design and Experiment of using Waveguide in the HELIUM3D System.....	278
11.4 Speckle Analysis and Measurements.....	279
11.4.1 Speckle Reduction using Optical Waveguides.....	281
<b>Appendix 1: Granulometry.....</b>	<b>283</b>
<b>List of Publications.....</b>	<b>287</b>

# Glossary

AFM	Atomic Force Microscopy
BPP	Beam Parameter Product
cm	Centimetre
CW	Continuous Wave
CNC	Computer Numerical Control
CCD	Charge Coupled Device
DAC	Digital Art Capture
DLP	Digital Light Processor
DMD	Digital Micro-mirror Device
DPSS	Diode Pumped Solid State
FC/PC	Fixed Connection/Physical Contact
FOCS	Fibre Optic Colour Synthesizer
GLV	Grating Light Valve
GUI	Graphical User Interface
HELIUM3D	High Efficiency Laser-Based Multi-user Multi-modal 3D Display
HPCF	Hard Plastic Cladding Fibre
IR	Infra Red
LCD	Liquid Crystal Display
LCoS	Liquid Crystal on Silicon
LED	Light Emitting Diode
MEMS	Micro Electronic Mechanical System
MHz	Mega Hertz
mm	milli metre
mrاد	milli radian

NS	Non Sequential
MT	Mechanical Transfer
MZI	Mach-Zehnder-interferometer
NA	Numerical Aperture
NECSEL	Novelux Extended Cavity Surface Emitting Laser
OPCB	Optical Printed Circuit Board
PM	Polarization Maintaining
PMMA	Polymethyl methacrylate
POF	Plastic Optical Fibre
PPLN	Periodically Poled Lithium Niobate
RGB	Red, Green, Blue
RMS	Root Mean Square
RPM	Revolutions Per Minute
Si	Silicon
SLM	Spatial Light Modulator
SMP	Scanning micro-mirror projectors
STD	Standard Deviation
TEM	Transverse Electro-Magnetic
UCL	University College London
UHP	Ultra High Pressure
UV	Ultraviolet
VBG	Volume Bragg Grating
VCSEL	Vertical Cavity Surface Emitting Laser
W	Watt
WDM	Wavelength Division Multiplexing

# Chapter 1: Introduction

## 1.1. The Aim

The aim of the research in this thesis was to design, model, analyse and experimentally test multimode optical waveguides and lightguides for manipulating infrared light for optical backplane interconnections and visible light for laser illuminated display systems.

The first section of the research explained in this thesis is the use of multimode polymer optical waveguides for board-to-board communications in optical backplane interconnect systems. The optical insertion loss of polymer waveguides is considered in order to explore the design rules for laying out the geometry of waveguides in optical backplane systems. The research focusses on the optical input/output coupling loss due to the entry and exit end facet roughness of polymer waveguides and the insertion loss of waveguide crossings. The aims of the research in this section are:

- To find the relationship between the waveguide end facet roughness and the optical coupling loss in optical printed circuit boards (OPCB).
- To find the best method to cut polymer waveguides based on the surface quality, cost and reliability of the method.
- To optimise the cutting parameters of the selected cutting method to reduce the end facet roughness of the waveguide and so optical input/output coupling loss .
- To find and apply a range of methods for polishing, reducing and minimising the end facet roughness.
- To find the relationship between the crossing angle and the optical insertion loss of waveguide crossings.
- To analyse and understand the reason for the optical loss in waveguide crossings and to characterise the optical insertion loss in the waveguide crossing sections.

## CHAPTER1: *Introduction*

The second section of the research explained in this thesis, is the use of multimode optical waveguides in the Light Engine of laser-illuminated display systems for beam combining, homogenization and beam shaping. In this application, multiple waveguides are proposed in the form of lightguides in the Light Engine to define an alternative approach to free space optical designs. The waveguides are also used to reduce the speckle contrast, which is an important factor in a display system. The research is focused on a 3D autostereoscopic laser illuminated display system where recently developed high power multi-emitter lasers are used as the light sources. The aims are:

- To propose and compare various possible new methods for laser beam combining and homogenization and beam shaping using optical waveguides.
- To design and test a new waveguide approach to solve the problem of multi-emitter interference patterns occurring in the free space approach when a multi-emitter laser is used.
- To optimise a slab waveguide for laser beam combining, beam homogenizing and beam shaping to be used in the 3D display system.
- To find the effect of optical waveguides on the speckle pattern and endeavour to reduce the speckle contrast by using waveguides.
- To investigate the effect of the output power of the lasers on waveguide and lens material ageing.

In order to achieve the aims of the thesis, the design and manufacture of polymer multimode buried channel waveguides are explained, and important issues such as waveguide coupling loss and waveguide crossings are investigated by two modelling techniques and experiment and the results compared to elucidate the behaviour of the light within the waveguide structures. Several waveguide samples cut with different types of cutting method and cutting parameter are measured and compared with respect to both their mechanical and optical properties. Waveguides with different crossing angles are designed, modelled and experimentally measured to characterise the optical insertion loss of waveguide crossings.

Several possible methods for using waveguides of different shapes and types are compared and the advantages and disadvantages are listed. The best method is chosen and the required optical system for the Light Engine of the 3D autostereoscopic display system is designed, modelled and

implemented in the system. The speckle pattern is measured and characterised and the effect of the waveguide design on the speckle contrast is investigated experimentally.

## **1.2. Motivation**

### **– Optical Backplanes**

Electrical interconnections have dominated data communication within, and between, digital machines in the past and optical techniques have been used increasingly for long distance communications[1.1;2]. Electrical interconnects are used for short range interconnection as they have been the most reliable method in this application. However, the demand for higher data rates (10 Gb/s and higher) increases the cost of the electrical interconnection and also there are some physical limitations that cannot be avoided such as the skin effect. Moore's law shows the exponential reduction of feature sizes and increases in numbers of transistors, electronic microprocessor speed and computing power due to increasing demand [1.3]. This creates physical and technical problems as increasing the data rate increases the clock frequency, which in turn increases the loss in the electrical circuit due to loss mechanisms in the electrical interconnections such as dielectric printed circuit board (PCB) loss and radiation leakage which become more significant at higher frequencies [1.2]. There are several limiting issues in using electrical interconnects at high data rates and some of the challenges for researchers seeking new solutions for replacing printed circuit boards are mentioned here; these are mainly ones that do not exist for optical interconnections. These challenges are as follows:

- The skin effect occurs in a conductor carrying an alternating current (AC) and is where the current tends to move near its outer surface. As the frequency increases, the current concentrates near the surface of the conductor (for example, the skin depth for copper at 1 GHz is about 2  $\mu\text{m}$ ). Due to this effect, the current is carried in a thin layer of the conductor and this increases the resistance as a result of reduced skin depth with higher frequency. The resistance is proportional to the square root of the current frequency [1.4].
- Conventional electrical lines have a resistance and a capacitance that limits the rise time of signals [1.5]. As a result, the rate of data that can be transferred via the line is limited. So, if two signals are sent too close to each other in time they could overlap due to the limited rise time [1.2]. This fact causes an issue referred to as the rise time scaling



## CHAPTER1: *Introduction*

problem [1.2]. It can be shown that in an electrical wire the rise time is determined by the resistance and the capacitance of the wire which determines the  $RC$  time constant [1.6]. If the size of the electrical track changes in three dimensions by shrinking the wire, the  $RC$  time constant does not change as the ratio of  $l/A$  is constant for a cylindrical wire ( $l$  is the diameter of the cylinder and  $A$  is the cross section area). Therefore, as the transistors in a microprocessor operate faster, the wires connecting the microprocessor cannot keep up with the microprocessor frequency and in total the system is limited [1.6]. There is no equivalent phenomenon in optics that limits the bandwidth in this way. Currently the speed of computers is limited by the limited speed of the interconnections rather than by the speed of the microprocessors and this is also impeding the development of high speed switching and storage systems.

- The dielectric leakage causes by the dipole rotation in the dielectric material and increases linearly with the clock frequency [1.7]. The dielectric loss in the case of glass-reinforced epoxy laminate sheet (FR4) material which is generally used as the printed circuit board substrate becomes even larger than the skin effect losses above a data rate of 1 Gb/s [1.8].
- Electrical crosstalk between signal lines increases at higher data rates as the electrical wires radiate more with increasing frequency and receive signals more readily from adjacent tracks [1.9]. Electrical crosstalk between signal lines also increases with the density of interconnections and the required density is increasing in 3D to accommodate the required data rates. For example, bus structures of multiple parallel lines can be used to send the same data volume, but at lower data rates on each line. However, they occupy more surface area of the PCB
- Signal degradation due to reflections at impedance mismatch between transmission lines and electronic components and at vias from one layer to another in the board [1.9]. Inductive and capacitance discontinuities causes reflections at connectors and these reflections can cause logic errors [1.10].
- Increase in fabrication cost of the interconnection for higher bit rates as it requires more advanced technology [1.6].

## CHAPTER1: *Introduction*

- Increase in power consumption to drive more copper tracks at high bit rates together with the associated need for more cooling by conduction, convection and forced air flow or liquid cooling.

There are several electronic solutions offered to overcome the above limitations, however, all of these are complicated and they increase the complexity of the circuit and development cost. These are only temporary solutions that are not scalable for future demands. For example, low dielectric loss materials available for high frequency use produced by the Rogers Corporation [1.11] increase the bandwidth density to 1 Gb/s but also increase the cost of the system by more than a factor of five [1.8]. There have been other methods used to overcome these limitations, the most popular of these being equalisation of the transmission lines to achieve a uniform response over a broad bandwidth which can also involve use of pulse pre-emphasis to offset the rounding of pulses due to impedance effects [1.12]. Designing a three-dimensional (3D) structure microprocessor or using different layers appears at first sight to be a solution to achieve a high data rate, however, the problem with this method is the power dissipation, especially at higher frequencies where the losses and radiation are increased.

Electrical interconnections can also be improved by cooling the microprocessor/system to reduce the resistance of the circuit. However, the circuit needs to be cooled significantly ( $< 77$  K) which is impractical in real situations. High-temperature superconductors are an alternative approach but these are not available yet for use at room temperature and the material needs to be improved which will involve a significant development cost. Therefore, this is a constant problem and creates a bottleneck. Most of the solutions are temporary, or work just for a particular application and bandwidth.

Optics is a very interesting alternative approach for interconnection that in principle can eliminate most of the limitations of electrical interconnections. For example, an electrical design might be suitable for 500 MHz and may work satisfactorily at this frequency but may not work at 600 MHz due to the different crosstalk, inductance and reflection phenomena. In contrast, an optical system designed for 500 MHz may work up to 500 GHz and higher as the modulation frequency has no effect on the optical signal propagation. Moreover, there is no degradation of the signal due to the medium/environment if free-space optics is used in the system. Several international groups and companies have published their work and research in this field [1.13-

17]. Long-distance optical interconnects work in the same way as short ones as the propagation distance does not affect the signal (the absorption of the material is negligible compared with the power loss in copper cables). Crosstalk does not increase with the distance or clock frequency for optical interconnects [1.6]. Increasing the modulation frequency does not change or degrade the propagation of the signal as the modulation frequency is negligible compared to the optical carrier frequency ( $\sim 10^{15}$  Hz) so the optics do not need to be redesigned if the clock frequency is increased [1.6].

Therefore, using optical interconnections essentially removes most of the limitations of electrical interconnections at higher bit rates. In addition, different techniques such as wavelength-division multiplexing (WDM), dense wavelength-division multiplexing (DWDM) or time-division multiplexing (TDM) can be used for coding the light to increase the spatial efficacy of the board so a single waveguide can carry more traffic and so the board area need not be taken up with multiple parallel waveguides.

– **Displays**

Another application of optical waveguides is in laser display systems which have made a substantial impact on consumer electronics in recent years [1.18] and have grown rapidly in terms of integration in many different industries, for example mobile and electronic gadgets [1.18;19]. In laser-illuminated display systems, red, green and blue lasers are employed and the image is formed by various methods (depending on the system), for example, using separate intensity modulators for each colour such as liquid crystal on silicon (LCoS) intensity modulators [1.20;21]. Laser illumination was chosen for the display described in this thesis as it offers sufficient optical power, large colour gamut and low étendue, thus enabling accurate control of the beam directions in the system. However, lasers have the disadvantages of generating speckle patterns, safety issues associated with using coherent light and increase of cost of the display system (due to the cost of lasers with output in the visible spectrum).

Laser beams used in the light engine of a display system need to be combined, homogenised, beam-shaped and delivered to the image formation part of the display. The conventional method of combining lasers in a display system makes use of dichroic filters (very accurate colour filters used to let a specific wavelength pass and reflect the other wavelengths of the incoming beam) in

## CHAPTER1: *Introduction*

the form of an X-cube [1.18;22]. The combined laser beams then go through other optics to shape them into the desired configuration and to homogenise them as necessary (more than 90% uniformity). In this thesis, the use of multimode waveguides as an alternative method to perform the functions of beam combining, homogenising and beam shaping is investigated. The aim is to couple the laser light into a multimode waveguide and to design it to deliver the light with the desired shape and properties.

Waveguides are beneficial for safety in the system for various reasons, for example, the laser light is confined inside the waveguide and only delivered where it is necessary. Using waveguides is very useful for cinema projection systems, where tens of watts of laser light are used, as the lasers can be kept away from the other parts of the display system and the optical power is delivered via the waveguide.

Speckle can be a serious drawback in laser display systems [1.23]. It will be shown, in this thesis, that waveguides can be used to give a significant improvement in the speckle contrast, which to the best of our knowledge has not been previously reported. The waveguides can be flexible which offers great flexibility in designing the display system. Rigid lens and free-space systems require the light to be directed carefully while a flexible waveguide can be bent or twisted to fit into the application package. This fact is a great benefit, particularly in the case of miniature display systems such as micro-projectors embedded in mobile phones [1.18;24].

The cost of the system is considered and suggestions for designing the system with the maximum efficiency and lowest cost are offered. The final goal of the research (not in this thesis) is to use a waveguide in the form of visible fibre lasers or doped waveguides for producing the laser beams, combining them together and delivering them in the required configuration to the display system. Not all aspects of this goal are covered in the thesis but waveguide knowledge and experience from other applications such as optical interconnection will be engaged to explore this application in greater depth.

### **1.3. Layout of the Thesis**

Chapter 1 is the aim, motivation and layout of the thesis. This is followed by technical literature reviews in chapters 2 and 3. Chapters 4 and 5 are mainly reviews of past or other related research carried out at UCL although the author of the thesis was involved in this research. The new

## CHAPTER1: *Introduction*

research is presented in chapters 6, 7, 8, 9, 10. Chapters 8 and 9 are related to each other. Finally, the conclusions and future work are in chapter 11.

In chapter 2, the optical printed circuit boards, optical interconnect systems and previous research which has been carried out by various groups in other universities, companies and institutes is reviewed. In this chapter, the research on designing optical backplanes and establishing the optical loss of polymer waveguides is reviewed. Previous research on the optical coupling loss between an optical source and the waveguide due to the waveguide end facet roughness and research on the insertion loss of waveguide crossings is also reviewed. It should be noted that we have kept all of the UCL research in this area out of this chapter and instead describe that separately in Chapter 4.

Chapter 3 reviews laser-illuminated display systems and the use of waveguides, lightguides and lightpipes in display systems. In this chapter, display systems that use waveguides for beam combining, image forming and optical power delivery are reviewed. Speckle in display systems and use of optical fibre for reducing the speckle contrast are also reviewed.

Chapter 4 describes the optical backplane and related research performed in our research group at University College London (UCL). A lot of this research was carried out in close collaboration with the company Xyratex Technology Ltd and with other partners such as IBM and their contributions and those of other members of the UCL research group are duly acknowledged where appropriate. A brief explanation of the UCL optically interconnected system design and configuration is presented and the light source and experimental arrangement which was used for the waveguide measurements are also explained. The fabrication technique, waveguide design, simulation theory and the experimental procedure are explained in this chapter. Various sources of optical loss in polymer optical waveguide printed circuit boards are reviewed. (The author of the thesis was involved in the design, testing, simulation and measurement of the waveguides, however, the research in this chapter is not the principal original work that was carried out by the author).

Chapter 5 describes a new autostereoscopic multi-view multi-user back projection 3D display system that was developed by UCL within the HELIUM3D (High Efficiency Laser-Based Multi-user Multi-modal 3D Display) project in close collaboration with a range of universities,

## CHAPTER1: *Introduction*

companies and institutes and their contributions and those of other members of the UCL research group are duly acknowledged where appropriate. This chapter describes the various parts of the 3D display system and then concentrates on the light engine of the system. The way in which the 3D image is produced, the light engine and the laser source used in the Light Engine are also explained.

In Chapter 6, the new research on optical loss due to the roughness of the end facet of the waveguide is explained and new research on the optimisation of the parameters of a milling router for cutting the waveguide and the effect of the cutting parameters on the end facet roughness is described. The reduction of roughness by polishing is considered and a new method for reducing the end facet roughness and improving the coupling loss is presented.

Chapter 7 describes new research on the effect of waveguide crossings on the optical loss and the relationship between the crossing angle and the optical loss. This is explored by comparison of simulation and experiments for several different types of loss.

In chapter 8, a new application for optical waveguides in laser-illuminated 3D display systems is introduced. Several different possible methods of using waveguides in the 3D autostereoscopic display system are compared and the best method is chosen.

In chapter 9, optical waveguides are implemented in the 3D display system, using the methods which were chosen in chapter 8, is designed, simulated and tested by experiment. A slab waveguide is used for homogenisation of the output of special multiple laser emitters and for shaping a laser beam to give a rectangular shape.

Chapter 10 focuses on speckle in the 3D autostereoscopic display system, the effect of optical waveguides on speckle and finally, speckle reduction. A new method of analysing speckle in display systems is introduced and the variation of speckle throughout the display system is described for the first time. In addition, the effect of waveguides and optical fibres on the speckle contrast and speckle spot diameter are investigated.

In chapter 11, the conclusions of the new research carried out in the thesis are presented and discussed and further possible research is suggested.

## References

- [1.1] I. Papakonstantinou and David R. Selviah, "Analysis design and measurement of guided wave optical backplane interconnection." PhD thesis University College London, 2007.
- [1.2] D. A. Miller and H. M. Ozaktas, "Limit to the bit-rate capacity of electrical interconnects from the aspect ratio of the system architecture," *Journal of Parallel and Distributed Computing*, vol. 41, no. 1, pp. 42-52, 1997.
- [1.3] R. R. Schaller, "Moore's law: past, present and future," *Spectrum, IEEE*, vol. 34, no. 6, pp. 52-59, 1997.
- [1.4] H. Cho, P. Kapur, and K. C. Saraswat, "Power comparison between high-speed electrical and optical interconnects for interchip communication," *Journal of Lightwave Technology*, vol. 22, no. 9, pp. 2021-2033, 2004.
- [1.5] Lawrence Mayes, "Rise time in RC circuits," <http://graffiti.virgin.net/ljmayes.mal/circuittheory/Riserc.htm>, 19 April 2008.
- [1.6] D. Miller, "Rationale and challenges for optical interconnects to electronic chips," *Proceedings of IEEE*, vol. 88, no. 6, pp. 728-749, 2000.
- [1.7] H. Johnson and M. Graham, *High-speed signal propagation: advanced black magic* Prentice Hall Press, 2003.
- [1.8] D. W. Huang, T. Sze, A. Landin, R. Lytel, and H. L. Davidson, "Optical interconnects: Out of the box forever," *IEEE J. Quantum Electron*, vol. 9, no. 2, pp. 614-623, 2003.
- [1.9] A. Deutsch, "Electrical characteristics of interconnections for high-performance systems," *Proceedings of IEEE*, vol. 86, no. 2, pp. 315-355, 1998.
- [1.10] R. E. Matick, "Transmission Lines for Digital and Communication Networks," *New York: McGraw-Hill*, 1969.
- [1.11] Sunstone, "FR-4 vs. Rogers PCB Material," <http://www.sunstone.com/products-services/quickturn-proto-boards/Rogers-Material.aspx>, February 2010.
- [1.12] W. J. Dally and J. Poulton, "Transmitter equalization for 4-Gbps signaling," *IEEE Microprocessors.*, vol. 17, no. 1, pp. 48-56, 1997.
- [1.13] R. Lytel, H. L. Davidson, N. Nettleton, and T. Sze, "Optical interconnections within modern high-performance computing systems," *Proceedings of IEEE*, vol. 88, no. 6, pp. 758-763, 2000.

## CHAPTER1: *Introduction*

- [1.14] F. E. Kiamilev, P. Marchand, A. V. Krishnamoorthy, S. C. Esener, and S. H. Lee, "Performance Comparison Between Optoelectronic and VLSI Multistage Interconnection Networks," *Journal of Lightwave Technology*, vol. 9, no. 12, pp. 1674-1692, 1991.
- [1.15] G. I. Yayla, P. J. Marchand, and S. C. Esener, "Speed and energy analysis of digital interconnections: comparison of on-chip, off-chip, and free-space technologies," *Applied Optics*, vol. 37, no. 2, pp. 205-227, 1998.
- [1.16] M. Haurylau, G. Chen, H. Chen, J. Zhang, N. A. Nelson, D. H. Albonesi, E. G. Friedman, and P. M. Fauchet, "On-chip optical interconnect roadmap: Challenges and critical directions," *IEEE Journal of Selected Topics in Quantum Electronic*, vol. 12, no. 6, pp. 1699-1705, 2006.
- [1.17] E. Cassan, D. Marris, M. Rouviere, L. Vivien, and S. Laval, "Comparison between electrical and optical global clock distributions for CMOS integrated circuits," *Optical Engineering*, vol. 44, no. 10 2005.
- [1.18] Kishore V.Chellappan, Erdem Erden, and Hakan Urey, "Laser Based Display," *Applied Optics*, vol. 49, no. 25, p. f 79-f 98, Mar 2010.
- [1.19] J. Y. Han, "Low-cost multi-touch sensing through frustrated total internal reflection," Proceedings of the 18th annual ACM symposium on User interface software and technology, 2005, pp. 115-118.
- [1.20] Hadi Baghsiahi, David Selviah, Eero Willman, Anibal Fernández, and Sally Day, "Beam Forming for a Laser Based Auto-stereoscopic Multi-Viewer Display," *SID Symposium Digest of Technical Papers.*, vol. 42, no. 1, pp. 702-705, June 2010.
- [1.21] J. P. Ruske, M. Rottschalk, B. Zeitner, V. Grober, and A. Rasch, "Integrated-optical three-colour-mixing device," *Electronics Letters*, vol. 34, no. 4, pp. 363-364, 1998.
- [1.22] D. R. Selviah and K. Wang, "Modeling of a Color-Separating Backlight with Internal Mirrors," *SID International symposium digest of technical paper.*, vol. 35, pp. 487-489, 2004.
- [1.23] V. Kartashov and M. N. Akram, "Speckle suppression in projection displays by using a motionless changing diffuser," *Journal of the Optical Society of America A-Optics Image Science and Vision*, vol. 27, no. 12, pp. 2593-2601, 2010.
- [1.24] (Microvision)., "Pico projector displays: Embedded," [http://www.microvision.com/pico\\_projector\\_displays/standalone.html](http://www.microvision.com/pico_projector_displays/standalone.html), July 2008.



## **Chapter 2: Polymer Waveguide Interconnects for Optical Backplanes Review**

### **2.1 Introduction**

In this chapter, earlier research on optical interconnections carried out by other research groups mentioned below is reviewed. The chapter focusses on the fabrication methods, waveguide parameters, waveguide size, coupling efficiency and transmission length as these are more relevant to the new research presented in this thesis [2.1]. After reviewing earlier research on optical interconnections, the chapter goes on to review the earlier research on optical waveguide crossings and coupling loss due to waveguide end facets.

Optical printed circuit boards have many advantages over conventional copper track PCB interconnections for data rates higher than 10 Gbit/s as explained in chapter 1. In this chapter, research on Optical Printed Circuit Boards (OPCB) using embedded polymer waveguides is reviewed. Due to the increased demand for higher data rates and limitations on electrical interconnections, several groups of international researchers and companies have carried out a range of OPCB research. DaimlerChrysler [2.2;3], Ulm University [2.4], Dortmund University [2.5;6], the University of Hagen [2.7], Siemens and the Fraunhofer Institute for Reliability and Microintegration [2.8;9] have worked on optical interconnections in Germany. Linköping University in Sweden [2.5] and a group in Helsinki University in Finland [2.10] are active in this subject and have published several papers in recent years [2.11-13]. Supélec Service de Mesures [2.7] and INTEXYS Photonics [2.14] are industrial companies in France which are working on an OPCB European project. There are other groups including Ghent University in Belgium [2.15;16] with whom we have been in communication during this project. IBM Zurich [2.14;17] and Vario-print [2.14] are companies in Switzerland working on OPCBs and we also collaborated with them in our backplane project. In the UK, Herriot-Watt University [2.18], Loughborough University [2.19], Exxelis Ltd and Xyratex Technology Ltd [2.20] have collaborated with us and they are working mainly on manufacturing waveguides using different methods which will be mentioned in chapter 3.

Apart from the above groups, Fujitsu laboratories in USA [2.21;22], Duke University [2.23-25], General Electric [2.23;24] Georgia Institute of Technology [2.23;26], AMP Global

Optoelectronics Technology [2.27;28], DuPont Photonics [2.29] are American companies and research institutes developing optical PCBs. In Japan, Nippon Telegraph and Telephone (NTT) is the main player in this area [2.30;31] but Hitachi Chemical and Mitsubishi [2.25] have also worked and developed some products used in the OPCB industry. In Korea the Electronics and Telecommunication University Daejeon [2.32-36] has carried out significant work and Samsung [2.30] also has shown interest in this area [2.32;34].

## 2.2 Review of optical backplane systems

### 2.2.1 DaimlerChrysler optical backplane

DaimlerChrysler research centre in Germany developed a backplane system for avionic, satellite and telecommunication applications due to the light weight of optical interconnects compared to copper interconnects. The system aimed for a 1 Gb/s data rate but they were able to report rates up to 2.5 Gb/s[2.2;37]. The waveguide material is a polymer with an attenuation of 0.03 dB/cm at 840 nm and the waveguides were made by the direct laser writing technique [2.37]. Figure 2.1 shows a schematic diagram of this backplane system.

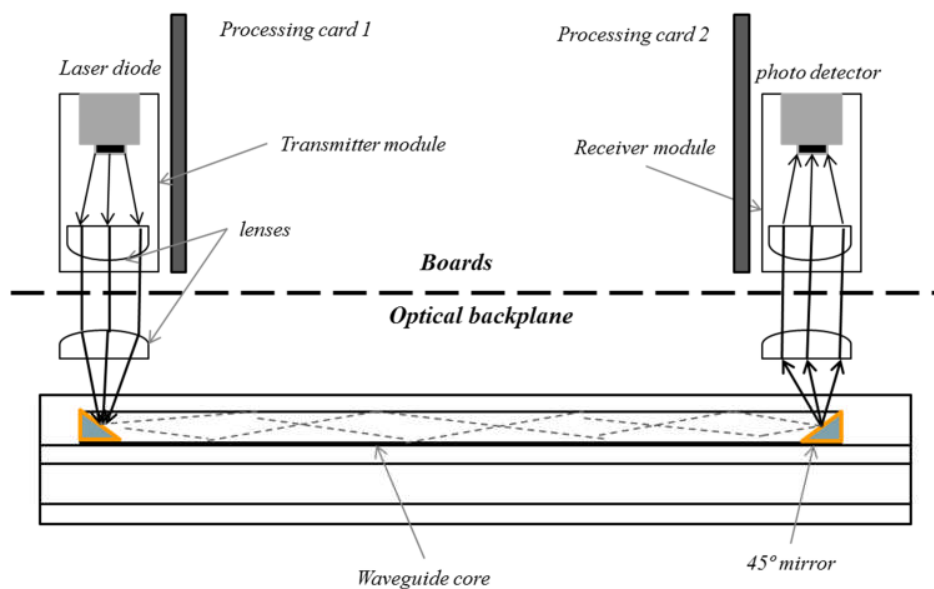


Figure 2.1: DaimlerChrysler Optical backplane structure. After[2.37].

The cross section of the waveguide is  $250\ \mu\text{m} \times 200\ \mu\text{m}$  and due to this large core area the light input/output coupling efficiency is higher than for more common  $50\ \mu\text{m} \times 50\ \mu\text{m}$  core

waveguides due to the higher misalignment tolerances. It is beneficial to have waveguides with larger size as far as coupling is concerned but in order to achieve maximum compatibility with Printed Circuit Boards, (PCB) and their manufacturing process, the size of the optical waveguide should be  $50\ \mu\text{m} - 100\ \mu\text{m}$  which is of the same order of magnitude as the microstrip lines in and on PCBs. The waveguides could be laid out on a substrate of  $1000\ \text{mm} \times 300\ \text{mm}$  but the longest waveguides they made were 550 mm and they demonstrated communication between processor cards via the backplane. The light source was an edge emitting laser diode at 780 nm implemented on the processor cards and light was coupled into the waveguide with the aid of half ball lenses and a  $45^\circ$  mirror. Similar lenses and mirrors were used at the other end of the waveguide where the light was redirected and focused into a  $400\ \mu\text{m}$  active area photo detector. This system has been tested up to 2.5 Gb/s data rates and passed several environment tests which are particularly important for aviation and satellite applications.

### **2.2.2 Siemens/ C-Lab Electro-Optical Circuit board**

Siemens SBS C-Lab, in Germany developed an OPCB system, which is a PCB board with integrated polymer waveguides. The waveguides were made by an embossing technique [2.38]. The light source was a VCSEL with a wavelength of 850 nm which was mounted on the surface of a PCB with a photodetector as shown in Figure 2.2 and Figure 2.3. The aim was to integrate waveguides into a PCB board without a significant modification of the board. The waveguides were  $50\ \mu\text{m} \times 50\ \mu\text{m}$  and they report the attenuation to be 0.15 dB/cm [2.39]. They developed two approaches, which they called indirect and direct light coupling. In the case of indirect coupling, the laser beam was coupled into the waveguide (and coupled from the waveguide into the receiver) by using  $90^\circ$  beam deflecting elements [2.40]. In the direct coupling approach, the laser was inserted into the Electrical-Optical Circuit Board (EOCB) and the light from the VCSEL was coupled into the waveguide directly. In the indirect method, an optical via was implemented to transmit the light from the surface laser and to deflect it through  $45^\circ$  instead of making  $45^\circ$  mirrors on the end facets of the waveguide. The implemented device, called an axis inverter, was a silicon (Si) rectangular block with an embedded waveguide [2.1]. One side of the block was cut with a dicing saw and metalized to form the deflecting surface to direct the light into the polymer waveguide.

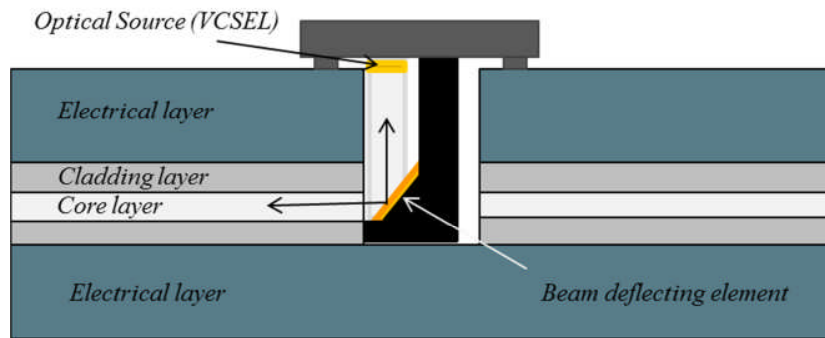


Figure 2.2: Indirect coupling of optical light source and the photo detector modules to the opto-electrical board developed by Siemens.

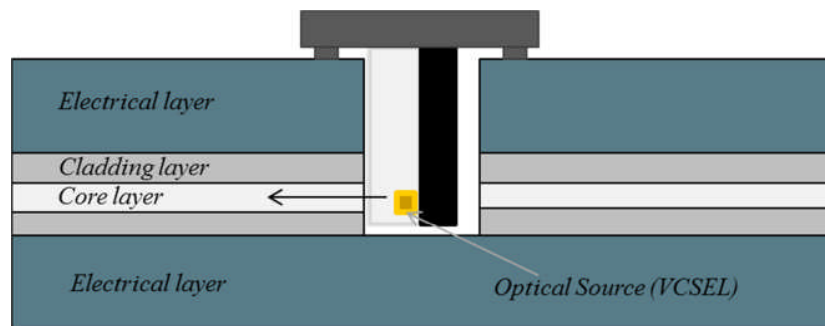


Figure 2.3: Direct coupling of optical light source and the photo detector modules to the opto-electrical board developed by Siemens. After [2.38].

### 2.2.3 IBM optical card to card demonstrator

A card to card optical interconnector was demonstrated by IBM in 2007 in which a VCSEL at 850 nm, was butt-coupled to the waveguide. Their system was designed for 12 parallel channels operating at 10 Gb/s (120 Gb/s aggregate) in a card to card link. IBM used polyurethane-acrylate-based polymer and employed laser direct writing for waveguide manufacture [2.14]. The waveguides had various sizes from  $30\ \mu\text{m} \times 30\ \mu\text{m}$  to  $50\ \mu\text{m} \times 50\ \mu\text{m}$  and they designed a waveguide interconnect layout covering an area of  $50\ \text{cm} \times 50\ \text{cm}$ . The attenuation of the waveguide was reported to be 0.03 dB/cm to 0.05 dB/cm due to material absorption. They built a connector based on the Mechanically Transferable (MT) fibre connector design.

The fabrication of the waveguides and the board with connector alignment features was carried out in several steps as is shown in Figure 2.4.

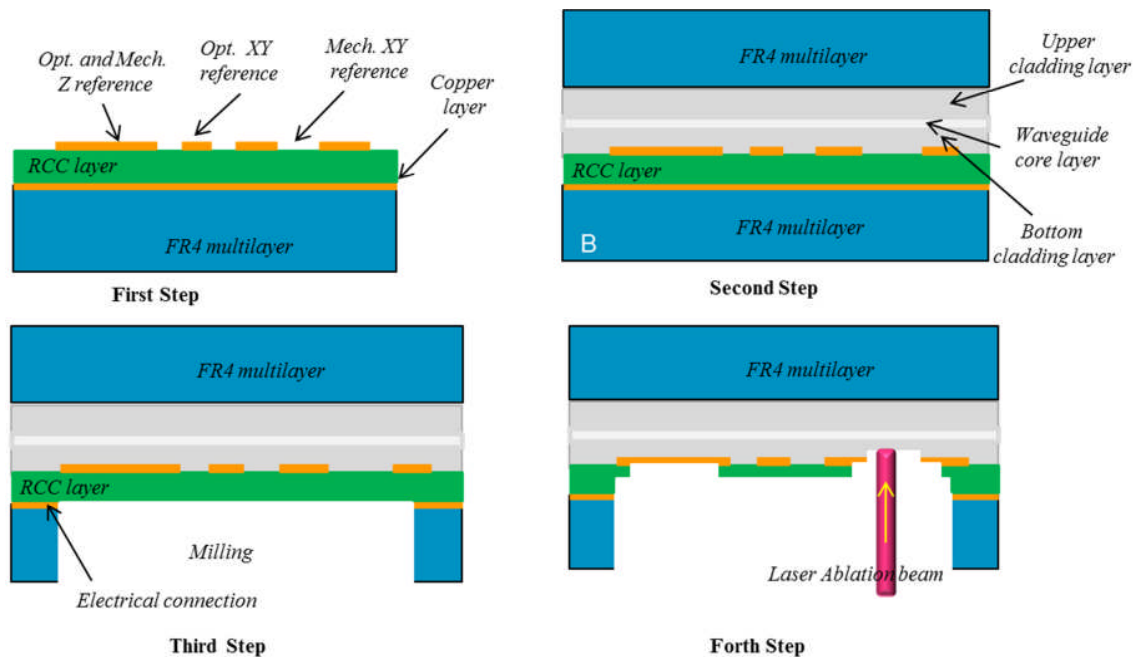


Figure 2.4: First step: FR4 substrate with marker structure (for alignment) on the top. Second step: Polymer waveguide and a FR4 layer on top of the upper cladding layer. Third step: Substrate and copper layer are removed by milling. Forth step: Laser is used to remove the resin from the marker. The laser stops on the copper layer but can go through the resin for XY reference opening. After [2.14].

Firstly, an FR4 layer was coated in a layer of Resin Coated Copper (RCC) and alignment features were defined on top of the RCC layer. These features were later used for aligning the connector (which contained the laser sources and the photodetectors) to the board. In the second step, the optical polymer waveguides were located using the laser direct writing method and the waveguides were covered by another layer of FR4. In the third and fourth steps, milling machines and lasers were used to remove the FR4, copper, and the RCC material where it was needed to retrieve the markers for the connector alignment [2.14]. Milling and laser drilling were used to remove the polymer and the resin, to prepare for the alignment technique. Laser milling is used in a clever way to make a precise opening for aligning the transceiver components and the embedded polymer waveguides. The method enabled passive alignment as described in reference [2.14] although the direct laser writing of the waveguides had to be aligned to the first copper alignment features. The XY alignment and the Z alignment of the connector are shown in Figure 2.5. The alignment features on the right side of the board shown in Figure 2.5 are used for

the lateral *XY* alignment and the alignment in the *Z* direction was carried out using the left side alignment features on the board. An accuracy of  $\pm 5 \mu\text{m}$  was reported for alignment of their connector[2.41].

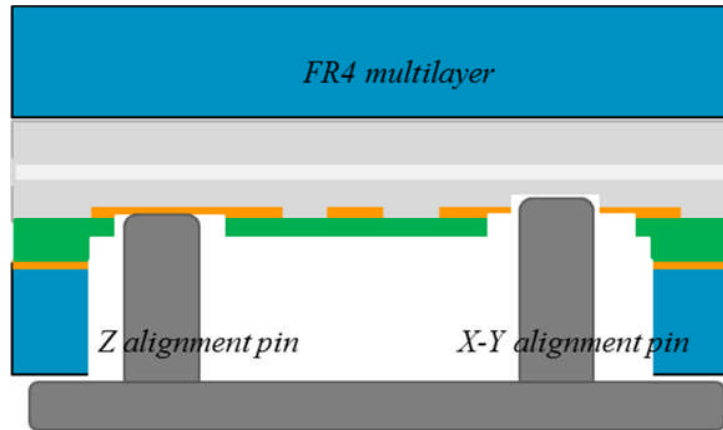


Figure 2.5: IBM connector alignment into the optical PCB.

#### **2.2.4 Plastic Optical Fibre (POF) for short distance optical interconnections**

In 2010, a new method of using POF in optical PCBs was reported by a group of researchers from the University of Delaware in the United States [2.42]. Optical fibre was used to reduce the manufacturing cost of optical PCBs and benefit from all the research previously carried out on optical fibres for other applications. Mechanical machines were used to make grooves in an FR4 substrate to bury the optical fibres inside the designed grooves. To manufacture the OPCB board, an FR4 substrate with the thickness of 1 mm was used and grooves were milled out using a computer-controlled milling machine. The depth of the grooves was chosen to be  $500 \mu\text{m}$  with a width of  $250 \mu\text{m}$ . The plastic optical fibres were placed inside the grooves manually. The fibre core refractive index was 1.49 at 650 nm and the core diameter was  $240 \mu\text{m}$  with an external diameter of  $250 \mu\text{m}$ . The optical loss of the core materials was reported to be 0.015 dB/cm. A low-viscosity epoxy was used to fill the remaining space in the grooves and it was cured to keep the fibres firmly in the grooves. The interesting point in their work is how they prepared the end of the waveguide to couple the light into the waveguide. They use a milling tool and cut the end of the waveguide to couple light into the waveguide by total internal reflection (TIR). Figure 2.6 shows a schematic diagram of the mirror formation at the end of the waveguide.

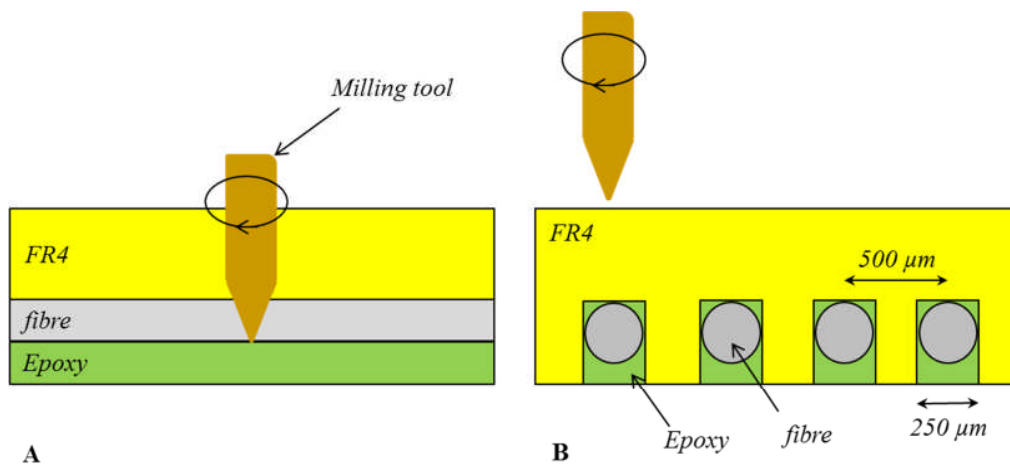


Figure 2.6: Two views of mirror formation in the embedded optical fibre. A: Side view. B: Front view: the milling tool moves to the right and cuts the end of the waveguide. After [2.42].

As shown in Figure 2.6, the FR4 board with embedded fibres and cured epoxy was turned over and placed inside the milling machine for mirror formation. They used a milling tool to drill into the board and cut across in the board perpendicular to the laid out fibres (in plane moving in Figure 2.6 part A). In this process the end of the fibres were cut with a 45° angle as is shown in Figure 2.7. In this figure, the fibres are shown after cutting the end of the waveguide and forming the TIR mirrors.

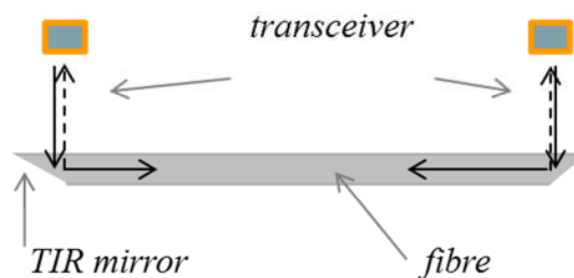


Figure 2.7: Embedded fibres and the TIR mirrors at the end of each fibre

In their demonstration board, the output of a laser with a wavelength of 650 nm is coupled into a 62.5/125 µm fibre using optical lenses and the other side of the fibre is brought close to the board with embedded fibres. The output of the fibres is directed into the embedded fibre using another lens designed for their board. They reported an insertion loss of  $3.14 \pm 0.32$  dB for one

embedded POF link. The loss of each mirror was reported to be about 1.6 dB. Further research is required to reduce the loss of the mirrors.

### **2.2.5 High Speed on-board optical interconnection (Cambridge University)**

Cambridge University used polymer waveguides to make an optical backplane [2.43]. They used Siloxane materials OE-4140 as the core material and OE-4141 for the cladding material developed and provided by Dow Corning Company. The refractive index of the core and cladding material is 1.52 and 1.50 respectively at 850 nm wavelength. Photolithography was used to fabricate the waveguides and the waveguide size was  $50\ \mu\text{m} \times 50\ \mu\text{m}$  with a separation of  $250\ \mu\text{m}$ . A propagation loss of 0.03 - 0.05 dB/cm was reported. The researchers developed, manufactured and tested several waveguide components including bent waveguides with different radius,  $90^\circ$  crossing waveguides, and Y shaped power splitter waveguides. Their detailed results are explained in the next section concerned with waveguide crossings and waveguide roughness.

## **2.3 Review of the Crossing waveguides**

Complex interconnection patterns in electrical PCBs have to use multiple layers of copper tracks. However, the same interconnections can be made in a single layer using optical waveguides as they cross on the same layer. Copper tracks cannot do this as they would short circuit so they have to use vias to other layers. To achieve an effective and complex integrated optical circuit, optical PCB designers make use of various elements in their designs such as bends, splitters, couplers and crossing waveguides. Increasing the compactness of the waveguide structure reduces the cost of the system as considerably as the available space on the boards is used more efficiently. Waveguide crossings where two waveguides intersect in the same optical layer are particularly important components as they offer OPCB layout designers additional flexibility to solve layout problems such as routing around cutout areas, electrical components and other obstacles on an OPCB [2.44]. Use of waveguide crossings can also help to avoid sharp bends in the design as these are an important cause of optical loss [2.44;45]. Despite all of the advantages of waveguide crossings, and although most of the light travels along the intended waveguide, a proportion of the optical power in one waveguide will couple into the crossed waveguide after passing each intersect point (Figure 2.8) or couple out of the original waveguide and into the cladding. This coupling phenomenon causes optical loss and crosstalk in the system [2.46]. The



amount of loss and crosstalk depends on the crossing angle between waveguides [2.47;48]. Consequently the crossings in OPCBs need to be carefully designed to reduce both loss and crosstalk to improve the performance of the system by reducing the bit error rate.

Waveguide crossings have been investigated in photonic devices [2.49]; for example crossings in photonic crystals [2.50], single mode waveguides [2.51] and Multimode Interference (MMI) devices [2.52] are some of the areas where waveguide crossings have a significant role. However, little research has been reported for the optical loss of polymer waveguide crossings at angles other than  $90^\circ$  in optical backplane applications.

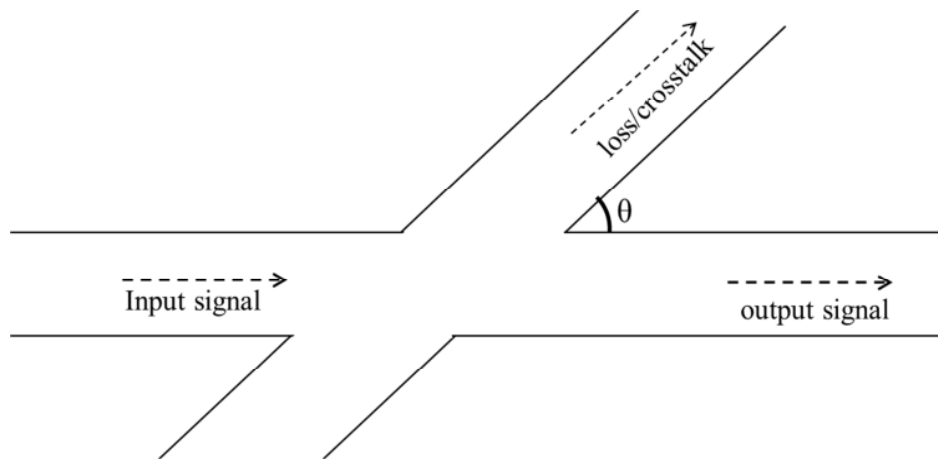


Figure 2.8: Top schematic view of a waveguide crossing with crossing angle  $\theta$ .

The optical loss for various angles of crossing was reported by MIC-Department of Micro and Nanotechnology, Technical University of Denmark [2.46]. In this research, the waveguides were made of epoxy-based negative photoresist (NANO SU-8 25 from MICROCHEM) and were photolithographically fabricated. The refractive index of the core material was 1.58 and the cladding material was 1.47. This structure produces a high refractive index contrast ( $\Delta n = 0.11$ ) between the core and the cladding material. The maximum size of the waveguide reported in this research was  $40 \mu\text{m} \times 40 \mu\text{m}$ . The optical loss for crossing angles of  $25^\circ$ ,  $35^\circ$ ,  $45^\circ$ ,  $55^\circ$  and  $90^\circ$  was measured. They achieved an optical loss of less than 0.03 dB for the  $90^\circ$  crossing and  $0.25 \pm 0.03$  dB for a  $25^\circ$  crossing and  $0.05 \pm 0.03$  dB at a  $55^\circ$  crossing angle [2.46]. This research is relevant for high step index contrast waveguides but is not applicable for most of the polymer waveguide backplanes as the refractive index contrast of 0.11 used in this work is much larger than the typical 0.01. Apart from this, another important fact in this work is that they used a

halogen lamp as the light source which was coupled into a fibre and then coupled into the waveguide. The halogen lamp was used as they tried to find the relationship between the optical loss and the input wavelength. This is interesting but not applicable for most of the polymers as most polymers are used at a wavelength where they have their lowest loss. Using polymers at other wavelengths reduces the efficiency of the system.

Cambridge University measured the optical loss for the crossing waveguides [2.43]. The structure of the waveguides fabricated in this group was explained in section 2.2.5. They only measured 90° angle crossings and achieved an average loss of 0.01 dB. Researchers at IBM Zurich reported an optical loss of 0.02 dB for 90° crossings [2.53]. DaimlerChrysler waveguide researchers measured a 0.08 dB loss for 90° crossings. The optical loss in this research was higher than that of Cambridge and IBM because their waveguides had a larger cross section area of  $200\ \mu\text{m} \pm 20\ \mu\text{m}$ .

Takashi Sakamoto with his group in Japan have published their work on crossing loss in multimode waveguides where tens of waveguides crossed each other [2.54]. In their research, the optical loss at crossing angles of 30°, 45°, 60°, and 90° was investigated experimentally. However their aim was to find the crossing angle which had the lowest optical loss so they concluded that a minimum crossing loss was obtained for 90° crossings and used this crossing angle in their design.

Crossing waveguides in semiconductors and other doped materials has been investigated [2.47;50] mainly concentrating on silicon-based waveguides [2.48;49;51;55]. However, this research is concerned with finding the optical loss in a particular waveguide with a particular structure. The crossing structure strongly depends on the manufacturing process and the material. In addition, it depends on the distribution of the power before the wave front impinges on the crossing area. Therefore, the optical crossing and the optical loss will be different if the prior section to the joint is a bent waveguide, another crossing, or a straight waveguide [2.44;56].

No research has been reported on modelling of waveguide crossings and comparison with experimental measurements which can lead to a deeper understanding of the behaviour of light at a crossing. This thesis addresses this by the new research in this area reported in chapter 7.

## **2.4 Review of Waveguide End Facet Roughness**

For polymer optical waveguides interconnect technology to become widespread, the cost must be minimised [2.57] so that it can displace the incumbent copper track technology. The most costly parts are the input and output connectors [2.58]. Single mode waveguides have small core dimensions of typically less than 9  $\mu\text{m}$  and so very precise active alignment in 6 axes (3 linear stages and 3 rotation) is required to align the socket to the waveguide and the plug to the optical source or detector. The socket and plug must be manufactured to tight tolerances and designed to allow precise mating. In order to avoid these costly procedures and the increased misalignment tolerance of a system, wider multimode waveguides are used in preference to single mode waveguides [2.45;59] and the waveguide cores are typically 50 – 100  $\mu\text{m}$ . Even so the connectors have to be sufficiently well-aligned in the six axes as these can still cause additional loss [2.45].

To develop low cost manufacturing techniques for integrated OPCBs, the coupling efficiency between the waveguide and the laser source is very important as it affects the optical power budget and the bit error rate [2.60]. The coupling efficiency depends on the roughness at the end facet of the waveguide, the lateral and transverse alignment of the waveguide to the laser [2.61;62] and the refractive index difference between the medium of the laser and the core material. The end facet profile of the waveguide depends on the method and the parameters used for cutting the waveguide [2.62]. The roughness at the end facet of the waveguide causes scattering of the incident light, thus, causing optical loss. Theoretical and experimental investigations of light scattering from rough surfaces have been studied by different research groups. Multiple scattering and enhanced back-scattering is the result of large amplitude roughness (this is when the correlation length ( $T$ ) (the full width half maximum in squared autocorrelation function) of the roughness is much larger than the incident wavelength and the root mean square (RMS) height ( $\sigma$ ) of the roughness is smaller than the correlation length) [2.63]. In this case, the incident light is scattered into a larger angle region compared to the incident angle [2.64-67]. Other numerical experiments have shown that the minimum reflected intensity is shifted toward the lower incident angle, so the lower incident angle causes less reflection [2.68;69]. It has also been shown that the total diffracted energy increases with the depth of the grooves[2.70]. For large  $\sigma$ , the back-scattering peak increases as  $\sigma/T$  increases and

M. Soto [2.63] shows that for a fixed  $T$  the scattering intensity distribution becomes broader with increasing  $\sigma$ . In this case, the distribution reaches to the Lambertian then by increasing the  $\sigma$  backscattering is increased [2.63]. When the correlation length is comparable to the wavelength of the light the surface is addresses to be slightly rough surface[2.71-77]. In this case the main effect of roughness is reflection loss, broadening of the scattered light and reduction of the Brewster angle [2.73].

The surface roughness of the end facet of the waveguide should, therefore, be treated in order to achieve a very small surface fluctuation. Maystre shows that the scattered field vanishes when the surface roughness is reduced to a perfectly flat surface [2.68]. Ideally, the surface roughness magnitude should be zero and the correlation value infinity, however, this is not possible in practice as surface fluctuations are always present on any surface. The scattered light (if it is not reflected back) enters the waveguide with a larger refracted angle (the scattered angle is larger due to the scattering and based on Snell's law) which causes more loss as it does not satisfy the total internal reflection condition[2.76;78;79]. Based on physical optics principles, the scattered light is coupled into the higher order modes of the waveguide [2.80;81]. The scattering from the end of the waveguide, therefore, causes less light to be transmitted into the waveguide.

In OPCB demonstrators, the daughter board is connected to the backplane with various methods such as butt-coupling (in-board coupling) [2.60], using 45° mirrors (out-of-board coupling) [2.38], or TIR coupling [2.42] for laser-waveguide coupling. The important issue that is shared in all of these results is the concern about the coupling efficiency due to the surface profile of the waveguides and mirrors.

Several methods and types of equipment have already been used by different groups in their demonstrations and waveguide sample preparation including dicing saws [2.53], laser cutting and milling [2.14;82;83]. Some groups use polishing after cutting [2.84;85] or design the backplane using a different approach such as the use of 45 degree mirrors [2.86-88]. Nevertheless, in any method or approach which is applied to optical backplane manufacturing, roughness is always a problem as it reduces the light coupling efficiency in the backplane [2.82]. A dicing saw is commonly used by engineers to cut waveguides and the end facet roughness depends upon the dicing saw grit size and rotation and translation speed of the cutter [2.68;89]. The use of a milling router to cut the board was considered as this is less likely to cause damage.

It is also easy to control as it uses a CNC machine and any range of cuts and shaped apertures are possible without causing any damage to the board. Milling routers have been used for cutting polymer [2.90;91]. However, the surface profile left after milling polymer waveguides on backplanes has not been previously investigated and it is essential to have information on the roughness produced [2.42]. Milling routers have been previously used for cutting waveguides in plastic, polymer and glass and a roughness investigation is important for the OPCB industry [2.42]. No one has considered the effect of the milling router on the roughness of the end facet of polymer waveguides. PCB manufacturers use milling routers for cutting PCBs. Some researchers have suggested that cutting OPCB boards by using a router will give a very smooth surface if this were followed by subsequent thermal polishing or annealing [2.42]. Thermal polishing means applying heat to the end facet to smooth the roughness. These are just suggestions and no one has measured the roughness after using milling routers or has investigated in depth by experiment or modelling. There has also been some research on waveguide sidewall roughness as this may be the main contributor to propagation loss [2.92;93], and some of the research has been on single mode waveguides such as Si on SiO<sub>2</sub> waveguides. These waveguides differ from multimode polymer waveguides used for optical board to board interconnections in several aspects such as the waveguide material, refractive index contrast, fabrication technique and waveguide properties [2.93;94].

## References

- [2.1] I. Papakonstantinou and David R. Selviah, "Analysis design and measurement of guided wave optical backplane interconnection." PhD thesis University College London, 2007.
- [2.2] J. Moisel, *Optical backplane for avionic applications using polymer multimode waveguides* IEEE Lasers and Electro-Optics Society (LEOS) Annual Meeting, pp. 567-568, 2000.
- [2.3] B. Lunitz, J. Guttmann, H. P. Huber, J. Moisel, and M. Rode, "Experimental demonstration of 2.5 Gbit/s transmission with 1 m polymer optical backplane," *Electronics Letters*, vol. 37, no. 17, p. 1079, 2001.
- [2.4] F. Mederer, R. Michalzik, J. Guttmann, H. P. Huber, B. Lunitz, J. Moisel, and D. Wiedenmann, "10 Gb/s data transmission with TO-packaged multimode GaAsVCSELs over 1 m long polymer waveguides for optical backplane applications," *Optics Communications*, vol. 206, no. 4-6, pp. 309-312, 2002.
- [2.5] S. Kopetz, E. Rabe, W. J. Kang, and A. Neyer, "Polysiloxane optical waveguide layer integrated in printed circuit board," *Electronics Letters*, vol. 40, no. 11, pp. 668-669, 2004.
- [2.6] A. Neyer, S. Kopetz, E. Rabe, W. J. Kang, and S. Tombrink, *Electrical-optical circuit board using polysiloxane optical waveguide layer* IEEE, 55th Electronic Components & Technology Conference, pp. 246-250, 2005.
- [2.7] P. Lukowicz, J. Jahns, R. Barbieri, P. Benabes, T. Bierhoff, A. Gauthier, M. Jarczyński, G. A. Russell, J. Schrage, W. Sullau, J. F. Snowdon, M. Wirz, and G. Troster, "Optoelectronic interconnection technology in the HOLMS system," *IEEE Journal of Selected Topics in Quantum Electronics*, vol. 9, no. 2, pp. 624-635, 2003.
- [2.8] S. Uhlig, L. Frohlich, M. X. Chen, N. Arndt-Staufenbiel, G. Lang, H. Schroder, R. Houbertz, M. Popall, and M. Robertsson, "Polymer optical interconnects - A scalable large-area panel processing approach," *IEEE Transactions on Advanced Packaging*, vol. 29, no. 1, pp. 158-170, 2006.
- [2.9] H. Schroder, J. Bauer, F. Ebling, and W. Scheel, "Polymer optical interconnects for PCB," *Polymers and Adhesives in Microelectronics and Photonics, 2001. First International IEEE Conference*, pp. 337-343, Mar 2001.
- [2.10] M. Immonen, M. Karppinen, and J. K. Kivilahti, "Fabrication and characterization of polymer optical waveguides with integrated micromirrors for three-dimensional

- board-level optical interconnects," *IEEE Transactions on Electronics Packaging Manufacturing*, vol. 28, no. 4, pp. 304-311, 2005.
- [2.11] J. Hietala, E. Muukkonen, T. von Lerber, and M. Immonen, *Volume production of on-board optical waveguides* IEEE, 55th Electronic Components & Technology Conference, pp. 1735-1738, 2005.
- [2.12] S. Uhlig and M. Robertsson, "Limitations to and solutions for optical loss in optical backplanes," *Journal of Lightwave Technology*, vol. 24, no. 4, pp. 1710-1724, 2006.
- [2.13] S. Uhlig and M. Robertsson, *Flip chip mountable optical waveguide amplifier for optical backplane systems* IEEE, 55th Electronic Components & Technology Conference, pp. 1880-1887, 2005.
- [2.14] L. Dellmann, C. Berger, R. Beyeler, R. Dangel, M. Gmuer, R. Hamelin, F. Horst, T. Lamprecht, N. Meier, T. Morf, S. Oggioni, M. Spreafico, R. Stevens, and B. Offrein, *120 Gb/s optical card-to-card interconnect link demonstrator with embedded waveguides*, pp. 1288-1293, 2007.
- [2.15] D. Israel, R. Baets, M. J. Goodwin, N. Shaw, M. D. Salik, and C. J. Groves-Kirkby, "Comparison of different polymeric multimode star couplers for backplane optical interconnect," *Lightwave Technology, Journal of*, vol. 13, no. 6, pp. 1057-1064, 1995.
- [2.16] E. Bosman, G. Van Steenberge, P. Geerinck, W. Christiaens, J. Vanfleteren, and P. Van Daele, "Embedding of optical interconnections in flexible electronics," IEEE, pp. 1281-1287, 2007.
- [2.17] G. L. Bona, B. J. Offrein, U. Bapst, C. Berger, R. Beyeler, R. Budd, R. Dangel, L. Dellmann, and F. Horst, *Characterization of parallel optical-interconnect waveguides integrated on a printed circuit board* Proceedings of the society of photo-optical instrumentation engineers (SPIE), pp. 134-141, 2004.
- [2.18] A. McCarthy, H. Suyal, and A. C. Walker, "45 degrees out-of-plane turning mirrors for optoelectronic chip carriers based on multimode polymer waveguides," *Eur. Conf. Opt. Communication*, pp. 808-809, September 2004.
- [2.19] D. Gwyer, P. Misselbrook, C. Bailey, P. P. Conway, and K. Williams, "Polymer waveguide and VCSEL array multi-physics modelling for OEBC based optical backplanes [opto-electrical circuit boards]," IEEE, Thermal and Mechanical Simulation and Experiments in Microelectronics and Microsystems. pp. 399-406, 2004.
- [2.20] Exxelis Ltd, "[www.exxelis.com](http://www.exxelis.com)," November 2007.
- [2.21] A. L. Glebov, M. G. Lee, and K. Yokouchi, *10+Gb/s board-level optical interconnects: Fabrication, assembly, and testing - art. no. 618501* Proceedings of the society of photo-optical instrumentation engineers (SPIE), p. 1850, 2006.

- [2.22] A. L. Glebov, M. G. Lee, and K. Yokouchi, "Integration technologies for pluggable backplane optical interconnect systems," *Optical Engineering*, vol. 46, no. 1 2007.
- [2.23] N. A. Jokerst, T. K. Gaylord, E. Glytsis, M. A. Brooke, S. Cho, T. Nonaka, T. Suzuki, D. L. Geddis, J. Shin, R. Villalaz, J. Hall, A. Chellapa, and M. Vrazel, "Planar lightwave integrated circuits with embedded actives for board and substrate level optical signal distribution," *IEEE Transactions on Advanced Packaging*, vol. 27, no. 2, pp. 376-385, 2004.
- [2.24] S. Y. Cho, S. W. Seo, N. M. Jokerst, and M. A. Brooke, "Board-level optical interconnection and signal distribution using embedded thin-film optoelectronic devices," *Journal of Lightwave Technology*, vol. 22, no. 9, pp. 2111-2118, 2004.
- [2.25] T. Suzuki, T. Nonaka, N. Ogawa, S. Y. Cho, S. W. Seo, and N. M. Jokerst, *Embedded optical interconnections on printed wiring boards* IEEE, 54TH Electronic components & technology conference, 2004, pp. 1524-1529.
- [2.26] Gee-Kung Chang, Daniel Guidotti, and Yin-Jung Chang, "Chip-to-Chip Optoelectronics SOP on Organic Boards or Packages," *IEEE Transactions on Advanced Packaging*, vol. 27, no. 2 May 2004.
- [2.27] Y.S.Liu, R.J.Wojnarowski, W.A.Hennessy, P.A.Piacente, J.Rowlette, and M.Kadar-Kallen, "Plastic VCSEL Array Packaging and High Density Polymer Waveguides for Board and Backplane Optical Interconnect," *IEEE Electronic Components and Technology Conference*, May 1998.
- [2.28] Y. S. Liu, R. J. Wojnarowski, W. A. Hennessy, P. A. Piacente, J. Rowlette, M. Kadar-Kallen, J. Stack, Y. Liu, A. Peczalski, and A. Nahata, *High density optical interconnect using polymer waveguides interfaced to VCSEL array in molded plastic packaging* Proceedings of the society of photo-optical instrumentation engineers (SPIE), pp. 60-72, 1998.
- [2.29] L. Eldada and L. W. Shacklette, "Advances in polymer integrated optics," *Ieee Journal of Selected Topics in Quantum Electronics*, vol. 6, no. 1, pp. 54-68, 2000.
- [2.30] S. Hiramatsu and T. Mikawa, "Optical design of active interposer for high-speed chip level optical interconnects," *Journal of Lightwave Technology*, vol. 24, no. 2, pp. 927-934, 2006.
- [2.31] S. Hiramatsu and M. Kinoshita, "Three-dimensional waveguide arrays for coupling between fiber-optic connectors and surface-mounted optoelectronic devices," *Journal of Lightwave Technology*, vol. 23, no. 9, pp. 2733-2739, 2005.
- [2.32] I. K. Cho, K. B. Yoon, S. H. Alm, H. K. Sung, S. W. Ha, Y. U. Heo, and H. H. Park, "Experimental demonstration of 10 Gbit/s transmission with an optical backplane system using optical slots," *Optics Letters*, vol. 30, no. 13, pp. 1635-1637, 2005.



- [2.33] S. H. Ahn, I. K. Cho, S. P. Han, K. B. Yoon, and M. S. Lee, "Demonstration of high-speed transmission through waveguide-embedded optical backplane," *Optical Engineering*, vol. 45, no. 8 2006.
- [2.34] I. K. Cho, K. B. Yoon, S. H. Ahn, M. Y. Jeong, H. K. Sung, B. H. Lee, Y. U. Heo, and H. H. Park, "Board-to-board optical interconnection system using optical slots," *IEEE Photonics Technology Letters*, vol. 16, no. 7, pp. 1754-1756, 2004.
- [2.35] K. B. Yoon, I. K. Cho, S. H. Ahn, N. Y. Jeong, D. J. Lee, Y. U. Heo, B. S. Rho, H. H. Park, and B. H. Rhee, "Optical backplane system using waveguide-embedded PCBs and optical slots," *Journal of Lightwave Technology*, vol. 22, no. 9, pp. 2119-2127, 2004.
- [2.36] B. S. Rho, S. Kang, H. S. Cho, H. H. Park, S. W. Ha, and B. H. Rhee, "PCB-compatible optical interconnection using 45 degrees-ended connection rods and via-holed waveguides," *Journal of Lightwave Technology*, vol. 22, no. 9, pp. 2128-2134, 2004.
- [2.37] J. Moisel, H. P. Huber, J. Guttmann, O. Krumpholz, B. Lunitz, M. Rode, and R. Schoedlbauer, "Optical Communication, 2001.ECOC'01.27th European Conference on Optical backplane," 3 ed IEEE, pp. 254-255, 2001.
- [2.38] D. Krabe, F. Ebling, N. Arndt-Staufenbiel, G. Lang, and W. Scheel, "New technology for electrical/optical systems on module and board level: The EOCB approach," IEEE, 50th Electronic Components and Technology Conference, pp. 970-974, 2000.
- [2.39] E. Griese, "A high-performance hybrid electrical-optical interconnection technology for high-speed electronic systems," *IEEE Transactions on Advanced Packaging*, vol. 24, no. 3, pp. 375-383, 2001.
- [2.40] E. Griese, "Optical interconnection technology on the printed circuit board level: fundamentals, technology, design," IEEE, Photonics and Microsystems, pp. 39-43, 2005.
- [2.41] R. Dangel, C. Berger, R. Beyeler, L. Dellmann, M. Gmur, R. Hamelin, F. Horst, T. Lamprecht, T. Morf, and S. Oggioni, "Polymer-waveguide-based board-level optical interconnect technology for datacom applications," *Advanced Packaging, IEEE Transactions on*, vol. 31, no. 4, pp. 759-767, 2008.
- [2.42] M. E. Teitelbaum, R. Nair, D. J. O'Brien, E. D. Wetzel, and K. W. Goossen, "Cost-effective integration of plastic optical fiber and total internal reflection mirrors in printed circuit boards for parallel optical interconnects," *Optical Engineering*, vol. 49, no. 6, pp. 456-461, 2010.
- [2.43] N. Bamiedakis, J. Beals, IV, R. V. Penty, I. H. White, J. V. DeGroot, and T. V. Clapp, "Cost-Effective Multimode Polymer Waveguides for High-Speed On-Board Optical Interconnects," *IEEE Journal of Quantum Electronics*, vol. 45, no. 4, pp. 415-424, 2009.

- [2.44] K. Wang, D. R. Selviah, J. Papakonstantinou, G. Yu, H. Baghsiahi, and F. A. Fernandez, "Photolithographically manufactured acrylate polymer multimode optical waveguide loss design rules," *Proceedings - 2008 2nd Electronics Systemintegration Technology Conference, ESTC*, pp. 1251-1255, 2008.
- [2.45] I. Papakonstantinou, K. Wang, D. R. Selviah, and F. Anibal Fernandez, "Transition, radiation and propagation loss in polymer multimode waveguide bends," *Optics Express*, vol. 15, no. 2, pp. 669-679, 2007.
- [2.46] D. A. Zauner, A. M. Jorgensen, and T. A. Anhoj, "High-density multimode integrated polymer optics," *Journal of Optics A: Pure and Applied Optics*, vol. 7, p 445, 2005.
- [2.47] M. G. Daly, P. E. Jessop, and D. Yevick, "Crosstalk reduction in intersecting rib waveguides," *Lightwave Technology, Journal of*, vol. 14, no. 7, pp. 1695-1698, 1996.
- [2.48] P. Sanchis, P. Villalba, F. Cuesta, Anderas Hakansson, and Amadeu Griol., "Highly efficient crossing structure for silicon-on-insulator waveguides," *Optics Letters*, vol. 34, no. 18, pp. 2760-2762, 2009.
- [2.49] H. Ma, A. K. Y. Jen, and L. R. Dalton, "Polymer-based optical waveguides: materials, processing, and devices," *Advanced Materials*, vol. 14, no. 19, pp. 1339-1365, 2002.
- [2.50] Y. Jiao, S. F. Mingaleev, M. Schillinger, D. A. B. Miller, S. Fan, and K. Busch, "Wannier basis design and optimization of a photonic crystal waveguide crossing," *Photonics Technology Letters, IEEE*, vol. 17, no. 9, pp. 1875-1877, 2005.
- [2.51] W. Bogaerts, P. Dumon, D. V. Thourhout, and R. Baets, "Low-loss, low-cross-talk crossings for silicon-on-insulator nanophotonic waveguides," *Optics Letters*, vol. 32, no. 19, pp. 2801-2803, 2007.
- [2.52] H. Liu, H. Tam, P. K. A. Wai, and E. Pun, "Low-loss waveguide crossing using a multimode interference structure," *Optics communications*, vol. 241, no. 1, pp. 99-104, 2004.
- [2.53] R. Dangel, U. Bapst, C. Berger, R. Beyeler, L. Dellmann, F. Horst, B. Offrein, and G. L. Bona, "Development of a low-cost low-loss polymer waveguide technology for parallel optical interconnect applications," *IEEE, Biophotonics/Optical Interconnects and VLSI Photonics/WBM Microcavities*, 2004.
- [2.54] T. Sakamoto, H. Tsuda, M. Hikita, T. Kagawa, K. Tateno, and C. Amano, "Optical interconnection using VCSELs and polymeric waveguide circuits," *Journal of Lightwave Technology*, vol. 18, no. 11, pp. 1487-1492, 2000.
- [2.55] M. A. Popovic, E. P. Ippen, and F. X. Kartner, "Low-loss Bloch waves in open structures and highly compact, efficient Si waveguide-crossing arrays," *IEEE LEOS, Lasers and Electro-Optics Society*, pp. 56-57, 2007.

- [2.56] I. Papakonstantinou, D. R. Selviah, and F. A. Fernandez, "Multimode polymer bent tapered waveguide modeling," 2 ed, pp. 983-984, 2004.
- [2.57] N. Bamiedakis, J. Beals, IV, R. V. Penty, I. H. White, J. V. DeGroot, and T. V. Clapp, "Cost-Effective Multimode Polymer Waveguides for High-Speed On-Board Optical Interconnects," *IEEE Journal of Quantum Electronics*, vol. 45, no. 4, pp. 415-424, 2009.
- [2.58] I. Papakonstantinou, D. R. Selviah, K. Wang, R. A. Pitwon, K. Hopkins, and D. Milward, "Optical 8-channel, 10 Gb/s MT pluggable connector alignment technology for precision coupling of laser and photodiode arrays to polymer waveguide arrays for optical board-to-board interconnects," *Proceedings - Electronic Components and Technology Conference*, pp. 1769-1775, 2008.
- [2.59] I. Papakonstantinou, D. R. Selviah, R. C. A. Pitwon, and D. Milward, "Low-Cost, Precision, Self-Alignment Technique for Coupling Laser and Photodiode Arrays to Polymer Waveguide Arrays on Multilayer PCBs," *IEEE Transactions on Advanced Packaging*, vol. 31, no. 3, pp. 502-511, 2008.
- [2.60] I. Papakonstantinou, D. R. Selviah, K. Wang, R. A. Pitwon, K. Hopkins, and D. Milward, "Optical 8-channel, 10 Gb/s MT pluggable connector alignment technology for precision coupling of laser and photodiode arrays to polymer waveguide arrays for optical board-to-board interconnects," *Electronic Components and Technology Conference, 2008. ECTC 2008. 58th*, pp. 1769-1775, 2008.
- [2.61] H. Baghsiahi, D. R. Selviah, G. Yu, K. Wang, M. Yau, and F. A. Fernandez, "Photolithographically manufactured acrylate multimode optical waveguide translation and rotation misalignment tolerances," *Proceedings- 2008 2nd Electronics System Integration Technology Conference, ESTC*, pp. 617-621, 2008.
- [2.62] B. Huang, J. Chen, and W. S. Jiang, "Effects of Surface Roughness on TE Modes in Rectangular Waveguide," *Journal of Infrared Millimeter and Terahertz Waves*, vol. 30, no. 7, pp. 717-726, 2009.
- [2.63] J. M. Sotocrespo and M. Nietovesperinas, "Electromagnetic Scattering from Very Rough Random Surfaces and Deep Reflection Gratings," *Journal of the Optical Society of America A-Optics Image Science and Vision*, vol. 6, no. 3, pp. 367-384, 1989.
- [2.64] A. A. Maradudin, T. Michel, A. R. McGurn, and E. R. Mendez, "Enhanced Backscattering of Light from A Random Grating," *Annals of Physics*, vol. 203, no. 2, pp. 255-307, 1990.
- [2.65] V. Celli, T. Tong, and P. Tran, "Light-Scattering from A Randomly Oriented Anisotropic Layer on A Rough-Surface," *Journal of the Optical Society of America A-Optics Image Science and Vision*, vol. 11, no. 2, pp. 716-722, 1994.

CHAPTER2: *Polymer Waveguide Interconnects for Optical Backplane Review*

- [2.66] A. Marvin, F. Toigo, and V. Celli, "Light-Scattering from Rough Surfaces - General Incidence Angle and Polarization," *Physical Review B*, vol. 11, no. 8, pp. 2777-2782, 1975.
- [2.67] A. A. Maradudin and E. R. Mendez, "Light scattering from randomly rough surfaces," *Science progress*, vol. 90, no. Pt 4, pp. 161-221, 2007.
- [2.68] M. Saillard and D. Maystre, "Scattering from Metallic and Dielectric Rough Surfaces," *Journal of the Optical Society of America A-Optics Image Science and Vision*, vol. 7, no. 6, pp. 982-990, 1990.
- [2.69] J.A.Sánchez-Gil and M.Nieto-Vesperinas, "Light scattering from random rough dielectric surfaces," *J. Opt. Soc.*, vol. 8, no. 8, pp. 1270-1286, 1991.
- [2.70] D. Maystre, "Rigorous theory of light scattering from rough surfaces," *Optics*, vol. 15, no. 1, pp. 43-51, 1984.
- [2.71] T. Kawanishi, H. Ogura, and Z. L. Wang, "Scattering of an electromagnetic wave from a slightly random dielectric surface: Yoneda peak and Brewster angle in incoherent scattering," *Waves in Random Media*, vol. 7, no. 3, pp. 351-384, 1997.
- [2.72] F. Morichetti, "Roughness Induced Backscattering in Optical Silicon Waveguides," *Physical Review Letters*, vol. 104, no. 3, 2010.
- [2.73] R. Schiffer, "Reflectivity of A Slightly Rough-Surface," *Applied Optics*, vol. 26, no. 4, pp. 704-712, 1987.
- [2.74] J. Nakayama, "Reflection, Diffraction and Scattering at Low Grazing Angle of Incidence: Regular and Random Systems," *Ieice Transactions on Electronics*, vol. E94C, no. 1, pp. 2-9, 2011.
- [2.75] S. O. Rice, "Reflection of Electromagnetic Waves from Slightly Rough Surfaces," *Communications on Pure and Applied Mathematics*, vol. 4, no. 2-3, pp. 351-378, 1951.
- [2.76] Born and Wolf., *Principle of Optics*, pp. 401-428, 1965.
- [2.77] D. Maystre, E.C.Mate, and A. Roger, "A new electromagnetic theory for scattering from shallow rough surface," *Optica Acta*, February 1984.
- [2.78] Beckmann P and Spizzichino, *The Scattering of Electromagnetic Waves from Rough Surfaces* Norwood, MA: Artech House Publishers, 1987.
- [2.79] M. W. Pruessner, N. Siwak, K. Amarnath, S. Kanakaraju, W. H. Chuang, and R. Ghodssi, "End-coupled optical waveguide MEMS devices in the indium phosphide material system," *Journal of Micromechanics and Microengineering*, vol. 16, no. 4, pp. 832-842, 2006.

- [2.80] H. W. Martin, *Fiber optics standard dictionary*, 1 ed Birkhauser, pp. 391-395, 2010.
- [2.81] S. K. Popalghat, A. Chaudhari, and P. B. Patil, "Effect of surface roughness on electromagnetic propagation through waveguides," *Indian Journal of Pure & Applied Physics*, vol. 37, no. 11, pp. 848-852, 1999.
- [2.82] D. Fischer and E. Voges, "Multimode polymeric waveguide devices fabricated by two-component injection moulding," *Electronics Letters*, vol. 33, no. 19, pp. 1626-1627, 1997.
- [2.83] H. Schroder, N. Arndt-Staufenbiel, A. Beier, F. Ebling, M. Franke, E. Griese, S. Intemann, J. Kostelnik, T. Kuhler, and R. Modinger, "Thin glass based electrical-optical circuit boards (EOCB) using ion-exchange technology for graded-index multimode waveguides," ECTC Electronic Components and Technology Conference, pp. 268-275, 2008.
- [2.84] C. A. Jones and K. Cooper, "Hybrid integration onto silicon motherboards with planar silica waveguides," *Optoelectronics, IEEE Proceedings*, vol. 143, no. 5, pp. 316-321, 1996.
- [2.85] M. A. Rosa, N. Q. Ngo, D. Sweatman, S. Dimitrijevic, and H. B. Harrison, "Self-alignment of optical fibers with optical quality end-polished silicon rib waveguides using wet chemical micromachining techniques," *Selected Topics in Quantum Electronics, IEEE Journal of*, vol. 5, no. 5, pp. 1249-1254, 1999.
- [2.86] Y. S. Liu, R. J. Wojnarowski, W. A. Hennessy, P. A. Piacente, J. Rowlette, M. Kadar-Kallen, J. Stack, Y. Liu, A. Peczalski, and A. Nahata, *High density optical interconnect using polymer waveguides interfaced to VCSEL array in molded plastic packaging* SPIE-INT Society of optical Engineering, pp. 60-72, 1998.
- [2.87] M. Hikita, R. Yoshimura, M. Usui, S. Tomaru, and S. Imamura, "Polymeric optical waveguides for optical interconnections," *Thin Solid Films*, vol. 331, no. 1-2, pp. 303-308, 1998.
- [2.88] A. L. Glebov, M. G. Lee, and K. Yokouchi, "Integration technologies for pluggable backplane optical interconnect systems," *Optical Engineering*, vol. 46, p. 5403, 2007.
- [2.89] S. Cvetkovic, C. Morsbach, and L. Rissing, "Ultra-precision dicing and wire sawing of silicon carbide (SiC)," *Microelectronic Engineering*, vol. 88, no. 8, pp. 2500-2504, 2011.
- [2.90] M. Komatsu, "Machining Performance of A Router Bit in the Peripheral Milling of Wood .2. Effects of the Helix Angle of the Peripheral Cutting-Edge on the Cutting Force and Machined-Surface Roughness," *Mokuzai Gakkaishi*, vol. 40, no. 2, pp. 134-141, 1994.

CHAPTER2: *Polymer Waveguide Interconnects for Optical Backplane Review*

- [2.91] H. Kamata and T. Kanauchi, "Analysis of Machined Surfaces with Distal Image-Processing .1. Effect of Grain Angle in Numerical Control Router Machining," *Mokuzai Gakkaishi*, vol. 39, no. 11, pp. 1253-1258, 1993.
- [2.92] B. Huang, J. Chen, and W. Jiang, "Effects of Surface Roughness on TE Modes in Rectangular Waveguide," *Journal of Infrared, Millimeter and Terahertz Waves*, vol. 30, no. 7, pp. 717-726, 2009.
- [2.93] K. K. Lee, D. R. Lim, H. C. Luan, A. Agarwal, J. Foresi, and L. C. Kimerling, "Effect of size and roughness on light transmission in a Si/SiO<sub>2</sub> waveguide: Experiments and model," *Applied Physics Letters*, vol. 77, no. 11, pp. 1617-1619, 2000.
- [2.94] A. Sakai, T. Fukazawa, and T. Baba, "Low loss ultra-small branches in a silicon photonic wire waveguide," *IEICE transactions on electronics*, vol. 85, no. 4, pp. 1033-1038, 2002.

## **Chapter 3: Waveguides, Lightguides and Lightpipes in Laser-illuminated Display Systems Review**

### **3.1 Introduction**

In this chapter, previous research on the use of optical waveguides in laser display systems is reviewed. Laser-illuminated displays have been under development since shortly after the invention of the first lasers in 1960 and many companies and researchers have developed systems which use lasers as the light source. There is considerable interest in laser-based projection displays due to their advantages of expanded colour gamut, high resolution and longer life time (compared to displays using ultra high performance (UHP) lamps as their illumination source) [3.1-3]. Lasers benefit from excellent monochromaticity which provides the high colour gamut and their beams are polarised so they can be very efficient when used in conjunction with liquid crystal components. They have a long lifetime and their power output does not degrade over time so the image remains high quality throughout their life span. However, most of these advantages come at the expense of cost, size and speckle [3.4].

Despite the benefits of laser-based display systems there are currently not many laser displays on the market. Mitsubishi reported a system called ‘Laser Vue’ [3.3] where they made their own lasers; it was on the market for a short time but they stopped producing the lasers for no clear reason. Other companies such as Sharp, LG, HDI and Sony have their own systems for laser display projectors [3.3]. Barco Technology has reported a light engine with 300 lumen output using lasers made by OSRAM and Oxxius [3.5]. Figure 3.1 shows a picture of the Barco display system in operation.



Figure 3.1: The laser projector demonstrated by Barco Technology[3.5]. The picture in the top left corner in the image is projected by a laser based projection system.

These systems, along with several other designs and patented systems [3.6-11] show great potential for this industry despite the inherent problems mentioned.

The problem with using lasers as the light source are the high price and the low efficiency. The price of a laser principally depends on its power and the price increases considerably when the optical output is more than a few milli-watts. There are different types of laser with the output wavelength in the visible range of the electromagnetic spectrum but not all of these are high power (high power in this thesis is defined as an optical power of more than 1 W for each colour) or are suitable for display applications. Argon lasers are able to provide high optical output power but are not suitable due to their large size and low efficiency [3.12]; the lasers are large (the length of the laser is about one metre for the 2-3 W laser) as the gas tube needs to be large due to the need for pumping and the demand for high optical power output. Solid-state lasers and diode lasers are the preferred candidate in display applications as they are capable of producing sufficient power as well as keeping the module compact and having good beam parameters. Diode pumped solid-state (DPSS) lasers are able to produce the necessary optical output with a high beam quality, however, the price of these lasers is high compared to other available illumination systems such as discharge lamp or LED systems [3.3]. This makes them unsuitable for commercial applications.

Another problem with laser-based display systems is speckle which is due to the high degree of coherence of laser light. Spatial and temporal speckle patterns reduce the image quality by producing an image with a granulated pattern. Speckle is an optical phenomenon due to the interference of multiple overlapping coherently related waves in a volume of space such that they



add constructively and destructively to give random patterns of bright and dark spots. The multiple overlapping waves can be caused when coherent light is scattered or reflected from a rough surface or transmitted through a rough or diffractive surface or when coherently related beams arrive in the same volume of space at different angles. If the wavefronts of the intersecting beam have passed through some randomly phase perturbing medium such as convection currents in air, the interference patterns will be random and may change in time if the perturbing medium changes in time. The degree of coherence quantified by the coherence length or coherence time is inversely proportional to the laser spectral bandwidth [3.4;11;13;14].

Another drawback of using lasers as the light source in the display system, in particular, for home display systems, is laser safety. The lasers need to be high power to provide sufficient optical energy at the output so the safety issues of using lasers in contact with human users are more considerable. All the lasers used in display projectors are in class three or four laser safety categories due to the power required. The main hazards of the lasers are the effects on the human eye and skin; lasers can damage the cornea and retina, can cause permanent blindness [3.15] and also can burn the skin and cause other problems such as inflammation or even skin carcinogenesis if there is IR or UV leakage from the laser. Lasers in display systems should be filtered for UV and IR radiation but there might still be some leakage, particularly with IR frequency doubled lasers [3.3;15].

There are several solutions proposed to solve the various drawbacks of using lasers, for example; improving the optical design to reduce the optical losses to increase the efficiency of the system and using several different mechanical and optical methods to remove the speckle.

Laser safety, speckle reduction and efficiency of the system are affected by introducing optical waveguides into the light engine of the display system. Optical waveguides have previously been used in display systems but new methods of using them, specifically in 3D display systems, have not been investigated [3.16;17] and form the subject of the new research reported later in this thesis in which new solutions to the problems created by using optical waveguides are investigated.

## **3.2 Review of Using Waveguides in Display Systems and Power Homogenisation**

Optical waveguides have been used in many industries and the display industry is one area where there has been increasing penetration in recent years. Fibre bundles have been used as integrators for projectors with laser or LED illumination [3.18;19]. Kai Wang and David R. Selviah at UCL introduced a liquid crystal display, LCD, colour-separating backlight that optimised efficiency by inserting a micromirror array within a light guide [3.20]. Waveguides are used to transfer light and increase the efficiency of the light engine by preventing light loss. The waveguide gathers the emitted light in all directions around the light source and delivers it to the designed apertures. Total internal reflection in the waveguides or light pipes is used to achieve colour and power uniformity [3.21;22]. Tapered waveguides have been investigated to increase uniformity in the light delivered [3.7;23] and power splitting and combining have been performed using circular waveguides such as larger optical fibres [3.24]. Fibres of lengths from a few millimetres to one metre have been used as well as lightguides and waveguides of rectangular or circular cross section [3.25].

Advances in projection displays and growth in display applications has demanded more miniaturisation in micro-projection displays which are flexible and can be adapted to different shapes and implemented in other devices such as a smart mobile phones[3.26;27]. Micro electro mechanical systems (MEMS) are able to provide high definition frames and digital micro-mirror devices (DMD), that are examples of MEMS components, have already been employed in digital light processor (DLP)-based projectors [3.28;29]. Scanning micro-mirror projectors (SMP) are another example of MEMS devices employed in micro-projectors [3.29-31]. SMPs employ a colour combiner and modulated light source and recently a commercial compact SMP which can be implemented in a mobile communication device has been introduced by MicroVision [3.32]. The colours are combined by a dichroic prism in these pico-projectors and this limits the reduction in overall size. Waveguides have been used to form an active electro-optically modulated, integrated-optical colour mixing device [3.33]. In Figure 3.2 the lasers are coupled into single-mode channel waveguides and are mixed after modulation by electro-optic Mach-Zehnder-Interferometer (MZI) modulators.

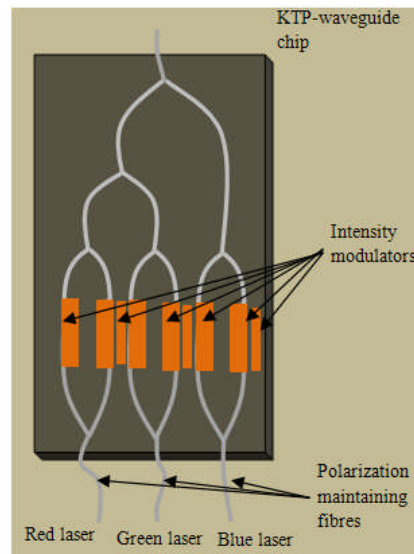


Figure 3.2: Colour image generation using an integrated optical three-colour mixing waveguide [3.33].

In a similar colour mixing arrangement (Figure 3.3), single-mode channel waveguides are used to combine three RGB lasers into a single waveguide. The waveguides are made of SU-8 which is an epoxy based photoresist material and the light is coupled into them and then combined by a  $3 \times 1$  planar waveguide [3.29]. The colour temperature can be adjusted by adjusting the R, G and B luminance of the light sources.

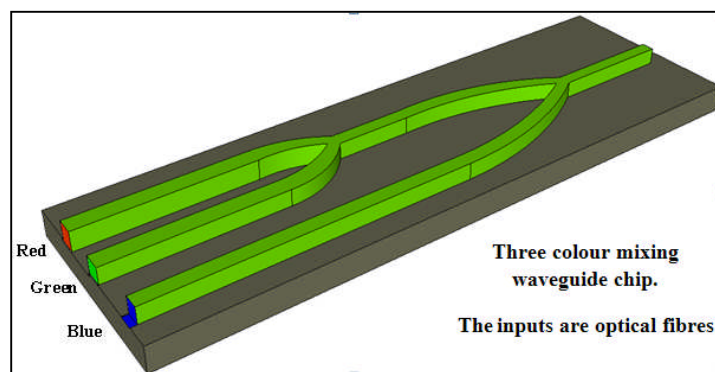


Figure 3.3: Three-colour mixing waveguide device used by Ju-Nan Kuo in an optical projection display system. Lasers are coupled into the waveguides by using single-mode fibres [3.29].

Optical waveguides are suitable for micro-optic or nano-optic technologies. Flexible waveguides can be used as a colour combiner and due to the flexibility of the device they can be designed to be embedded in any display structure [3.34]. Despite highly sophisticated technological

achievements in optical fibres and waveguides, most of the work carried out has been in IR optical communication applications and very little has been reported in visible spectrum applications. Recently a fibre optic colour synthesizer (FOCS) based on a 1×3 hard plastic cladding fibre (HPCF) coupler which can be used in a micro-scanning display has been reported by Y. Jeong [3.35]. However, all of the fibre optic colour synthesizer or waveguide colour synthesizer methods that are explained in references [3.29;36;37] that use single-mode waveguides and have reduced coupling efficiency due to their small cross sectional size.

Single mode fibre optics have been used for homogenization in research by Xijia Gu where an optical fibre with a Long Period Grating (LPG) for changing a Gaussian beam into a top hat profile is used[3.38]. In this research, the LPG is used to couple the core modes into low order modes in the cladding to achieve a uniform intensity away from the fibre by interfering these two modes. This work has been carried out in the IR region.

Slab waveguides have been considered for homogenising high power laser diodes [3.39]. In this research a source with 200  $\mu\text{m}$  width is used in a ray tracing simulation and its light is coupled into a slab waveguide with 10 mm width and 200 mm length. They conclude that achieving homogenised output using a waveguide is more independent of the original laser beam compared to using micro-optics and also there is better conservation of the beam quality after homogenisation. However, the micro-optics are smaller compared to the slab waveguide that they used which had dimensions of 10 mm  $\times$  200 mm. The laser comprised a diode laser array with emitters arranged in a row and a set of mirrors to rearrange the laser beam [3.39]. The results show good homogenisation (94 %).

Waveguides have also been used as mode scramblers for changing Gaussian beams into a top hat profile [3.40] and in another device called Kaleidoscope, light pipes are used for changing the profile of a Gaussian laser into a more uniform intensity distribution. High power lasers (2 kW CO<sub>2</sub> laser) were used in this work and the light pipe was 5.28 cm  $\times$  11.18 cm  $\times$  94.5 cm. Figure 3.4 shows a schematic diagram from the system. As shown in this figure, a lens system is used to diverge the laser beam and then it is homogenised by propagating inside the waveguide. Waveguides of this size are not justified in display systems.

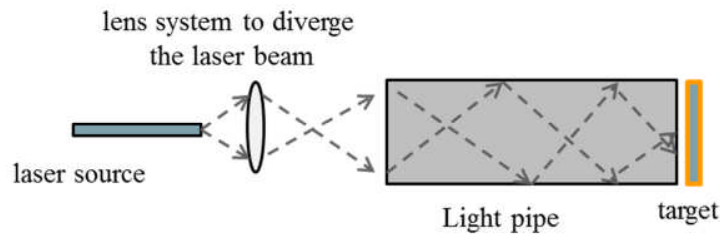


Figure 3.4: Kaleidoscope used for homogenizing a high power laser beam

Research has been carried out on waveguides for head mounted display (HMD) systems in the South University of Taiwan in collaboration with the University of Washington[3.16]. HMD systems are mounted on the head of the viewer and are worn like a helmet or glasses. They can be referred to a micro-displays as the optical and image forming system must be compact. Reducing the dimension of the display system is always beneficial in this application as it is lighter and more comfortable, however, reducing the size always comes with several difficulties such as possibly reducing the number of pixels and increasing diffraction which reduces the resolution of the image [3.16].

The group in Taiwan used an optical waveguide to develop a 2D display system using a micro-fabricated polymer-based cantilever waveguide. In this system, output light from a LED is coupled into an optical fibre which is connected to a specially designed waveguide. This is connected to a piezoelectric crystal which is triggered by an FPGA (field-programmable gate array) unit and voltage amplifier. The piezoelectric device is connected to the waveguide and performs as a scanner. The FPGA unit modulates the LED and sends a signal to the piezoelectric device to synchronize a raster scan to display the image created by the modulated LED. The waveguide is made of SU-8 which is an epoxy based photoresist [3.41] and the cross-section of the waveguide was  $54.4 \mu\text{m} \times 102.8 \mu\text{m}$ . This is relevant to the research in this thesis but the extension to use a laser source would create an additional speckle problem which would need to be overcome.

Ritsumeikan University in Japan has used waveguides as part of backlights for flexible displays. Their waveguides are layed out in a spiral shape and the light leaks away from the waveguide by fabricating several grooves on its surface [3.42]. They used a plastic optical fibre as the flexible waveguide [3.42] which was embedded in a spiral trench made on an Acrylate plate substrate

(Figure 3.5). The light was coupled out from the fibre at each of the grooves and a diffuser plate was used to make the illumination uniform with the grooves on the surface of the fibre acting as an array of point sources. Following the work of Kai Wang and David R. Selviah at UCL [3.20] who first proposed to put mirrors inside of lightguides, they also designed a branching planar waveguide with reflectors inside it to redirect the light outwards. This design was different to the spiral shape and effectively worked as a power divider and power distributor.

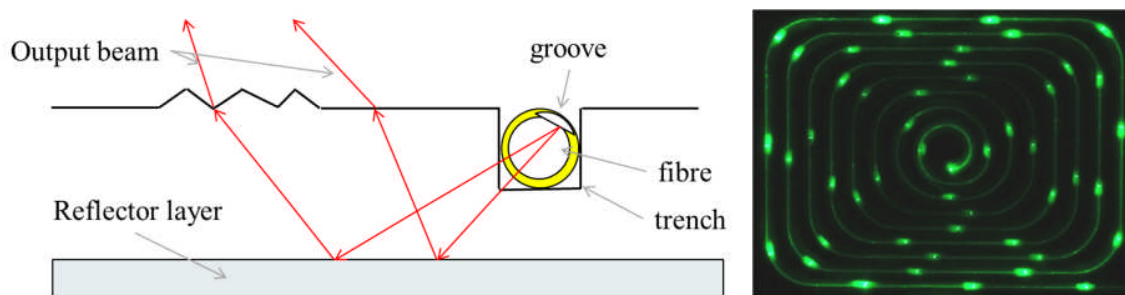


Figure 3.5: Cross section of a backlight using an optical fibre with several grooves (left), light emitted from a spiral fibre(right). The picture on the right was taken from ref. [3.42]

However, the difficulty of making the reflectors, grooves and inserting and aligning the waveguide means the fabrication cost will be high.

Eyal at Tel Aviv University in Israel attached a planar waveguide to an optical fibre by pressing a multimode fibre between metal plates while heating it [3.43]. They manufactured the waveguide for a different application (for 10.6  $\mu\text{m}$  wavelength) but what makes the work interesting here is that the planar waveguide was already pigtailed and the fibre coupling and means for aligning and attaching the fibre to the waveguide is not a concern. The problem with this configuration and method is that if the waveguide is to be multimode with a large diameter, such as required in chapter 5 (10 mm  $\times$  100  $\mu\text{m}$ ), the optical fibre must be large which reduces the flexibility of the system.

Waveguides in the form of light pipes, optical fibres, or specially designed glass or polymer waveguides have been used by researchers for power homogenisation, optical power transformation/distribution and colour combination. Chapters 8 and 9, describe our new research in which a slab waveguide is used with multi-emitter high power lasers to combine colours, homogenise the beams and shape the beams as well as reducing the perceptible speckle at the output of the waveguides.

### **3.3 Review of the use of Waveguides for Reducing Speckle in Display Systems**

The investigation of speckle is of importance in laser illuminated displays and is of more general use in other fields such as telecommunications. When coherent light, such as a laser beam is reflected from (or transmitted through) an optically rough surface, such as a paper, a wall or a screen, the scattered/transmitted light presents a fine granular structure in the intensity distribution. These fine-scale fluctuations of the intensity caused by interference effects, due to the coherence of the light source, are called speckle. The speckle is caused by differently angled rays or waves overlapping and constructively and destructively interfering in a volume of space [3.44]. Speckle tends to be distinguished from diffraction patterns, holograms and other coherent interference patterns in that it appears to be random and to have a fine granular structure and in some cases may move or change pattern as function of time. Speckle has a profound effect on the information that can be extracted from an image as it reduces the quality of the pictures by randomly modulating the intensity. Speckle can be disturbing to viewers of laser illuminated displays distracting their attention from the actual image being displayed. This is particularly a problem when the speckle moves or drifts very slowly but noticeably across the image.

For laser display systems, a major barrier to achieving high image quality is the laser speckle pattern so various methods have been tried to reduce the speckle contrast. Theoretical and experimental research, related to speckle patterns and different reduction methods, are explained in the literature [3.45-77]. Reduction of speckle contrast has been proposed using the following methods: widening the laser bandwidth [3.45;46;78-80], using a fibre for illumination [3.66;81;81], using a fibre bundle [3.65], superposition of a pulsed laser [3.61], diversity of space and wavelength with a spectrometer [3.60], modulation of a laser diode with the help of an optical feedback effect [3.57-59], using broadband continuous wave laser, a moving aperture [3.57;58], a moving diffuser [3.46], vibration in a fibre [3.46;56;72;82], liquid crystal [3.45;72] and many other methods.

Depending on the situation, more than one method may be required to reduce the speckle contrast to below the threshold of speckle perception by the observer. Contrast is a measure of the strength of the intensity fluctuation in the speckle pattern. Multimode waveguides support several modes which are different distributions of the power inside the waveguides. The

electromagnetic field propagating inside the waveguide is formed from the superposition of several individual modes [3.83;84]. Each mode propagates with its own generally different velocity inside the waveguide. From a geometrical optics point of view, various rays of a beam are coupled into a multimode waveguide with different angles to the axis of the guide. These rays propagate inside the waveguide along different paths with different path lengths thus giving a range of phase delays at the output of the waveguide. Therefore, as long as the phase delays between the modes are less than the coherence length of the light, the superposition of the rays produces an interference pattern. Each point of the optical field at the output of the waveguide is the superposition of several modes with different phase shifts. The number of the modes in a multimode step index fibre is:

$$M = 2 \left( \frac{\pi a (NA)}{\lambda} \right)^2$$

Where  $a$  is the radius of the fibre core and,  $\lambda$  is the wavelength of light, and NA is the numerical aperture of the fibre which is related to the refractive index different between the core and cladding material of the fibre.

A fibre with a higher numerical aperture or a higher ratio of core radius to the wavelength of light contains a larger number of modes [3.85]. Speckle patterns in the beam output from an optical fibre are important and have been studied for displays [3.45], biotechnology applications and tomography[3.86], holography[3.87], and modal or speckle noise in data communication links [3.88]. The coherence of light and the effect of a waveguide on the coherent light has been investigated since just after the invention of the laser [3.89]. Joseph Goodman investigated the speckle phenomenon in optical fibres, principally with regard to modal or speckle noise considerations [3.44;90]. Reduction of the speckle contrast by shaking the fibre and using mode scrambling techniques has been also reported [3.69;88;91]. Ultrasound transmitters have been used to reduce speckle in optical fibres[3.92], speckle patterns have been studied in both multimode step index fibre and in graded index fibres [3.85;93] and interesting work by Crosignani explores the relationship between the spectral bandwidth of the optical source and the length of the fibre on the speckle visibility [3.94]. Arranging for light sources having changing wavelengths or using light sources with wider spectra is another way to reduce the speckle either in fibre optics or in free space due to wavelength diversity[3.48].



Waveguides in the shape of light pipes have been used in conjunction with diffractive optical elements [3.95]. Light pipes were used to homogenize the output beams to give several uncorrelated speckle patterns. The speckle contrast of a multimode fibre and so the modal or speckle noise, has been investigated by Maystre in terms of the effect of the source spectrum for step index and graded index fibres [3.96]. It was shown that as the light becomes depolarised in the multimode fibre the speckle contrast is reduced by  $2^{1/2}$ . They also investigate the reduction of modal or speckle noise in long fibres due to loss of the coherence. They found that the reduction depends on the width of the individual longitudinal modes rather than the total width of the spectrum of the laser source [3.96].

Optical fibres are also used in the research of Toshiaki Iwai [3.45]. He carried out a mathematical investigation into speckle in coherent systems and used a rotating optical fibre (Figure 3.6) to reduce speckle noise by control of the spatial coherence. They also use a vibrator to shake the fibre.

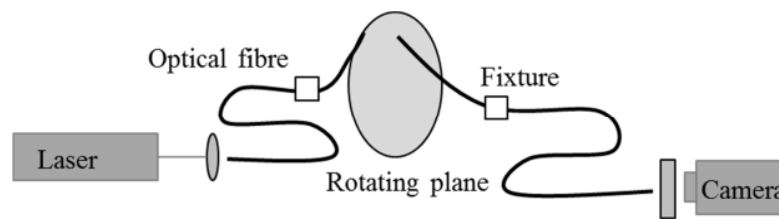


Figure 3.6: Schematic diagram of the experiment configuration for reducing speckle noise by rotation of a multimode fibre.

Most of the work on speckle in optical fibres suggests reduction methods such as vibrating the fibre in order to vary the speckle pattern with time. What is lacking is the investigation of the effect on speckle contrast reduction of waveguides with different sizes, and also discussions on the reduction of speckle contrast in display systems and other applications.

## References

- [3.1] M. Jansen, B. D. Cantos, G. P. Carey, R. Dato, G. Giaretta, S. Hallstein, W. R. Hitchens, D. Lee, *Visible laser and laser array sources for projection displays - art. no. 61350T* SPIE-INT Society of optical engineering, 2006, p. 1350.
- [3.2] G. Zheng, B. Wang, T. Fang, H. Cheng, Y. Qi, Y. W. Wang, "Laser Digital Cinema Projector," *Journal of Display Technology*, vol. 4, no. 3, pp. 314-318, 2008.
- [3.3] Kishore V.Chellappan, Erdem Erden, and Hakan Urey, "Laser Based Display," *Applied Optics*, vol. 49, no. 25, p. f 79-f 98, Mar 2010.
- [3.4] H. J. Park, J. P. Allebach, and Z. Pizlo, "Psychophysical investigation of the effect of coring on perceived toner scatter," *Journal of Electronic Imaging*, vol. 19, no. 1 2010.
- [3.5] P.Janssens and K.Malfait, "Future prospects of high-end laser projectors," *Photo-Optical Instrumentation Engineers, SPIE*, no. 3, pp. 253-257, 2009.
- [3.6] J. L. Jansson, T. P. Jansson, and J. M. Lerner, "Liquid crystal display system with internally reflecting waveguide for backlighting and non-Lambertian diffusing," Google Patents/ US5838403, 1998.
- [3.7] T. Shibatani, T. Shinomiya, T. Yamatani, H. Hamada, and H. Nakanishi, "Projection display system including a collimating tapered waveguide or lens with the normal to optical axis angle increasing toward the lens center," Google Patents US5459592, Oct.17, 1995.
- [3.8] M. A. Rockwell, "Optical waveguide display system," WO/1993/009450, Jan.21, 1997.
- [3.9] A. F. Kurtz, B. E. Kruschwitz, and S. Ramanujan, "Laser projection display system," Google Patents/US6577429, 2003.
- [3.10] M. Karakawa, "Monochromatic R, G, B laser light source display system and method," Google Patents/US6304237, 2001.
- [3.11] D. E. Hargis, C. G. Fink, R. A. Bergstedt, and G. W. Flint, "Multi-beam laser scanning display system with speckle elimination," Patent US6154259, Nov. 28, 2000.
- [3.12] U. Steegmuller, M. Kuhnelt, H. Unold, T. Schwarz, R. Schulz, K. Auen, C. Walter, and M. Schmitt, *Visible lasers for mobile projection - art. no. 70010D* SPIE-INT Society of optical engineering, p. D10, 2008.
- [3.13] Z. J. Liao, T. W. Xing, G. X. Cheng, and W. M. Lin, "Speckle reduction in laser projection display by modulating illumination light - art. no. 662229," *International Symposium on Photoelectronic Detection and Imaging 2007: Laser, Ultraviolet, and Terahertz Technology*, vol. 6622, p. 629, 2008.

CHAPTER 3: *Waveguides and Lightguides in Laser-illuminated Display Systems*

- [3.14] J. W. Goodman, "Some Fundamental Properties of Speckle," *Journal of the Optical Society of America*, vol. 66, no. 11, pp. 1145-1150, 1976.
- [3.15] D. Corder, J. O'Hagan, and J. Tyrer, "Safety assessments of visible scanned laser beams," *Journal of Radiological Protection*, vol. 17, no. 4, pp. 231-238, 1997.
- [3.16] C. Takahashi, H. J. Wang, W. S. Hua, P. Reinhall, and W. C. Wang, "Polymeric waveguide design of a 2D display system," *Proceedings of SPIE, the International Society for Optical Engineering*, pp. 219-223, 2006.
- [3.17] P. Surman, R. S. Brar, I. Sexton, and K. Hopf, *Muted and Helium3D Autostereoscopic Displays* IEEE International Conference on Multimedia and Expo, pp. 194-199, 2010.
- [3.18] E. H. S. Matthew S. Brennessoltz, *Projection Display second Edition*. JohnWiley & Sons Ltd, pp. 125-127, 2008.
- [3.19] H. Golnabi and A. Haghightzadeh, "Beam shape and intensity profile of a fiber-bundle prism-coupled waveguide," *Optics and Lasers in Engineering*, vol. 48, no. 6, pp. 720-726, 2010.
- [3.20] D. R. Selviah and K. Wang, "Modeling of a Color-Separating Backlight with Internal Mirrors," *SID International symposium digest of technical paper.*, vol. 35, pp. 487-489, 2004.
- [3.21] F. Fournier, W. J. Cassarly, and J. P. Rolland, "Method to improve spatial uniformity with lightpipes," *Optics Letters*, vol. 33, no. 11, pp. 1165-1167, 2008.
- [3.22] J. F. Van Derlofske, "Computer modeling of LED light pipe systems for uniform display illumination," *proc. SPIE*, vol. 45, pp. 119-129, 2001.
- [3.23] H. Murat, H. D. Smet, and D. Cuypers, "Compact LED projector with tapered light pipes for moderate light output applications," *Displays*, vol. 27, no. 3, pp. 117-123, 2006.
- [3.24] J. K. Kim, H. R. Kim, A. nerman, and K. Oh, "Synthesis of pure white color and its equal power, equal chromatic splitting through a novel 3x3 fiber optic visible multiplexer," *Opt. Express*, vol. 16, no. 22, pp. 17319-17328, 2008.
- [3.25] M. J. Large, T. Large, and A. R. L. Travis, "Parallel Optics in Waveguide Displays: A Flat Panel Autostereoscopic Display," *Journal of Display Technology*, vol. 6, no. 10, pp. 431-437, 2010.
- [3.26] T. Levola, "Stereoscopic near to eye display using a single microdisplay," *SID International Symposium, Digest of Technical Papers*, vol. 38, pp. 1158-1159, 2007.
- [3.27] Y. Okuda and I. Fujieda, "Polymer waveguide technology for flexible display applications," *Proceedings of SPIE*, vol. 8280, pp. 122-131, 2012.

### CHAPTER 3: Waveguides and Lightguides in Laser-illuminated Display Systems

- [3.28] D. Armitage, I. Underwood, and S. Wu, *Introduction to Microdisplays* John Wiley & Sons Ltd, West Sussex, 2006.
- [3.29] J. N. Kuo, H. W. Wu, and G. B. Lee, "Optical projection display systems integrated with three-color-mixing waveguides and grating-light-valve devices," *Optics Express*, vol. 14, no. 15, pp. 6844-6850, 2006.
- [3.30] A.K.Bhowmik, *Mobile displays: technology and applications* John Wiley & Sons Ltd, West Sussex, p. chap 21, 2008.
- [3.31] H. Schenk, P. Durr, D. Kunze, H. Lakner, and H. Kuck, "A resonantly excited 2D-micro-scanning-mirror with large deflection," *Sensors and Actuators A-Physical*, vol. 89, no. 1-2, pp. 104-111, 2001.
- [3.32] (Microvision)., "Pico projector displays: Embedded," [http://www.microvision.com/pico\\_projector\\_displays/standalone.html](http://www.microvision.com/pico_projector_displays/standalone.html), Nov. 2008.
- [3.33] J. P. Ruske, M. Rottschalk, B. Zeitner, V. Grober, and A. Rasch, "Integrated-optical three-colour-mixing device," *Electronics Letters*, vol. 34, no. 4, pp. 363-364, 1998.
- [3.34] L.Booth and A.Fisher, "Optical Interconnections using Polymer Waveguides," Optical InterLinks,<http://www.opticalinterlinks.com/pdf/Paper.Poly.WG.Conn.pdf>, Dec. 2007.
- [3.35] Y. Jeong, D. Lee, J. W. Lee, and K. Oh, "Fiber-optic color synthesizer," *Optics Letters*, vol. 31, no. 14, pp. 2112-2114, 2006.
- [3.36] Y. S. Jeong, S. C. Bae, Y. Jung, J. W. Lee, and K. Oh, "Fiber optic full color synthesizer," *2005 Conference on Lasers & Electro-Optics (CLEO), Vols 1-3*, pp. 624-626, 2005.
- [3.37] J. K. Kim, H. R. Kim, A. Tunnermann, and K. Oh, "Synthesis of pure white color and its equal power, equal chromatic splitting through a novel 3x3 fiber optic visible multiplexer," *Optics Express*, vol. 16, no. 22, pp. 17319-17328, 2008.
- [3.38] X. Gu, W. Mohammed, L. Qian, and P. W. E. Smith, "All-fiber laser beam shaping using a long-period grating," *Photonics Technology Letters, IEEE*, vol. 20, no. 13, pp. 1130-1132, 2008.
- [3.39] M. Traub, H. D. Hoffmann, H. D. Plum, K. Wieching, P. Loosen, and R. Poprawe, "Homogenization of high power diode laser beams for pumping and direct applications," *Spie*, vol. 6104, p. 610, 2006.
- [3.40] R. E. Grojean, D. Feldman, and J. F. Roach, "Production of flat top beam profiles for high energy lasers," *Review of Scientific Instruments*, vol. 51, p. 375, 1980.

### CHAPTER 3: Waveguides and Lightguides in Laser-illuminated Display Systems

- [3.41] H. Lorenz, M. Despont, N. Fahrni, N. LaBianca, P. Renaud, and P. Vettiger, "SU-8: a low-cost negative resist for MEMS," *Journal of Micromechanics and Microengineering*, vol. 7, p. 121, 1997.
- [3.42] Y. Okuda and I. Fujieda, *Polymer waveguide technology for flexible display applications*, SPIE, Advances in display technologies, pp. 122-131, 2012.
- [3.43] O. Eyal, V. Scharf, S. Shalem, and A. Katzir, "Single-mode mid-infrared silver halide planar waveguides," *Optics Letters*, vol. 21, no. 15, pp. 1147-1149, 1996.
- [3.44] Joseph W. Goodman, *Speckle Phenomena in Optics*, 1 ed Roberets and company, 2008.
- [3.45] T. Iwai and T. Asakura, "Speckle reduction in coherent information processing," *Proceeding of the IEEE*, vol. 84, no. 5, pp. 765-781, 1996.
- [3.46] J. W. Goodman, "Some Fundamental Properties of Speckle," *Journal of the Optical Society of America*, vol. 66, no. 11, pp. 1145-1150, 1976.
- [3.47] F. Riechert, G. Bastian, and U. Lemmer, "Laser speckle reduction via colloidal-dispersion-filled projection screens," *Applied Optics*, vol. 48, no. 19, pp. 3742-3749, 2009.
- [3.48] J. I. Trisnadi, "Speckle contrast reduction in laser projection displays," *Projection Displays*, vol. 4657, pp. 131-137, 2002.
- [3.49] A. Furukawa, N. Ohse, Y. Sato, "Effective speckle reduction in laser projection displays - art. no. 69110T," *Emerging Liquid Crystal Technologies Iii*, vol. 6911, p. 110, 2008.
- [3.50] W. H. Gao, V. Kartashov, G. M. Ouyang, Z. M. Tong, M. N. Akram, and X. Y. Chen, "The matrices used to reduce speckle in laser projector system," *Speckle 2010: Optical Metrology*, vol. 7387 2010.
- [3.51] V. Kartashov and M. N. Akram, "Speckle suppression in projection displays by using a motionless changing diffuser," *Journal of the Optical Society of America*, vol. 27, no. 12, pp. 2593-2601, 2010.
- [3.52] Z. M. Tong, M. N. Akram, and X. Y. Chen, "Speckle reduction using orthogonal arrays in laser projectors," *Applied Optics*, vol. 49, no. 33, pp. 6425-6429, 2010.
- [3.53] V. Kartashov and M. N. Akram, "Speckle suppression in projection displays by using a motionless changing diffuser," *Speckle 2010: Optical Metrology*, vol. 7387, pp. 232-235, 2010.
- [3.54] M. N. Akram, "Effect of projection lens numerical aperture and aberrations on speckle reduction in line-scan laser projectors," *Speckle 2010: Optical Metrology*, vol. 7387, pp. 112-115, 2010.

CHAPTER 3: *Waveguides and Lightguides in Laser-illuminated Display Systems*

- [3.55] M. N. Akram, Z. M. Tong, G. M. Ouyang, X. Y. Chen, and V. Kartashov, "Laser speckle reduction due to spatial and angular diversity introduced by fast scanning micromirror," *Applied Optics*, vol. 49, no. 17, pp. 3297-3304, 2010.
- [3.56] Y. Imai and Y. Ohtsuka, "Laser Speckle Reduction by Ultrasonic Modulation," *Optics Communications*, vol. 27, no. 1, pp. 18-22, 1978.
- [3.57] B. Goebel, L. L. Wang, and T. Tschudi, "Multilayer technology for diffractive optical elements," *Applied Optics*, vol. 35, no. 22, pp. 4490-4493, 1996.
- [3.58] R. W. Gerchber and W. O. Saxton, "Practical Algorithm for Determination of Phase from Image and Diffraction Plane Pictures," *Optik*, vol. 35, no. 2, p. 237, 1972.
- [3.59] N. George and A. Jain, "Speckle Reduction Using Multiple Tones of Illumination," *Applied Optics*, vol. 12, no. 6, pp. 1202-1212, 1973.
- [3.60] M. T. Gale, M. Rossi, H. Schutz, P. Ehbets, H. P. Herzig, and D. Prongue, "Continuous-Relief Diffractive Optical-Elements for 2-Dimensional Array Generation," *Applied Optics*, vol. 32, no. 14, pp. 2526-2533, 1993.
- [3.61] J. R. Fienup, "Iterative Method Applied to Image-Reconstruction and to Computer-Generated Holograms," *Optical Engineering*, vol. 19, no. 3, pp. 297-305, 1980.
- [3.62] L. L. Wang, T. Tschudi, T. Halldorsson, and P. R. Petursson, "Speckle reduction in laser projection systems by diffractive optical elements," *Applied Optics*, vol. 37, no. 10, pp. 1770-1775, 1998.
- [3.63] W. Thomas, C. Middlebrook, and J. Smith, "Laser Speckle Contrast Reduction Measurement Using Diffractive Diffusers," *Emerging Liquid Crystal Technologies*, vol. 7232, pp. 57-58, 2009.
- [3.64] S. An, A. Lapchuk, V. Yurlov, J. Song, H. Park, J. Jang, W. Shin, S. Kargapol'tsev, and S. K. Yun, "Speckle suppression in laser display using several partially coherent beams," *Optics Express*, vol. 17, no. 1, pp. 92-103, 2009.
- [3.65] DINGEL B, KAWATA S, "Speckle reduction with virtual incoherent laser illumination using a modified fiber array," *Optik*, vol. 94, no. 3, pp. 133-136, 1993.
- [3.66] Jutamulia.S, Asakura.T, and Amba.H, "Reduction of coherent noise using various artificial incoherent sources," *Optik*, vol. 70, pp. 52-57, Mar.1985.
- [3.67] F. T. S. Yu and E. Y. Wang, "Speckle Reduction in Holography by Means of Random Spatial Sampling," *Applied Optics*, vol. 12, no. 7, pp. 1656-1659, 1973.
- [3.68] T. S. Mckechni, "Reduction of Speckle by A Moving Aperture - Theory and Measurement," *Optik*, vol. 41, no. 1, pp. 34-44, 1974.

CHAPTER 3: *Waveguides and Lightguides in Laser-illuminated Display Systems*

- [3.69] Y. Kawagoe, N. Takai, and T. Asakura, "Speckle Reduction by A Rotating Aperture at the Fourier-Transform Plane," *Optics and Lasers in Engineering*, vol. 3, no. 3, pp. 197-218, 1982.
- [3.70] Y. Imai and Y. Ohtsuka, "Laser Speckle Reduction by Ultrasonic Modulation," *Optics Communications*, vol. 27, no. 1, pp. 18-22, 1978.
- [3.71] Y. Imai, M. Imai, and Y. Ohtsuka, "Optical Coherence Modulation by Ultrasonic-Waves .2. Application to Speckle Reduction," *Applied Optics*, vol. 19, no. 20, pp. 3541-3544, 1980.
- [3.72] P. Harihara and Z. S. Hegedus, "Reduction of Speckle in Coherent Imaging by Spatial Frequency Sampling .2. Random Spatial Frequency Sampling," *Optica Acta*, vol. 21, no. 9, pp. 683-695, 1974.
- [3.73] P. Harihara and Z. S. Hegedus, "Reduction of Speckle in Coherent Imaging by Spatial Frequency Sampling," *Optica Acta*, vol. 21, no. 5, pp. 345-356, 1974.
- [3.74] N. George and A. Jain, "Speckle Reduction Using Multiple Tones of Illumination," *Applied Optics*, vol. 12, no. 6, pp. 1202-1212, 1973.
- [3.75] S. M. Gehlbach and F. G. Sommer, "Frequency Diversity Speckle Processing," *Ultrasonic Imaging*, vol. 9, no. 2, pp. 92-105, 1987.
- [3.76] C. B. Burckhardt, "Speckle in Ultrasound B-Mode Scans," *IEEE Transactions on Sonics and Ultrasonics*, vol. 25, no. 1, pp. 1-6, 1978.
- [3.77] H. Ambar, Y. Aoki, N. Takai, and T. Asakura, "Fringe Contrast Improvement in Speckle Photography by Means of Speckle Reduction Using Vibrating Optical Fiber," *Optik*, vol. 74, no. 2, pp. 60-64, 1986.
- [3.78] G. E. Trahey, J. W. Allison, S. W. Smith, and O. T. Vonramm, "A Quantitative Approach to Speckle Reduction Via Frequency Compounding," *Ultrasonic Imaging*, vol. 8, no. 3, pp. 151-164, 1986.
- [3.79] C. Saloma, S. Kawata, and S. Minami, "Speckle Reduction by Wavelength and Space Diversity Using A Semiconductor-Laser," *Applied Optics*, vol. 29, no. 6, pp. 741-742, 1990.
- [3.80] B. Dingel and S. Kawata, "Speckle-Free Image in A Laser-Diode Microscope by Using the Optical Feedback Effect," *Optics Letters*, vol. 18, no. 7, pp. 549-551, 1993.
- [3.81] H. Ambar, Y. Aoki, N. Takai, and T. Asakura, "Mechanism of Speckle Reduction in Laser-Microscope Images Using A Rotating Optical Fiber," *Applied Physics B-Photophysics and Laser Chemistry*, vol. 38, no. 1, pp. 71-78, 1985.
- [3.82] S. Jutamulia, T. Asakura, and H. Ambar, "Reduction of Coherent Noise Using Various Artificial Incoherent Sources," *Optik*, vol. 70, no. 2, pp. 52-57, 1985.

CHAPTER 3: *Waveguides and Lightguides in Laser-illuminated Display Systems*

- [3.83] E. Snitzer and H. Osterberg, "Observed Dielectric Waveguide Modes in the Visible Spectrum," *JOSA*, vol. 51, no. 5, pp. 499-505, 1961.
- [3.84] B. Crosignani and P. Di Porto, "Coherence of an electromagnetic field propagating in a weakly guiding fiber," *Journal of Applied Physics*, vol. 44, p. 461, 1973.
- [3.85] Masaaki Imai, "Statistical properties of optical fiber speckles," *Bulletin of the faculty of engineering*, vol. 130 Nov.1985.
- [3.86] J. M. Schmitt, S. H. Xiang, and K. M. Yung, "Speckle in optical coherence tomography," *Journal of Biomedical Optics*, vol. 4, p. 95, 1999.
- [3.87] T. Suzuki and R. Hioki, "Speckled Diffraction Pattern and Source Effect on Resolution Limit in Holography," *Japan. J. Appl. Phys*, vol. 5, p. 814, 1966.
- [3.88] E. G. Rawson, J. W. Goodman, and R. E. Norton, "Analysis and Measurement of the Modal-Noise Probability-Distribution for A Step-Index Optical Fiber," *Optics Letters*, vol. 5, no. 8, pp. 357-358, 1980.
- [3.89] H. Takahara, "Visibility of interference fringes: effect of the optical guide length in coherent light," *Applied Optics*, vol. 16, no. 2, pp. 494-496, 1977.
- [3.90] E. G. Rawson, J. W. Goodman, and R. E. Norton, "Analysis and measurement of the modal-noise probability distribution for a step-index optical fiber," *Optics Letters*, vol. 5, no. 8, pp. 357-358, 1980.
- [3.91] W. Ha, S. Lee, Y. Jung, J. Kim, and K. Oh, *Speckle reduction in multimode fiber with a piezoelectric transducer in radial vibration for fiber laser marking and display applications* SPIE Society of Optical Engineering, p. U380-U387, 2008.
- [3.92] I. Fujieda, T. Kosugi, and Y. Inaba, "Speckle Noise Evaluation and Reduction of an Edge-Lit Backlight System Utilizing Laser Diodes and an Optical Fiber," *Display Technology, Journal of*, vol. 5, no. 11, pp. 414-417, 2009.
- [3.93] B. Crosignani, B. Daino, and P. Di Porto, "Interference of mode patterns in optical fibers," *Optics Communications*, vol. 11, no. 2, pp. 178-179, 1974.
- [3.94] B. Crosignani, B. Daino, and P. D. Porto, "Speckle-pattern visibility of light transmitted through a multimode optical fiber," *Journal of Optical Society of America*, vol. 66, no. 11, pp. 1312-1313, 1976.
- [3.95] G. Ouyang, Z. Tong, M. N. Akram, K. Wang, V. Kartashov, X. Yan, and X. Chen, "Speckle reduction using a motionless diffractive optical element," *Optics Letters*, vol. 35, no. 17, pp. 2852-2854, 2010.
- [3.96] R. Dandliker, A. Bertholds, and F. Maystre, "How Modal Noise in Multimode Fibers Depends on Source Spectrum and Fiber Dispersion," *Journal of Lightwave Technology*, vol. 3, no. 1, pp. 7-12, 1985.



## **Chapter 4: Polymer Waveguide Optical Backplane UCL Research Review**

### **4.1 Introduction**

Chapter 2 reviewed and explained some of the polymer waveguide optical backplane systems developed and demonstrated by various research groups around the world but excluded most research on this subject carried out at UCL. This chapter concentrates on reviewing the past research carried out at UCL on polymer waveguide optical backplanes. This research review has been put in a separate chapter as it is particularly relevant to the new research reported in this thesis and is described so that the new aspects of the new research reported can be clearly distinguished from earlier research carried out at UCL. However, the author of this thesis was also involved in this past work and so the author's contribution is also acknowledged where appropriate. Although this chapter concentrates on the research carried out at UCL some of the research was carried out in collaboration with several industrial companies and universities including Xyratex Technology Ltd., Exxelis Ltd., Loughborough University, Heriot-Watt University and the National Physical Laboratory (NPL). So related research by these collaborators is also reviewed in this chapter. The overall goal of the research was to develop polymer waveguide technology into a more advanced state whereby it could be used to make an optically interconnected demonstration rack system meeting real industrial constraints with collaborator Xyratex Technology. In this way, the problems being solved would be of direct use to industry and would help to overcome problems and obstacles standing in the way of widespread use in optically interconnected products. The aim was to develop an optical printed circuit board to operate in excess of 10 Gb/s for board to board optical communication.

Two particular polymers developed by Exxelis and Dow Corning were investigated for fabrication of polymer waveguides. These polymers had been developed to have a low (0.05 dB/cm) absorption coefficient at 850 nm. Therefore, for use in the demonstrator, the light source was chosen to be an array of VCSELs with output wavelengths of 850 nm. VCSELs (vertical cavity surface emitting laser) also have the advantage of low cost and small size (the cost of a VCSEL is less than one dollar) and photodiodes (PD) were used in the receivers. A variety of different waveguide fabrication techniques were developed by the project partners: photolithography (Exxelis Ltd, Dow Corning Corporation), direct laser-writing (Heriot-Watt

University, Varioprint and IBM Zürich), laser ablation (Loughborough University), and inkjet printing (Loughborough University) [4.1-3].

Each waveguide, which connects two boards, may contain several bends, crossings and taper sections and may suffer from optical loss and crosstalk [4.4-6]. To quantify the loss and to estimate and design the overall performance the optical loss was measured of each waveguide component. This enabled waveguide design rules to be established for each fabrication technique with the aim of incorporating them into the Cadence commercial automatic design rule checker and constraint manager layout software. Such software is in regular use by PCB designers for laying out copper interconnected boards. Therefore, by including optical design rules for waveguides the PCB designers could easily include optical connection layers without detailed knowledge of the optics involved. The optical board layout could then be optimised to minimise the waveguide optical transmission loss and optical crosstalk; this is the first time this has been done for integrated design and layouts for both electronic and photonic interconnects.

It should be clarified that the author of this thesis was involved in the design and measurement of the waveguide components in order to find the design rules. Most of the components were simulated using the beam propagation method (BPM) to compare the results with the experiments. The main person designing the waveguides and in charge of the experiments was Kai Wang, however, the work described in Chapters 6 and 7 on the crossing waveguides and end facet roughness was carried out by the author.

Figure 4.1 shows a schematic diagram of the rack based backplane interconnect concept for the demonstrator and a photograph taken from the daughter boards looking towards the separate electrical and optical backplanes used in the previous so called “StorLite” demonstrator made by Xyratex and UCL. The aim was to extend this to design and demonstrate a single hybrid optical and electrical backplane. In this concept, both the lasers and photodiodes are attached to and powered from the daughterboard. The daughterboards clip into the backplane at special connectors which enable the lasers and photodiodes to couple directly to the backplane waveguide by butt coupling. This has the benefit of avoiding the need, fabrication cost and loss of 45 degree mirrors as described in chapter 2 but is at the expense of the difficulty of automatically aligning the lasers and photodiodes to and from the waveguide each time the daughterboards are plugged in and out to very tight tolerances. However, UCL invented a low-

cost method for passive self-alignment of the laser source and photodiodes to the waveguides [4.1;7;8].

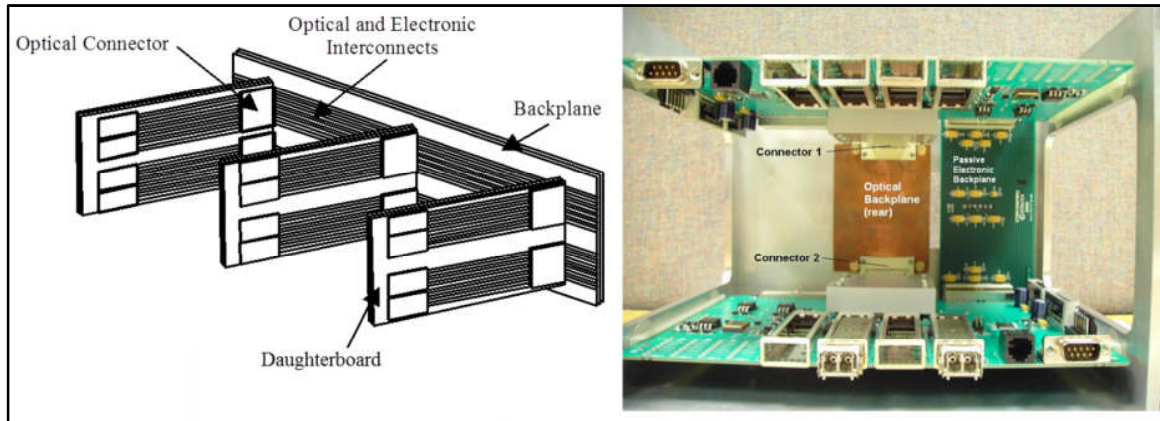


Figure 4.1: Schematic diagram of the arrangement of the daughterboard and the back plane (left (drawn by David Selviah)) and the actual daughterboard connected to the backplane (right (picture was taken by Richard Pitwon)).

In the new demonstrator, called the FirstLight Demonstrator, the aim was to fully interconnect four daughter boards in both directions by optical interconnections implemented on the motherboard/backplane. The waveguide layout was designed at UCL by Kai Wang using the established optical design rules in computer-aided design (CAD) with Cadence commercial software. The design included waveguides with different separations, bend radius and angles of crossing including bends crossing straight waveguides and bends crossing each other. To the best of our knowledge, this work has not been undertaken previously by any other group and pushes forward the boundaries of this technology. The designed waveguides were manufactured by other partners and were then measured and characterised at UCL. They were shown to operate in good agreement with optical insertion losses close to those predicted and gave error free data transmission beyond 10 Gb/s.

In this chapter, one type of waveguide fabrication, namely photolithography, is explained and the design of the optical PCB is described. As the optical loss in the waveguides depends on the waveguide components and their shape used in the optical route from the optical source to the receiver, the different types of optical loss in the waveguide making up the insertion loss are reviewed. UCL has taken a particular lead in subdividing the insertion loss in this way [4.5]. Several techniques for simulation of propagation of light through waveguides are overviewed

and one that is made particular use of in the new work in Chapters 6 and 7 in explained in more detail together with its limitations. The chapter goes on to describe the experimental configuration used for testing and analysing the waveguides and finally some relevant performance characteristics of VCSELs are described.

#### **4.1.1 Photolithographic Fabrication Technique**

In this research, waveguide samples were manufactured by different methods. Laser direct writing was used in Heriot-Watt University, laser ablation and inkjet printing were used by Loughborough University and Exxelis used photolithography. Although the author was involved with measurement of all of the different types of waveguide, the waveguide samples used in the new work reported in Chapters 6 and 7 were photolithographically fabricated by Exxelis. Therefore, this section concentrates on the photolithographic manufacturing process. Waveguides were made by photolithography due to the good quality of the resulting waveguides. Laser ablation and inkjet printed waveguides were also investigated in order to find the best parameters for manufacturing them and laser direct-written waveguides were used too to compare the results of the waveguides manufactured by different methods.

Waveguides were made of polymer and for the core and cladding material two UV curable Polyacrylate transparent polymers called Truemode<sup>®</sup> with different formulae (to achieve different refractive indices) developed by Exxelis were used. The manufacturing process is illustrated in Figure 4.2.

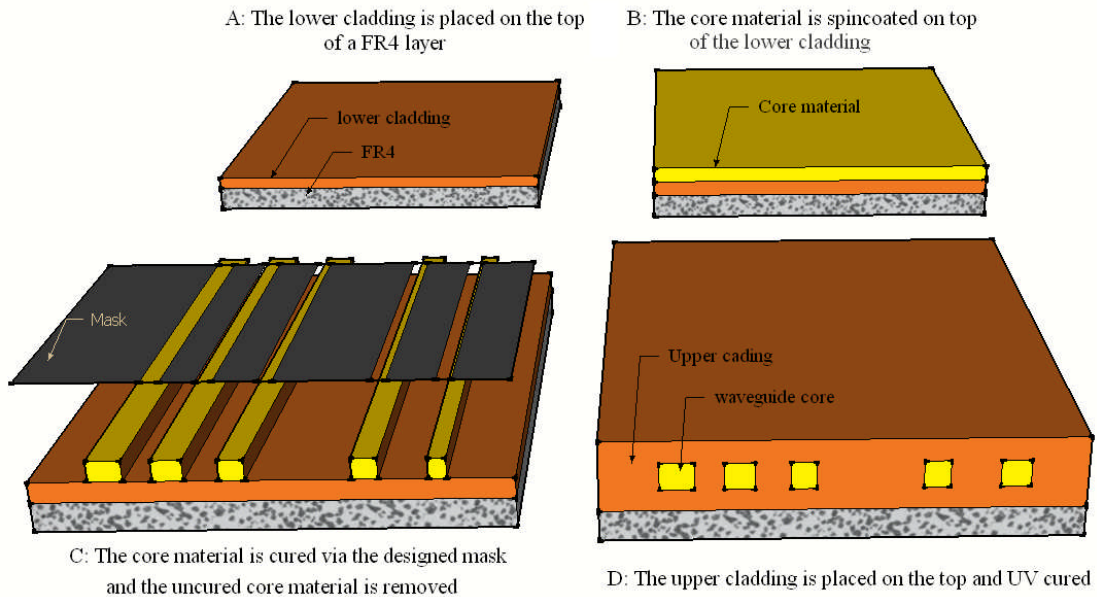


Figure 4.2: Schematic diagram of the process for manufacturing the optical interconnections using the photolithographic method.

Waveguide fabrication started with spin coating a liquid lower cladding polymer material (130 rpm for 30 seconds) on an FR4 (glass reinforced epoxy) substrate at an optimized acceleration rate to achieve a uniform typically 50 micron thickness of the lower cladding layer. A 350 nm – 450 nm UV light source was used to cure the lower cladding polymer; the exact wavelength being dependent on the particular formula of the polymer used for the cladding. The cured lower cladding material was then baked for 30 minutes at 100° C in a baking oven to remove the solvent residuals. (The curing process in this fabrication method was taken place inside a nitrogen chamber where the polymer is covered with a layer of nitrogen gas ( $N_2$ ) called nitrogen blanket).

Secondly, the liquid core polymer material is spin coated on the top of the lower cladding by the same process as the cladding deposition. A custom-designed e-beam high-resolution mask is aligned with the wafer using a UV mask aligner. The e-beam mask is more expensive than a photomask but minimizes digitization problems from the mask fabrication, especially along bends, due to its finer resolution [13]. The non-smooth edges of the mask cause waveguide wall roughness [4.5]. The wall roughness at the edge of the waveguide patterned on the mask is thought to be the principal source of loss and crosstalk between two adjacent waveguides [4.9].

Reducing the space between the mask and the liquid core material to 100  $\mu\text{m}$  during the UV exposure, avoids physical contact with the material while minimising spreading of the light through the mask. The wafer is covered by nitrogen gas for 1 minute to exclude oxygen. The core layer is then exposed to UV light through the patterned mask to cure the polymer and any remaining uncured polymer material is washed away after the curing process. An additional two minute, 15  $\text{mW}/\text{cm}^2$ , UV exposure completely polymerized the waveguides. Finally, the same technique used to deposit the lower cladding layer is applied to deposit and UV cure the upper cladding which fills in the gaps between the core polymer waveguides and also coats them above to a thickness of 50 microns.

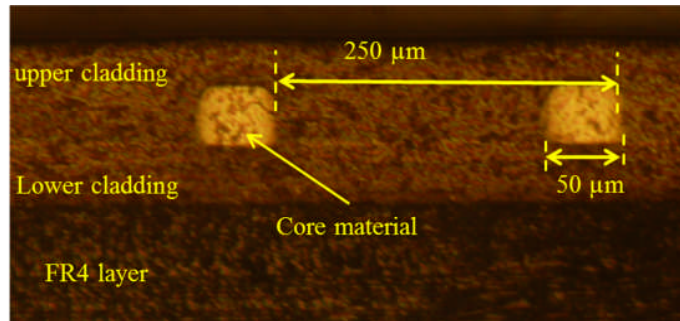


Figure 4.3: End facets of 50  $\mu\text{m} \times 50 \mu\text{m}$  straight photolithographic manufactured waveguides photographed through a Nomarski Microscope using both back and front light illumination.

Figure 4.3 is a photograph of the end facet of a polymer waveguide array observed through a Nomarski microscope. The refractive index of the core was 1.5560 and slightly higher than the cladding index of 1.5264 giving a theoretical numerical aperture (NA) of 0.302 ( $\text{NA} = [\text{n}_{\text{core}}^2 - \text{n}_{\text{clad}}^2]^{1/2}$ ). The waveguides analysed and reported in this research have 50  $\mu\text{m}$  thick cores unless otherwise stated and the pitch between two adjacent waveguides is 250  $\mu\text{m}$ . The Truemode<sup>®</sup> polymer previously used in 1 m spiral waveguides, gave a propagation loss of  $0.08 \pm 0.02 \text{ dB}/\text{cm}$  at 850 nm.

## 4.2 Optical Backplane Designed for 10 Gb/s Interconnection FirstLight Demonstrator

In this section, the optical design of the backplane used for high data rate (10 Gb/s) interconnection is explained and the problems which needed to be overcome in the design are described. It should be clarified that the author was involved in the design and testing of the

board but the main person who designed the board was Kai Wang with David R. Selviah. The backplane was designed to accommodate 4 daughter boards connected into the Optical Printed Circuit Board, OPCB backplane (Figure 4.4) and communicate with each other in both directions via the backplane.

As shown in Figure 4.4, there are four identical rectangular optical engagement apertures in the middle of the optical board for insertion of connectors from the 4 daughter boards. These allow four daughter boards to be integrated each having 4 high bit rate (12.5 Gb/s) optical transceivers that are engaged at right angles to the OPCB backplane. All of the four line cards, or daughterboards, are interconnected by a point-to-point waveguide network, whereby every optical transceiver is connected to 3 transmission waveguide channels and 3 reception channels, resulting in a total of 12 waveguides on the board. There are two main advantages of this design: Firstly, all of the optical interfaces were designed to face the same direction and to be identical to each other so that the line-cards are interchangeable, therefore, significantly reducing the manufacturing and maintenance costs as any line-card can be plugged into any engagement aperture without special modification and this is what is required in an industrial rack system product. Secondly, the OPCB is very compact as the line-cards are closely spaced to meet the design specification of a highly populated storage bridge bay. There are also some restrictions on the design based on the configuration of the backplane and the daughterboard. It should be remembered that the system is designed for the optical sources and photodiodes to be attached to the daughter-boards and directly butt-coupled to the waveguides implemented on the backplane. Waveguides have to bend almost immediately after short straight sections in order to avoid other connectors. The waveguide structures need to be designed carefully according to the design rules to minimise the optical loss in every waveguide section and to keep the aggregate optical loss of each optical interconnect below the minimum bit error-free sensitivity of the optical receiver.

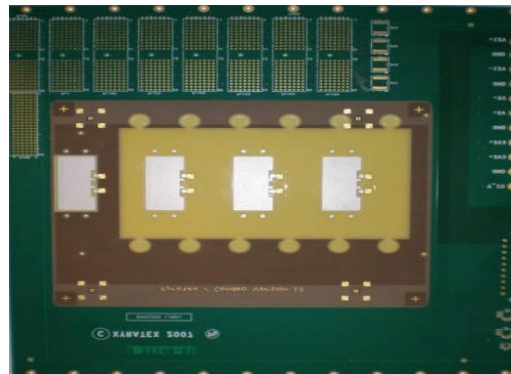


Figure 4.4: Optical PCB board waveguide interconnect. The three white rectangles are the cut out connector sites where the daughter boards are plugged into the board.

The design of the board and the waveguide routes between the lasers and the receivers must be considered carefully as the layout configuration of the waveguides will affect the optical loss in the system. Figure 4.5 shows the schematic diagram of the optical interconnect layout. Linear arrays of 4 VCSEL and 4 PDs on a centre-to-centre pitch of  $250\ \mu\text{m}$  were arranged to match the 12 waveguides. (The VCSELs and PDs are purchased as a package of 4 unit in one array. The forth one is not in used)

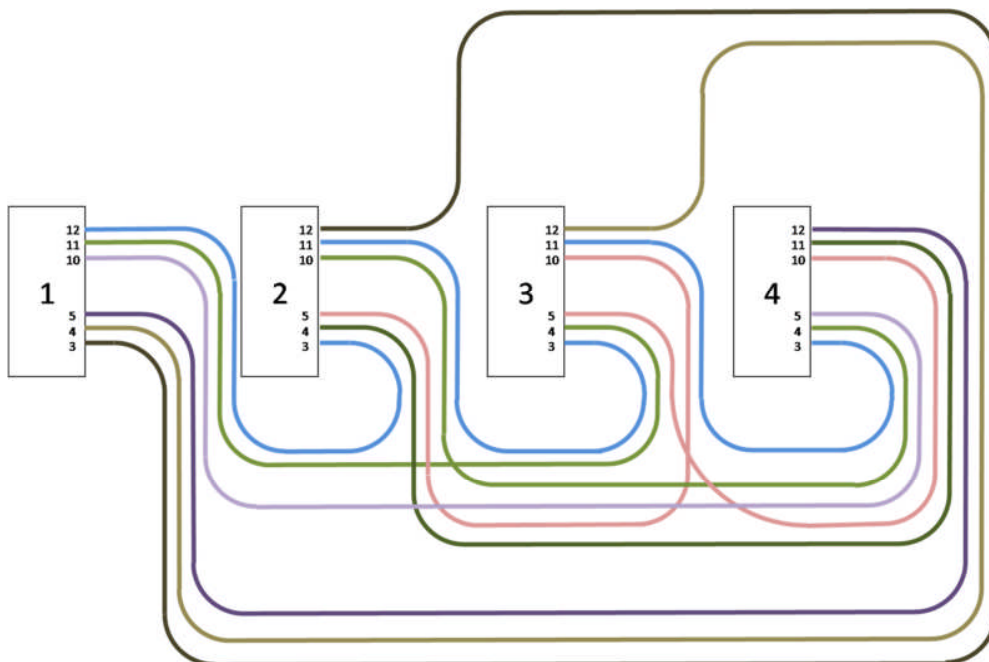


Figure 4.5: Schematic diagram of the optical waveguide interconnection layout (designed and drawn by Kai Wang at UCL).



The waveguides are laid out between the lasers (source) and the photo-detectors (PD) (receivers) (Figure 4.5). The connection configuration between the sources and the receivers depends on the application, but normally the waveguides need to be bent or cross each other to establish links between the source on one board and the receiver on another board. Curved waveguides are a source of optical loss in the form of leaky mode and radiation mode loss and should be avoided if possible [4.4;5]. The size of the board and the available space for the designer depends on the manufacturing technique and the company. Although larger space enables the designer to use shallower bends this does not mean the loss is reduced as the length of the waveguide is increased due to the larger bend radius thus causing an increase in the absorption loss.

The VCSELs were placed at the position 2-5 and the PDs placed at 9-12 in Figure 4.5; positions 2 and 9 are currently not in use due to technical problems with the light source module. Each waveguide was designed to have an approximately square cross section  $50\ \mu\text{m} \times 50\ \mu\text{m}$  to minimise both insertion loss and crosstalk [4.9]. According to waveguide bend design rules determined by UCL, the radius of each waveguide was chosen to be close to 15.5 mm [4.9] as the transmitted power is maximised around this radius and does not vary much if the radius is slightly incorrect due to manufacturing tolerances. As the transmitters (VCSELs) and the receivers (PDs) on the line-card were located at the same position and pointing in the same direction, the waveguides had to cross each other at some points to achieve full interconnection.

### **4.3 Review of Optical Loss in Polymer Waveguides**

Understanding the optical loss that occurs in the waveguides and the causes of the loss is crucial for evaluating the optical loss in any waveguide route. That is why, in this research, design rules were established to be incorporated in Cadence PCB layout software. Then, even if a waveguide designer is not aware of the waveguide theory, they can design the required OPCB. In this section, the possible sources of optical loss in a polymer waveguide are reviewed. The theory of optical loss in waveguides has been investigated in several books and papers [4.10-12]. In the theory of optical waveguides, the optical loss is explained based on the modes in the waveguides. Each mode is a distribution of the optical power inside a waveguide [4.12]. There are different types of mode defined based on their behaviour [4.13]. Some modes are called leaky modes as they attenuate as they propagate along the waveguide. Others are called bound modes as they propagate inside the waveguide [4.14]. The optical power can redistribute between different

bound modes and can also couple to radiation modes through sidewall roughness [4.11;13;14]. Radiation modes are not bound to the waveguide. There are several different ways to lose optical power in an OPCB system, for example optical loss in the waveguide depending on the shape of the waveguide and the waveguide material or optical loss at the sources and photodetectors. These sources of optical loss are summarised below:

- *Propagation loss*: Propagation loss has two causes:
  - The material absorption. The optical energy is absorbed by the waveguide material. This type of loss depends on material formulation and the manufacturing process. Different materials have different absorption bands due to their atomic structure and impurities, which are mixed with the material during the fabrication process. The material absorption changes for different wavelengths of light and are characterised by the absorption spectrum of the material. In this type of optical loss, the optical energy is converted into another type of energy such as heat energy [4.12;15].
  - The coupling of optical energy into radiation modes due to wall roughness. The top and bottom surfaces of the waveguide can be made to have a very smooth surface by spinning the liquid core and curing. When the sidewall is formed by lithography, it suffers from wall roughness especially at the bent sections due to the roughness at the edge of the mask [4.16;17]. The distribution of the optical energy inside the propagating mode changes due to wall roughness and this can scatter light into modes which produce radiation away from the waveguide [4.12;17].
  - Radiation modes can also be created due to the waveguide bend and crossing [4.18]. This kind of optical loss is called *transition loss or mode mismatch loss*, which happens when two waveguide sections with different geometrical and refractive properties are connected together. Each waveguide section supports its own mode structures and optical loss occurs if there is any mismatch between the modes in the two sections [4.15]. For example, if the output of a multimode fibre is to be coupled into a square waveguide, the modes in the optical fibre are different as it is a cylindrical shape and not all of those modes, if any may be supported by the rectangular waveguide into which the light is travelling. Another

example is when a straight waveguide with a rectangular cross section is connected into a waveguide bend section. As explained in section 4.2, to route the waveguides from the optical source to the receiver, the waveguides may have to bend or cross another waveguide. Therefore, one can imagine the light propagates in a straight multimode waveguide and the optical power is distributed between the bound modes of this waveguide. Now if the straight waveguide is connected to a bend waveguide section, the power output of the straight waveguide must be redistributed into the propagating modes of the bend waveguide which are not the same as the straight waveguide [4.5]. In this process and due to the mismatch between the modes in two sections, some of the optical power is lost by coupling into radiation modes [4.15;18;19]. Optical loss due to these dissimilar sets of modes in different sections of waveguides can occur at any joint between different waveguide structures.

- Propagation of light inside a bend section also causes optical loss as the modes in a bend are leaky modes and radiate energy away from the waveguide [4.4;5;15]. This is usually referred to as radiation loss. The difference between this type of optical loss with the previous loss (optical loss due to the mode mismatch) is that the loss inside a bent section is because of the creation of leaky mode due to the structure of the bend section itself but in the previous section, the optical loss is due to the non-continuity in the geometrical shape of the waveguide design and so different supported mode distribution in each different geometry.
- *Coupling loss*: Coupling loss is one of the most important sources of optical loss in optical waveguides. This is the loss between the source and the waveguide at the input of the waveguide or the loss between the waveguide and the receiver at the output of the waveguide. The coupling loss occurs due to two main physical phenomena:
  - Fresnel reflection loss: This is due to the discontinuity of refractive index of the waveguide material and the source medium. The optical beams reflect back at the input of the waveguide when there is a change in refractive index. Fresnel reflection increases with increasing refractive index difference so this loss will be a maximum when there is an air gap between the source and the waveguide.

- Scattering loss: This is due to the scattering of the light from any roughness or imperfections at the end facet of the waveguide. The light is scattered into a large solid angle in the forward and backward directions, which results in more light lost or coupled into radiation modes.
- Optical loss due to the mismatch of the beam parameters of the light source and the waveguide: In fact, the light diverges into a cone from the source, which depends on the numerical aperture (NA) of the source. On the other hand, the waveguide only accepts light, which is inside a converging cone and is, therefore, dependent on the waveguide NA. The same effect occurs when light is focussed into a waveguide with an NA larger than the NA of the waveguide in which case loss results. The magnitude of the loss is  $(NA_1/NA_2)^2$  where  $NA_1$  is the NA of the waveguide and  $NA_2$  is the NA of the source.
- Misalignment: Misalignment loss is due to the spatial and angular misalignment between the source and the waveguide. The misalignment generates radiation modes, which radiate away from the waveguide [4.20;21].

The total loss is the summation of the individual losses which must all be taken into consideration when determining the power budget and designing the OPCB [4.5].

#### **4.4 Waveguide Simulation Methods**

In this section, the simulation techniques used in the following chapters are explained. Numerical methods are essential for analysing waveguides to evaluate the behaviour of the waveguides in the backplane design. In this thesis, two methods of wave propagation and ray tracing are employed to analyse the waveguide structures. Commercially available software from RSoft Inc. and Zemax were used for wave propagation and ray tracing respectively. The beam propagation method (BPM) is based on Maxwell's equations and wave properties of the light [4.12;15]. A commercially available software package developed by RSoft Design Group Inc. [4.22] was used for BPM simulation as it was available in the group and has been used and tested before for waveguide simulations [4.5;15]. However, other available packages such as Optiwave [4.23] were considered and evaluated. BPM is implemented in all of the software packages; it is a well-developed technique and there was no noticeable difference between them in the test waveguide evaluation.

Zemax was chosen for the ray tracing technique as it was available in our group. However, some of the waveguides were tested by ASAP which is a more sophisticated ray tracing package although we found it more difficult to learn and use, to compare the results and these results are presented in the following chapters.

#### 4.4.1 Beam Propagation Method, BPM

BPM is the most frequently used method for simulating complex waveguide structures where the propagation direction follows the structure of the waveguide. BPM solves Maxwell's equations [4.24] by employing some approximations such as the slowly varying envelope approximation (SVEA) and the paraxial wave approximation (PWA). The finite difference (FD) method is employed for the numerical calculations. The waveguides are regarded as comprising the core material surrounded by a layer of lower refractive index (cladding). The finite difference Beam propagation method (FD-BPM) algorithm samples the waveguide structure and the field to propagate the light inside the waveguide. The sampling interval is performed at regular constant spatial intervals but the sampling can also be dynamic which is more suitable for a complex structure [4.25]. Regular constant sampling is used in this research unless otherwise mentioned.

The BPM algorithm solves the wave equation derived from Maxwell's equations. For a dielectric medium with zero charge density and current density these can be written as:

$$\nabla \cdot E(r, t) = 0 \quad \text{Equation 4.1}$$

$$\nabla \cdot B(r, t) = 0 \quad \text{Equation 4.2}$$

$$\nabla \times E(r, t) = - \frac{\partial B}{\partial t} \quad \text{Equation 4.3}$$

$$\nabla \times B(r, t) = \mu\epsilon \frac{\partial E}{\partial t} \quad \text{Equation 4.4}$$

Where  $E(r)$  and  $B(r)$  are the electric and magnetic field,  $\epsilon$  is the permittivity of the dielectric and  $\mu$  is the permeability of the medium. The magnetic field in the third equation of Maxwell's equations (Faraday's law in Equation 4.3) can be removed by taking a curl operator ( $\nabla \times$ ) from this equation and substituting from the fourth equation:

$$\nabla \times (\nabla \times E(r, t)) = - \frac{\partial}{\partial t} (\nabla \times B(r, t)) = - \mu\epsilon \frac{\partial^2 E(r, t)}{\partial t^2} \quad \text{Equation 4.5}$$

The time dependence of the electric field can be written as:

$$E(r, t) = E(r)e^{-i\omega t} \quad \text{Equation 4.6}$$

Where  $\omega = 2\pi f$  ( $f$  is the frequency of the propagating wave). By substituting Equation 4.6 in Equation 4.2, the wave equation in the form of the Helmholtz equation for the electric field can be derived [4.12;26]:

$$\nabla^2 E(r) + \mu\varepsilon\omega^2 E(r) = \nabla^2 E(r) + n^2 k_0^2 E(r) = 0 \quad \text{Equation 4.7}$$

Where the  $E(r)$  is the electric field,  $n$  is the refractive index of the propagation medium, and  $k$  is the wave number.

$$k_0 = \frac{2\pi}{\lambda}$$

$$c = \frac{1}{\sqrt{\mu\varepsilon}}$$

Where  $\lambda$  is the wavelength of the propagating field in the vacuum and  $c$  is the speed of light in the waveguide medium. Equation 4.7 is the wave equation in  $x$ ,  $y$  and  $z$  direction but solving this equation in three dimensions is a very complicated physical and mathematical challenge. BPM uses some approximations to simplify the equation. The first assumption is that the wave is propagated along the axis of the waveguide, which normally is considered the  $z$  direction (PWA). Also, based on the SVEA approximation, the optical field is defined to have an envelope which has a slow variation in the propagation direction and a fast phase section:

$$E(x, y, z) = \phi(x, y, z)e^{-in_r k_0 z} \quad \text{Equation 4.8}$$

Where  $\phi(x, y, z)$  is the envelope of the electric field and  $n_r$  is the background refractive index (cladding materials) [4.27]. The exponential term shows the rapid varying factor. The first and the second derivative of Equation 4.8 in the propagation direction  $z$  is:

$$\frac{\partial}{\partial z} (\phi_x e^{-in_r k_0 z}) = \left( -in_r k_0 \phi_x + \frac{\partial \phi_x}{\partial z} \right) e^{-in_r k_0 z}$$

$$\text{Equation 4.9}$$

$$\frac{\partial^2}{\partial z^2} (\phi_x e^{-in_r k_0 z}) = \left( \frac{\partial^2 \phi_x}{\partial z^2} - 2in_r k_0 \frac{\partial \phi_x}{\partial z} - n_r^2 k_0^2 \right) e^{-in_r k_0 z}$$

Replacing Equation 4.9 in the wave equation in Equation 4.8 gives the main equation for BPM algorithm:

$$\left( \frac{\partial^2}{\partial z^2} + \frac{\partial^2}{\partial x^2} + \frac{\partial^2}{\partial y^2} - 2in_r k_0 \frac{\partial}{\partial z} - n_r^2 k_0^2 + n^2 k_0^2 \right) \phi_x = 0 \quad \text{Equation 4.10}$$

Here the phase is regarded to be invariant with the transverse parts as it is an orthogonal system. This is the full BPM equation to be solved and it is a second order derivative equation. BPM uses some approximations to simplify the equation as in practice, direct calculation of the second derivative in the  $z$  direction is problematic [4.27].

#### 4.4.1.1 Paraxial Approximation

The simplest method is to assume that the second derivative in the propagation direction is zero or much smaller than the first derivative, that can be ignored without affecting the results. In other words BPM uses the SVEA approximation that implies that the electric field changes slowly in the  $z$ -direction:

$$\frac{\partial^2 \phi}{\partial z^2} \ll 2n_r k_0 \frac{\partial \phi}{\partial z} \quad \text{Equation 4.11}$$

And the BPM equation is simplified to:

$$\frac{\partial \phi}{\partial z} = \frac{i}{2n_r k_0} \left( \frac{\partial^2 \phi}{\partial x^2} + \frac{\partial^2 \phi}{\partial y^2} \right) + \frac{i}{2n_r} (n^2 - n_r^2) k_0 \phi \quad \text{Equation 4.12}$$

This situation is called the paraxial approximation or Padé order zero and can become inaccurate when the light rays are travelling in the waveguide at a large angle relative to the propagation direction, for example, in the case of  $90^\circ$  crossing waveguides. In this case, higher Padé orders or a wide angle method should be used. However, it should be noted that increasing the Padé order increases the number of calculations significantly and, therefore, the simulation time [4.28]. Even so there is still a limit to the maximum angle that the rays can travel from the initial propagation direction, which was quantified by Papakonstantinou [4.5].

BPM solves the initial value problem by iterating the field along the  $z$  axis by using finite differences for the  $x$  and  $y$  derivatives. The field launched into the waveguide is considered as the field at  $z = 0$  and FD-BPM finds the electrical field at any point based on the sampling grid defined by the user by iteration methods. The BPM algorithm sets the fields to zero outside the simulation area. This condition removes the field at the boundary and prevents the reflected light from the boundary interfering with the simulation. This boundary condition is called the transparent boundary condition (TBC) [4.29;30].

## 4.5 Experimental Configuration for Optical Loss Measurements

In this section, the experimental procedures used in the following chapters are explained. The measurement of optical loss is strongly dependent on the choice of optical source, the roughness of the end facets of the waveguides, the type of light source, the type of receiver and, more importantly, the relative positions of all sources, detectors and waveguides in both position and angle. We mainly used either a VCSEL TOSA (transmission optical sub-assembly) with a TO-46 component having a ball lens a ST receptacle (STVXCEL-850, Access Pacific Ltd) connected to a standard 50/125  $\mu\text{m}$  step index multimode (MM) fibre with  $NA_{\text{fibre}}$  of 0.22 which is less than the waveguide  $NA_{\text{wg}}$  of 0.302. Figure 4.6 shows a schematic diagram of an optical insertion loss measurement using an 855 nm light source launched via a 10 m long MM fibre. The fibre has ST and FC/PC connectors and was wound 25 times around a 35 mm diameter circular mandrel post to fill the  $NA_{\text{fibre}}$ . We measured the NA of the fibre to ensure it was fully filled with a large number of transverse modes [4.31]. The FC/PC end of the fibre was then aligned and butt-coupled to one of the waveguides on a waveguide sample to be tested. A 70  $\mu\text{m}$  pinhole was placed in front of a large area integrating sphere PD to spatially filter much of the light travelling through the cladding and to simulate the aperture of the PD used in the current demonstrator [10]. This is a new measurement technique; that gives more accurate results than those obtained by using photodiode detectors that can give inconsistencies due to laser speckle (modal noise) and spatial variation of efficiency across the active area of the optical power sensor. Index-matching fluid ( $n = 1.5433 \pm 0.0005$  for 840.0 nm at 25°C), which is close to the refractive index of the waveguide core index of  $1.5560 \pm 0.0005$  at 850 nm) was applied to the MM fibre-waveguide interfaces to reduce coupling loss. It was also applied to the waveguide-pinhole interface to reduce loss due to the scattering occurring at the rough entry and exit facets of the waveguide.



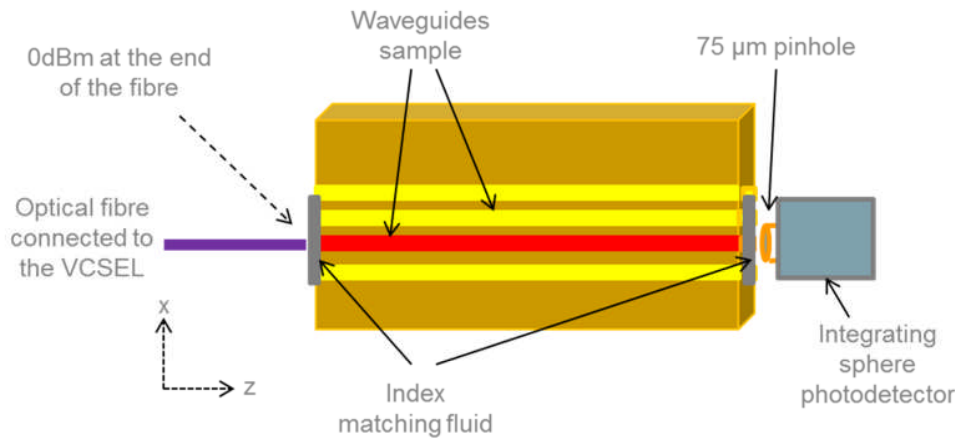


Figure 4.6: One 850 nm VCSEL was connected to a 50/125  $\mu\text{m}$  MM fibre via an ST connector and was set to provide an output optical power of 0 dBm at the output end of the fibre.

Both the input source and PD were mounted on high-precision (minimum increment of 0.1  $\mu\text{m}$ ) motorized translation stages for accurate alignment and sub-micron step adjustment to maximize the light through the waveguide. Figure 4.7 shows the schematic diagram of the measurement arrangement including the design of the stages. The lighter and smaller stages ( $y$  vertical stage and  $z$  forward and backward stage) were mounted on top of a heavier and larger stage ( $x$  lateral stage). The order of the stages was arranged to allow the group to support the maximum load within their specifications (Table 4.1).

Table 4.1: Specifications of the Selected Translation Stages

Stage Position	Manufacturer	Model	Driver	Travel Range (mm)	Resolution ( $\mu\text{m}$ )	Bi-directional Repeatability ( $\mu\text{m}$ )
X	Newport	GTS150	XPS-DRV01	150	0.05	0.2
Y	Newport	GTS30V	XPS-DRV01	30	0.05	0.2
Z	Newport	VP-25XA	XPS-DRV03	25	0.1	0.2

We choose a model of the translation stage, which is symmetric with respect to the vertical axis, so that when all of the stages are mounted along the vertical axis (perpendicular to the optical table) the weight of the upper stages is counter balanced. The 3-axis stages were orthogonally assembled by the manufacturer and gave an off-axis error of  $\pm 25 \mu\text{rad}$ . The stages were controlled using a LabVIEW program on an attached laptop computer via stage drivers.

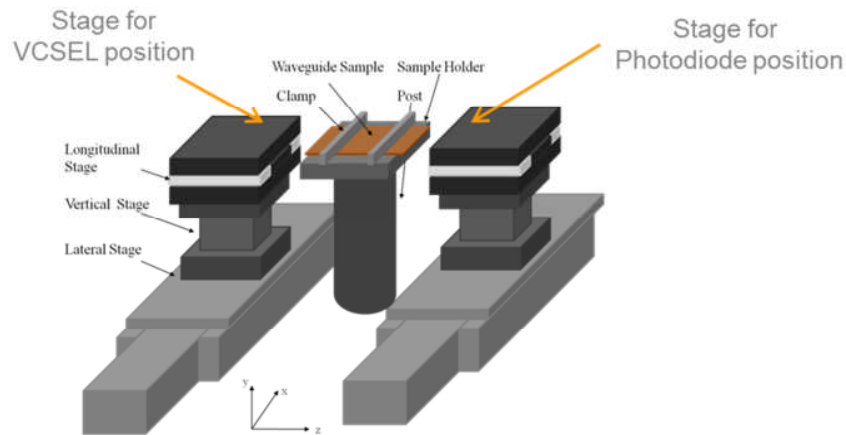


Figure 4.7: Schematic diagram of the measurement arrangement

The waveguide sample needs to be securely held to prevent unexpected movement during the measurement, and to be parallel to the optical table to align with the light launching axis  $z$ . Flat metal plates with different lengths were made to support the variety of sizes (20 mm to 120 mm length) of waveguide samples. The plates were cut 2 to 5 mm shorter than the length of their corresponding sample; if the holder plate is longer than the waveguide sample it will prevent the light source and the PD approaching the waveguide and, therefore, will cause higher optical loss. If the holder is cut too short, it leaves a large proportion of the waveguide sample without sufficient support and it will vibrate during the measurement causing the results to fluctuate. Two clamps, having soft rubber clamping surfaces to avoid damage to the polymer surface are used to secure the waveguide sample flat to its holder.

The light source, the waveguide and the PD need to be aligned properly and the following procedure was adopted:

1. The bearing slide of each of the translation stages was positioned to their centre in order to leave sufficient travel in all directions.
2. A multimode fibre with an FC/PC fibre connector was used as the light source input. This has a screw type of metal casing which makes it very easy to engage to an appropriate adapter and the fibre ferrule provides good protection to the fibre core. One end of the MM fibre was manually aligned to one of the waveguides on a sample and moved close, but without pushing too hard, to the waveguide end facet to prevent the fibre ferrule scratching the waveguide end facet. The other end of the fibre was

connected to a 650 nm Class 3 red laser via a standard FC/PC fibre connector for the aid of visual alignment between the fibre and the waveguide.

3. The PD was placed close to the waveguide output end facet and a pin hole was aligned to the bright spot and was attached.
4. The red laser was replaced by the infrared VCSEL. The position of the input fibre and the PD were precisely adjusted until the maximum output power from the waveguide was recorded. All of our measurements were carried out in similar environment conditions, namely: room temperature 25.7°C – 27.2°C and air humidity 35% - 40%.

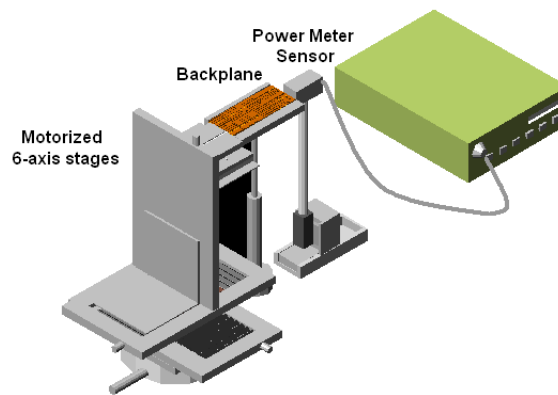


Figure 4.8: Schematic diagram of the experimental apparatus. The source is mounted on the motorised stages and the waveguide is a straight polymer waveguide.

## 4.6 VCSEL as the Optical Source

VCSELs with a modulation rate of 10 Gb/s were used as the source for all of the experiments. The wavelength of 850 nm was chosen as the polymer material has a low absorption coefficient at this wavelength. VCSELs are one of the most important components in the system and have complicated electrical, optical and thermal characteristics that must be taken into consideration, especially in theoretical modelling. As they have very small cavities of about 1  $\mu\text{m}$  length and several microns in lateral size, they support typically one longitudinal mode and several transverse modes [4.32]. The small cavity is prone to self-heating and consequently VCSELs exhibit thermally-dependent behaviour [4.33-36]. Laguerre-Gaussian (LG) modes can be used to represent VCSEL transverse mode distributions in a cylindrical coordinate system [4.35]. The LG field profile is given by:

$$E_{ml} = \alpha_{ml} \cdot \left( \frac{\sqrt{2}r}{w_0} \right)^l \cdot L_m^l \left( \frac{2r^2}{w_0^2} \right) \cdot e^{-2(r/w_0)^2}$$

For computer modelling, the VCSEL (ULM photonics, ULM850-10-TT-C010104U) was used as the light source and up to four transverse mode distributions were used at the output of the light source. A list of the intensity of each mode is shown in Table 4.2 and Figure 4.9 shows VCSEL outputs of these combinations.

Table 4.2: VCSEL output mode fields intensity distribution

Modes		Power Distribution		
1	1			
2	0.5	0.5		
3	0.125	0.75	0.125	
4	0.06	0.44	0.44	0.06

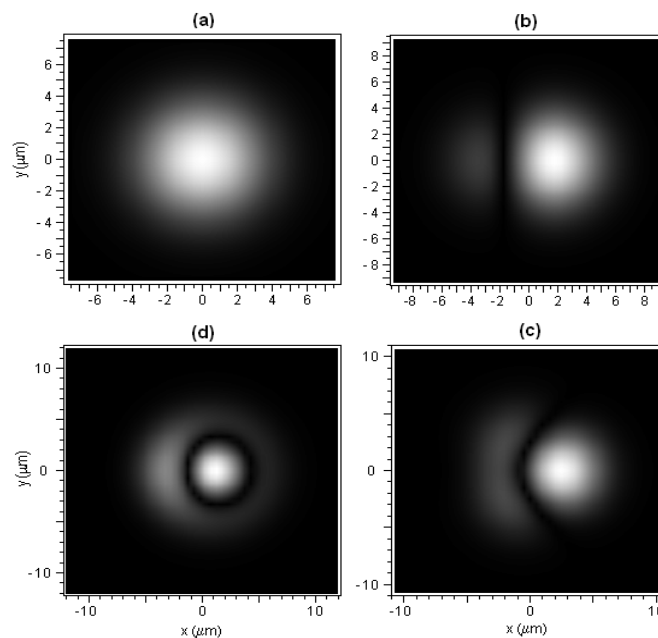


Figure 4.9: VCSEL output field containing (a) one mode, (b) two modes, (c) three modes and (d) four modes (Thanks to Guoyu Yu from UCL for supplying the table and mode profiles).

The VCSEL TOSA was connected to a dual channel digital power supply. Figure 4.10 shows the VCSEL wavelength and output power as a function of operating time. For the measurement, the wavelength and the output optical power of the VCSEL was monitored using a spectrum analyser (HEWLETT PACKARD model 86420B) and an optical power metre (Newport 2931-C). Figures 4.10 and Figure 4.11 show that it is necessary to wait ideally 2500 s or 42 mins after turning on to stabilize the optical output before carrying out any measurements or before using it in the demonstrator to ensure stable reproducible output.

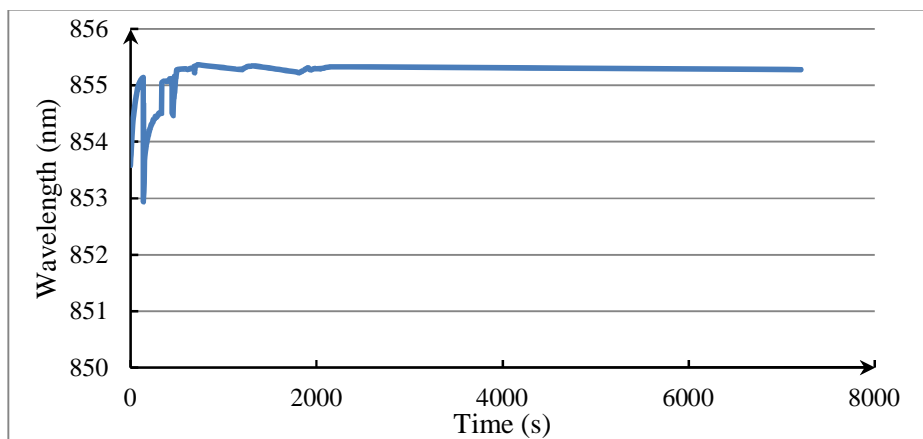


Figure 4.10: VCSEL output measured wavelength and power as a function of time

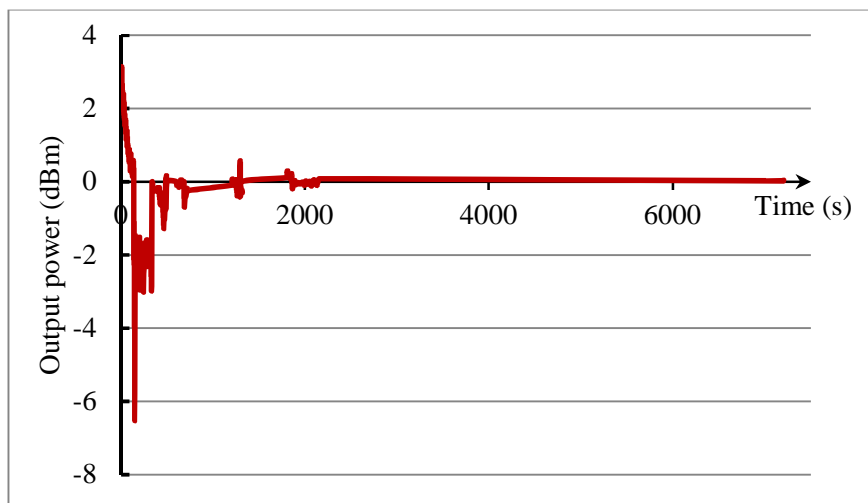


Figure 4.11: VCSEL measured power as a function of time

The power supply ideally should have an output monitor loop, which could automatically adjust the drive current to supply a consistent optical output. The output from the MM fibre was

measured periodically at one hour intervals to calibrate the output variation against temperature of the VCSEL chip.

#### **4.7 Conclusions:**

In this chapter, the optical PCB boards developed in UCL was introduced and the manufacturing process was explained. The waveguide samples used in chapter 6 and chapter 7 are made by the same method (photolithography) which is explained in this chapter. As optical losses in the waveguides are the main concern in this research, the source of these losses are reviewed and two numerical methods of BPM and Ray tracing were mentioned which are used in the next chapters for numerical investigations. At the end, the experimental configuration and the optical source were calibrated. It was found that the laser source (VCSEL) should be used 30 minutes after it is turned on due to instable output of the laser.

## References

- [4.1] I. Papakonstantinou, D. R. Selviah, R. C. A. Pitwon, and D. Milward, "Low-Cost, Precision, Self-Alignment Technique for Coupling Laser and Photodiode Arrays to Polymer Waveguide Arrays on Multilayer PCBs," *IEEE Transactions on Advanced Packaging*, vol. 31, no. 3, pp. 502-511, 2008.
- [4.2] I. Papakonstantinou, D. R. Selviah, K. Wang, R. A. Pitwon, K. Hopkins, and D. Milward, "Optical 8-channel, 10 Gb/s MT pluggable connector alignment technology for precision coupling of laser and photodiode arrays to polymer waveguide arrays for optical board-to-board interconnects," *Proceedings - Electronic Components and Technology Conference*, pp. 1769-1775, 2008.
- [4.3] D. R. Selviah, E. A. Fernandez, I. Papakonstantinou, K. Wang, H. Bagshiahi, A. C. Walker, A. McCarthy, H. Suyal, D. A. Hutt, P. P. Conway, J. Chappell, S. S. Zakariyah, and D. Milward, "Integrated optical and electronic interconnect printed circuit board manufacturing," *Circuit World*, vol. 34, no. 2, pp. 21-26, 2008.
- [4.4] I. Papakonstantinou, D. R. Selviah, and F. A. Fernandez, "Multimode polymer bent tapered waveguide modeling," *Conference Proceedings - Lasers and Electro-Optics Society Annual Meeting-LEOS*, vol. 2, pp. 983-984, 2004.
- [4.5] I. Papakonstantinou, K. Wang, D. R. Selviah, and F. Anibal Fernandez, "Transition, radiation and propagation loss in polymer multimode waveguide bends," *Optics Express*, vol. 15, no. 2, pp. 669-679, 2007.
- [4.6] I. Papakonstantinou, D. R. Selviah, K. Wang, R. A. Pitwon, K. Hopkins, and D. Milward, "Optical 8-channel, 10 Gb/s MT pluggable connector alignment technology for precision coupling of laser and photodiode arrays to polymer waveguide arrays for optical board-to-board interconnects," *Electronic Components and Technology Conference, 2008. ECTC 2008. 58th*, pp. 1769-1775, 2008.
- [4.7] B. Huang, J. Chen, and W. Jiang, "Effects of Surface Roughness on TE Modes in Rectangular Waveguide," *Journal of Infrared, Millimeter and Terahertz Waves*, vol. 30, no. 7, pp. 717-726, 2009.
- [4.8] K. K. Lee, D. R. Lim, H. C. Luan, A. Agarwal, J. Foresi, and L. C. Kimerling, "Effect of size and roughness on light transmission in a Si/SiO<sub>2</sub> waveguide: Experiments and model," *Applied Physics Letters*, vol. 77, no. 11, pp. 1617-1619, 2000.
- [4.9] K. Wang, D. R. Selviah, I. Papakonstantinou, G. Yu, H. Bagshiahi, and F. A. Fernandez, "Photolithographically manufactured acrylate polymer multimode optical

CHAPTER 4: *Polymer Waveguide Optical Backplane UCL Research Review*

- waveguide loss design rules," *Electronics System-Integration Technology Conference. ESTC 2008.*, pp. 1251-1256, 2008.
- [4.10] K. Okamoto, *Fundamentals of optical waveguides* Academic press, San Diego city, 2006.
- [4.11] R. G. Hunsperger, "Losses in optical waveguides," *Integrated Optics*, pp. 107-128, 2009.
- [4.12] A. Yariv, "Coupled-mode theory for guided-wave optics," *Quantum Electronics, IEEE Journal of*, vol. 9, no. 9, pp. 919-933, 1973.
- [4.13] A. W. Snyder and W. R. Young, "Modes of optical waveguides," *JOSA*, vol. 68, no. 3, pp. 297-309, 1978.
- [4.14] A. K. Ghatak, "Leaky modes in optical waveguides," *Optical and Quantum Electronics*, vol. 17, no. 5, pp. 311-321, 1985.
- [4.15] I. Papakonstantinou and David R. Selviah (supervisor), "Analysis design and measurement of guided wave optical backplane interconnection." PhD thesis University College London, 2007.
- [4.16] D. Marcuse, "Radiation losses of tapered dielectric slab waveguides," *Bell Syst. Tech. J.*, vol. 49, no. 2, pp. 273-290, 1970.
- [4.17] D. Marcuse and R. M. Derosier, "Mode conversion caused by diameter changes of a round dielectric waveguide," *Bell Syst. Tech. J.*, vol. 48, no. 10, pp. 3217-3232, 1969.
- [4.18] C. Winkler, J. D. Love, and A. K. Ghatak, "Loss calculations in bent multimode optical waveguides," *Optical and Quantum Electronics*, vol. 11, no. 2, pp. 173-183, 1979.
- [4.19] M. Rivera, "A finite difference BPM analysis of bent dielectric waveguides," *Lightwave Technology, Journal of*, vol. 13, no. 2, pp. 233-238, 1995.
- [4.20] I. Papakonstantinou, D. R. Selviah, and K. Wang, "Insertion loss and misalignment tolerance in multimode tapered waveguide bends," *IEEE Photonics Technology Letter*, vol. 20, no. 9-12, pp. 1000-1002, 2008.
- [4.21] H. Baghsiahi, D. R. Selviah, G. Yu, K. Wang, M. Yau, and F. A. Fernandez, "Photolithographically manufactured acrylate multimode optical waveguide translation and rotation misalignment tolerances," *Proceedings- 2008 2nd Electronics System Integration Technology Conference, ESTC*, pp. 617-621, 2008.
- [4.22] Rsoft, "Rsoft Group," <http://www.rsoftdesign.com/>, 14 november 2011.
- [4.23] "Optiwave, Design sotware for Photonics," <http://www.optiwave.com/>, June 2009.
- [4.24] M. Born and E. Wolf, *Principles of Optics.*, 6 ed Cambridge University, 1999.



CHAPTER 4: *Polymer Waveguide Optical Backplane UCL Research Review*

- [4.25] Pao-Lo Liu, S L Yang, and D M Yuan, "The Semivectorial Beam Propagation Method," *IEEE J. Quantum Electron*, vol. 29, no. 4, pp. 1205-1211, Apr. 1993.
- [4.26] M. Born and E. Wolf, *Principles of Optics* 1999.
- [4.27] "The Finite Difference – Beam Propagation Method and Finite Difference Mode Solver," [http://www.nottingham.ac.uk/ggiemr/downloads/SL\\_chapt3.pdf](http://www.nottingham.ac.uk/ggiemr/downloads/SL_chapt3.pdf), March 2011.
- [4.28] G. R. Hadley, "Wide-angle beam propagation using Pade approximant operators," *Optics Letters*, vol. 17, no. 20, pp. 1426-1428, 1992.
- [4.29] J. P. Berenger, "A perfectly matched layer for the absorption of electromagnetic waves," *Journal of computational physics*, vol. 114, no. 2, pp. 185-200, 1994.
- [4.30] G. R. Hadley, "Transparent boundary condition for the beam propagation method," *Quantum Electronics, IEEE Journal of*, vol. 28, no. 1, pp. 363-370, 1992.
- [4.31] I. Papakonstantinou, K. Wang, D. R. Selviah, and F. A. Fernández, "Transition, radiation and propagation loss in polymer multimode waveguide bends," *Optics Express*, vol. 15, no. 2, pp. 669-679, Jan. 2007.
- [4.32] K. Iga, "Surface-emitting laser - Its birth and generation of new optoelectronics field," *Ieee Journal of Selected Topics in Quantum Electronics*, vol. 6, no. 6, pp. 1201-1215, 2000.
- [4.33] I. Vurgaftman, J. R. Meyer, and L. R. Ram-Mohan, "Mid-IR vertical-cavity surface-emitting lasers," *IEEE Journal of Quantum Electronics*, vol. 34, no. 1, pp. 147-156, 1998.
- [4.34] J. Piprek, H. Wenzel, and G. Sztefka, "Modeling Thermal Effects on the Light Vs Current Characteristic of Gain-Guided Vertical-Cavity Surface-Emitting Lasers," *IEEE Photonics Technology Letters*, vol. 6, no. 2, pp. 139-142, 1994.
- [4.35] G. Hasnain, K. Tai, L. Yang, Y. H. Wang, R. J. Fischer, J. D. Wynn, B. Weir, N. K. Dutta, and A. Y. Cho, "Performance of Gain-Guided Surface Emitting Lasers with Semiconductor Distributed Bragg Reflectors," *IEEE Journal of Quantum Electronics*, vol. 27, no. 6, pp. 1377-1385, 1991.
- [4.36] G. Hasnain, K. Tai, N. K. Dutta, Y. H. Wang, J. D. Wynn, B. E. Weir, and A. Y. Cho, "High-Temperature and High-Frequency Performance of Gain-Guided Surface Emitting Lasers," *Electronics Letters*, vol. 27, no. 11, pp. 915-916, 1991.

## **Chapter 5: Multiple Viewer Laser Illuminated Autostereoscopic 3D Display System**

### **5.1 Introduction**

In this chapter, an auto stereoscopic display system that was developed at University College London (UCL) is explained. This autostereoscopic display enables viewers to see 3D images or 3D video by presenting stereo images; one to each eye. The autostereoscopic, multi-user back projection display system was developed within a European Union-funded project called HELIUM3D. The other collaborators in this research were; Koç university in Turkey (KOC), De Montfort University in the UK (DMU), Nanjing University in China (NJU), Philips in Holland (PHI), Barco in Belgium (BAR), the Technical University of Eindhoven in the Netherlands (TUE) and Fraunhofer Heinrich Hertz Institute, HHI in Germany. Although the author was involved in the design, and implementation of the system described in this chapter, the main aim is to present the background necessary to understand the new research carried out by the author which is documented in chapters 8, 9, and 10 and summarised in the conclusions in Chapter 11.

In chapter 3, several laser illuminated display systems were introduced and reviewed. The use of lasers in display systems provides a larger colour gamut and lower étendue (a measure of the light divergence [5.1]) which enables a higher degree of light control than displays which use incoherent illumination. However, these advantages come at the expense of laser speckle observed by the viewer on the image, optical power safety considerations and high system cost.

Figure 5.1 shows a schematic diagram of the HELIUM3D display system. This system is essentially a back-projection system that operates by scanning a column of light across a liquid crystal on silicon (LCoS) two dimensional optical modulator “light valve” device. The resulting image column passes through the system and the beam is modulated in such a way that the images are directed to each of the viewers’ eyes continuously over the duration of the scan and different stereo images to the left and right eye are presented time sequentially [5.2]. There are ten separate areas shown in the block diagram, some are relatively simple, for example the Intermediate Image Stage and others such as Image Generation (shown in Figure 5.2) are complex. However, for the purposes of the specification of the overall system architecture the

interfaces between the blocks provide natural boundaries to separate the different functionalities of the parts.

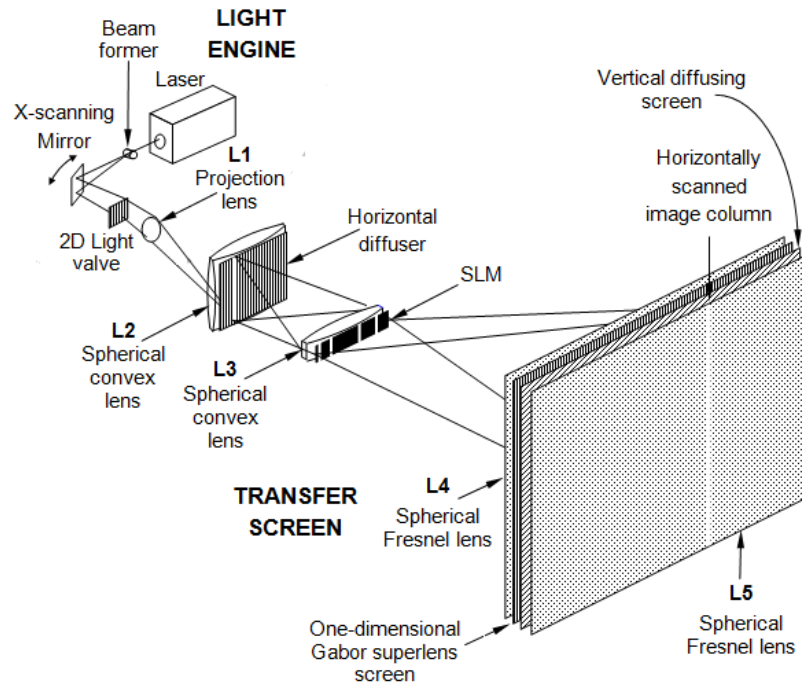


Figure 5.1: Schematic diagram of the HELIUM3D laser projection display system.

In Figure 5.1, the image formed on the 2D light valve (the light valve, LV, is a Liquid Crystal on Silicon, LCoS, device for modulating the light intensity and generating the image) is projected onto lens L2 by projection lens L1. The figure is a simplified version of the actual display and only shows one laser for clarity; the actual display employs red, green and blue lasers whose outputs are combined. Also, three light valves, one for each colour, with associated splitting and combining optics are used. The light valve is illuminated with a column of light that is produced by beam forming optics and is scanned horizontally by an electromechanical device such as a galvanometer mirror [5.3]. The components generating the image are referred to as the light engine which can be considered as an entity whose purpose is to produce a projected image onto lens, L2. The remainder of the display hardware is referred to as the Transfer Screen and its purpose is to magnify the image from, L2, and to control the direction of the light emerging from the front screen. This control is performed by a one-dimensional High Speed Liquid Crystal

## CHAPTER 5: *Multiple Viewer Laser Illuminated Autostereoscopic 3D Display System*

Spatial Light Modulator, SLM that allows light to pass through regions selected by the output of a multi-target pupil tracker (it is a camera system that can track multiple viewer eyes position). The transfer screen comprises three components and is used to steer the image over a large field of view [5.4]. Figure 5.2 is a plan view of the components and viewing field drawn with dimensions that are close to the actual requirements.

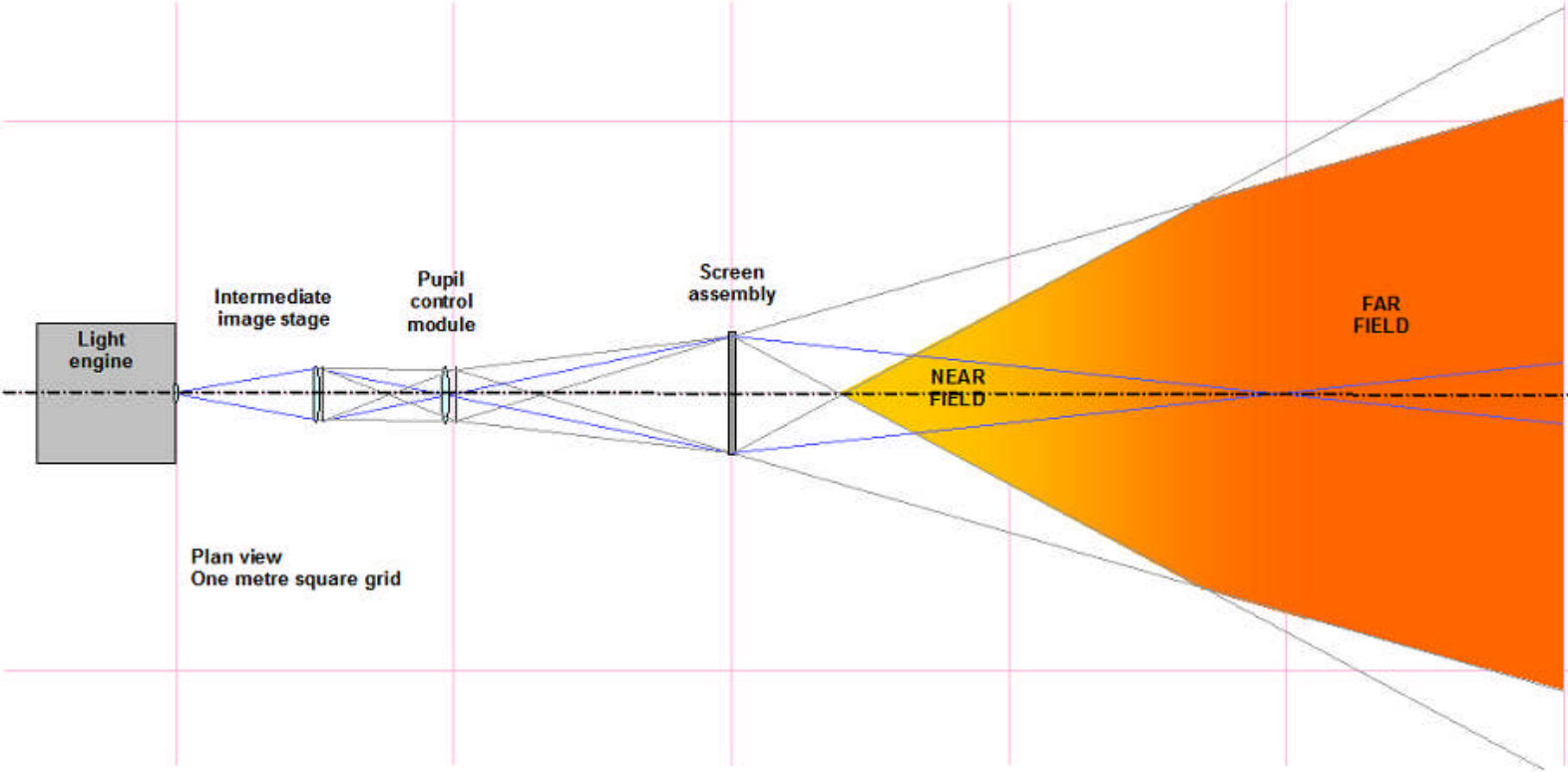


Figure 5.2: Plan view of the 3D display system which was developed in UCL. The viewer’s eye is placed in the shaded (orange (shaded) coloured) area.

In this chapter, the HELIUM3D system optical parts are first introduced and then the functionality of the system is presented. Following this the light engine and two different prototypes of the light engine using low and high power lasers, developed in UCL, are described. For each prototype the laser sources and the optical design is explained in detail. The research was performed jointly with other partners, in particular Koç University and De Montfort University.

The focus in this thesis is on the light engine and speckle issues as the author's research concentrated on these aspects of the system. Further details can be found in publications by our research group [5.2-5]. In the next sections of this chapter, different optical parts of the HELIUM3D system and the reason for the selection of the optical design for each section are described as well as the functionality of that part within the system. Finally, two different prototypes using low power and high power lasers and the lasers used for each prototype are explained. These prototypes were developed at UCL by the author of this thesis.

## **5.2 Light Engine for the HELIUM3D System**

Figure 5.3 shows a schematic diagram of the system [5.2]. Red, green, and blue laser beams are combined and shaped into a light column that is scanned horizontally across the LCoS light modulator. The output image from the LCoS modulator is projected by lens (L1) into the Intermediate Image Stage of the display system.

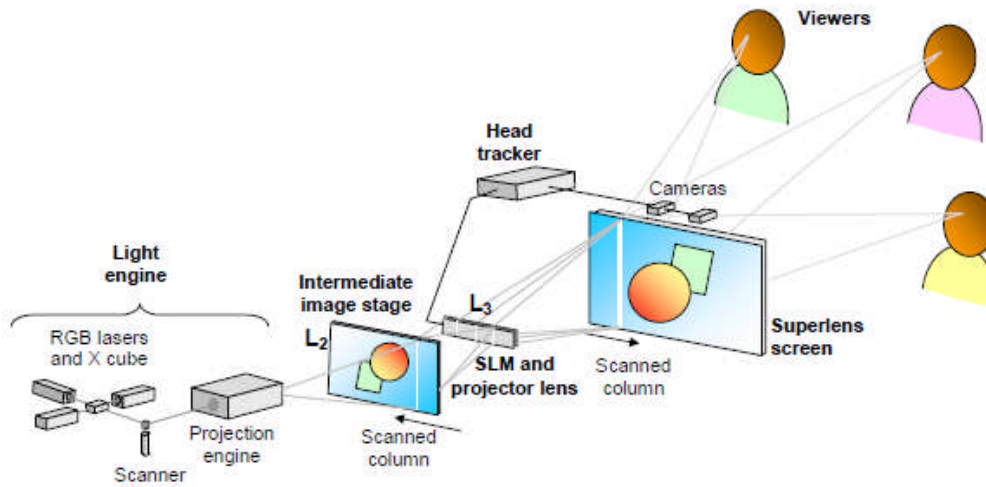


Figure 5.3: Schematic diagram showing the light engine, Transfer Screen and viewers in the HELIUM3D display system (This picture was drawn by Phil Surman fellow researcher from DMU and used with his permission).

Figure 5.4 is a schematic diagram of the light engine. The light engine can be divided into 5 sections, these are; lasers, beam combining optics, beam shaping optics, beam scanning mirror and image formation. The beam combining and shaping depends on the choice of lasers as their beam properties will determine the specific methods used and the optical elements requirements.

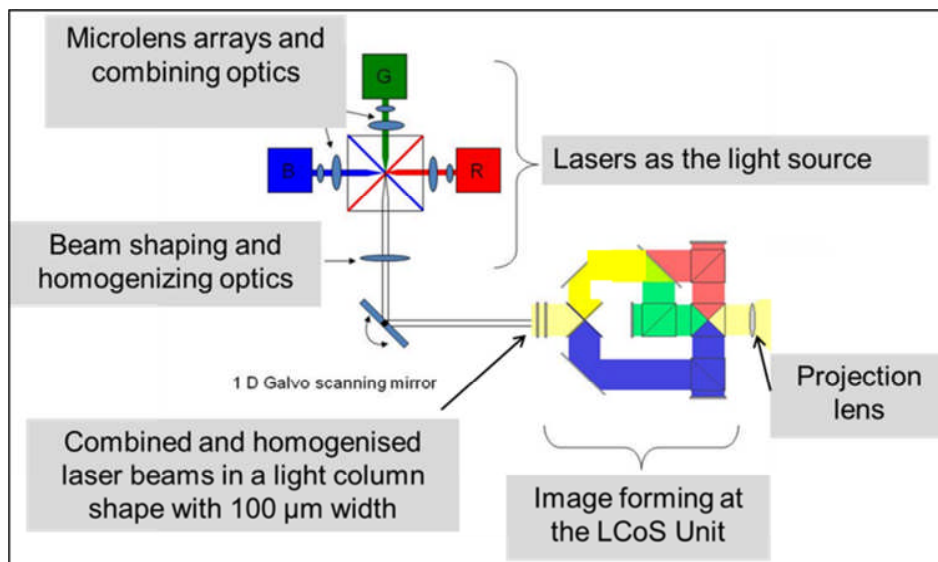


Figure 5.4: HELIUM3D light engine. In prototype one the light source comprises low power single-emitter lasers whose outputs are combined by an X-cube. The combined beam is shaped into a line using a cylindrical lens.

The image forming section in Figure 5.4 separates the red, green, and blue colours, as there is one LCoS device allocated to each colour to generate the image, and then combine them into a unite beam. The light engine of the HELIUM3D system delivers a vertical uniform white light column with dimensions of  $10\text{ mm} \times 100\text{ }\mu\text{m}$ , which is scanned across a liquid crystal on silicon, LCoS, light valve with the use of a scanning mirror. Three lasers are used and their outputs are combined, homogenised and shaped to deliver a uniform light column on to the LCoS device with a non-uniformity of  $< 10\%$ . Uniformity (or non-uniformity) is determined by dividing the minimum value of the intensity in a picture by the maximum intensity value[5.6;7]. Figure 5.5 explains the relationship between the width of the scanning line on the LCoS and width of the image at the position of the viewer's eye. The exit pupil in this figure is where the viewer is positioned. The function of the transfer screen is to convey the images produced on the LCoS devices to the front screen via the Spatial Light Modulator, that controls the directions of the emergent light so that this always passes to the pertinent viewers' eyes. The overall magnification between the LCoS devices and the screen is the ratio of their widths and this magnification factor determines the design of the Gabor superlens front screen. For a 30" screen the magnification is of the order of 50 [5.4].

Figure 5.5 shows that a real image of the SLM is produced in the viewing field by the Gabor superlens front screen [5.4]; its location is referred to as the conjugate plane of the SLM. This figure shows the position of the image column at two different instants over the duration of the scan. Ideally the column width would be negligible in order for defocusing not to occur as this contributes to crosstalk where the left image is seen partially by the right eye and vice versa. For a  $100\text{ }\mu\text{m}$  beam width on the LCoS device a magnification of  $\times 50$  gives an image column width of 5 mm. If the conjugate plane is 2000 mm from the screen and the viewer is 500 mm from the screen then the defocusing will be 3.8 mm which is small compared to the interocular distance of around 65 mm. As crosstalk is determined by many factors including scattering at the front screen, imperfect Gabor superlens collimation, SLM element pitch, SLM response time, diffraction by the LCD sub-pixels, scattering at the front screen and imperfect collimation of the superlens it is preferable to keep the scanned beam width to a minimum.



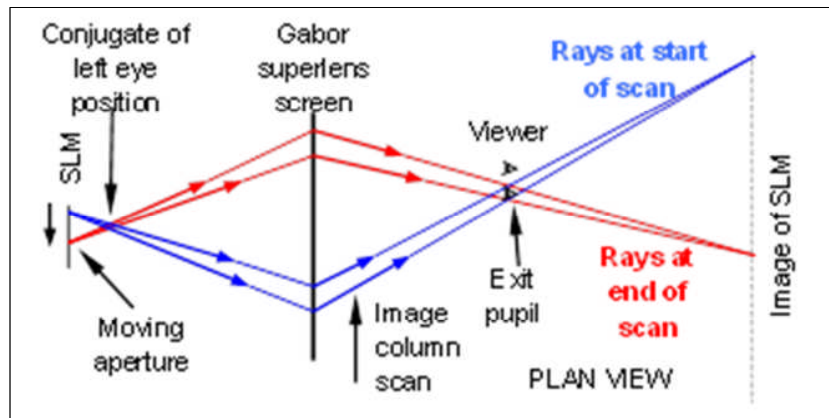


Figure 5.5: The exit pupil is formed dynamically from a laterally-scanned image column whose emergent light direction changes in order to arrive at the eye during the scan. It should be noted that the width of the beams shown are not the actual width of the exit pupil but indicate the defocusing effect on the ideal top hat intensity profile of the pupil.

Therefore, to summarise, red, green and blue, lasers are employed in the light engine and a system is required to combine the laser beams, homogenise the power and shape it into a column of light with a width of 100  $\mu\text{m}$  and height of 10 mm that is determined by the height of the active area of the LCoS modulation device. It should be noted that the width of 100  $\mu\text{m}$  is the ideal size for the light on the LCoS, however, the system performance is not seriously degraded if the beam is as wide as up to 1 mm. The increase in width of the light at the LCoS modulation device can be compensated in the later stages in the HELIUM3D system.

The light engine comprises several principal components. These are:

- **Light source:** Three lasers are used for the illumination source, these are: red (639 nm), green (532 nm) and blue (465 nm).
- **Beam-shaping optics:** this is required to convert the combined RGB laser beam into the fan of rays that illuminates the LCoS 2D modulator. The operation of the beam former is critical as the performance of the system (in terms of cross talk) depends on a narrow light beam entering the LCoS devices (100 microns).
- **Horizontal scanner :** this device is used to provide lateral scanning of the vertical fan of laser rays and scans up to 120 Hz for one viewer prototype. An off-the shelf galvanometric closed-loop scanner was used in this project. These require a controlled ramp scan waveform that is synchronised with the video frame.

- **LCoS Assembly and drivers:** The LCoS assembly provides a projector that forms an image in the Intermediate Image Stage.
- **Beam splitter and recombining optics:** this comprises X-cubes and dichroic mirrors/filters (dichroic filters are very accurate colour filters which are used for colour combining and colour separating) that separate the red, green and blue wavelengths into three separate channels that illuminate each of the three LCoS devices and then recombine their outputs. The optics were obtained from commercial projectors and by fabrication with off-the-shelf components.
- **Projection lens:** This is required to focus the scanned image columns reflected from the LCoS devices on to the Intermediate Image Stage.

### 5.3 Transfer Screen in the High Efficiency Laser-Based Multi-user Multi-modal 3D Display System

In this section the optical parts from the light engine to the viewers' eyes are explained and explored. This section is called the transfer screen and consists of the Intermediate Image Stage, the Pupil Control Module and the Front Screen. Figure 5.6 shows a plan view of different parts of the system.

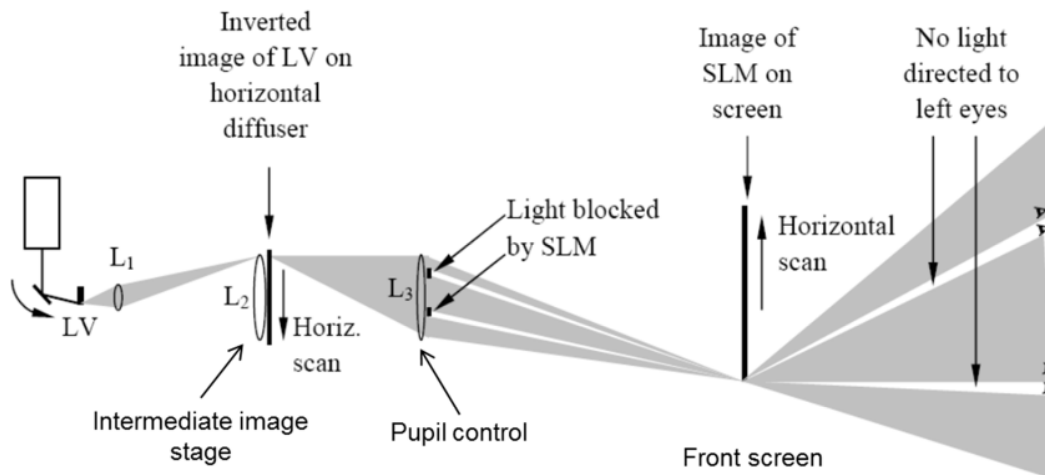


Figure 5.6: Plan view of the HELIUM3D system showing different sections of the system (This picture was drawn by Phil Surman from DMU and is used with his permission).

### **5.3.1 Intermediate Image Stage**

This stage consists of a spherical lens and a diffuser which forms a real image and diffuses the image in the horizontal direction (but not vertically) in order for the light from each image column to fill the entire width of the following section (SLM).

The spherical convex lens, L2 (Figure 5.6), located before a diffuser, acts as a field lens to concentrate the axes of the diffuser towards the centre of the SLM in the horizontal direction. In the vertical direction it focuses the projection lens, L1, onto the SLM. In principle, a holographically-produced diffuser is preferable compared to a microlens diffuser after L2, as the top-hat function of the holographic diffuser gives a more even illumination than the Gaussian distribution of the lenticular microlens diffusers and microlens diffuser also causes Moiré fringing patterns in the final image. The specification of the diffuser is less critical here than it is in some applications as any component of scattering in the vertical direction will merely result in some light loss but will not contribute to crosstalk between right and left eyes. However, the type of the diffuser can affect the speckle patterns which are explained in chapter 10. A cylindrical microlens array is, therefore, used as the horizontal diffuser. The pitch of the array was measured to be 0.385 mm with a radius of 0.72 mm. However, this is larger than the size of the pixels imaged onto L2 ( $302 \text{ mm} / 800 \text{ pixels} = 0.3775 \text{ mm/pixel}$ ). This means that in some cases a pixel may be imaged between two adjacent micro lenses. The result of this may be “gaps” or dark vertical bands appearing in the final image.

### **5.3.2 Pupil Control Module**

The Pupil Control Module, PCM, comprises the spherical convex lens, L3 and a linear SLM (with driver) having switchable vertical apertures. At a given position of the horizontal scan these aperture positions correspond to particular emergent horizontal angles from the screen. L3 is actually a spherical lens that is effectively the projection lens for projecting the image onto the Transfer screen.

The SLM must be fast enough in order to cope with exit pupils that are furthest from the conjugate plane of the SLM in the viewing field. This is due to the fact that the dynamic aperture forming the pupil must move position during the horizontal scan. The specification of the PCM section is listed in Table 5.1.

Table 5.1: Pupil Control Module Component Specification

Projection lens L3	Width	200 mm
	Height	20 mm
	Focal length	330 mm
SLM	Length L	$96 \text{ mm} < L < 192 \text{ mm}$
	Width	50 mm
	Pixel pitch	$L / 128 \text{ mm}$
	Response time	100 $\mu\text{s}$
	Aperture ratio	> 95 %
	Contrast ratio	> 100:1
	LC type	Ferroelectric

The SLM is a fast ferroelectric LC device consisting of an array of 128 pixels. The dimensions of the pixels are such that a 150 by 20 mm rectangular area is filled by them (the pixel width is 1.17 mm), as shown in Figure 5.7. The actual size of the device surrounding the active LC region is larger, in order to connect the pixels.

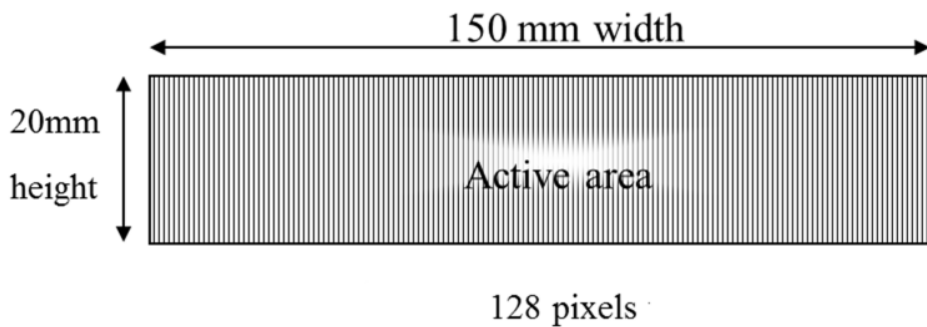


Figure 5.7: Schematic diagram of the SLM

The SLM operates over the range of wavelengths ranging from 460 to 640 nm and acts as a half wave plate at 532 nm.

### 5.3.3 Front Screen

The screen assembly performs the function of magnifying the relatively small input angle that is determined by the SLM being a relatively short length (200 mm) into an angle that is sufficiently

large to provide an acceptably wide viewing field. A real horizontally-scanned image from the Pupil Control Module, where the rays from certain directions have been blocked enters the screen assembly. The light from each image column is directed to all the viewers' left eyes during even-numbered scans and a right image directed towards all the viewers' right eyes during odd-numbered scans.

The screen comprises four components as shown in Figure 5.8; their functions are as follows:

- **Fresnel lens, L4:** The diverging rays from the SLM are collimated by spherical Fresnel lens 1 so that they enter the superlens assembly orthogonally to its surface.
- **Superlens assembly:** It consists of 4 microlens surfaces arranged as two telescopes. More detailed description of its operation is given in [5.4].
- **Fresnel lens, L5:** The rays are concentrated towards the axis in the vertical direction in order to reduce losses caused by light being directed above and below the viewing region. The rays are concentrated in the horizontal direction to give the viewing field shown in Figure 5.2.
- **Vertical diffuser:** The light is diffused in the vertical direction to provide image information in the complete height of the viewing field.

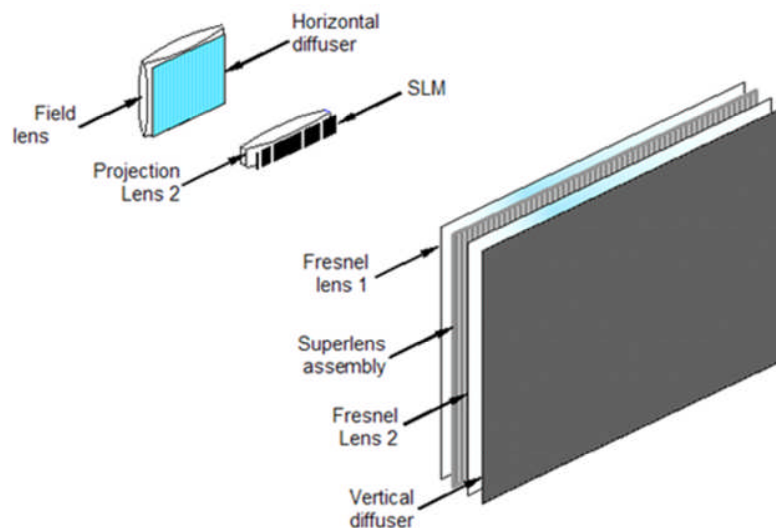


Figure 5.8: Front screen assembly and the various parts of the screen.

Figure 5.8 shows a schematic diagram of the front screen assembly and different sections of this screen. In this picture, the Intermediate Image Stage and the Pupil Control Module are indicated to show how they are placed in the system. The numbers in this picture are the sequence; for example projection lens 2 means the second projection lens in the system which is L3.

### **5.3.4 Pupil Tracker**

It was originally intended that the Pupil Tracker should provide lateral head position coordinates to a precision that enabled the images to be rendered in accordance with the viewer's lateral position, thus, permitting the presentation of motion parallax. This means that as the viewer moves sideways the image that is presented to them is changed to what they would see if they really moved around a 3D object. In a previous display, the head tracker was merely used to place exit pupils in the vicinity of the viewers' eyes. Provided the eyes are within the exit pupils, in such a way that the images remain constant in terms of perceived brightness and crosstalk, the tracker is performing to a sufficient degree of accuracy.

## **5.4 Light Engine Developed at UCL**

The HELIUM3D system and different parts of this display system were explained in the previous section. In this thesis the new research is focused on the light engine and speckle problems in the system. So in this section, two different prototypes for the light engine are explained. The prototypes are different in terms of the lasers and the power in each colour. The reason that two prototypes were developed was to check the system with low power lasers before designing the optics for the high power lasers. The low power lasers were available at the time and the tests could be carried out on the system. The two prototypes explained in this chapter are two different light engine designs. The transfer screen and the rest of the system are the same. However, there were several different prototypes of the transfer screen which the author was also involved in designing and experimental alignment and testing, but this is not explained in this thesis as it is not the subject of the main research.

### **5.4.1 Low Power Laser as the Light Source in the High Efficiency Laser-Based Multi-user Multi-modal 3D Display (Prototype one):**

In this section, the first prototype of the light engine for HELIUM3D system is explained. For the first system, the lasers were to be chosen with lower power (compared to the power of the

lasers in the final design) being single emitters with Gaussian beams. The reason for choosing such a system was to make the light engine for the display system with the available low-power lasers and the beam shaping components. The prototype was used to test the performance of the transfer screen and the switching times of the LCoS and SLM. The off-the-shelf lasers purchased had lower power than the requirements for the final prototype of the light engine (this requires about 1 W optical power for each colour at the output of the light engine to achieve enough optical power at the viewer position). The provided power by the low power lasers enabled some tests on the HELIUM3D system to be carried out even if the light engine output was not uniform and homogenised.

Two diode pumped solid state (DPSS) lasers with wavelengths of 532 nm (green) and 457 nm (blue) and one diode laser with a wavelength of 640 nm were chosen as the light sources. The maximum power of the lasers was 300 mW for green, 200 mW for blue and 200 mW for red. The specification of the lasers is listed in Table 5.2. The laser beam quality is very close to diffraction limited (it can be focused to a smallest possible spot for a particular wavelength [5.8]) and a free space method using lenses was employed to combine and shape the lasers. The advantage of using these lasers was that they were readily available and that their performance was sufficient for testing the system.

Table 5.2: The laser specifications of the low power lasers for the light engine system

Laser type	DPSS	DPSS	Diode laser
Wavelength (nm)	457±1	532±1	640±5
Output power (mW)	200	300	200
Transverse mode	Near TEM01	TEM00	Near TEM00
Operating mode	CW	CW	CW
Power stability (rms, over 4 hours)	< 3%	< 3%	<5%
Beam divergence, full angle (mrad)	< 0.2	< 1.5	1
Beam diameter at the aperture (mm)	4	2	1 × 1.5
Polarization ratio	>100:1	>100:1	>100:1

The laser beams were combined using an X-cube and expanded using a 10× beam expander and shaped into a line using a cylindrical lens. The optical power distribution of the combined laser beams after the X-cube was not top-hat shape (it was more like a Gaussian shaped circular spot with a measured full width at half maximum diameter of 3-5 mm). This spot was expanded in

## CHAPTER 5: *Multiple Viewer Laser Illuminated Autostereoscopic 3D Display System*

order to illuminate the entire height of the LCoS. Using a 10× beam expander converts the spot into a beam with 50 mm height which is larger than the height of the LCoS (10 mm). The beam is expanded to a larger diameter to increase its uniformity by expanding the beam and selecting the central region [5.9-12].

The cylindrical lens shapes the beam and focuses the power into a column or line as the light is focused in the horizontal direction and remains unaltered in the vertical direction. The width of the column was  $300 \mu\text{m} \pm 100 \mu\text{m}$ . This column is scanned with a frequency of 60 Hz onto the LCoS modulator (which forms the image) device by means of a mirror (Figure 5.10). The LCoS device and the projection lens were taken from a Canon SX60 projector. The projector was taken apart with the assistance from Koç University and the combined and shaped laser beams replaced a halogen lamp which was already in the projector as the light source. Due to this approach we did not have to design and manufacture an image forming and projection system ourselves.

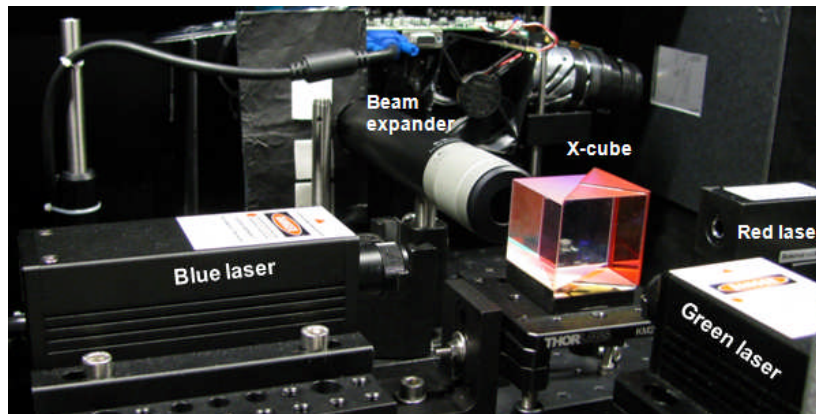


Figure 5.9: Lasers, X-cube and the beam expander in the low power prototype light engine of High Efficiency Laser-Based Multi-user Multi-modal 3D Display.



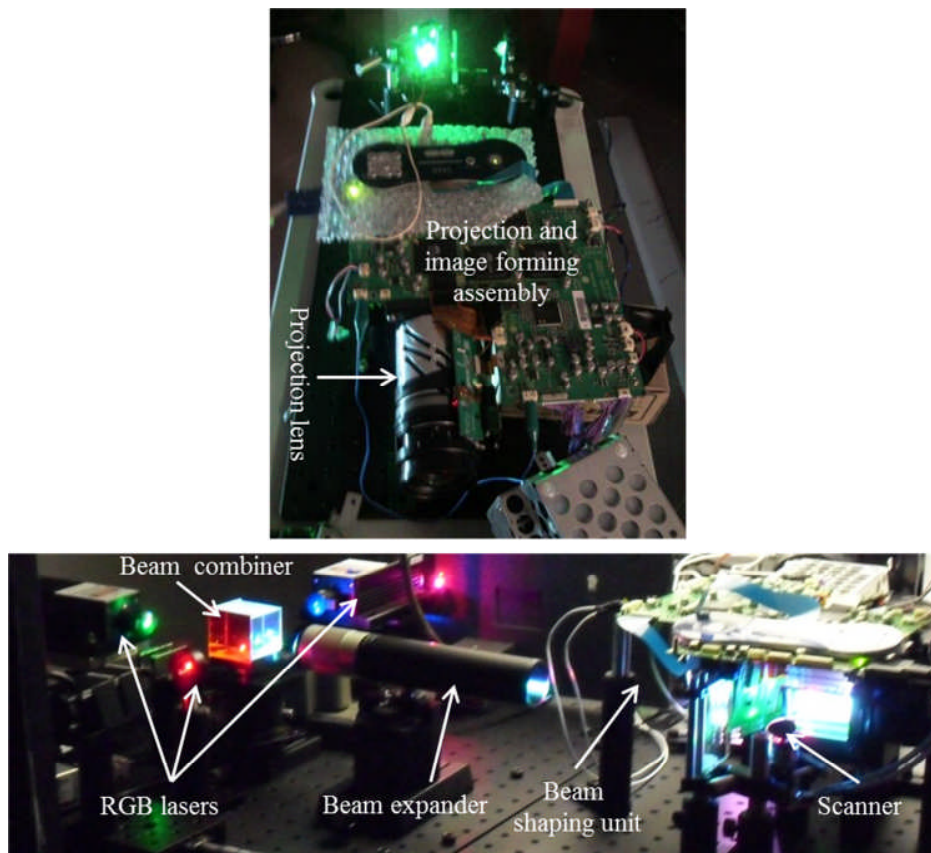


Figure 5.10: Low power light engine system. The three lasers are combined using an X-cube and the combined beam is directed into the beam expander. The expanded white light is shaped by a cylindrical lens and scanned onto the LCoS modulator.

Figure 5.9 and Figure 5.10 show the light engine and different optical elements were used in the system to combine the laser beams and shape the combined lasers into a light line. A schematic diagram of the complete prototype is shown in Figure 5.11 and its photograph in Figure 5.12. Within the light engine the beam is split into the primary colours with an X-cube and illuminates three LCoS modulators on which the images are formed. These are then recombined with another X-cube and projected on to the L2/diffuser assembly. The image produced on this assembly is focussed to a narrow horizontal line on the next stage which projects the image to the front screen and also controls the emergent light directions with the use of an SLM which in this case is a 120 Hz LCD. The front screen forms magnified real images of the transmitting apertures in the SLM and also diffuse light in the vertical direction. This provides exit pupils that are spread over a vertical direction.

CHAPTER 5: Multiple Viewer Laser Illuminated Autostereoscopic 3D Display System

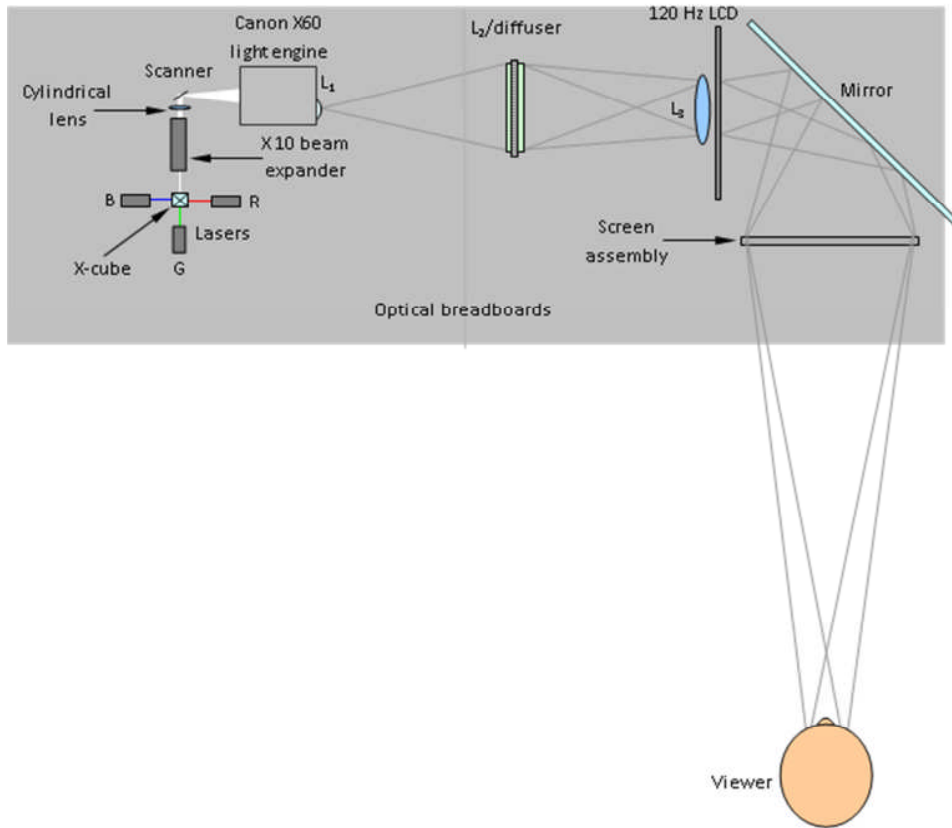


Figure 5.11: This is a schematic diagram of the complete arrangement. As the light path axis is long it is folded through 90° by the mirror in order to accommodate it on two optical breadboards against a wall behind them.

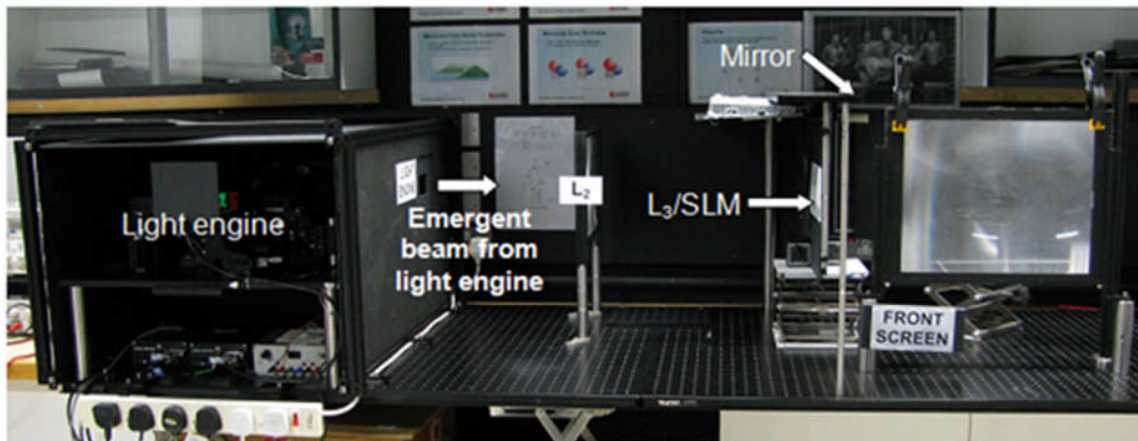


Figure 5.12: For safety reasons the light engine is completely enclosed. This is particularly important as the axis of the complete display is at eye height

## CHAPTER 5: *Multiple Viewer Laser Illuminated Autostereoscopic 3D Display System*

Laser safety is particularly important as three class four lasers are used in the display. For this reason the complete light engine assembly is enclosed with the output exiting an aperture of 75 mm square. Particular care must be taken as the axis of the complete optical system is at eye level, thus, increasing the possibility of eyes receiving stray beams.

Figure 5.13 and Figure 5.14 show the output of the projector when it is scanning at frequencies of 1 Hz and 60 Hz respectively.

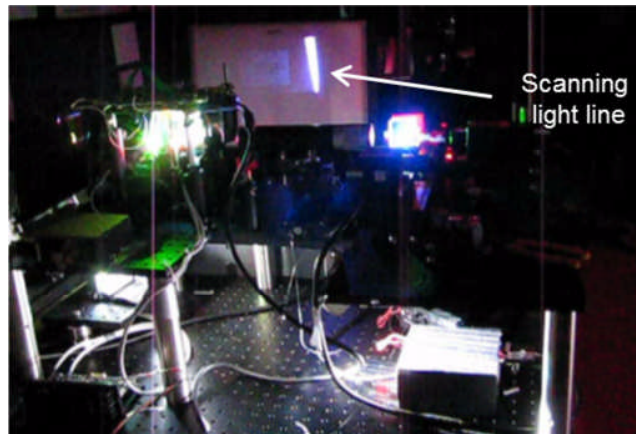


Figure 5.13: A picture from the width of the scanned image column at 1 Hz (exposure time of the camera was 0.01 s). If the scanner stops it is possible that the LCoS devices could be damaged due to the high optical power intensity of the light line.



Figure 5.14: Projector Image at 60 Hz Scanning rate. The image appears to have reasonable colour uniformity; it is possible that the lasers were subsequently subjected to disturbance before evaluations were carried out.

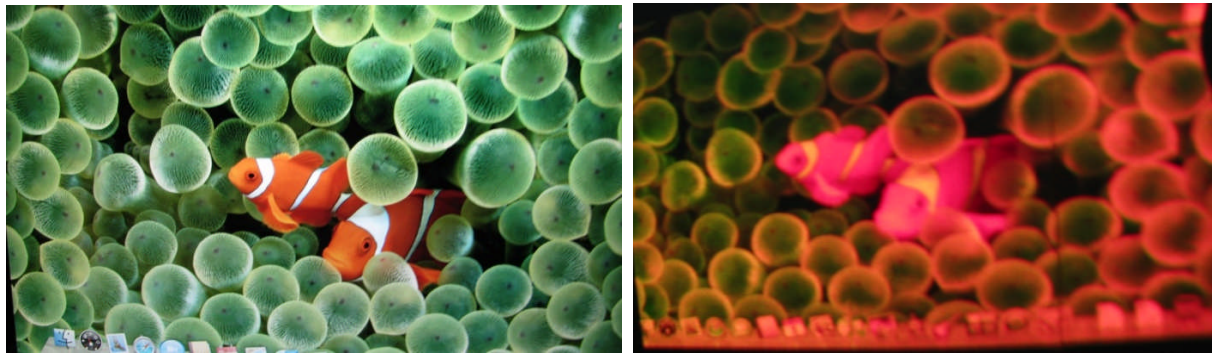


Figure 5.15: The resultant image from the low power laser projection system. These pictures were taken by using a conventional camera from the screen. The picture on the left is the input picture from the computer and how it is shown on the monitor. The picture on the right hand side is the output of the system.

In Figure 5.15, the colours are different between the two pictures. The reason is that we did not apply any colour balancing in the system at this stage as this was not the primary aim of this prototype which had been configured to test the concept of the system.

#### **5.4.2 High Power Lasers as the Light Source in the High Efficiency Laser-Based Multi-user Multi-modal 3D Display (Prototype two):**

The display system must provide sufficient luminance at the final screen; this is principally determined by the efficiency of the system and the available optical power of the lasers. The power efficiency of the system was estimated to be less than 5% as light is lost in the beam combining, shaping and image forming stages. The lasers must therefore, provide sufficient output power at the first stage (Brightness= 200 cd/m<sup>2</sup>).

Several laser suppliers around the world were investigated when choosing suitable lasers and the final choice was based on the power, specification and cost. Several different companies were considered and five of them were shortlisted on the basis of the cost of the lasers, technical support, reliability and the laser specifications. The five companies were; Arasor, QPC, Frankfurt laser, Mitsubishi and RGB laser. After further investigation and evaluation, NECSEL (Novalux Extended Cavity Surface Emitting Laser) lasers, supplied by Arasor, were chosen as the light source.

A NECSEL is a frequency-doubled surface-emitting diode laser and is a multi-emitter laser generating green and blue light. The red laser was chosen to be a multi-emitter edge-emitting

diode laser from the DILAS Company. The NECSEL lasers have 48 emitters in 2 rows (Figure 5.16). The pitch between the emitters is reported by Arasor Company to be 320  $\mu\text{m}$  and the beam waists of the top and bottom rows are 15.5 mm away from each other. However, we found that this is not the distance between the emitters. The specification of these lasers is based on the company's data sheet and is listed in Table 5.3.

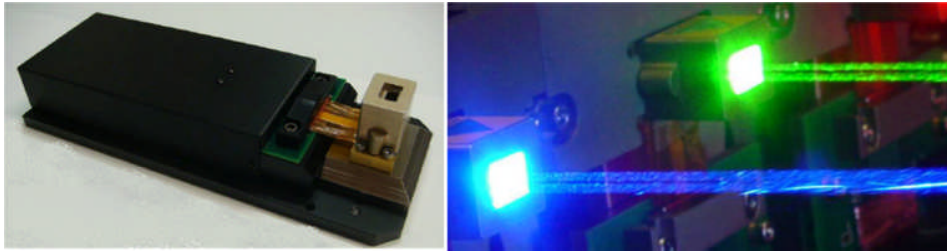


Figure 5.16: NECSEL emitters for the green and blue laser. A total of 3W laser power is emitted in two rows which are separated 2.1 cm from each other. The full angle divergence of each emitter is  $10\pm 4$  mrad which is the same for the fast and slow axis (these are the specifications from the data sheet provided by Arasor).

In Figure 5.17, a schematic diagram for the NECSEL is presented. The PPLN (Periodically Poled Lithium Niobate) crystal is used to double the frequency of the output beam from a surface emitting diode laser. The infra-red (IR) output of the VCSEL resonates in a cavity between the VCSEL and the VBG (Volume Bragg Grating) component used to stabilise the laser and form a cavity. The IR radiation passes through the PPLN and the frequency of the beam is doubled by nonlinear optics. The light with doubled frequency radiates away from the laser cavity from the back and front. The back radiation is diverted using mirrors to make the second row of emitters.

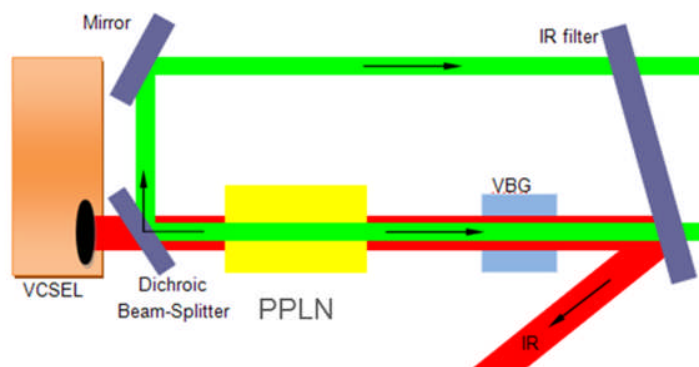


Figure 5.17: NECSEL 3W Blue/Green dual row block diagram of one single emitter.

The NECSEL can be driven in continuous wave (CW) or pulsed mode and the power can be controlled via duty cycle, frequency or applied voltage. The pulse rate can be chosen to be up to

1 MHz. The output is vertically (perpendicular to the rows of the emitters) polarized and the maximum optical power is 3W.

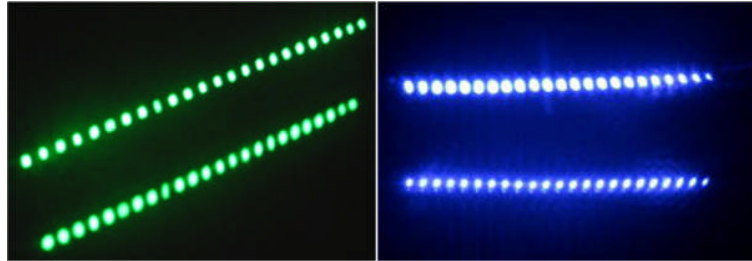


Figure 5.18: NECSEL emitters for the green and blue laser. 48 emitters are configured in two rows with 2.1 cm separation (these are the specifications from the data sheet provided by Arasor).

Red illumination is provided by a diode laser which has 20 emitters in one row with 200  $\mu\text{m}$  pitch. The divergence along the fast axis is 85 degrees and along the slow axis is 9 degrees as it is shown in Figure 5.19. (Fast axis and slow axis refers to the directions where high and low laser beam divergence in diode lasers occur). Edge-emitting diode lasers have a large divergence along the fast axis as the size of the emitting area is typically small (a few micrometres). Micro-lens structures are a popular candidate for divergence reduction in these lasers. Consequently, a cylindrical micro-lens array has been implemented in the red diode lasers used in this project and the divergence has been reduced to 0.5 degree (8.7 mrad). Therefore, in the fast axis the beam is well collimated and in the slow axis the full-angle divergence is reported by the suppliers DILAS to be 9 degrees (0.157 rad).

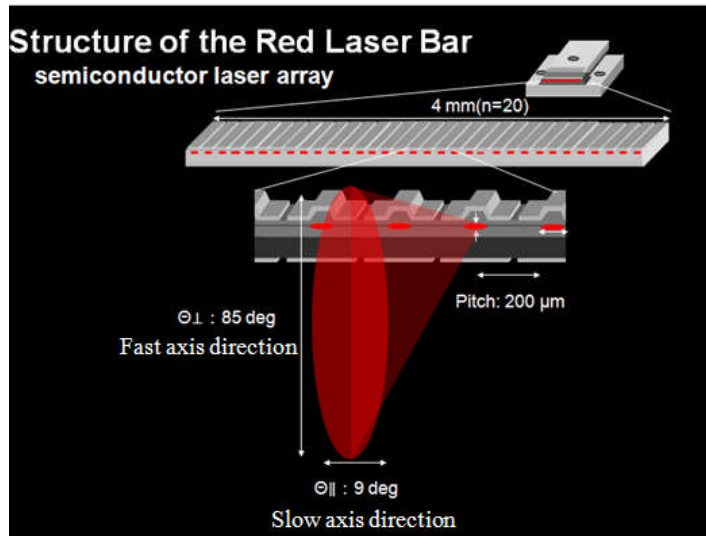


Figure 5.19: Schematic diagram of the red laser which is an edge emitting diode laser with 20 emitters separated 200 μm from each other. n=20 is the number of the emitters and the laser beams are polarised parallel to the fast axis.

The parameters of the red, green and blue lasers are listed Table 5.3. NECSELs were new developed lasers (developed 2009) at the time this research was carried out and there was very little information available apart from that given in the company specification. Therefore, we characterised the laser beam ourselves in order to find the parameters used for designing the optical system.

Table 5.3: Specification provided by Arasor and DILAS Company of the red, green and blue lasers used in the HELIUM3D light engine

Laser type	Surface emitting diode laser	Surface emitting diode laser	Edge emitting Diode laser
Wavelength (nm)	457±5	532±5	639±5
Output power (mW)	3000	3000	5000
Spectral width (nm)	0.2	0.2	3-5
Number of emitters	48	48	20
Number of output beams per row	24	24	20
Space between two emitters (mm)	0.320±0.001	0.320±0.001	0.200 ± 0.001
Space between two rows (mm)	2.1±0.1	2.1±0.1	NA
Beam Diameter @1/e <sup>2</sup> (µm)	80	80	1-2 × 40
Operating mode	CW/pulsed	CW/Pulsed	CW/Pulsed
Power stability (rms, over 4 hours)	< 5%	< 5%	<5%
Beam divergence, full angle (degree)	10± 4	10± 4	9 (slow axis) 85 (fast axis)
Beam diameter at the aperture (mm)	3 × 8	3 × 8	1 × 4
Polarization ratio	>150:1	>150:1	>100:1

The red laser is not a new laser and has been used with other companies in their projects. Off the shelf micro lenses are available with the right pitch (200 µm) for collimation in either slow or fast axis. In this research, the focus is on the green and blue NECSELs which were newly developed lasers.

## 5.5 Evaluation of the NECSEL Beam Parameters

An evaluation of the laser beam parameters was carried out in order to verify the information given on the data sheet. This is important as this information is used in the design for the beam shaping and homogenising. The divergence, beam waist location and distance between the emitters in the horizontal and vertical directions were measured.

Figure 5.20 shows the experimental arrangement for measuring the beam divergence. A 250 µm diameter pinhole was used to block all of the emitters apart from one.



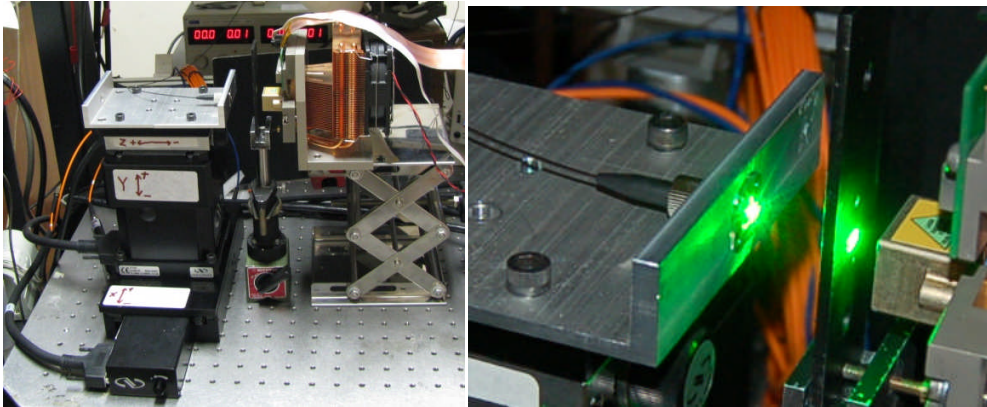


Figure 5.20: Experimental arrangement for measuring the divergence of the beam and the location of the beam waist.

Multi-mode fibres with core diameters of 100  $\mu\text{m}$  and 50  $\mu\text{m}$  were used to monitor the power of a single emitter. It should be noted that the beam waist of the laser beams is 80  $\mu\text{m}$  but it is located inside the laser housing. The size of the beam at the output of the housing is at least 140  $\mu\text{m}$ . Some experiments using an optical fibre with 9  $\mu\text{m}$  core diameter were also carried out to check the measurements. The fibre was attached to a power meter (Newport model 2931-C) and the power recorded on a computer. The fibre was mounted on a three-axis motorised stage and the system was programmed to scan the beam at different distances from the output of the laser (laser housing). The movement increments were set at 50  $\mu\text{m}$  using 100  $\mu\text{m}$  fibre (20  $\mu\text{m}$  using 50  $\mu\text{m}$  fibre and 5  $\mu\text{m}$  using 9  $\mu\text{m}$  fibre) in order to provide a sufficiently complete profile of the emitter when scanned. Different emitters were measured to find any variation between them. The data was also used to investigate the divergence of the beam. This was calculated from the diameter of the emitter (when the power drops to  $1/e^2$  of the maximum) at the different distances. The half-angle divergence was calculated to be  $4.8 \pm 2$  mrad.

The emitter spacing was also measured and two methods were used. In the first method a multi-mode fibre was used to scan the output power of the laser by placing the fibre as close as possible to the laser output aperture. The fibre was moved around until the maximum power was recorded. The fibre was then moved across each row and the power recorded at each 50  $\mu\text{m}$  step. The distance between two peaks is the distance between emitters. This experiment was repeated moving the fibre in the vertical direction in order to find the spacing between two rows.

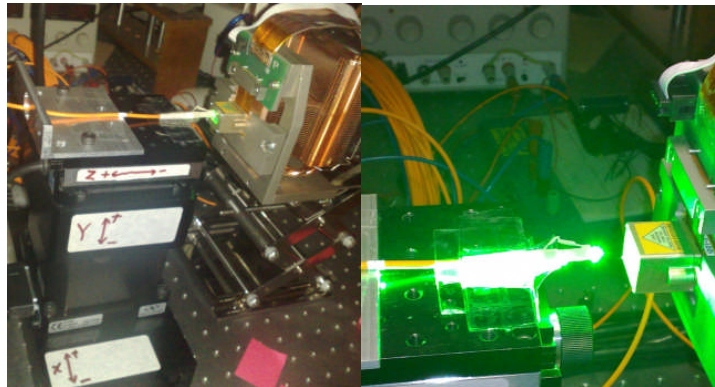


Figure 5.21: Measurement arrangement for the beam spacing in the NECSEL. The fibre is placed as close as possible to the output aperture and scans the power of the emitters by using a motorized stage for moving the fibre precisely.

In the second method, a spherical convex lens was used to form a larger image of the emitters at the location of the fibre. The fibre was kept in a fixed position and the laser was moved using the accurate motorised stages. The fibre was located on the maximum point of the power of a selected emitter. The laser was moved to one side until the fibre received maximum power from the adjacent emitter. The movement of the laser gave the distance between the emitters and the experiment was repeated for other emitters

The distance between the emitters was found to be  $328 \pm 1 \mu\text{m}$  and the results are summarized in Table 5.4 and Figure 5.22.

CHAPTER 5: Multiple Viewer Laser Illuminated Autostereoscopic 3D Display System

Table 5.4: Measured data for the NECSEL.

Size of the laser head (cm)	20×28×6
Maximum power (W)	3
Maximum number of emitters (full power)	2×24
Minimum number of the emitters can be turned on	2×1
Polarisation	Perpendicular to the row of emitters
Pitch between two emitters in one row (μm)	328 ± 1
Pitch between two emitters in two rows (μm)	2271 ± 1
Divergence full angle (mrad)	Mean value = 9.5 ± 3
The dimension of the beam at the output window (bottom emitter) (diameter at 1/e <sup>2</sup> of power) (μm)	140
The dimension of the beam at the output window (top emitter) (diameter at 1/e <sup>2</sup> of power) (μm)	288
Distance between two beam waists (mm)	15 ± 1

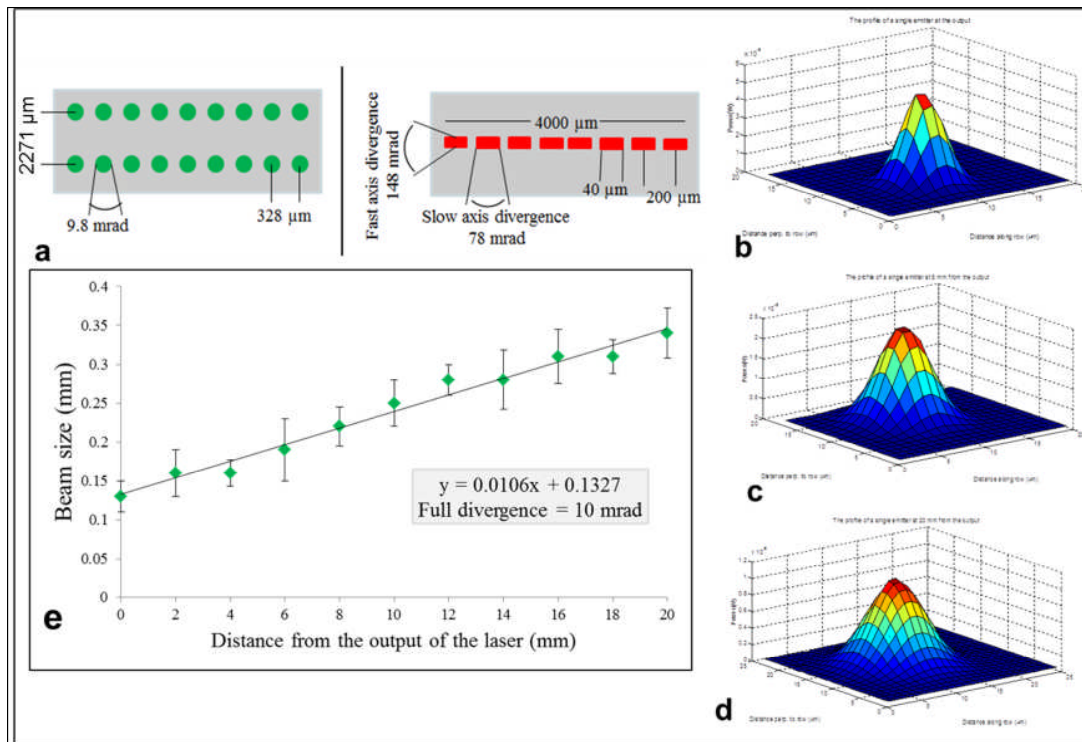


Figure 5.22: **a**: Laser parameters for the green (the same as the blue NECSEL) and the red light sources. **b**, **c** and **d**: the profile of one emitter of the green laser at different distances from NECSEL output. **e**: the divergence of the laser beam.

The distance between two adjacent NECSEL emitters was found to be  $328 \pm 1 \mu\text{m}$  and the distance between the rows  $2271 \pm 1 \mu\text{m}$ . Figure 5.22 shows the laser parameters for the green (and also blue) and red beams.

## **5.6 Conclusions and discussions:**

The optical system and different elements of a laser based autostereoscopic 3D system called HELIUM3D system was explained in this chapter. Various parts with the performance of each optical element were reviewed. A new developed multi-emitter laser, called NECSEL, was chosen and characterised to be used as the light source. The laser beam is formed from 48 emitters in two rows of 24 emitters. the spacing between the emitters, beam divergence and beam waist location was found to be different with the data sheet and it was reported to the NECSEL fabrication company to correct the information in the data sheet.

## References

- [5.1] Eugene Hecht and Alfred Zajic, *Optics*, 4 ed Addison Wesley, San Fransisco, CA, 1990.
- [5.2] P. Surman, R. S. Brar, I. Sexton, and K. Hopf, *Muted and Helium3D Autostereoscopic Displays*, pp. 1594-1599, 2010.
- [5.3] Hadi Baghsiahi, David Selviah, Eero Willman, Anibal Fernández, and Sally Day, "Beam Forming for a Laser Based Auto-stereoscopic Multi-Viewer Display," *SID Symposium Digest of Technical Papers.*, vol. 42, no. 1, pp. 702-705, June 2010.
- [5.4] Eero Willman, Hadi Baghsiahi, David Selviah, and Sally Day, "The Optics of an Autostereoscopic Multiview Display," *SID Symposium Digest of Technical Papers*, vol. 41, pp. 222-225, 2010.
- [5.5] Kishore Chellappan, Erdem Erden, and Hakan Urey, "Laser Based Display," *Applied Optics*, vol. 49, no. 25, p. f 79-f 98, 2010.
- [5.6] R. Barczyk, B. Kabzinski, D. Jasinska-Choromanska, and A. Stienss, "Measuring of the Basic Parameters of LCD Displays," *Journal of Automation Mobile Robotics and Intelligent Systems*, vol. 6, no. 1, pp. 46-48, 2012.
- [5.7] Tom Kimpe, "White Paper Uniform Luminance Technology" Barco Technology, June 2008.
- [5.8] Rüdiger Paschotta, "Laser physics and technology," [http://www.rp-photonics.com/diffraction\\_limited\\_beams.html](http://www.rp-photonics.com/diffraction_limited_beams.html), September 2010.
- [5.9] K. Jasper, S. Scheede, B. Burghardt, "Excimer laser beam homogenizer with low divergence," *Applied Physics A: Materials Science*, vol. 69, no. 7, pp. 315-318, 1999.
- [5.10] X. Zhu, A. Schulzgen, H. Li, J. V. Moloney, and N. Peyghambarian, "Gaussian beam shaping based on multimode interference," *7579 ed*, pp. 735-736, 2010.
- [5.11] M. Wagner, H. D. Geiler, and D. Wolff, "High-performance laser beam shaping and homogenization system for semiconductor processing," *Measurement Science and Technology*, vol. 1, p. 193, 1990.
- [5.12] K. J. W. Reinhard Voelkel, "Laser Beam Homogenizing: Limitations and Constraints," *SPIE Europe, Glasgow, Scotland, UK*, vol. 5456 Sept. 2008.

## **Chapter 6: Polymer Waveguide End Facet Cutting, Smoothing, Roughness and Waveguide Input/Output Optical Coupling Efficiency.**

### **6.1 Introduction:**

The demand for optical printed circuit board (OPCB) products is growing rapidly as the demand for high data rate communication is growing [6.1]. However, manufacturing cost and sufficient optical power transmission are two of the challenges for this approach [6.2]. New research reported in this thesis aims to determine the best method of manufacturing, assembling and designing OPCBs. To develop low-cost manufacturing techniques for integrated OPCBs, the optical coupling efficiency between the waveguide and the laser source is very important as it affects the optical power budget and the bit error rate [6.3]. The optical coupling efficiency depends on the roughness of the end facet of the waveguide, the lateral and transverse alignment of the waveguide to the laser [6.4;5] and the refractive index difference between the medium of the laser and the core material. In the OPCB design developed at UCL and explained in chapter 4, the daughter board is connected to the backplane by butt-coupling to the waveguide using the new UCL and Xyratex optical interconnector design [6.3]. Therefore, the backplane board needs to be cut to make places for the connector mounted on the daughterboard. Research by other groups uses edge connectors where optical connectors make contact with the OPCB only around its edges. In such an arrangement the board may be cut with a dicing saw. However, this limits the flexibility of layout possible and does not match the requirements for replacement of PCB backplanes in existing rack system configurations. The UCL and Xyratex mid-board connector offers layout flexibility and compatibility with rack system configurations but dicing saws cannot be used to cut out small apertures in the middle of the board. Figure 6.1 shows a picture of an OPCB developed at UCL and four places to be cut (white rectangular parts in the middle of the board).

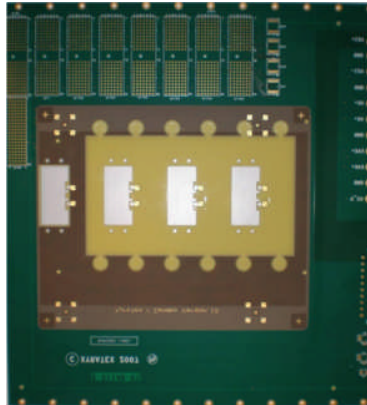


Figure 6.1: Optical PCB board waveguide interconnect. The three white rectangles are the cut-out connector sites where the daughter boards are plugged into the backplane.

There are several sources of optical loss in polymer waveguides [6.2], however, this chapter concentrates on the coupling loss due to the end facet roughness.

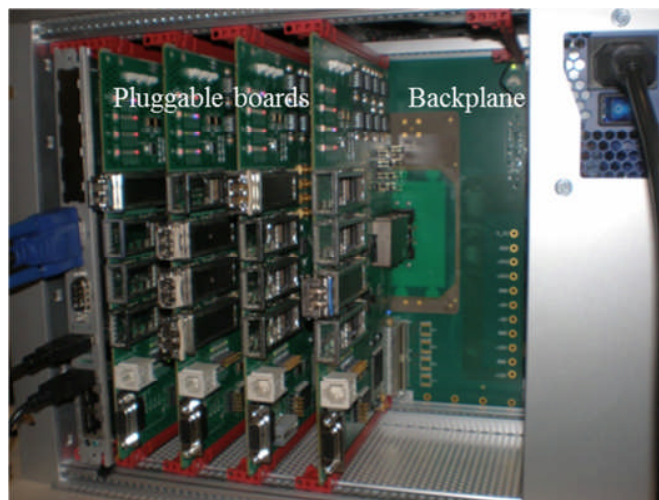


Figure 6.2: Demonstrator containing integrated electronic and optical interconnections on the backplane and 4 fully bi-directionally connected line cards.

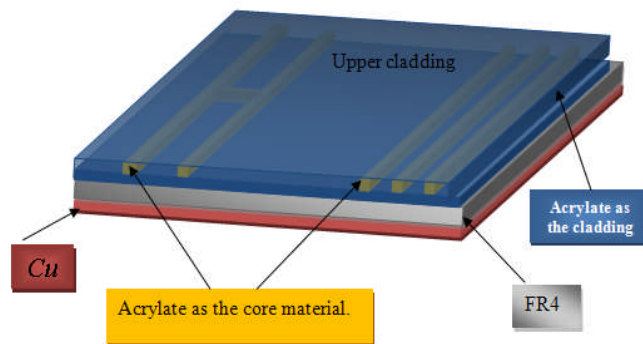


Figure 6.3: The structure of the photo-lithographically manufactured polymer waveguide.

The polymer waveguide samples used in this research were made by photolithography and cut by two different methods: dicing saw and milling router. A milling router is used to cut optical polymer waveguide and the effect of this method on the waveguide surface profile is investigated in details. The cutting parameters are also optimised to achieve the best surface quality after cutting. Without applying any modification, the end facet roughness of the waveguide samples were scanned using atomic force microscopy (AFM) to measure and compare the surface profiles. In this chapter, the results are presented in terms of roughness variation and chip load. Chip load is a measurement of the removed material by cutting edge during a cut using a router[6.6]. Chip load is the ratio of the Feed rate/ (rotation speed in RPM  $\times$  number of flutes). Feed rate is the translation speed and flutes are the cutting edges on the router. The optical loss was also measured and the results are reported.

## **6.2 End Facet Roughness of the Waveguide due to Various Cutting Methods**

Various methods can be used for cutting the PCB and OPCB boards such as using a dicing saw, laser ablation, chemical etching etc. The problem with using a diamond saw cutter to cut the OPCB is that the saw only cuts in a straight line; therefore, if it were to be used to form rectangular apertures such as the white parts shown in Figure 6.1, the cuts could pass through parts of the board not intended to be cut and damage multilayer copper tracks or other waveguide components around the connector area (the board might be fabricated in multiple layers with several electronic and optical layers).



A dicing saw can be used to cut out the required rectangular shape using plunge cutting, but it must be borne in mind that the board must be cut at least in two steps where realigning the workpiece in the computer numerical control (CNC) cutting machine requires extra design and manufacturing cost. There are no alignment features on the board to be recognised by the CNC machine and adding any of these aspects in the board and CNC machine increases the cost and creates problems for mass production. Moreover, the apertures in the board required by the UCL and Xyratex connector have a complex shape to ensure alignment and simple rectangular holes are not sufficient.

Laser cutting is another option that might be considered, however, Figure 6.1 and Figure 6.3 show that the laser needs to cut a very fine polished line through different layers of material. Therefore, the laser characteristics and beam size and shape (power distribution profile) control is crucial. If the beam is not well-collimated and shaped the end facet will not be sharp as different parts of the beam have different power so the laser beam removes different amounts of material across the beam. Alignment of the laser beam into the required cutting area is another consideration here as the lasers (or beam shaping and power control optics) must be changed to cut through the different layers which comprise two different polymers, FR4 and a copper layer [6.7;8].

### **6.2.1 Waveguide End Facets Cut with a Dicing Saw**

A dicing saw is commonly used by engineers to cut waveguides and the end facet roughness depends upon the dicing saw grit size and rotation and the translation speed of the cutter [6.9;10]. Figure 6.4 shows the end facet surface profile of a waveguide cut by a Disco DAD320 dicing machine (30,000 rpm, cutting speed = 0.6 m/min, diamond particle size on the resin blade 30  $\mu\text{m}$ ). As indicated in Figure 6.4, there are some lines or grooves on the end facet waveguide cross section surface and the AFM results show a roughness with standard deviation of  $66.3 \pm 10$  nm; this magnitude of roughness will be compared with the milling methods later in this chapter (Matlab software was used to calculate the standard deviation of the roughness from the roughness data measured by the AFM machine).

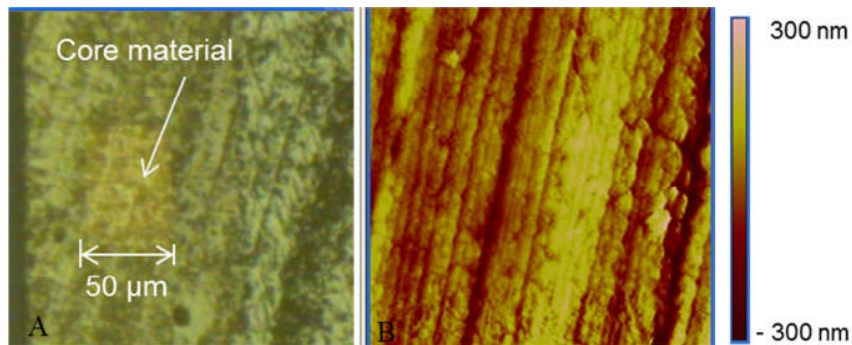


Figure 6.4: The roughness profile of the surface of a waveguide cut by a Disco DAD320 dicing saw with 30,000 rpm, cutting speed = 0.6 m/min. A: picture taken with an optical microscope, B: 30 μm × 30 μm area of the core surface scanned by an AFM.

### 6.2.2 Waveguide End Facet Cut with a Milling Router

The use of a milling router to cut the board was considered and tried. It is easy to apply and control any cut by CNC machines and any range/size of cuts and shaped apertures are possible without causing any damage to the other part of the OPCB board. Milling routers have been used for cutting polymer waveguides [6.11;12]. However, the surface profile left after milling polymer waveguides has not been previously investigated in the backplane systems and it is essential to have the information on the roughness produced and the surface profile after cutting [6.13]. Milling routers have previously been used for cutting waveguides in plastic, polymer and glass and a roughness investigation is important for the OPCB industry. In the research explained in reference [6.13], which is the most recent work found in this area, milling routers are used to form 45° mirrors, but without any investigation on the effect of the milling on the surface roughness.

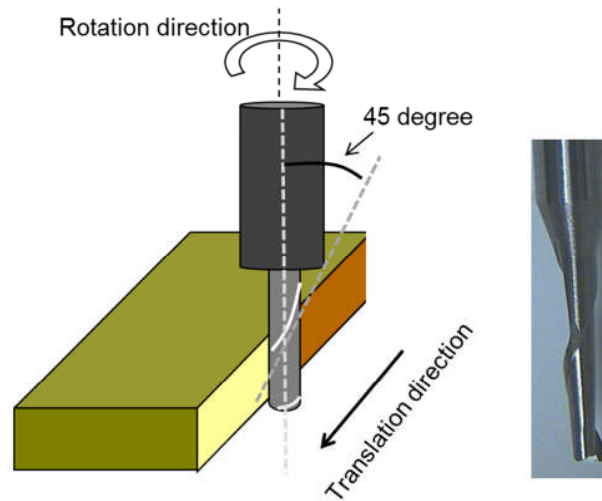


Figure 6.5: Schematic diagram of a one flute router and the cutting procedure used for the roughness investigation (from Lamar UK Ltd).

Three different router cutters with different numbers of cutting edges (flutes) were chosen to determine the most suitable for giving the end facet the smoothest surface. This is new research and no information is available for using flute routers to cut polymer waveguides. The waveguides were photo-lithographically manufactured acrylate waveguides and were cut by the PCB manufacturing company Stevenage Circuit in order to obtain realistic results from an actual PCB manufacturer. A silicon carbide 1.6 mm diameter flute router supplied by Lamar UK Ltd was used with a CNC milling machine, RLG 615 Drill/Router from Ernst Wessel Machinebau GmbH, (Figure 6.5). The surface profiles of the samples were investigated principally using an optical microscope and AFM; however, the surface roughness was also measured using a DEKTAK, and interferometric microscopes.

The experiments were started by making some samples to find in which way the waveguide should be placed in the CNC machine. There are two ways: first the waveguide (upper cladding) is facing up and secondly the copper/FR4 is facing up. Both of these options were tried and the first point was noted, which can be observed in Figure 6.6, is that when the waveguide is on the top surface during routing, the end of the waveguide is broken rather than being cut. Figure 6.6 which is the end of the waveguide after cutting, shows that the end of the waveguide is not flat but has been broken when the router is inserted from waveguide side (part A).

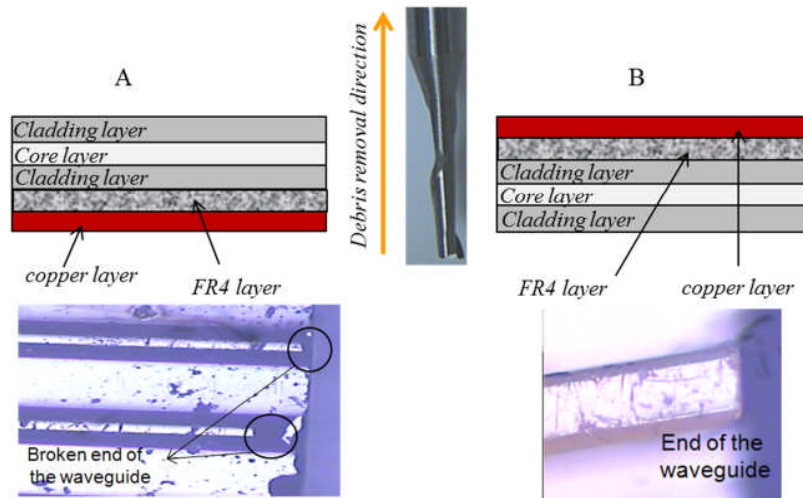


Figure 6.6: The end of the waveguide after cutting with the router entering the sample from A: waveguide and B: Copper/FR4 side

When the waveguide is facing up (part A in Figure 6.6), there is only one layer of cladding on top of the core material and rotating the router pulls the layers upward and causes delamination and the broken end, however, when the waveguide is facing down (part B in Figure 6.6) during milling (the Copper/ FR4 layer is on the top in this situation), the force from the router on the waveguide tends to push the waveguide towards the surface on which it has been fabricated during cutting. Also there are more layers on top of the core material as a protection, namely, the lower cladding, FR4 and a copper layer, so we observed that, in this arrangement, the end facet was cut cleanly and not damaged.

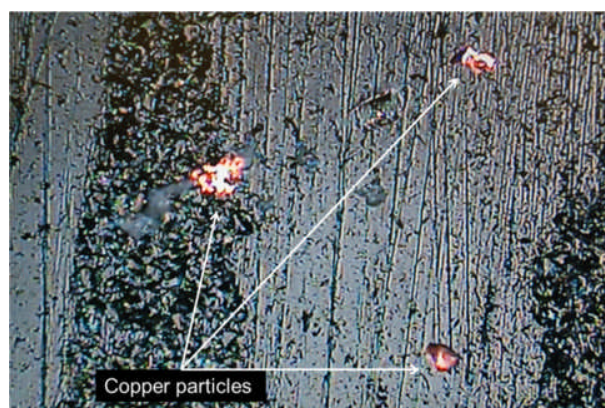


Figure 6.7: Copper contamination on the waveguide end facet after cutting without removing the copper layer with waveguide is facing up. Sample was cut using the Dicing saw mentioned in section 8.2.1 and the picture was taken by an optical microscope with magnification of 100 ×.

The router was cut through different layers including a copper layer. In most of the samples, some shiny parts were observed under microscope which were the copper dust created during the milling the copper layer. It is better to remove the copper layer in the cutting region before milling the sample to avoid copper dust contamination of the waveguide surface as shown in Figure 6.7 . However, even if the copper layer is not removed the contamination will be less when the waveguide is facing down (Figure 6.6) as the material is pulled upwards by the router cutter due to its shape.

It was necessary to determine the effect of the number of router cutter flutes on the surface finish. The shape of the router and the numbers of flutes on the router has been reported to affect other surfaces such as metal or plastic material cut by a milling machine (this information was provided by Stevenage Circuits Ltd.). Therefore, to find the effect of the number of flutes on the polymer waveguide surface quality, three cutters with different numbers of flutes, but with the same flute properties (material, flute angle, flute direction, etc.) were chosen and used to cut the waveguide samples. Figure 6.8 shows the surface profile of the waveguide cut by cutters with different numbers of flutes. The pictures were taken by using a Nomarski microscope and the waveguides back-illuminated. The yellow part is the core material of the waveguide surrounded by the cladding material; the yellow colour is due to the illumination source as the colour changes depending on the light source (for example, compare Figure 6.8 and Figure 6.10).

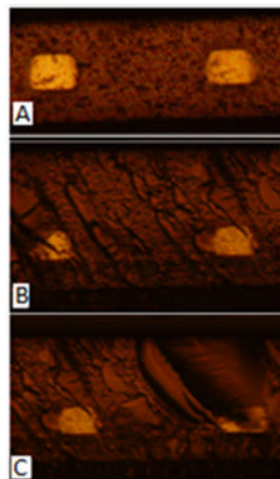


Figure 6.8: The surface profile of the waveguide cut by A: a one-flute router cutter ( $\sigma=183$  nm), B: a two-flute cutter ( $\sigma=540$  nm), C: Three-flute cutter ( $\sigma=900$  nm). The waveguides were cut with the same spindle and cutting speed (15000 rpm, 0.25m/min translation speed) for a valid comparison.

As shown in Figure 6.8 there are some cracks and grooves in the samples cut by the two and three-flute router cutters. Figure 6.9 shows the roughness of the surface of the core material measured by the AFM.

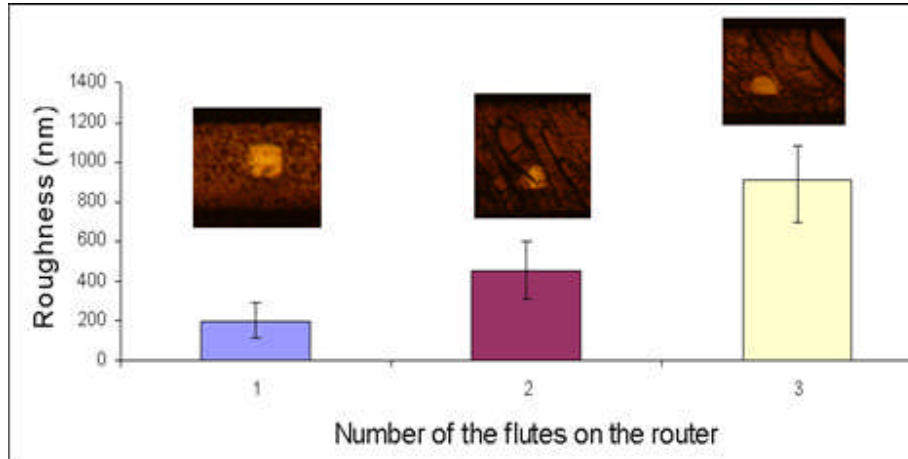


Figure 6.9: A sample of the Standard deviation of roughnesses of the surfaces cut by router cutters with different numbers of flutes. 15000 rpm, cutting speed = 0.25 m/min

Figure 6.9 indicates that roughness increases with number of flutes on the router. The three-flute router cutter leaves a very rough surface (standard deviation,  $\sigma$ , of  $911 \pm 285$  nm). Some groove or gouge-shape structures could be observed on the surface cut by a three-flute cutter. The one-flute cutter gives a better and smoother surface (standard deviation,  $\sigma$ , of  $183 \pm 13$  nm). The AFM had to be controlled (by moving the tip up and down) manually for the samples cut by the three-flute router as the roughness was too high to be followed by the AFM tip. Moreover, a larger area, more than  $30 \mu\text{m} \times 30 \mu\text{m}$ , of the waveguide surface could not be scanned by the AFM as there was a large groove which caused the AFM machine to show errors. It was observed that the samples cut by the two and three-flute routers were too rough for the AFM (we were able to take a few scans by choosing a smoother area. 3 tips were broken during scanning the surface cut by the three flute router) and another method should be used to measure the roughness.

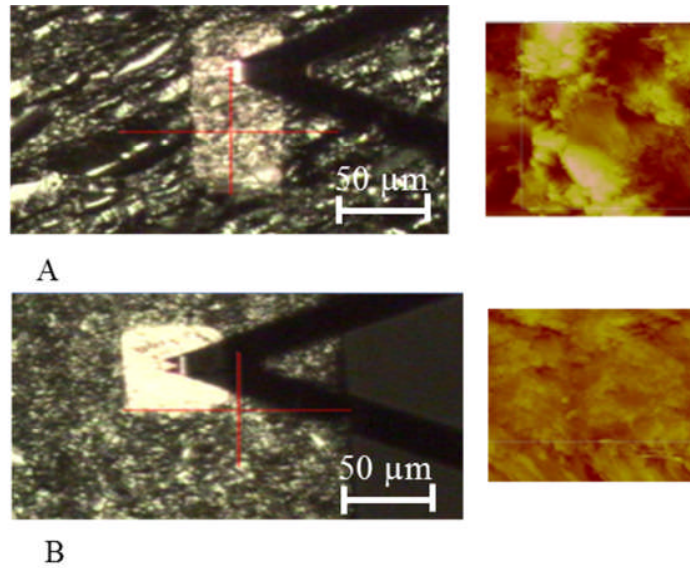


Figure 6.10: The surface roughness of the waveguide under the AFM. The triangle shape on the left hand photographs is the AFM cantilever and the shiny square shape under the cantilever is the core of the waveguide. A: Three flute router sample B: One flute router sample. The pictures on the right show the profile of the  $30\ \mu\text{m} \times 30\ \mu\text{m}$  area scanned by the AFM.

Other methods and equipment to scan the roughness at the surface of the waveguide were also used to compare the results for different techniques and to prove that the AFM results matched with those recorded by other methods. Figure 6.11 and Figure 6.12 are the results taken using two interferometer microscopes. Figure 6.11 was taken with a Zygo New View<sup>TM</sup> 7000 series interferometric microscope and Figure 6.12 is the result from a Taylor-Hobson PGI-840 profilometer. The graphs show that the three-flute router cutter produces a surface that is too rough even for these measurement techniques and the graphs could not be completed in either case.

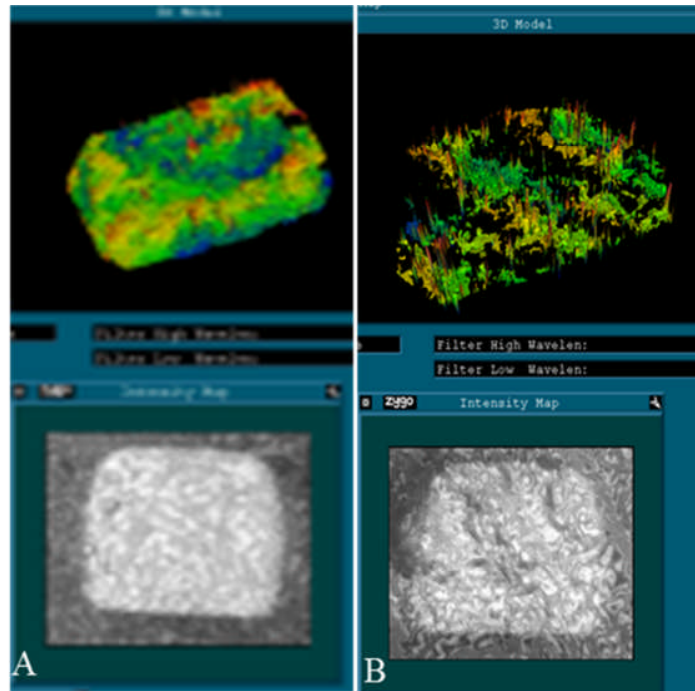


Figure 6.11: Surface profile from New view Zygo Microscope. A: One-flute router and B: three-flute router

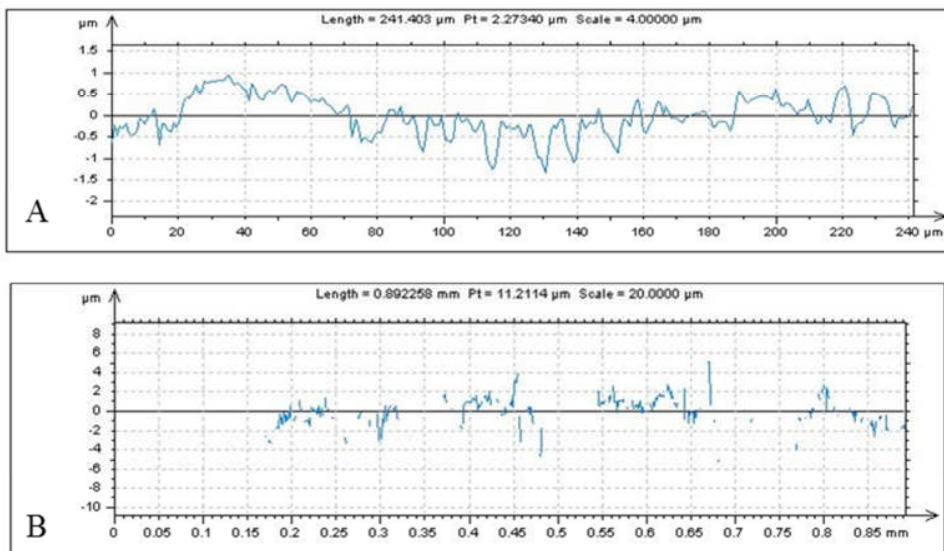


Figure 6.12: The roughness measurement taken by a Taylor-Hobson interferometer. A: one-flute router cutter B: the three-flute cutter.

The results from the AFM and the interferometer microscopes show a large magnitude of fluctuation (up to  $2\ \mu\text{m}$ ) for the surface cut by the three flute router. Therefore, we conclude as a



CHAPTER 6: *Polymer Waveguide End Facet Cutting, Roughness and Coupling Efficiency*

new result, that the one-flute router cutter gives the best surface quality. The optimum spindle and cutting speeds required for minimum surface roughness were determined. The samples were prepared at UCL and cut by Stevenage Circuits Ltd using a CNC milling machine (CNC MLB2 drill/router from Wessel). Table 6.1 shows the standard deviation of the roughness of the various surfaces cut at different cutter rotation and translation speeds. To calculate the average roughness, three or four parts of each sample (from the same face) were scanned by AFM and for each part the standard deviation of the roughness was calculated. Then the standard deviation between these results values for various scans was taken as the error and the average value is the roughness of the surface.

Table 6.1: Standard deviation of the surface roughness (in nanometers) for surfaces cut with a one-flute router at different rotation and translation speeds. The unit of the roughness, chip load and translation speed are nm,  $\mu\text{m}$  and m/min respectively.

Rotation speed (RPM) →		Translation Speed (m/min)			
		5000	15000	34000	50000
0.10	Roughness	389 ± 61	310 ± 12	384 ± 10	342 ± 23
	Chip load	20	6.6	2.9	2
	Surface speed	50.34	150.82	341.73	502.5
0.25	Roughness	376 ± 30	183 ± 13	358 ± 12	339 ± 42
	Chip load	50	16	7.4	5
	Surface speed	50.49	150.97	341.88	502.65
0.50	Roughness	474 ± 32	381 ± 18	205 ± 24	410 ± 15
	Chip load	100	33	15	10
	Surface speed	50.74	151.22	342.13	502.9
0.75	Roughness	434 ± 54	386 ± 20	407 ± 43	296 ± 12
	Chip load	150	50	22	14
	Surface speed	50.99	151.47	342.38	503.15

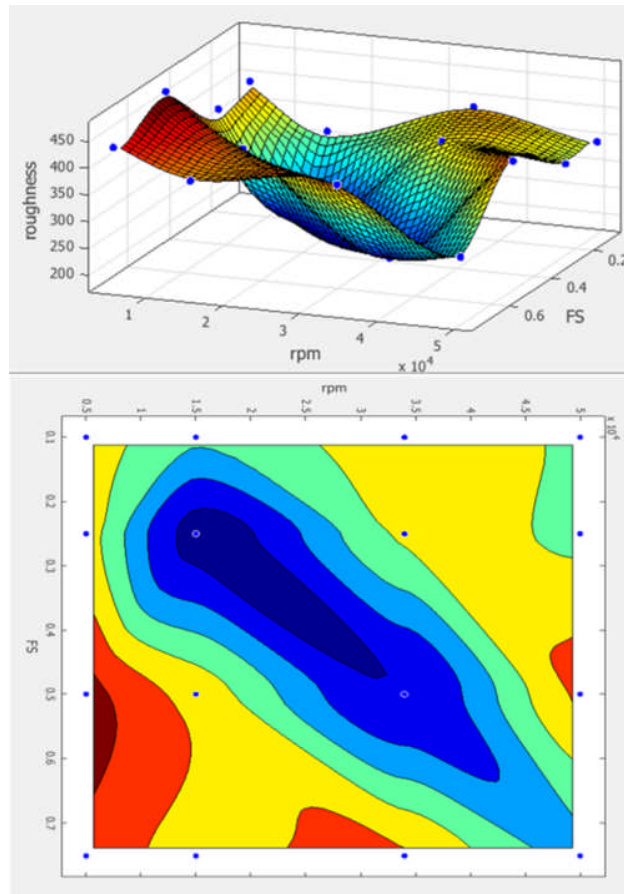


Figure 6.13: End facet roughness for different rotation and feed speeds. Blue indicates low roughness and red high roughness.

Figure 6.13 shows a 3D plot of the end facet roughness data presented in Table 6.1. The graph shows a minimum area like a diagonal valley in the middle of the plot. This is the blue area in the contour plot in Figure 6.13. This means that to achieve a surface with lower magnitude of roughness, the translation speed should be increased if there is an increase in the rotation speed. In other words, small rotation speeds should be used with small translation speed and vice versa.

To analytically calculate the rotation speed and the translation speed where the roughness is minimum based on our measurements, the data in the row and the column which contain the lowest surface roughness are plotted in Figure 6.14. Then, a curve was fitted to each graph and by differentiating the equation of this curve to find the minimum point, the best rotation speed and translation speed were calculated to be 16,667 rpm and 0.24 m/min respectively.

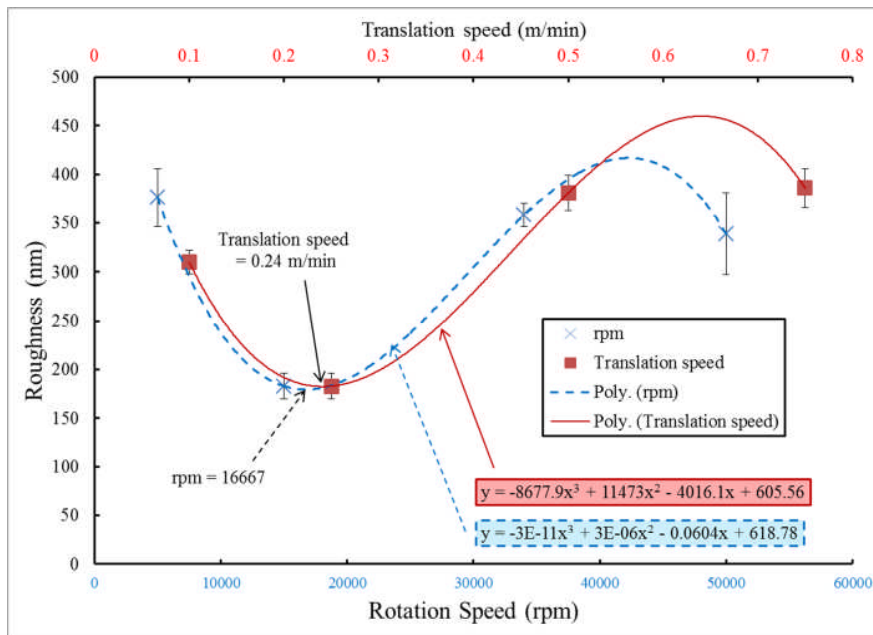


Figure 6.14: Curve fitted to the data calculated for different rotation speed and translation speed. The graphs are for the column and the row which contains the lowest roughness (183 nm) in Table 6.1.

In theory, higher translation speeds are possible with higher rotation speeds as the material is removed faster. The question is: is a higher translation speed better for reducing the surface roughness as the router touches the surface just once, or is it better to touch the surface several times by using a higher rotation speed and a slower translation speed to reduce the roughness? The next question is: what is the best rotation speed? The standard deviation of the roughness in Table 6.1 shows that the roughness is not improved at the highest rotation speed of 50,000 rpm compared to the lowest rotation speed (5,000 rpm).

Greater rotational speed generates higher frictional heating between the router cutter and the sample which can melt the polymer and also create increased mechanical wear on the cutting edge. It has also been proposed that the additional heat produced by increasing the rotation speed can reduce the roughness [6.13] but it is not clear whether this would also apply to PMMA. This is new research and no one has investigated the surface roughness with this level of accuracy before.

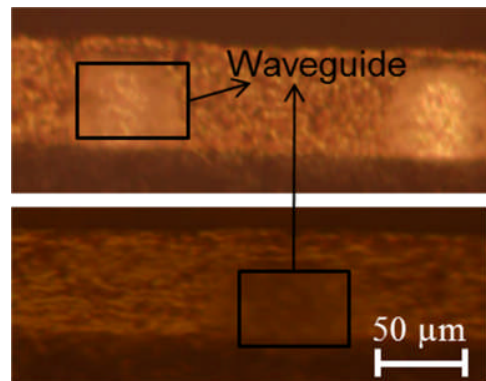


Figure 6.15: A photograph of the waveguide end facet taken by a Nomarski Optical microscope from a sample cut with rotation speed = 34,000 rpm, translation speed = 0.75 m/min

Figure 6.15 shows the end facet of a waveguide sample that was cut at 34,000 rpm. The waveguide sample was back illuminated to distinguish the core materials but the waveguides were either blurred or blocked as we could not observe a clear waveguide core. It appears as if the waveguide surface has been covered with another layer. It is not dust or small swarf particles that can be cleaned off the surface. A lens cleaning air spray was used to clean the surface by blowing air on the surface but nothing was removed and the surface picture did not change. The rotation speed was increased to 70,000 rpm but with no improvement in the roughness.

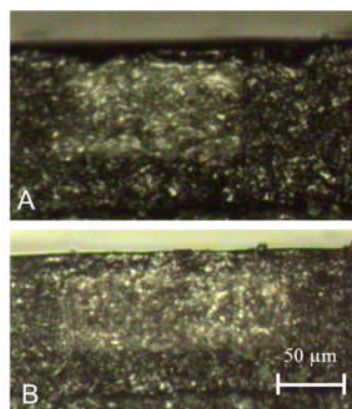


Figure 6.16: A photograph taken by an optical microscope of an end facet surface cut with a cutting speed of 0.50 m/min and A: 60,000 rpm, B: 70,000 rpm. The surface roughness in case A is  $395 \pm 18$  nm and case B:  $432 \pm 21$  nm.

Figure 6.16 shows the end facet profile of the samples cut at 60,000 rpm and 70,000 rpm. The end facet roughness is of the same order of magnitude as the values in Table 6.1 but it looks like Figure 6.16 may show a smeared layer on the surface that was not produced at the lower speeds.

It could be due to the heat created or a chemical reaction and further investigation is required to explore the reason for this issue.

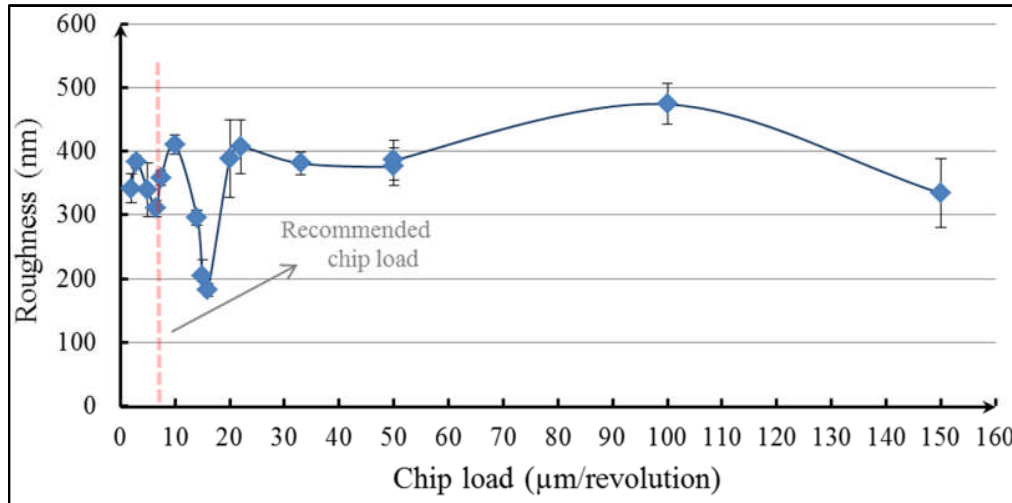


Figure 6.17: Chip load calculation based on the rotation and translation speeds. The red dotted line shows the recommended chip load by the router manufacture company.

Figure 6.17 shows the end facet roughness versus the chip load. Chip load was calculated for each pair of rotation and translation speeds in Table 6.1 based on the chip load formula explained in the introduction section for the one flute router. The recommended chip load from the router manufacturer for incurring the least damage to the router and giving the smoothest surface is 8  $\mu\text{m}/\text{revolution}$ , which gives us for example a spindle and feed speed (translation) of 60,510 rpm and 0.484 m/min respectively (other combinations of RPM and feeding speed are possible too) and, indeed, Figure 6.17 does show a minimum at this chip load. However, the results shown in Figure 6.17 indicate that a much deeper minimum roughness is obtained at a chip load of 16  $\mu\text{m}/\text{revolution}$  for the best surface quality. It is interesting that this is 2 times the recommended chip load. We also noted that Stevenage Circuits use this one flute router to cut FR4 glass fibre reinforced epoxy PCBs and they have optimised that to operate at 17  $\mu\text{m}/\text{revolution}$  which is close to the 16  $\mu\text{m}/\text{revolution}$  that we have found for the polymer.

Figure 6.18 is the roughness in terms of the speed of the edge of the router cutter flute at the surface of the waveguide and is calculated based on the rotation and the translation speed directions shown in Figure 6.5. There are two speeds to be added together. The first one is the

speed of the cutting edge due to the rotation which is in rpm unit. The unit of this speed is converted to rad/min below (each revolution is  $2\pi$  radian):

$$RPM \left( \frac{rev}{min} \right) = RPM \left( \frac{rev}{min} \times 2\pi \frac{rad}{rev} \right) = RPM \times 2\pi \left( \frac{rad}{min} \right)$$

The linear velocity of the cutting edge due to the rotation is:

$$v_{rpm} = \omega r \rightarrow v \left( \frac{m}{min} \right) = \left[ (RPM \times 2\pi) \frac{rad}{min} \right] \times r(m)$$

Therefore:

$$v_{total} = v_{rpm} + v_{Translation\ speed}$$

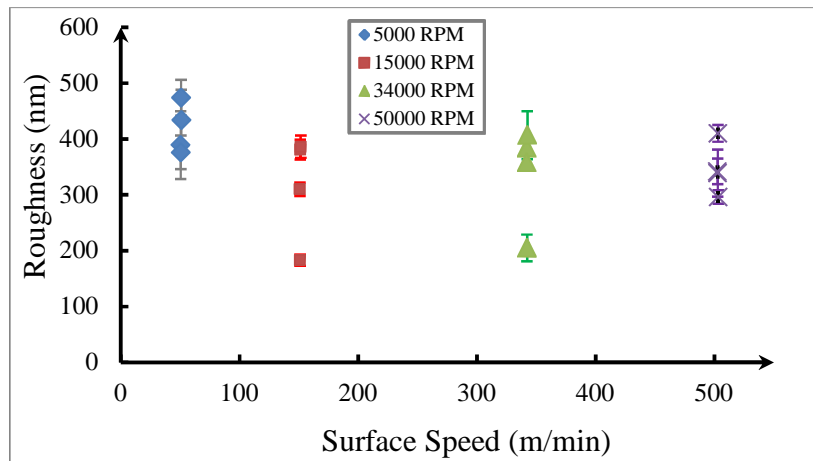


Figure 6.18: End facet roughness of the waveguide versus the speed of the edge of the router cutter flute on the waveguide surface. These speeds have been calculated for the one flute router information listed in Table 6.1. At each speed 4 points with different rpm number were measured.

In Figure 6.18, which shows the surface speed of the cutting edge at the waveguide surface, there is a trend for lower roughness at 150 m/min increasing more quickly towards lower speeds and also increasing although less quickly towards higher speeds. Based on the experiments and the measurements, the best results are achieved at a rotational speed of 15,000 RPM and a translation speed of 0.25 m/min for a 1 flute router. The magnitude of the roughness in this case is  $183 \pm 13$  nm and, in addition, the waveguide surface is clear as the core material can be observed properly under the microscope (Figure 6.19).

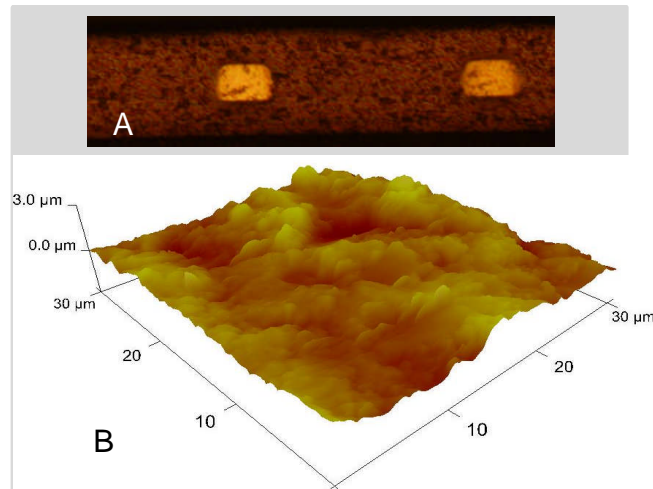


Figure 6.19: The surface fluctuation of the waveguide cut by the one-flute router A: Picture taken by Nomarski microscope. B: 3D plot from the surface roughness of the core material taken by AFM.

To find the analytical speed for the minimum end facet roughness in Figure 6.18, a curve was fitted to the graph and based on the equation of the fitted line, the speed which gives a minimum roughness is calculated by differentiation. The results show that the graph shown in Figure 6.20 has a minimum where the speed is 221.72 m/min. this number was achieved by calculating the roots of the first derivative of the fitted line equation.

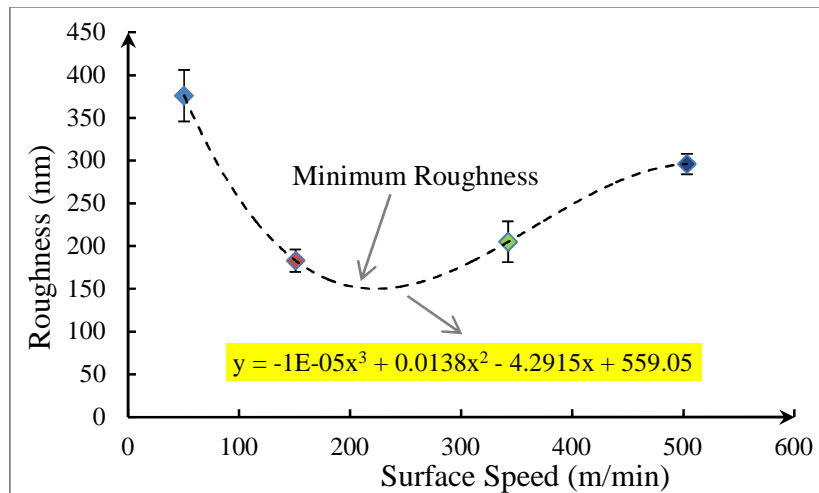


Figure 6.20: Curve fitted line to the data calculated for the surface speed of the cutting edge at the surface of the waveguide.

### 6.2.3 Comparing the Waveguide Surface Roughness with that of a Silicon Wafer

Having determined the best rotation and feed speeds for cutting the waveguides, the three different surfaces roughnesses in Figure 6.21 were compared after milling. The roughness of a silicon wafer was considered as an ideal polished surface for comparison of the waveguide roughness cut by a diamond saw and the same waveguide cut by the one flute router.

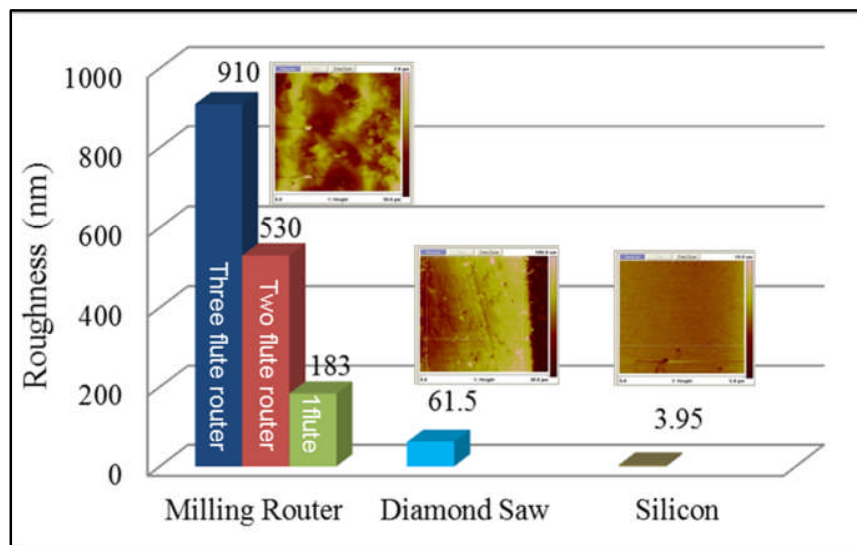


Figure 6.21: Roughness of the surfaces of silicon and waveguides cut by dicing saw and routers with different number of cutting edges. An AFM picture is shown for each surface for comparison of the surface profile. The number on top of each bar is the standard deviation of the roughness in nm for that sample.

Figure 6.22 shows other aspects of the roughness; this is the way in which the roughness changes across each sample and also the surface uniformities are compared for the three materials measured in Figure 6.21. For Figure 6.22 an area of  $30\ \mu\text{m} \times 30\ \mu\text{m}$  of each sample was scanned and the result was saved in a  $256 \times 256$  array of data (roughness value). The standard deviation of each column of the roughness data was then calculated and plotted in Figure 6.22.



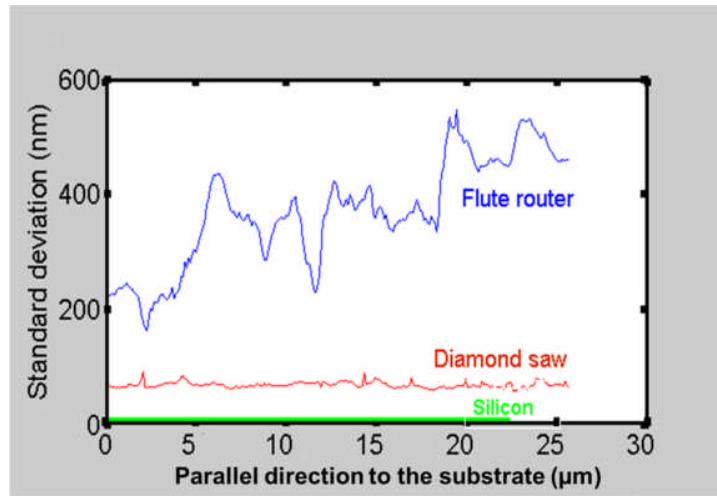


Figure 6.22: The variation of the surface roughness for three different materials across the sample; one-flute router, diamond saw and silicon. The vertical axis shows the standard deviation of the roughness.

The comparison in Figure 6.21 and the graphs in Figure 6.22 show that, although the end facet roughness has been reduced by using one flute router and characterising the RPM and translation speed, however, the magnitude of roughness on the surface cut by milling router is higher than the sample cut by dicing saw. Compare to the surface of the silicon sample, the milling router is much more rough and the roughness needs to be reduced to achieve a better surface quality.

### 6.3 Optical Input/Output Coupling Loss due to Roughness of Waveguide End Facets

In this section, the input/output optical loss due to the different end facet roughness is measured. The length of the samples was 10 mm in order to fit under the AFM tip and a multimode fibre coupled VCSEL with 853 nm wavelength was used as the source. The receiver was a photo-detector with a circular aperture of 70 µm and the waveguides' cross section was 50 µm × 50 µm. The measurements were performed based on the experimental method described in Chapter 4. An index matching fluid was also used to reduce the coupling loss without reducing the physical roughness. The liquid penetrates between the microstructure of the roughness and fills the space between waveguide surface fluctuations. An index matching fluid with  $n = 1.5694 \pm 0.0005$ , made by Cargille Laboratories (code: LCABK), was applied to the multimode fibre and

the input facet of the waveguide. It was also added between the output facet roughnesses of the waveguide. Figure 6.23 and Figure 6.24 show the results of the measurement.

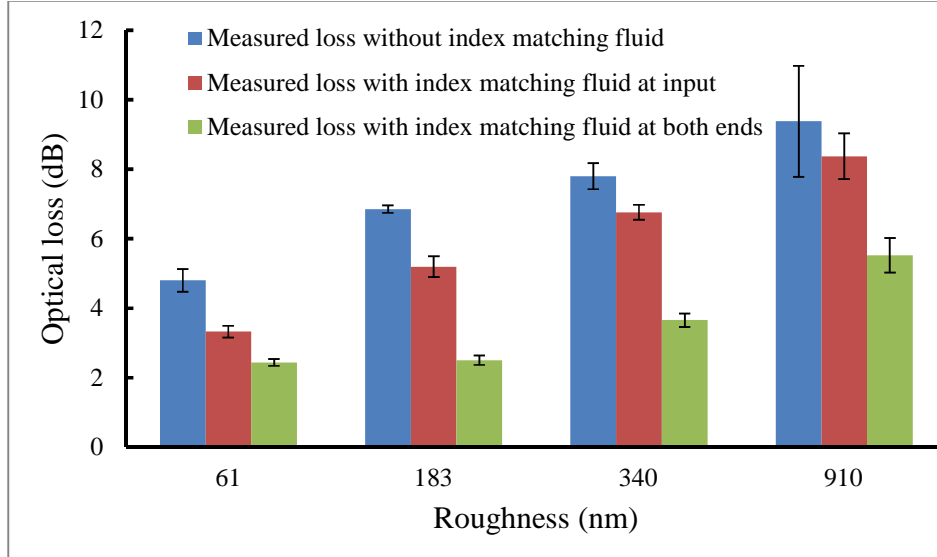


Figure 6.23: Experimental results for the optical input and output coupling loss due to the roughness at the end of the waveguide.

Figure 6.23 shows the measured loss for four different magnitudes of end facet roughness. To be precise, the measured loss is the insertion loss which is the coupling loss plus the optical loss due propagation loss which includes losses due to sidewall roughness scattering and due to material absorption; however, as the waveguide samples are 1 cm long and the propagation loss is 0.05 dB/cm (has been measured previously in our research group), the insertion loss can be ignored compared to the coupling loss. The samples were four waveguides fabricated on the same wafer. In fact it was a large (10 cm) straight waveguide which was cut into several pieces. Both ends of each sample were cut with the same method; therefore the roughness quoted on the horizontal axis is for both ends (the samples used in this section are exactly the same as the samples mentioned in the previous sections in this chapter).

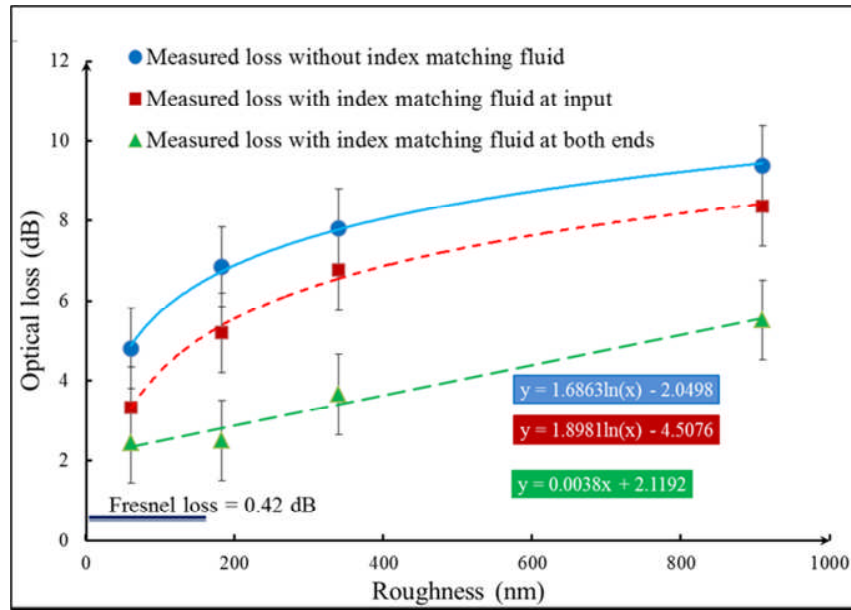


Figure 6.24: Experimental result of the optical input and output coupling loss due to the roughness at the end of the waveguide. The horizontal axis is RMS roughness.

Figure 6.24 shows the results of optical loss in the waveguide samples with different magnitudes of roughness (the data in this figure are the same as Figure 6.23). The results show an average improvement of 2 dB for each end after applying index matching fluid which penetrates and fills the rough surface.

In theory, the minimum loss should be due to the Fresnel reflection at the input and output of the waveguide if the surface had no roughness. Fresnel reflection at the interference of two media with different refractive indexes of,  $n_1$ , and,  $n_2$  is given by [6.14]:

$$R = \left( \frac{n_1 - n_2}{n_1 + n_2} \right)^2 = \left( \frac{1.556 - 1}{1.556 + 1} \right)^2 = 0.0473$$

$$\text{Optical loss} = 10 \text{ Log } (1 - R) = 10 \text{ Log } (0.952) = 0.21 \text{ dB}$$

$R$  is the Fresnel reflection coefficient and,  $n_1$ , and,  $n_2$  are the refractive indices of the waveguide core and the air respectively. The calculations show that the optical loss due to the Fresnel reflection should be 0.21 dB at each input and output surface of the waveguide. In theory, for a surface with no roughness the optical loss should be reduced to the Fresnel loss. This means that the three graphs in Figure 6.24 should cut the y axis at 0.42 dB (the Fresnel reflection for the

index matching fluid is 0.43 dB) plus a small additional propagation loss. The data shown with triangle markers in Figure 6.24 indicates that the minimum loss is 2.1 dB. This could be because the index fluid matching is not exactly correct for this wavelength or degraded because of aging or because of a large propagation loss. These calculations assume that all of the optical output of the waveguide is collected by the photodetector which may not be true in practice.

To investigate the improvement of the coupling loss in more detail, Figure 6.25 shows the optical loss reduction after applying index fluid matching at the output and at both ends of the waveguide samples. The results show that the reduction in the optical loss is more significant for the roughness up to 250-300 nm and after this range (higher roughness), the improvement is constant. Another result is that the optical loss reduction is larger when the index matching fluid was applied at the output especially in the samples with higher roughness.

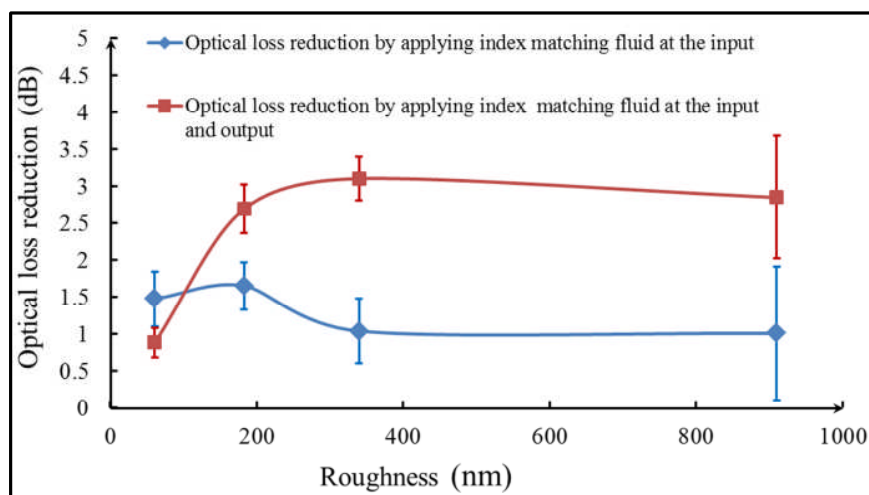


Figure 6.25: Optical loss improvement after applying index matching fluid at the input and output of the waveguide.

## 6.4 End Facet Waveguide Roughness Reduction after Cutting

Index matching fluid does not provide an ideal solution for reducing the effects of waveguide facet roughness as the insertion loss increases gradually as the index matching liquid dries out (The coupling loss for the sample with 61 nm and 910 nm RMS roughness was 3.9 dB and 8.1 dB after two days of applying index matching fluid at both ends of the waveguides). A more durable method is needed as index matching fluid is just a temporary solution. Liquid

contamination is added to the board which is undesirable and liquid would have to be injected into the area constantly which is impractical.

Surface fluctuations and the magnitudes of the roughness in Figure 6.21, Figure 6.22 and the loss measurement results indicate that the roughness of the surface after milling is high (3 times in the best situation) compared to that obtained using the diamond saw and much higher (45 times) than the silicon surface. Therefore, the scattering from the surface will be significant and the end facet roughness will have to be reduced by polishing after cutting the waveguide.

#### **6.4.1 End Facet Waveguide polishing**

The waveguide samples cut by the milling router and dicing saw were polished in order to examine its effect and to determine the challenges of manual polishing. Three types of silicon carbide grinding paper were used from coarse to fine grain. Polishing was carried out using a sequence of operations with increasingly fine grains, these were; 20  $\mu\text{m}$  grit sand cloth, 3 $\mu\text{m}$  aluminium oxide polishing cloth, 1  $\mu\text{m}$  fine grit aluminium oxide polishing cloth. The samples were rubbed on the surface of the polishing paper in a figure of eight-shaped path where the polishing paper was in a fixed position. Two persons operated on each sample in two minute sessions with 1-2 sessions for smoothing and 2-4 sessions for polishing. Each sample was held perpendicularly to a sanding table mounted and fixed on the floor. The sample was flipped 180° around the vertical axis every 5-6 seconds to minimise the polishing error caused by sample orientation and rotation speed of the hand.



Figure 6.26: Waveguide end facet roughness hand polishing

In Figure 6.26 the sample is sandwiched between two plastic plates to be held for polishing. Figure 6.27 shows a picture taken by the Zygo interferometer microscope of the sample polished by hand as explained above and a surface profile of the polished waveguide end facet scanned by AFM. Two important facts can be observed from Figure 6.27. The first is that the surface is not flat but tilted at different angles with deviations up to a few degrees to the horizontal direction. This is due to the sample being tilted during polishing or can be due to the hardness of different materials such as FR4 and polymer. Another result can be observed in the picture taken by the interferometer microscope (Figure 6.27 (B)) and should be investigated with more samples. The core material, the blue hole in the middle of the part B in this figure, has worn down more than the cladding. If this is proved to happen for other samples, it can be concluded that the core material is softer than the cladding material. This fact explains why the surface of the waveguide is further down in relation to the cladding area. The daughter boards are aligned to the surface of the cladding so there will be an undetermined distance between the laser source and the waveguide which increases the coupling loss. The laser beam diverges as it propagates from the source towards the waveguide so by the time it reaches the waveguide the size of the beam is increased. Increasing the size of the laser beam can cause more coupling loss.

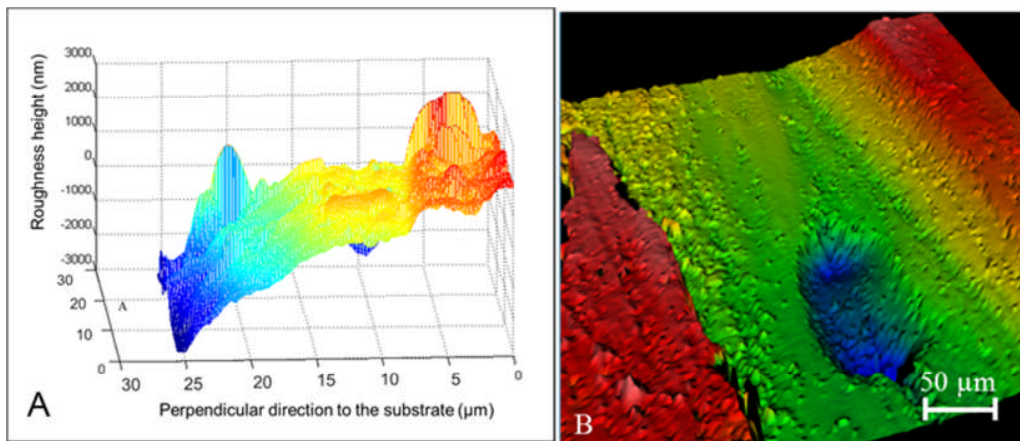


Figure 6.27: Surface of the waveguide after hand polishing. The sample was made by photolithography and the material was Truemode™ acrylate. A: AFM scanned data from an area of  $40\mu\text{m} \times 40\mu\text{m}$  of the core material. B: The scanned surface of the waveguide by Zygo interferometry microscope.

Hand polishing is not a reliable method of reducing roughness as the finished surface quality is dependent on the ability of the polishing operative, the force applied and other human factors.

Moreover, it is not suitable for mass production as a mechanical arm or any other configuration is needed to do the polishing which increases the cost and the results are inconsistent for a given type of board for several reasons. Firstly, the copper layer must be removed otherwise there will be a large copper dust contamination on the waveguide surface. Secondly, and more importantly, polishing removes some of the waveguide material so the polished end facet of the waveguide will not be exactly where it was cut, thus increasing the gap between the laser source and the waveguide. These results in increasing coupling loss and increasing laser beam size due to divergence unless the amount of material polished away is taken in to account so that the optical source is moved that much closer to the waveguide.

The fluted router cutter was replaced by a cylindrical cutter whose surface is covered with abrasive material (provided by Abrasive Technology Ltd.). The idea was to try various polishing routers such as a rubber sleeve on a cylinder with jewellers rouge and a cylindrical router with and without diamond particles. The advantage of using the polishing router tool over other polishing techniques such as hand polishing is that it can be controlled by the same CNC machine that cuts the waveguide and is suitable for mass production. No other equipment is required and so there is no extra cost in the production. Abrasive wheels are used in the finishing of metals and ceramics and provide a better surface finish and less damage to the system. In abrasive wheels, many diamond particles are brazed or bonded to the shank or body to act as multiple cutting points or polishing materials.

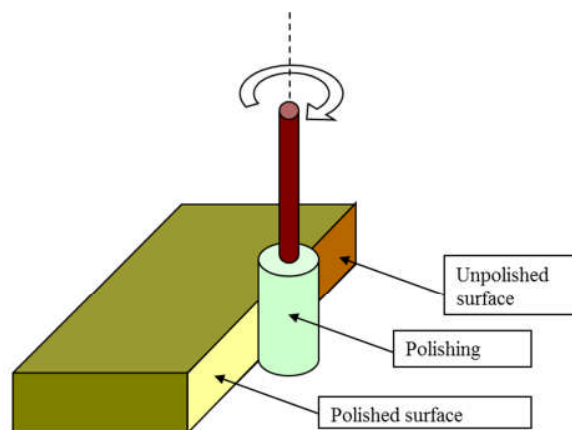


Figure 6.28: Schematic diagram of polishing router.

Using a polishing router tool for polishing the end facet of the waveguide is a potentially viable solution as it is fast, incurs no extra cost, is reliable and is suitable for mass production. Figure 6.29 shows the results of using a polishing router tool with 8000 grit and polishing diamonds with 1  $\mu\text{m}$  size. The Standard deviation of the end facet roughness of a waveguide sample before polishing was measured to be  $350 \pm 40$  nm. The results in Figure 6.29 show some kind of force may have pushed the roughness pattern in the rotation direction of the tool on the surface. The polishing did not improve the roughness; this could be due to the size and hardness of the diamond particles on the surface of the polishing router and cerium oxide (jewellers rouge) should have been used as this breaks down progressively during polishing to smaller size erasing one set of polishing grooves by another finer set.

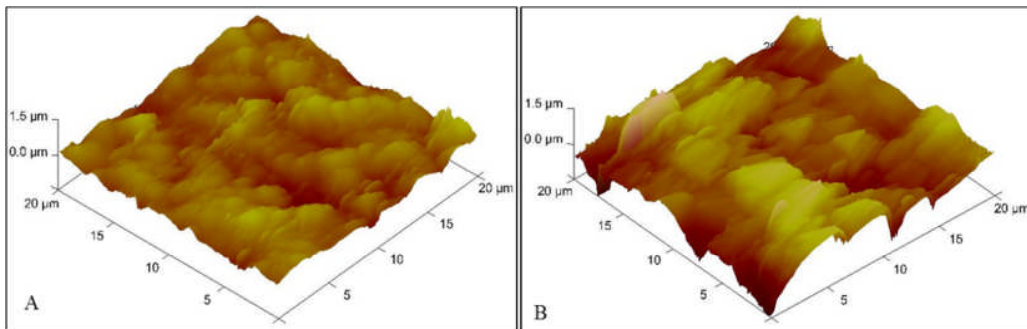


Figure 6.29: A surface roughness picture taken by AFM A: before and B: after applying the polishing router. The RMS of the roughness before polishing is 350 nm. It is the same order after polishing

More investigation on the router and the polishing materials is required for this application. Unfortunately due to limited time and budget the polishing parameters were not optimised.

## 6.5 End Facet Roughness Treatment Using a Layer of Polymer

The last section of this chapter describes a new method that has been developed for removing the end facet roughness permanently; this is the use of waveguide core material to form a thin layer at the end facet of the waveguides to reduce its roughness. This idea was suggested by David R. Selviah and was applied by the author with Kai Wang and Richard Pitwon. This behaves like an index matching fluid but without its drawbacks. The procedure implemented is shown in Figure 6.30. Firstly a small amount of liquid core polymer is applied to one end of the optical layer. Secondly a silicone lubricant aerosol release agent (CP1051 produced by CRC Industries UK



Ltd) covers one side of a glass slide (made by Menzel-Glaser) and is pushed (about 400 Pa pressure) against the waveguide end facet. The surface roughness of the microscope slide is  $9 \pm 3$  nm (measured by AFM). The slide was used for two reasons; first to achieve a flat surface at the end of the waveguide and second, to be transparent and to make sure the added core material does not go beyond the cut waveguide.

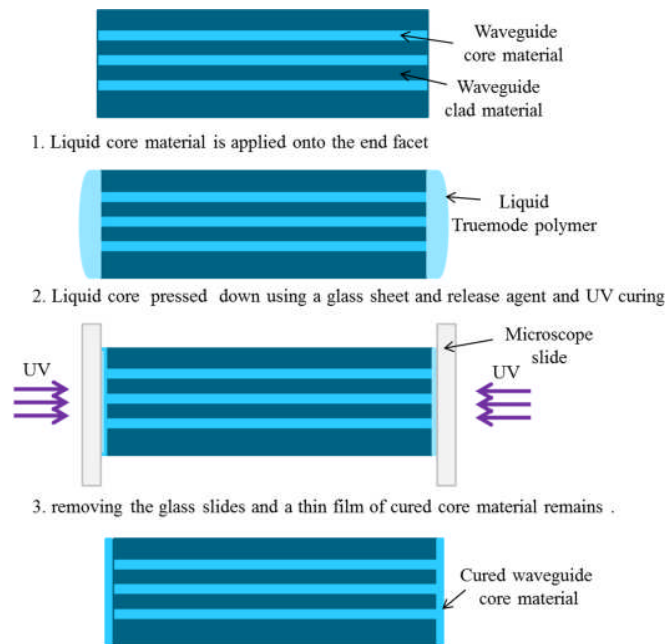


Figure 6.30: Procedure for waveguide end facet smoothing technique using core material.

Ultraviolet (UV) light was then used to cure the polymer through the glass slide which was then removed. The coupling loss was measured and the process repeated for the other side of the waveguide facet.

Nine waveguides of different lengths in an OPCB board [6.8] were measured before and after applying the refractive index matching fluid. Figure 6.31 shows the measurements of the insertion loss in comparison with optical loss measurements after applying the core material to the end of the waveguide. The graph indicates that the loss is reduced by the same or a greater extent than by using the index matching fluid method.

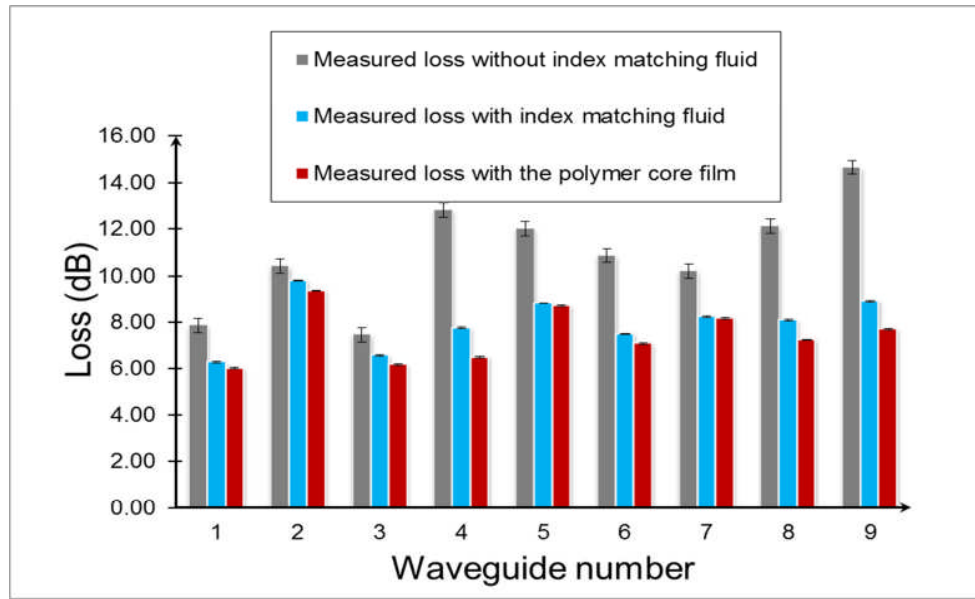


Figure 6.31: The measured loss for different values of end facet roughness. The improvement of the coupling loss after applying index matching fluid averages  $2.23 \pm 1.2\text{dB}$ , and after applying Truemode<sup>TM</sup> is  $2.60 \pm 1.3\text{dB}$ .

## 6.6 Conclusions:

In this chapter, the end facet roughness due to the use of dicing saw and flute router for cutting waveguides was investigated. It was found that the surface of the waveguide cut by a dicing saw is smoother than a flute router as the average roughness after using dicing saw was 61 nm (cutting with 30,000 rpm, cutting speed = 0.6 m/min, diamond particle size on the resin blade 30  $\mu\text{m}$ ) while the lowest RMS roughness achieved for milling router was  $183 \pm 13$  nm.

To find the relation between the waveguide surface quality and the router parameters, several routers with different numbers of cutting edges (flutes) were tested. The results from using routers with one, two and three flutes show that one flute router provides a better surface quality in terms of the roughness magnitude. The three-flute router cutter leaves a very rough surface (standard deviation of  $911 \pm 285$  nm). Some groove or gouge-shape structures could be observed on the surface cut by a three-flute cutter. The one-flute cutter gives a better and smoother surface (standard deviation of  $183 \pm 13$  nm).

After choosing the one flute router, to optimise the parameters for this router, several samples were cut with different rpm and cutting speed and were tested to find the best cutting parameters.

The best surface quality in terms of low magnitude of the roughness was achieved with 15000 rpm, and 0.25 m/min cutting speed.

Another issue to consider happened at higher rpm (between 34000- 70000 rpm). The end facet of the waveguides cut within this range of rotation speed appeared to be covered with another layer of material and the waveguide source (core material) was not clear under the microscope even with back illuminating of the waveguide. The layer might be due to the heat created on the surface of the waveguide.

We also found that the best experimental results were achieved when the rotation and translation speed are increased or decreased in step with each other. In other words, high rotation speed should be used with high translation speed and vice versa. This is an interesting result, as in the case of a high rpm with a low translation speed the cutter touches the surface more and heat produced causing polymer melting. In addition, a low rotation speed with a high translation speed applies a translational force to the cutter. In this case the cutter might be tilted, which affects the end facet quality. More research should be undertaken in this area to clarify the results.

Optical coupling loss for samples cut with different end facet roughness was measured. The results indicate that increasing the roughness increases the coupling loss but not in a linear fashion. The optical loss was increased from 4.8 dB for a sample with 61 nm roughness to 6.8 dB for a sample with 183 nm roughness. However, for the sample with 340 nm roughness the coupling loss was increased to 7.8 dB.

To decrease the end facet waveguide roughness a new method of curing a layer of core material on the waveguide roughness was invented and successfully tested. The results of this research show an average improvement of  $2.23 \pm 1.2$  dB in the coupling loss after applying index matching fluid, and  $2.60 \pm 1.3$  dB after applying a layer of Truemode.

## References

- [6.1] I. Papakonstantinou and David R.Selviah (Supervisor), "Analysis design and measurement of guided wave optical backplane interconnection." PhD thesis University College London, 2007.
- [6.2] D. R. Selviah, A. C. Walker, D. A. Hutt, K. Wang, and H. Baghsiahi, "Integrated Optical and Electronic Interconnect PCB Manufacturing Research," *Circuit World*, vol. 36, no. 2, pp. 5-19, 2010.
- [6.3] I. Papakonstantinou, D. R. Selviah, K. Wang, R. A. Pitwon, K. Hopkins, and D. Milward, "Optical 8-channel, 10 Gb/s MT pluggable connector alignment technology for precision coupling of laser and photodiode arrays to polymer waveguide arrays for optical board-to-board interconnects," *Electronic Components and Technology Conference, 2008. ECTC 2008. 58th*, pp. 1769-1775, 2008.
- [6.4] H. Baghsiahi, D. R. Selviah, G. Yu, K. Wang, M. Yau, and F. A. Fernandez, "Photolithographically manufactured acrylate multimode optical waveguide translation and rotation misalignment tolerances," *Proceedings- 2008 2nd Electronics System Integration Technology Conference, ESTC*, pp. 617-621, 2008.
- [6.5] B. Huang, J. Chen, and W. S. Jiang, "Effects of Surface Roughness on TE Modes in Rectangular Waveguide," *Journal of Infrared Millimeter and Terahertz Waves*, vol. 30, no. 7, pp. 717-726, 2009.
- [6.6] Vortex tool ltd, "Chip load chart and information," <http://www.vortextool.com/images/chipLoadChart.pdf>, 21 June 2011.
- [6.7] S. S. Zakariyah, P. P. Conway, D. A. Hutt, D. R. Selviah, K. Wang, H. Baghsiahi, J. Rygate, J. Calver, and W. Kandulski, "Polymer optical waveguide fabrication using laser ablation," *Electronics Packaging Technology Conference, 2009. EPTC'09. 11th*, pp. 936-941, 2009.
- [6.8] K. Wang, D. R. Selviah, J. Papakonstantinou, G. Yu, H. Baghsiahi, and F. A. Fernandez, "Photolithographically manufactured acrylate polymer multimode optical waveguide loss design rules," *Proceedings - 2008 2nd Electronics Systemintegration Technology Conference, ESTC*, pp. 1251-1255, 2008.
- [6.9] M. Saillard and D. Maystre, "Scattering from Metallic and Dielectric Rough Surfaces," *Journal of the Optical Society of America A-Optics Image Science and Vision*, vol. 7, no. 6, pp. 982-990, 1990.

CHAPTER 6: *Polymer Waveguide End Facet Cutting, Roughness and Coupling Efficiency*

- [6.10] S. Cvetkovic, C. Morsbach, and L. Rissing, "Ultra-precision dicing and wire sawing of silicon carbide (SiC)," *Microelectronic Engineering*, vol. 88, no. 8, pp. 2500-2504, 2011.
- [6.11] M. Komatsu, "Machining Performance of A Router Bit in the Peripheral Milling of Wood .2. Effects of the Helix Angle of the Peripheral Cutting-Edge on the Cutting Force and Machined-Surface Roughness," *Mokuzai Gakkaishi*, vol. 40, no. 2, pp. 134-141, 1994.
- [6.12] H. Kamata and T. Kanauchi, "Analysis of Machined Surfaces with Distal Image-Processing .1. Effect of Grain Angle in Numerical Control Router Machining," *Mokuzai Gakkaishi*, vol. 39, no. 11, pp. 1253-1258, 1993.
- [6.13] M. E. Teitelbaum, R. Nair, D. J. O'Brien, E. D. Wetzel, and K. W. Goossen, "Cost-effective integration of plastic optical fiber and total internal reflection mirrors in printed circuit boards for parallel optical interconnects," *Optical Engineering*, vol. 49, no. 6, pp. 456-461, 2010.
- [6.14] M. Born and E. Wolf, *Principles of Optics.*, 6 ed Cambridge University, 1999.

## **Chapter 7: Experimental Measurement and Computer Modeling of Loss and Crosstalk in Multimode Step-index Photolithographically Fabricated Polyacrylate Polymer Waveguide Crossings**

### **7.1 Introduction**

In this chapter, the optical loss of crossing polymer waveguides with low refractive index contrast between core and cladding material (0.03) is considered by simulation and experiment. The waveguides are simulated using ray tracing and beam propagation methods. The aim of the simulations is to find the optical loss in a channel waveguide due to the crossing waveguide for various crossing angles and widths.

The optical part on an OPCB can be more compact and has fewer layers than the electrical part as optical signals can cross each other without suffering from severe crosstalk. Crossings where two or more waveguides intersect in the same optical layer become critical components in the optical design of the OPCB layout. Waveguide crossings are useful and can be applied in the design of the OPCB boards as waveguides need to route around cutout areas, electrical components and any other obstacles on an OPCB (Figure 7.1)[7.1]. It will also help to avoid sharp bends in the design as bent waveguides are a principal source of optical loss [7.1;2]. Waveguide intersections can occur in several possible configurations, for example; straight-straight, straight-bend and bend-bend. Despite the benefits of using crossing waveguides, and although most of the light travels along the intended waveguide, a proportion of the optical power in one waveguide is coupled into the crossed waveguide after passing each intersection point, especially for small crossing angles (Figure 7.1). This coupling phenomenon causes optical loss and crosstalk in the system which is dependent on the crossing angle between waveguides [7.3;4]. Apart from the optical energy which is coupled into the crossed waveguide, some of the optical energy is lost by entering the cladding area as beams contain this energy do not satisfy the total internal reflection (TIR) criteria. Consequently the crossings in OPCBs need

to be carefully designed to reduce both loss and crosstalk and to increase the performance of the system by reducing the bit error rate.

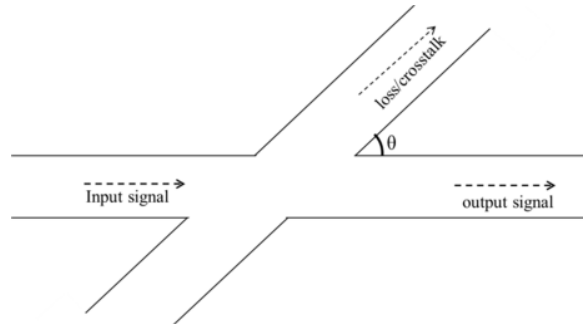


Figure 7.1: Top schematic view of a waveguide crossing with crossing angle  $\theta$ .

Optical loss at waveguide crossings can be explained by geometrical optics and wave optics. Considering Figure 7.1 and based on wave optics, the optical power is distributed between the confined modes inside the horizontal waveguide. Waveguide crossing will cause a change in the modal distribution of the travelling light at the crossing as the waveguide structure and so the boundary condition changes at the crossing[7.5]. Some of the power contained within a waveguide may be coupled to radiation modes[7.5] and, hence, be lost to another waveguide or coupled into the cladding. From a geometrical point of view, when the incoming or internal reflected light reaches the intersection point, the incident angles are larger than the critical angle of the waveguides due to the different geometry at the crossing part and the optical power in the rays, which do not satisfy total internal reflection condition, will be lost. For the crosstalk, all of the light that enters the branch waveguide at the incident angles less than the critical angle of the waveguides will continuously propagate along the branch waveguide. (All waveguides are made of the same core and cladding materials and have the same TIR condition).

The optical loss due to several crossings has been tested by experiments and simulation and the research in this area was reviewed in Chapter 2. However, most of the previous research is on high index difference silicon based waveguides for semiconductors. In addition, no one has considered the optical loss due to the waveguide crossing by both simulation and experiments and explained the factors affecting the loss.

## 7.2 Computer Modeling and Simulation

The crossing waveguides are simulated using beam propagation and ray tracing techniques. The simulated structure is a channel waveguide with a cross-section of  $50\ \mu\text{m} \times 50\ \mu\text{m}$ . The wavelength of the source is 853 nm and the refractive indices of the core and the cladding are chosen (based on the minimum absorption loss 853 nm) to be 1.5560 and 1.5264 respectively; the simulation parameters were chosen to be as close as possible to the manufactured waveguide for comparison with the experimental results. Figure 7.2 shows a photograph of a set of  $50^\circ$  crossings and a straight reference waveguide which was used in the experimental measurement of optical loss due to the crossing waveguides explained in the next section.

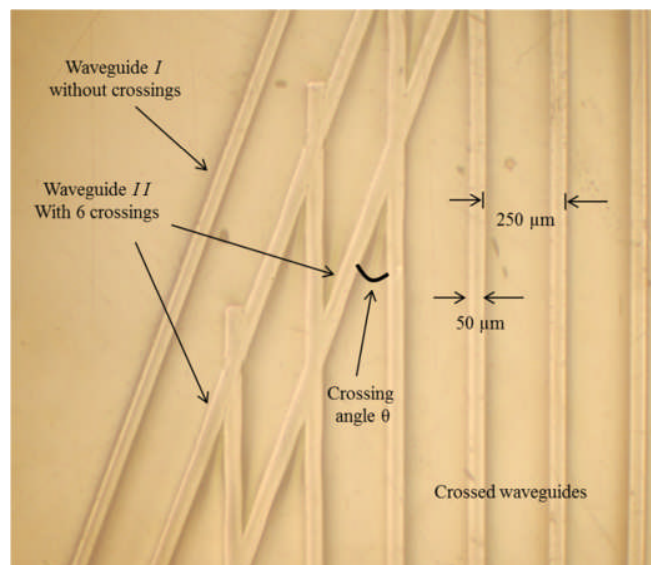


Figure 7.2: Photograph of  $50^\circ$  waveguide crossings taken with a Nomarski microscope using front illumination.

### 7.2.1 Beam Propagation Method (BPM) Using R-soft BPM Software

The aim of the simulations is to find the optical loss in a channel waveguide due to the crossing waveguide for various crossing angles and widths. The simulation should be as similar as possible to the experimental configuration where we use a multimode optical fibre as the light source and the output of the VCSEL is coupled into the fibre as explained in chapter 5. In addition, the loss just due to the crossing waveguides and, therefore, the optical loss due to the fibre-waveguide mode mismatch and the radiation mode at the start of the waveguide can be deduced from the results. To fulfil this goal, the input field is launched from air into the



waveguide and propagated to reach to the stable situation after radiating away all the radiation modes and then the crossed waveguide is placed after the stabilisation length of the waveguide and simulated. In this case, all the loss will be just due to the crossing and not excited radiation modes at the input.

To find the distance over which all the radiation modes radiate away and the power is stable inside the waveguide, two Gaussian input fields, located in the centre and diagonally off-centre were launched into a straight waveguide. Two Gaussian source in the centre of the waveguide and off-centre causes all the symmetric and anti-symmetric modes to be excited and the results is more realistic. The launched field in the centre excites all the symmetric modes and the off-centre field excites the anti-symmetric modes in the waveguide. Some of the optical power is radiated away from the waveguide at the input of the waveguide due to the mismatch between the input field and the modes of the waveguide. The waveguide length over which the optical power becomes stable inside the waveguide was calculated from the power fluctuation across the waveguide. Figure 7.3 shows an example of the simulation.

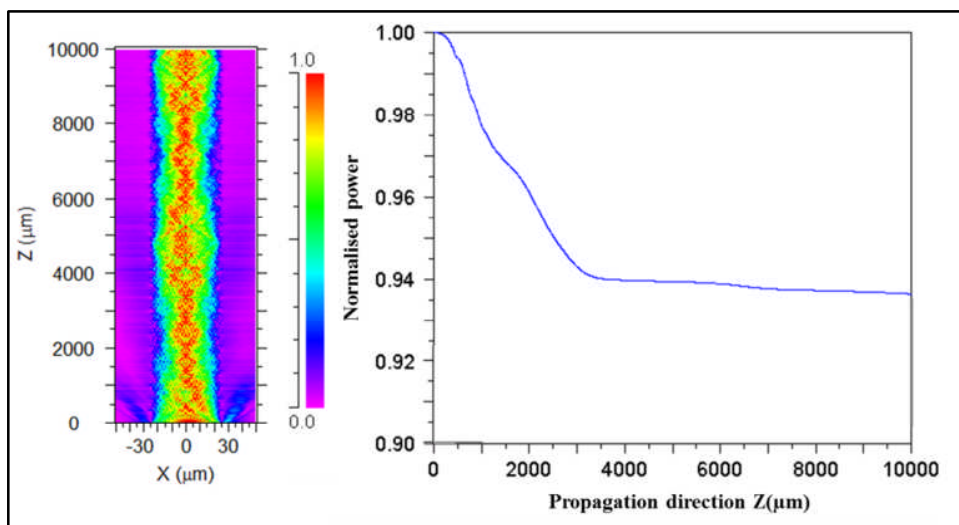


Figure 7.3: The simulation of a straight channel waveguide and the power fluctuation inside the waveguide. The input is two Gaussian beams. One in the centre and the other 2 are offset from the centre.

As indicated in Figure 7.3 the power is stabilised inside the waveguide after about 4000  $\mu\text{m}$  and propagates with slowly decreasing power level. Several simulations were performed by changing the number of source, position of the offset sources from 3  $\mu\text{m}$  to 10  $\mu\text{m}$  offset from the centre of

the waveguide. The stabilising distance was found to be  $5 \pm 1$  mm. This number (5mm) is used for simulating the crossing waveguides. The input source was Gaussian with a width and height of  $50\mu\text{m}$ . The stabilising distance shows where the crossing should be placed to find the optical loss due to the crossing only. If the crossing point is within the stabilising distance then the loss will depend where the crossing is in the initial propagation region of the waveguide and so will not be consistent. Therefore, to avoid the effect of mode mismatch loss at the start section of the waveguide, the waveguides are placed with a distance of at least  $6000 \mu\text{m}$  from launching position. Another reason for doing this simulation is that we save the complex data including direction, amplitude and phase after the straight waveguide when the power is stable inside the waveguide and then launch it into a crossing section as the input (chapter 4). In this case, the length of the waveguide can be chosen to be smaller (at least  $5000 \mu\text{m}$ ) so the simulation time is reduced.

#### **7.2.1.1 Waveguide Crossing Simulation Using BPM Method**

To find the optical loss at the waveguide crossings with different crossing angles, several simulations were performed where all the parameters were the same except the crossing angle. Waveguides with several crossings were simulated to average the results and reduce the error of the optical loss calculation. In the case where there is more than one crossing, the waveguides have sufficient separation (at least 5 mm) to enable the modes to become stable again before striking the next crossing area. The optical loss was calculated by finding the average for all crossings. Figure 7.4 shows a view of the simulated waveguides and also the waveguide parameters. The crossing angles were changed from  $5^\circ$  to  $20^\circ$  due to the limitation in BPM algorithm. The crossing angles look larger in Figure 7.4 which is just due to the aspect ratio of the figure.

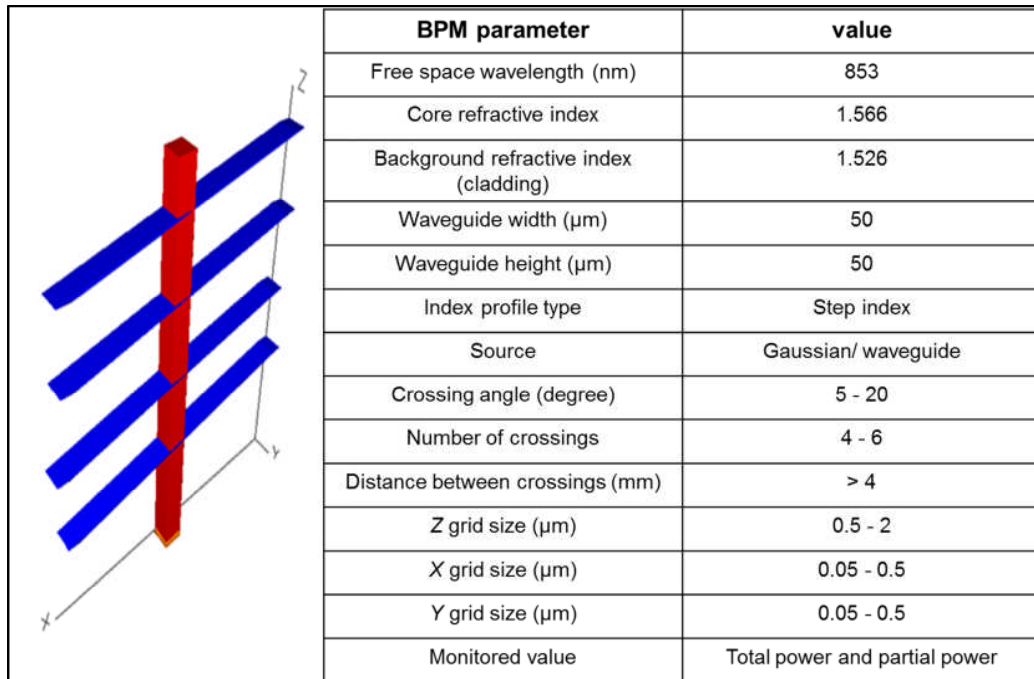


Figure 7.4: Schematic diagram from layout and BPM parameters for the waveguide crossing simulation where four crossing are investigated. Source was either a Gaussian beam or the saved profile at the end of a straight waveguide.

The crossing waveguide in this figure shows the core material; all the background is regarded as the cladding area. Figure 7.5 shows a result of simulation using BPM method. The optical power inside the core material (green graph) and inside the simulation area (blue graph) is monitored and the optical loss at each crossing is shown. The saved data (amplitude and phase) of a 10 mm straight waveguide was used as the input source to avoid the 5 mm waveguide length required for stabilising the optical power.

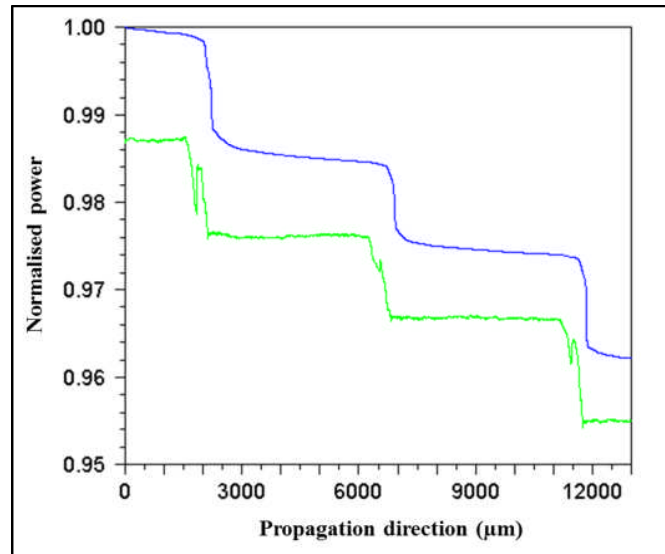


Figure 7.5: The normalised power inside a waveguide for 4 crossings with angle of  $20^\circ$ . The green graph is the power inside the core material and the blue graph is the power inside the simulation area which is  $30\ \mu\text{m}$  larger in height and width.

Several simulations with different input and grid size were performed and the optical loss for each crossing was calculated. The result for the simulations is plotted in Figure 7.6.

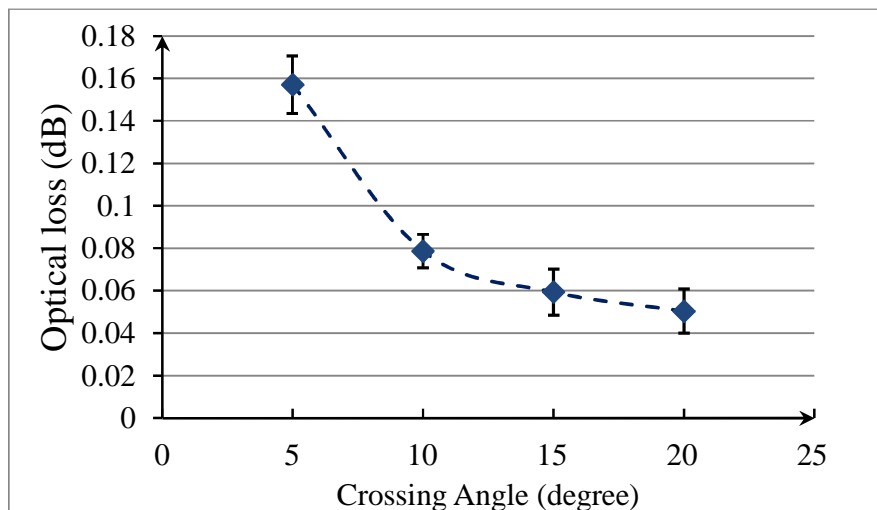


Figure 7.6: Optical loss for crossing waveguides with different crossing angles. The width of the waveguides is  $50\ \mu\text{m}$ .

The optical loss in Figure 7.6 is the result of the crossing waveguide in each case and as it is predicted the optical loss reduces by increasing the crossing angles. However, the reduction in loss is not linear and the graph descends more rapidly for the small angles (up to  $10^\circ$ ). The

crossing angle has been increased up to  $20^\circ$  due to the limitation of the BPM method. Waveguides with 4 and 6 crossings were simulated and the error bars calculated by finding the standard deviation of the optical losses for several crossings. This result is compared with the ray tracing method and experimental results in the following sections.

### 7.2.1.2 Crossings with Different Width:

Waveguides with various crossing widths were simulated. The main waveguide is the same as in the previous section and has a cross-section of  $50\ \mu\text{m} \times 50\ \mu\text{m}$ . The crossed waveguide width varied between  $10\ \mu\text{m}$  to  $90\ \mu\text{m}$  and optical loss was calculated for crossing angles of  $10^\circ$ ,  $15^\circ$  and  $20^\circ$ . The results are shown in Figure 7.7. This simulation was carried out after comparing the experiment with simulation results achieved in section 7.2.1.1, as the results did not agree with each other. It will be discussed in this chapter in section 7.4 in detail.

The purpose of this simulation will be explained in the discussion section but here it should be mentioned that the final size of the waveguide depends on the manufacturing process due to over or under etching, particularly for small crossing angles (less than  $20^\circ$ ). Therefore, it is very useful to find the value of optical loss with size variation of one of the crossed waveguides.

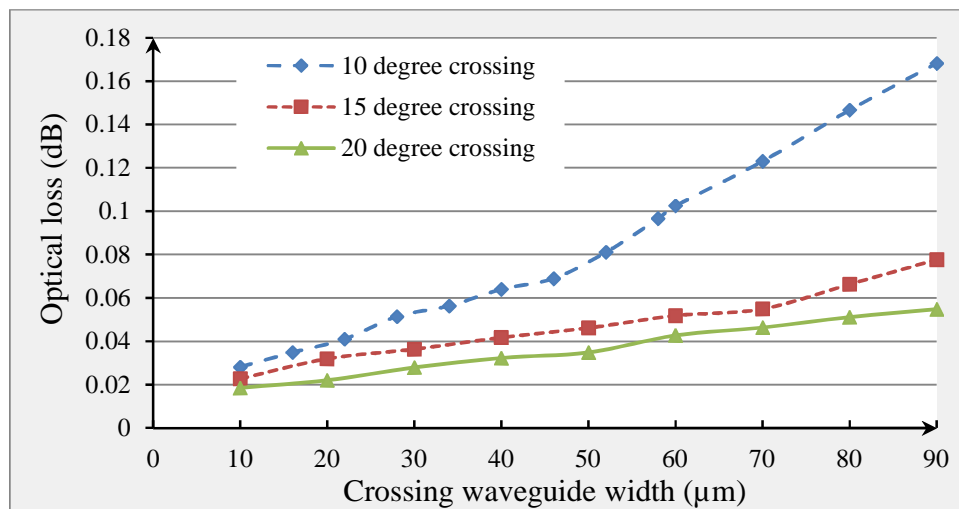


Figure 7.7: Optical loss for the  $50\ \mu\text{m} \times 50\ \mu\text{m}$  waveguide with various cross widths.

Increasing the width of the crossing waveguide enlarges the area into which light can be coupled into the crossing waveguide from the main waveguide. Therefore, the wavefront expands into a larger area, or, in other words, new modes are excited which are unguided for the main

waveguide as the side wall is missing at the crossing region. The expanded wavefront loses some of the energy as it arrives at the end of the crossing and must be guided inside the main waveguide. Figure 7.7 also indicates that the optical loss is more severe for smaller crossing angles which correspond to a longer region of the main waveguide in which the sidewall is missing.

### 7.2.2 Simulating Crossings with Ray Tracing

Simulation of waveguide crossing using wave optics has some limitations, in particular, with respect to the crossing angle. If we were to solve Maxwell's equations in full vectorial mode, the amount of memory and calculation time is significantly increased. Classical geometrical optics where light is considered as rays or particles rather than waves, can be used for simulation. In this method, the rays are traced through the system starting from the light source and change direction when they pass through an object with a different refractive index [7.6]. In the waveguide, millions of rays (defined by the user) are emitted from the source depending on its design, and each ray is traced inside the waveguide. The ray tracing method uses total internal reflection and Fresnel equations to trace the rays and calculates the number of rays that are detected at the desired detector. In terms of simulation by computers, ray tracing programs require less memory and are much faster (a calculation which takes 2 days in BPM, takes 10 minutes in ray tracing) and there is no limitation on the crossing angle.

The schematic diagram in Figure 7.8 shows the simulation model for waveguide crossings using the ray tracing method. A crossing structure basically contains two straight  $50\ \mu\text{m} \times 50\ \mu\text{m}$  waveguides that intersect each other at an angle between  $0$  to  $90^\circ$ . The waveguides have a core layer inside a cladding layer. The core has a relatively higher refractive index of  $1.5560$  while the cladding's refractive index is  $1.5264$  in order to guide the light.

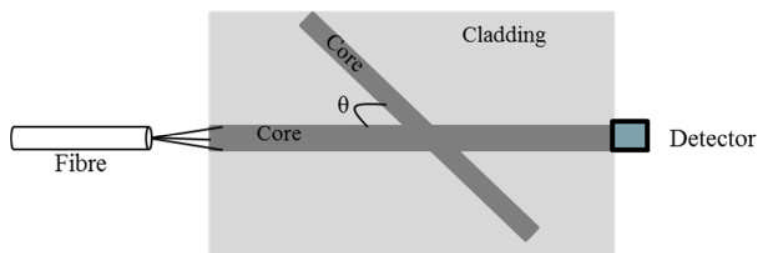


Figure 7.8: Schematic diagram of the crossing waveguide

## Chapter 7: *Experimental Measurements and Computer Modelling of Optical Loss in Waveguide Crossings*

The source used in this simulation is a step index multimode fibre with the core diameter of 50  $\mu\text{m}$  at a wavelength of 853 nm and NA= 0.22 which matches the NA of the fibre used for the experiment.

The length of each straight section is 100 mm and the input fibre source is placed 1-2  $\mu\text{m}$  away from the entrance of the waveguide. 1-2  $\mu\text{m}$  is the distance between the fibre as the source and the waveguide in the experiment. The intersection takes place at the centre of the two waveguides. This distance is after the stabilisation length and the rays are confined in the core area before striking the crossing section. Two rectangular shape detectors are placed at the end of each waveguide to measure the power output from each waveguide. One detector also records the power before the crossing section in the main waveguide (with the input source). This detector is placed after the stabilising distance and close to the crossing section. Power is measured by counting the number of rays that impinge on the detector surface. The power of the source is set to be 1 mW and 1,000,000 rays are generated from this source and power loss is simulated at crossing angles from  $10^\circ$  to  $90^\circ$  in steps of  $10^\circ$ . Figure 7.9 shows the results of the ray tracing simulation for the waveguides with various crossing angles. The NA of the fibre as the light source was chosen to be 0.22 and the optical loss for crossing with different angle was found. Figure 7.9 shows the results for the waveguides with various crossing angles. The results show a high magnitude of loss (more than one dB) for sharp angles (less than  $20^\circ$ ).

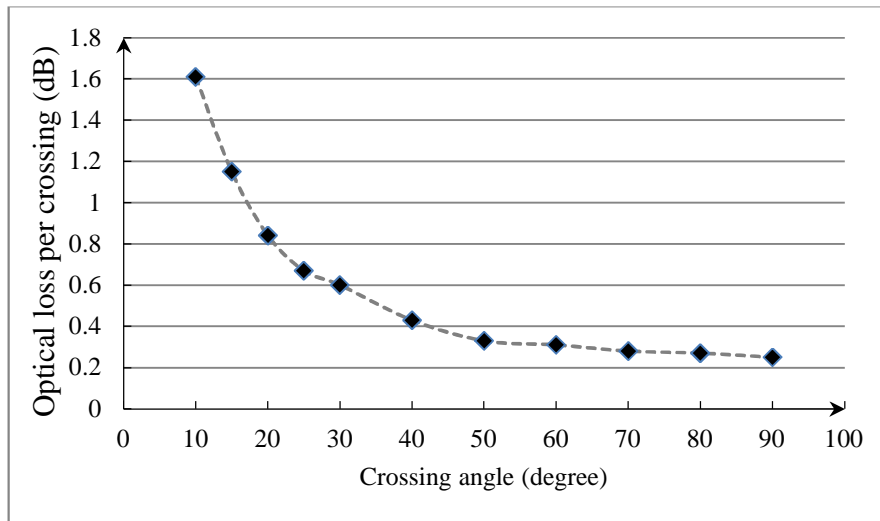


Figure 7.9: Ray tracing results for simulation of crossing waveguides with different crossing angles.

### 7.3 Experiment

In this section the experimental results of the optical loss in crossing waveguides are presented. It should be noted that this research was carried out with Kai Wang. The light source used is an 853 nm VCSEL launched into a standard 50/125  $\mu\text{m}$  step index multimode fibre ( $\text{NA} = 0.22$ ). The fibre source was aligned and butt-coupled to the waveguide. Crossing angles were measured from  $10^\circ$  to  $30^\circ$  in increments of  $5^\circ$ , and  $40^\circ$  to  $90^\circ$  in increments of  $10^\circ$  giving 11 crossing angles in total. There are a number of loss mechanisms involved when light propagates through the crossing including coupling and propagation losses which were reviewed in chapter 4 section 4.3. However, as only the loss purely due to the crossing structure is of interest, all the optical losses were excluded from the experiment results to achieve the optical loss due to the crossing by arranging the experiment below.



## Chapter 7: *Experimental Measurements and Computer Modelling of Optical Loss in Waveguide Crossings*

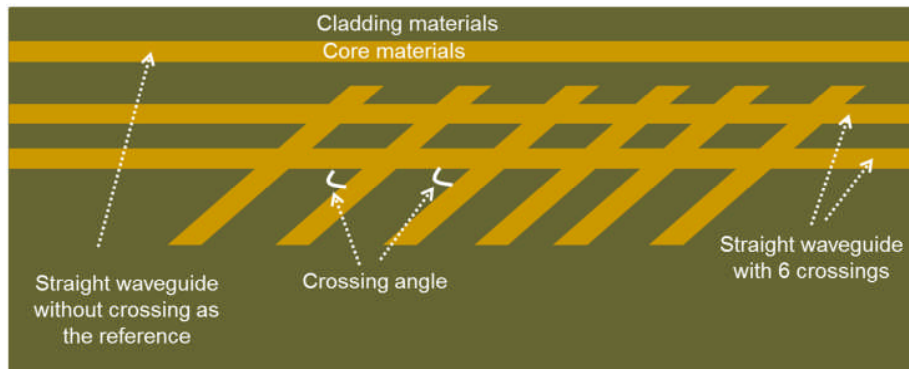


Figure 7.10: Schematic diagram of the crossing waveguides used for measuring the optical loss caused by the waveguide crossings. The size of the waveguides was designed to be 50  $\mu\text{m}$ .

Figure 7.10 shows a schematic diagram of the waveguides. Three identical straight waveguides were fabricated on an FR4 substrate. 2 waveguides out of these three were crossed with 6 identical waveguides. Therefore, there were 6 crossings for each crossing angle. Since the 3 straight waveguides were exactly the same, the output power of these straight waveguides was expected to be equal. Hence, when crossings are placed in one of the waveguides, the difference in output power between the straight waveguides with and without crossing is purely due to the crossing waveguides. The optical loss for each crossing angle was measured 50 times as the input power was set to be 0 dBm and the output power was low (-10 dB) and the measurement was repeated to reduce the error bar by averaging 50 measurements. The crossing angles were; 10°, 15°, 20°, 25°, and from 30° to 90° in increments of 10°, giving a total of 11 different angles. The optical power loss (in dB) detected at the end of the waveguide with crossings was subtracted from the optical loss detected at the end of the waveguide without crossings to find the optical loss due to the 6 crossings (The input power for this experiment was arranged to be 0 dBm). The mean value of the optical loss for each crossing angle in the 50 measurements was divided by 6 to find the optical loss due to one crossing.

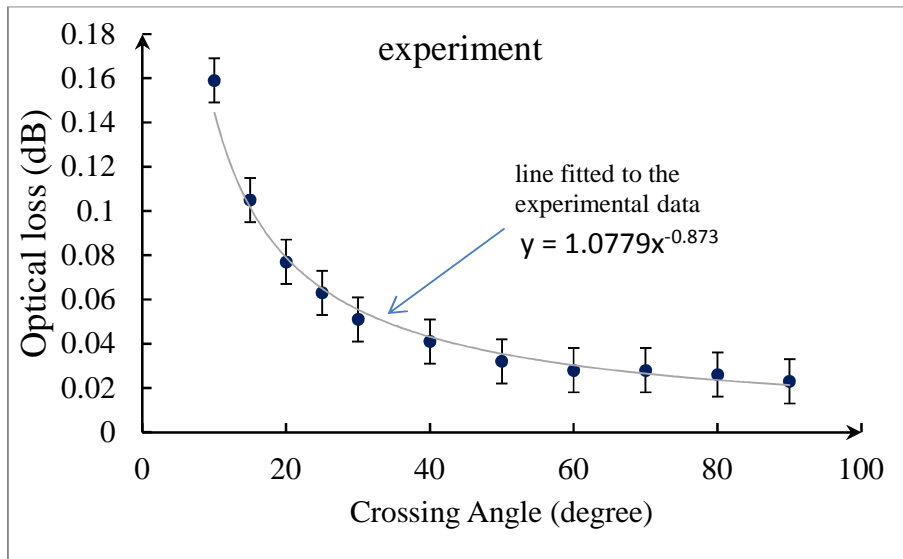


Figure 7.11: Experiment results for the optical loss per crossing for different crossing angle

Figure 7.11 shows the optical loss measurement for each crossing versus the crossing angles. The vertical axis in this figure is the optical loss per crossing which is defined as the power measured at the end of the straight waveguide containing 6 crossings divided by 6.

## 7.4 Discussion of the Results of Crossing Waveguide Simulation and Experiment

Two sets of data from simulations with BPM and ray tracing methods are compared with the experiment results in Figure 7.12. The results show a large difference between the experimental and the ray tracing simulation results. First the BPM and experimental results are compared. The experimental results are referred to as the main results and are of a similar order of magnitude to those reported by other partners in other institutes and universities [7.7].

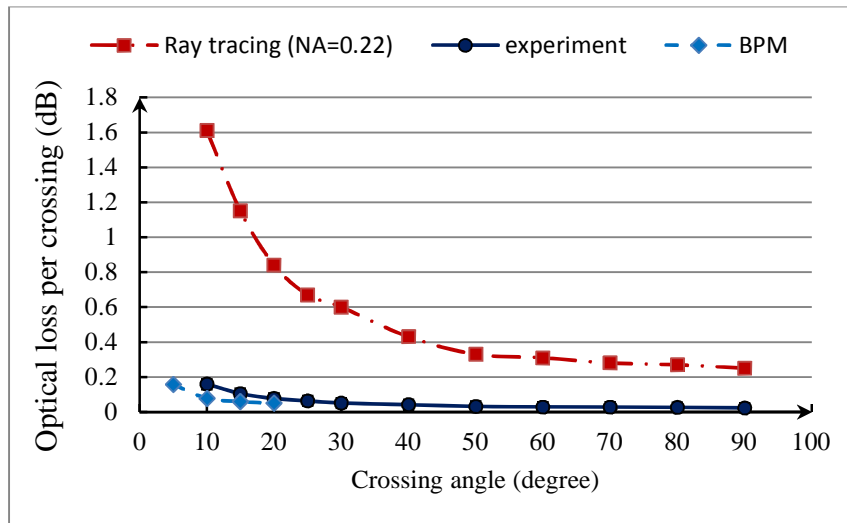


Figure 7.12: Simulation and experimental results for the crossing with various angles. BPM method, ray tracing, and experiment results are compared.

### 7.4.1 Comparison between BPM results and experiments

Figure 7.13 shows the BPM results and the experimental results on the same graph. The results show that the optical loss for any particular crossing angle is smaller in the BPM results compared to the ray tracing method and the experiment results. On the other hand the graphs have a very similar form. In order to determine the possible source of the difference, the waveguide structure which is shown in Figure 7.2 and Figure 7.14 was considered.

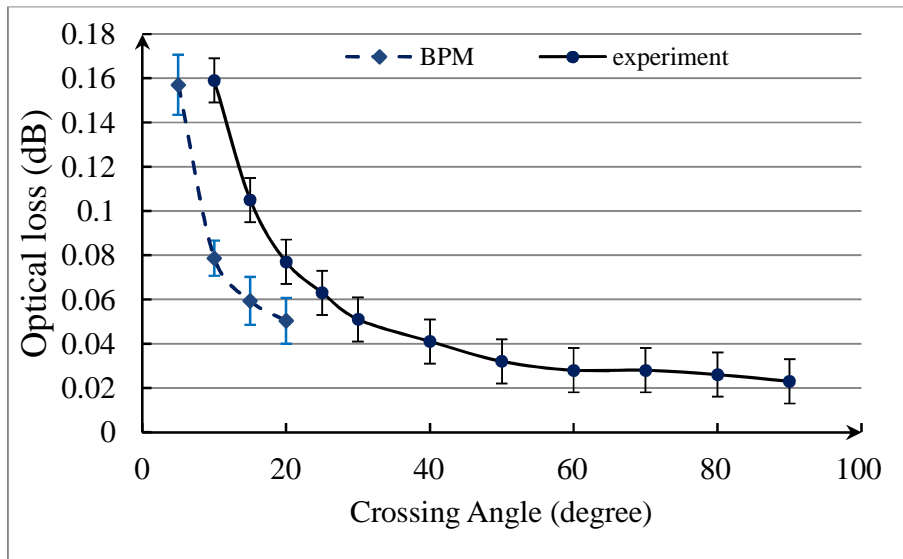


Figure 7.13: Comparing the experimental results with BPM simulation results for the crossing waveguide with various crossing angle

The sizes of the waveguides in these figures were designed to be  $50\ \mu\text{m}$  but the pictures show that the angle corners of the waveguides are not quite sharp. This is due to the manufacturing technique where there are remains of residual core material after UV curing and washing the non-cured polymer.

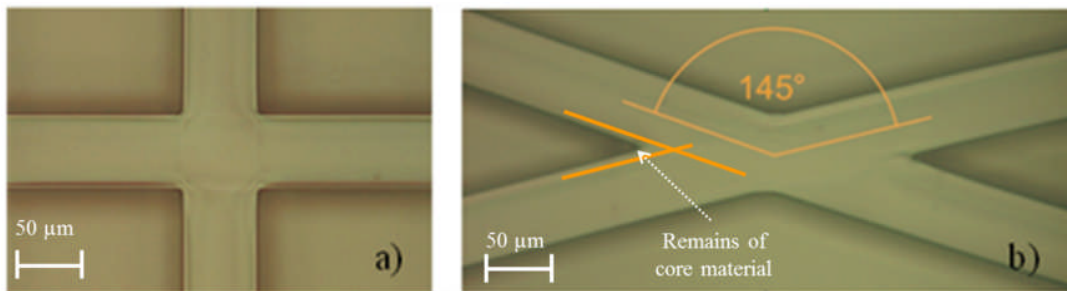


Figure 7.14: Top view micrographs showing two waveguides intersecting with (a) an optimum crossing angle of  $90^\circ$  and (b) a crossing angle of  $35^\circ$

As explained in Chapter 2, in the manufacturing process, the core material is exposed to UV light through a mask where the designed waveguides are printed. Although the mask is kept as close as possible to the material (about  $100\ \mu\text{m}$ ) the UV light is not collimated and diverges after the mask and gives a larger cured area. Therefore, some of the core material becomes trapped in the corners and is cured in the cladding curing process. In any case, it is harder to wash away uncured polymer from the acute section of small angled crossings. In Figure 7.15 the size of the

waveguides appears to be larger at the position of the waveguide crossing due to the residual material of the core produced during the manufacturing process.

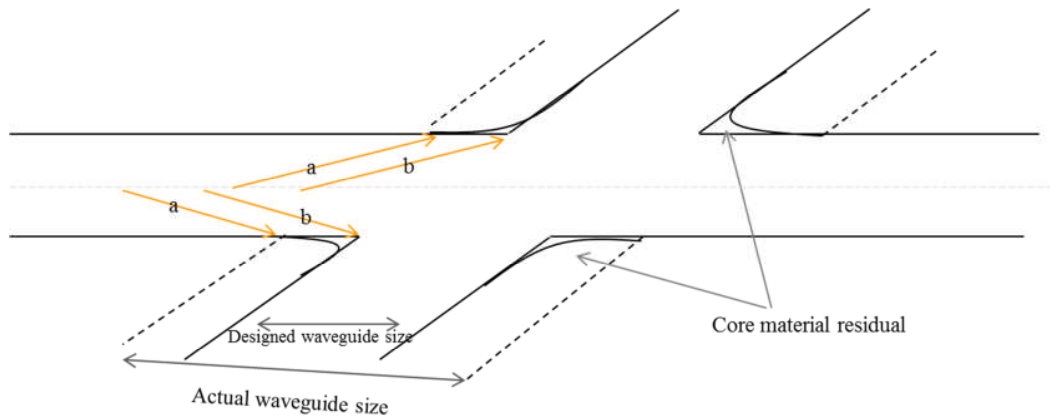


Figure 7.15: Schematic diagram of a crossing section and the residual core material (Figure 7.14). In the designed waveguide only rays marked (b) are coupled out at the crossed waveguide, however, in reality any rays between (b) and (a) will escape into the crossed waveguide

Figure 7.15 shows the effect of the residue at each crossing on the propagation rays. Without the residual part only rays marked (b) will be coupled out at the crossing waveguide, however, with the presence of residue, there is an increase of the width of the crossed waveguide. Therefore, all of the rays which impinge on the distance between rays marked with (b) and (a) will escape the waveguide as this area is covered with the core material and rays continue to propagate which goes to the crossing waveguide.

Figure 7.7 can now be reconsidered to find the particular size for the waveguide for each crossing angle taking the residue into account. The diagrams show that for a sharp angle such as  $10^\circ$  the optical loss approaches the experimental value (0.159 dB) when the crossing waveguide size is about  $75 \mu\text{m} \pm 5 \mu\text{m}$ . This means that the residual gives an increase of 20% to the waveguide size on each side; the increase reduces with increasing crossing angle. Therefore, a potential source of the difference between the results of the BPM simulation and experiments could be the residual core material.

#### **7.4.2 Comparison between ray tracing results and experiments**

Figure 7.16 shows the ray tracing simulation results and the experimental results and it can be seen that the simulation results predict a much larger optical loss for each crossing angle.

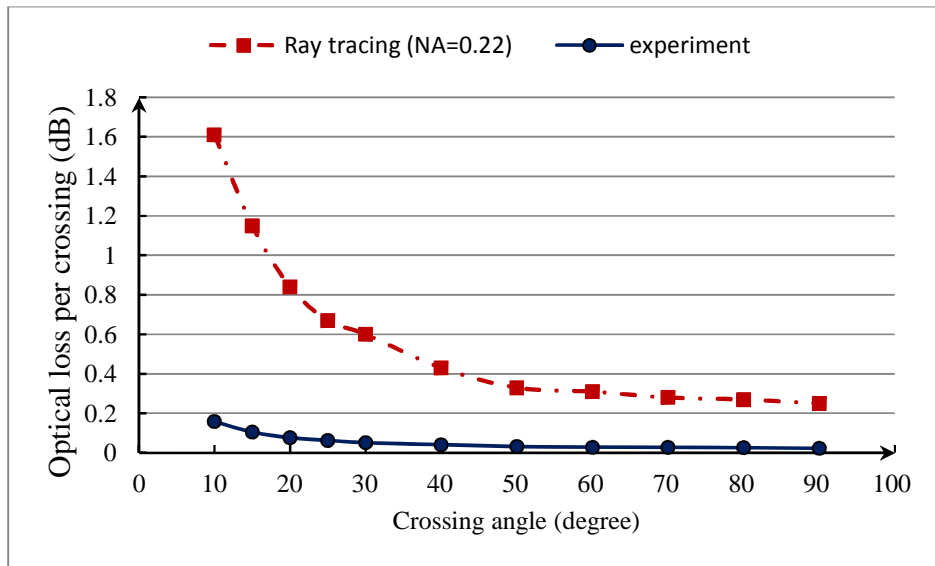


Figure 7.16: Optical loss of one crossing as a function of the angle of the crossing for a calculation using ray tracing compared to the experimental result. The input source has an NA= 0.22.

The difference in the optical loss measured by experiment and calculated by ray tracing method is shown in Figure 7.17. The light source for the simulation is an optical fibre with 50  $\mu\text{m}$  core diameter and NA= 0.22, which is the same as for the experiments. The difference between the simulation and the experiments must be considered; for example ray tracing assumes a rectangular waveguide with smooth walls and no wall roughness.

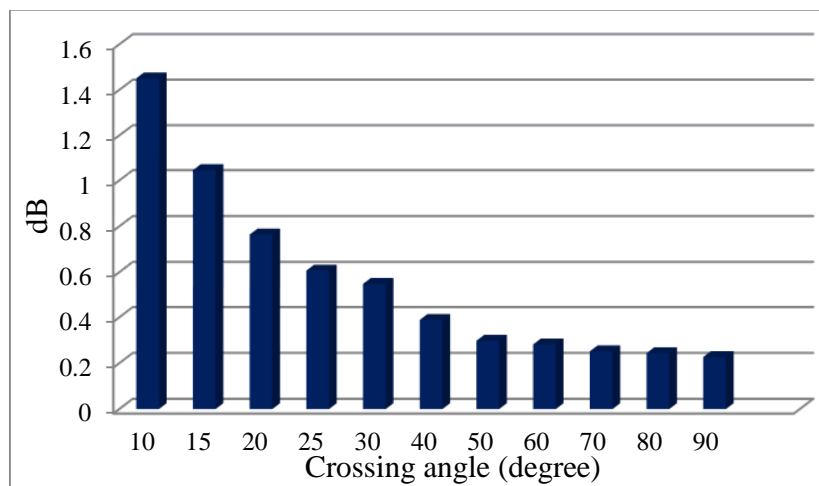


Figure 7.17: Difference between the optical loss in ray tracing simulation and the experiments. The input source for the simulation is a fibre with 50  $\mu\text{m}$  core diameter and NA= 0.22

The ZEMAX software traces millions of rays in a cone for NA= 0.22 inside the waveguide and then follows them until they strike the detector or are lost. Therefore, any ray which is subject to total internal reflection will be guided inside the waveguide. The NA of the fibre indicates that rays are emitted in the cone with half angle of  $12.70^\circ$  and Snell's law determines the maximum angle inside the waveguide is  $8.1^\circ$  which means the incidence angle on the core cladding interface is  $81.9^\circ$ . These numbers were calculated based on the numerical aperture formula for a waveguide[7.5].

$$NA = n \sin \theta = \sqrt{n_{core}^2 - n_{clad}^2}$$

$$\sin \theta_c = \frac{n_{clad}}{n_{core}}$$

Where  $n$  is the refractive index of the medium outside the waveguide/fibre and,  $\theta_c$  is the critical angle of the waveguide/fibre. The critical angle of the waveguide is  $78^\circ$  so that any ray which enters the waveguide will propagate within it. The difference from an actual waveguide is the existence of wall roughness across the waveguides which causes scattering to radiation modes which are lost [7.2;7]. Therefore, only rays with a shallow angle (low order modes) propagate in the waveguide. To determine the range of angles which propagate a colleague (Kai Wang) has measured the output of the waveguide; his measurement shows that the maximum output angle is about  $7^\circ \pm 2^\circ$ .

To simulate the low order mode inside the waveguide the NA of the source was reduced to find the smallest NA which shows optical loss comparable to the experiments. The best results were achieved where the NA = 0.05. The results are shown in Figure 7.18 where the loss in the experiment is the same magnitude as the simulation when experimental error is taken into account.

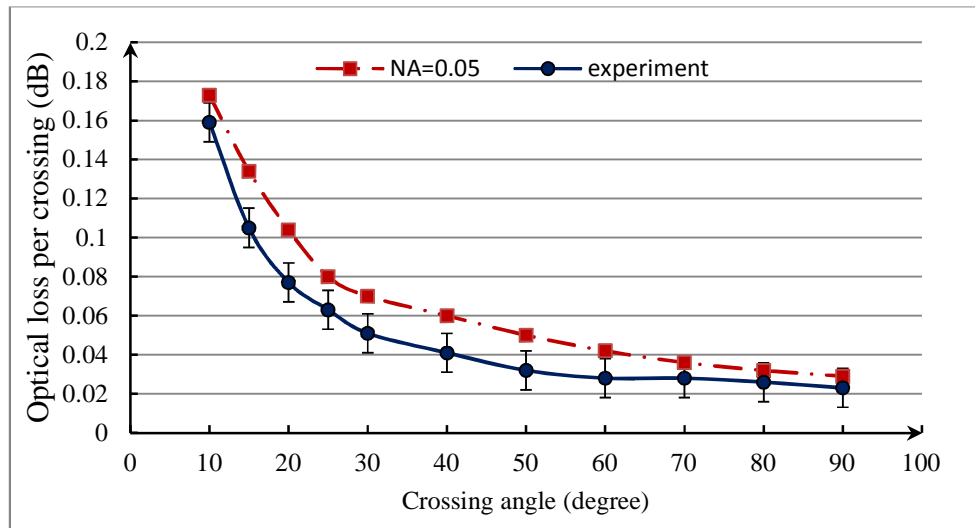


Figure 7.18: Experimental results and the ray tracing results for the source with NA=0.05.

The NA = 0.05 indicates that the output angle is  $5.7^\circ$  which is in good agreement with the measured  $7^\circ$ .

## 7.5 Conclusions:

In this chapter, the optical loss due to crossing waveguides was calculated for different crossing angles. For the first time the results from two different simulation approaches, beam propagation and ray tracing were used and the simulation results were compared with the experiment results. Most of the previous research on crossing is for different material, such as silicon waveguides, or just for  $90^\circ$  crossings.

The results showed that the beam propagation method estimates a lower loss than the experiments, especially for sharper angles. For example, the optical loss due to a crossing angle of  $10^\circ$  was estimated by the BPM to be 0.078 dB while it was measured to be 0.159 dB. To investigate the source of the difference and as the difference in the results was larger for the smaller crossing angles, the measured waveguide was studied and it was found that there is some core material left at the corners of the crossing waveguides, which makes the width of the crossed waveguide larger. This is due to the residue remaining during the waveguide fabrication. This can be improved by either bringing the mask more close to the core material during the



curing or by using more collimated light during the curing process. It cannot be removed completely due to the diffraction of the UV curing light at the edge of the mask.

To find the estimated increase in the waveguide width due to the residue, crossing waveguides with different width on the crossed waveguide were simulated and it was found that if the increase of the waveguide width is  $20\% \pm 5\%$ , the experimental results agree with the simulation. On the waveguide sample, the residue was measured to increase the waveguide width for  $15\% \pm 3\%$ , which is a good agreement with the simulation.

Ray tracing methods was also used for the waveguide simulations, as the BPM algorithm can simulate the crossing angles only up to  $20^\circ$ . The results from ray tracing were opposite to the BPM results as they showed 10 times higher optical loss. To find the source of this error, the process of optical loss at the crossing was reconsidered. The optical source for the simulation was an optical fibre with NA of 0.22 and the waveguide NA is 0.3. The critical angle of the waveguide is  $78^\circ$  so that any ray which enters the waveguide will be propagated within the waveguide. In an actual waveguide wall roughness causes beams with sharper angles (high order modes) to radiate away from the waveguide. Therefore, only rays with a shallow angle (low order modes) are propagated in the waveguide. To determine the range of angles that propagate inside the waveguide, the NA of the source was reduced to find the smallest NA which shows optical loss comparable to the experiments. The best results were achieved where the  $NA = 0.05$ . This NA corresponds to an angle of 6 degrees. The interesting result is that the output angle of the waveguide was measured in our group by Kai Wang to be  $7^\circ \pm 2^\circ$ .

## References

- [7.1] K. Wang, D. R. Selviah, I. Papakonstantinou, G. Yu, H. Baghsiahi, and F. A. Fernandez, "Photolithographically manufactured acrylate polymer multimode optical waveguide loss design rules," *Electronics System-Integration Technology Conference, ESTC 2008*, pp. 1251-1256, 2008.
- [7.2] I. Papakonstantinou, K. Wang, D. R. Selviah, and F. Anibal Fernandez, "Transition, radiation and propagation loss in polymer multimode waveguide bends," *Optics Express*, vol. 15, no. 2, pp. 669-679, 2007.
- [7.3] M. G. Daly, P. E. Jessop, and D. Yevick, "Crosstalk reduction in intersecting rib waveguides," *Lightwave Technology, Journal of*, vol. 14, no. 7, pp. 1695-1698, 1996.
- [7.4] P. Sanchis, P. Villalba, F. Cuesta, Anderas Hakansson, and Amadeu Griol., "Highly efficient crossing structure for silicon-on-insulator waveguides," *Optics Letters*, vol. 34, no. 18, pp. 2760-2762, 2009.
- [7.5] A. W. Snyder and J. D. Love, *Optical waveguide theory*, 190 ed Springer, 1983.
- [7.6] Eugene Hecht and Alfred Zajac, *Optics*, 4 ed Addison Wesley, San Fransisco, CA 1990.
- [7.7] K. Wang, D. R. Selviah, J. Papakonstantinou, G. Yu, H. Baghsiahi, and F. A. Fernandez, "Photolithographically manufactured acrylate polymer multimode optical waveguide loss design rules," *Proceedings - 2008 2nd Electronics Systemintegration Technology Conference, ESTC*, pp. 1251-1255, 2008.

## **Chapter 8: Waveguides and Lightguides for Laser Beam Combining, Homogenisation, and Beam Shaping for Display Backlighting**

### **8.1 Introduction**

In this chapter, a new method of using multimode optical waveguides as part of the light engine for laser backlit displays is explained. The aim is to use optical waveguides to combine, homogenise and shape the optical power of three red, green and blue lasers which were discussed in chapter 5 as part of the 3D autostereoscopic HELIUM3D display. Although the focus in this chapter is on the light engine for this 3D autostereoscopic system, the discussion and comparison are more generally applicable to other laser beam and laser backlit display applications. Several different designs of waveguide for use in a light engine are proposed, for the first time, and compared and the most suitable option (based on the laser beam structure, efficiency, safety, and cost) for the light engine of the HELIUM3D system is selected. The designs include sending the laser beams into a single waveguide directly or using an intermediate section for laser-waveguide coupling. The selected proposed designs are simulated and experimentally tested in the next chapter (chapter 9).

In chapter 5 the HELIUM3D system was described and the lasers chosen as the light source were introduced. It was also mentioned that the light engine in this system is responsible for combining and shaping laser beams to deliver a uniform white beam with ideal dimensions of  $10 \text{ mm} \times 100 \text{ }\mu\text{m}$  for scanning across the image forming section which uses a liquid crystal on silicon (LCoS) modulator [8.1;2]. The light sources were chosen to be multi-emitter lasers with at least 3 W of optical power for each colour to provide enough optical power and reduce the speckle contrast. It should be reminded that due to the structure of the NECSELs the beam waist of the emitters are inside the laser housing and are not accessible. The housing is blocked with an infrared filter and there is no access into the housings.

In this chapter, different approaches for light engine designs are proposed and their advantages and disadvantages are considered and then the challenges for using waveguides in light engines are investigated. In section 8.3, various possibilities for laser-waveguide coupling are considered

and the challenges are compared in order to choose the best option by considering the lasers and the waveguide structure taking into account safety, reliability, and cost of the system. At the end of the chapter, the ageing properties of a newly developed polymer material supplied by Microsharp Ltd. for use in microlens and waveguide fabrication is tested by experiment to find the effect of high optical power intensity on the polymer's optical performance.

## **8.2 Proposal and Comparison of Various Approaches for Designing the Light Engine for HELIUM3D System**

Several approaches can be employed for beam shaping and power homogenisation across the output light column required for the light engine of HELIUM3D. Free space, fibre combiner and waveguide combining methods were considered.

- Free space combining utilises lenses, prisms and other optical elements in the system without confining the beam inside a fibre or waveguide. Several free space methods have been reported [8.3]. They use diffraction, reflection and refraction phenomena to change the beam to a favourable profile.
- In the fibre combiner method, laser beams are combined while they are propagating inside an optical fibre. In this approach, each laser beam is coupled into a single fibre and then the fibres are joined into the combiner unit which is normally a fibre with larger core area [8.4]. The HDI Company has developed a system using a fibre to combine red, green, and blue laser beams. The output of these one watt lasers is coupled into a 50  $\mu\text{m}$  core diameter fibre and the output white light is reported to be 1000 lumens [8.5]. Employing a fibre combiner has the disadvantage of depolarizing the laser light (the image forming in some display systems, particularly those employing liquid crystal modulators, such as HELIUM3D, requires polarized light). The use of a single mode polarisation maintaining (PM) fibre could maintain the polarisation of the laser beam but there are issues regarding the coupling efficiency between laser beams and the single mode fibre. The core diameter of a single mode fibre is a few microns and the laser beam must be coupled into this small area. The efficiency of the HDI system is 20% and the lasers are single emitter diode pumped solid state lasers (DPSS). The laser-fibre coupling requires sophisticated optical design of the optical elements for multi-emitter lasers due to the low beam quality (typically  $M^2 > 100$ ) and the large diameter of the laser beam

(compared to the fibre diameter) which increases the cost of the system. Moreover, the light needs to be shaped after emerging from the fibre so that other optical components are required to shape the beam.

- In the waveguide combining method the laser beams are combined, homogenized and shaped using just a waveguide, so there is no need for other optical components to shape the beam after combining. In addition, laser coupling into the waveguide can be more efficient for larger diameters of waveguide. The waveguide method has not been considered before in the literature and is explained and clarified in the next section in detail.

The optical design and required elements for beam shaping depend on the laser beam quality or étendue which depend on its lateral dimensions and angular divergence [8.6-8]. Single emitter lasers have a better beam quality or étendue ( $M^2=1$ ) than multi-emitter lasers ( $M^2\geq 30$ ) and the energy is confined in a small area which provides a high intensity. (Beam quality factor or étendue shows how close a laser beam is to the diffraction limited situation. The best situation is when  $M^2=1$  which is called diffraction limited. Other laser beam quality factors are derived from dividing the beam quality into the diffraction limited situation [8.9]).

### **8.2.1 Free Space Method for Designing the HELIUM3D Light Engine**

The light engine in the HELIUM3D system is responsible for shaping the beam and delivering a uniform white column of light. To achieve the required beam shape, a specific free space system was designed by Koç University to transform the laser beams into a single uniform line. The design consists of beam shaping optics which includes a beam combiner and a microlens homogenizer. The microlens homogeniser was first proposed by David R. Selviah [8.10] in 1995 for use with an LED source. Kurtz [8.11] followed this research and extended it by including additional field lenses. Figure 8.1 shows a schematic diagram from the optical configuration used by Koç University for the free space approach in the light engine of the HELIUM3D system.

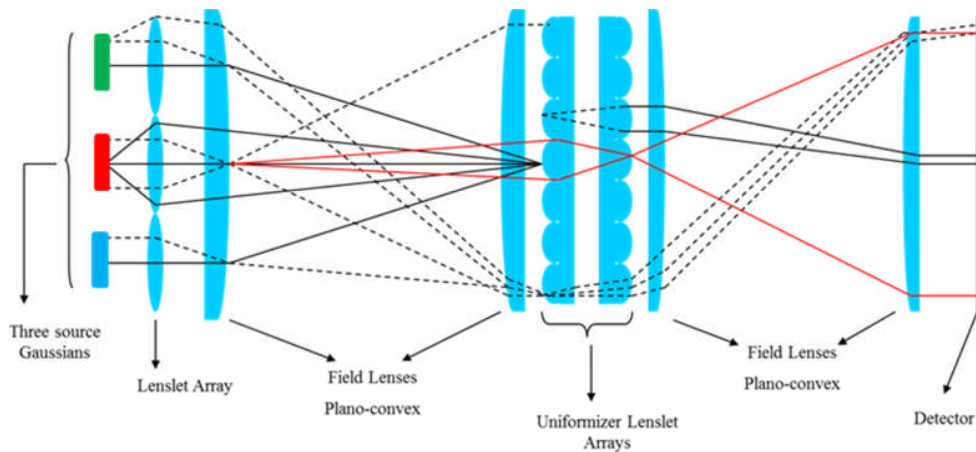


Figure 8.1: Optical layout of the microlens array for 1D laser array homogenizer.

Both the designs of Selviah and that of Koç were aimed at homogenising a single source of a small lateral extent. There are two problems with using this approach for several multi-emitter lasers as shown in Figure 8.1. Firstly, based on the structure of the NECSEL laser beam and the optical design in Figure 8.1, just one row of emitters can be used and consequently half of the power is lost at the first stage as the second row of the emitters is not used. Secondly, as the laser is a multi-emitter laser, a multi-spot structure is formed at the final stage which causes non-uniformity across the image. Figure 8.2 shows the scanned line on the LCoS device after beam shaping and homogenizing using the microlens array. In this case, uniform illumination of the LCoS modulation device cannot be achieved with only static components and both interference and speckle will cause non-uniformities in the intensity distribution of the line which is scanned across the LCoS modulation device, thus resulting in brighter and darker horizontal bands on the display (Figure 8.2).



Figure 8.2: The recorded pattern of the scanned line after using free space homogenisation of the NECSEL laser beam

## Chapter 8: *Waveguides for Laser Beam Combining, Homogenisation, and Beam shaping for Display Backlighting*

In order to solve this problem, four possible solutions were considered:

1. The use of a non-periodic microlens array having variable pitch across the array to produce different interference patterns overlapping each other which give a uniform illumination [8.12].
2. Vibrate the micro-lens array [8.13] which increases the uniformity by integrating the multiple patterns in time but this needs to be changed faster than the response time of the human eye.
3. The use of a deformable MEMS membrane before the micro-lens array to average out the interference pattern [8.14].
4. The use of an optical fibre/waveguide[8.15].

The first solution requires the optical system to be redesigned as the width and length of the light line at the final stage depends on the microlens arrays and their properties. Moreover, manufacturing a custom designed microlens costs about \$10,000 which increases the cost of the system.

The second solution is not appropriate as mechanical vibration can introduce more difficulties into the system. The microlens array consists of several different layers glued together and the vibration could degrade the performance and de-laminate the lens assembly. The best solution is to use an optical waveguide to couple the optical power of different emitters into the waveguide modes. In this method the laser is coupled into a single multi-mode fibre. The light is homogenized by multi-mode propagation inside the fibre and the fibre can be vibrated to reduce the speckle if required.

The first advantage of this method is that it is very convenient and safe to use. If the lasers are coupled into an optical fibre, the output light can be used anywhere away from the laser module whether far or distant by increasing the fibre length. Here the idea is to couple the optical power of the laser emitters into the waveguide/fibre and remove the multi-spot problems that occurred in the free space. The optical power is distributed between the propagation modes of the waveguide/fibre and there is no multi-emitter source at the output of the fibre. Another advantage is that optical fibres can propagate tens of watts of optical power and deliver it anywhere where it is needed in the system without any issues arising relating to laser safety. However, the challenge of using fibre is that if the fibre is to be multi-mode to achieve a high

optical power coupling efficiency, the output from the fibre will be unpolarised and must be polarised if the image-forming device is sensitive to the polarisation. Also, the output beam has a circular shape so that if the output profile is required to be in any other configuration an extra beam-shaping process will be required which increases the cost and complexity of the system. These are the compromises that will have to be made. In the rest of this chapter, several possible designs for the light engine using optical waveguides are discussed.

### **8.3 Laser Beam Coupling, Homogenising, and Beam Shaping using Optical Waveguides.**

In this section several approaches for using optical waveguide in the light engine of the HELIUM3D system are proposed, discussed and compared. Coupling the laser beam into the waveguide is one of the challenges which must be considered carefully to achieve an acceptable efficiency and sufficient power at the output. The beam product parameter (BPP) must be considered for the various laser beam coupling options to make sure that an efficient coupling is possible. BPP quantifies the beam quality of a laser beam. It is the product of the beam radius at the beam waist (in mm) and the half angle beam divergence (in mrad). It specifies the beam quality and higher BPP indicates the lower beam quality. The lowest BPP possible is for a diffraction limited beam where the value is  $\lambda/\pi$  [8.9]. For a circular beam the BPP is the same in any direction but it can be different for a noncircular beam such as an edge-emitting diode laser. BPP is a constant value and it does not change as the beam passes through non-aberrative optical elements. Non-ideal optics can increase the BPP and hence degrade the beam quality [8.9].

To achieve maximum coupling efficiency the BPP of the laser beam must be equal to or smaller than the BPP of the fibre. In fact, a laser beam's BPP defines a cone inside which the laser light propagates after emerging from the laser cavity. Waveguide/fibre's BPP describes a cone for which any light beam inside this volume will be captured by the waveguide/fibre and be coupled into the waveguide/fibre and the light outside the cone will be lost. Therefore, if the BPP for the laser beam is larger than the BPP of the fibre then some part of the laser beam will be beyond the coupling limitation and subsequently that amount of power will be lost.

The object here is to couple all of the laser light into a waveguide with the same size as the required line (10 mm × 100 µm) so that the output of the waveguide is a shaped, homogenised



light column that is scanned on to the LCoS modulation device. Figure 8.3 shows a drawing of the waveguide and the actual structure of the lasers; it should be noted that the sizes shown are to scale. The aim is to couple the output of the red, green, and blue lasers with the size shown in the figure into a slab waveguide with cross section area of  $10 \text{ mm} \times 100 \mu\text{m}$ . The length of the waveguide must be calculated to achieve the required homogenisation.

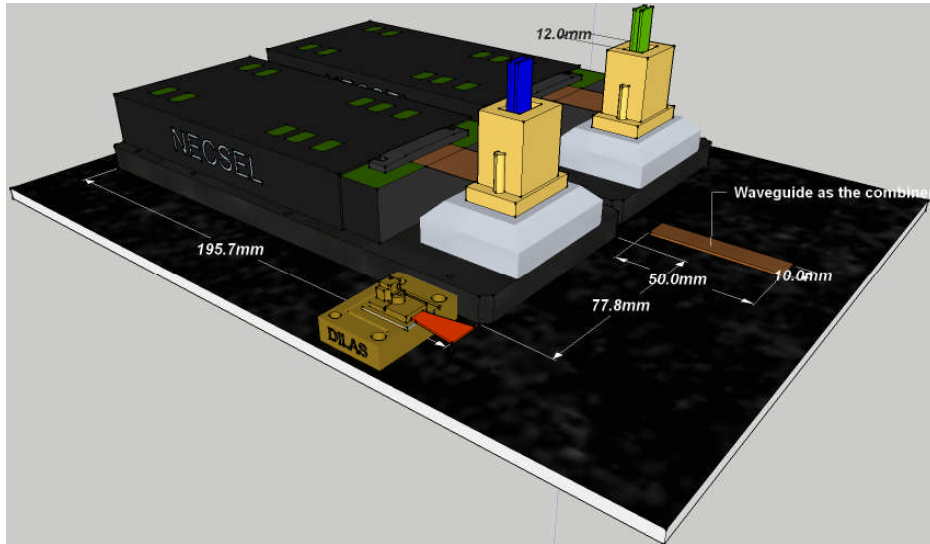


Figure 8.3: Schematic diagram of the three lasers when they are placed next to each other. The waveguide is also shown as well in order to indicate the difficulties of coupling the three lasers into a waveguide in free space. The waveguide thickness is  $100 \mu\text{m}$ .

### 8.3.1 Coupling NECSEL Laser Beams into a Waveguide using Lenses

The first option for NECSEL-waveguide coupling is to use a lens system and couple each laser beam directly into the waveguide. Two different options can be considered; firstly to image the emitters of the NECSELS on the input facet of the waveguide. The beam waist of each laser emitter is  $80 \mu\text{m}$  and imaging this part of the beam on the waveguide (which has a thickness of  $100 \mu\text{m}$ ) can provide a good coupling efficiency. However, the NECSELS contain two rows of emitters with a distance separation of  $2271 \mu\text{m}$ , therefore the emitters cannot be imaged on a  $100 \mu\text{m}$  waveguide surface. The second option is to focus the laser beam onto the waveguide surface. Figure 8.4 shows an example of using 6 lenses to couple the NECSEL's output into the waveguide.

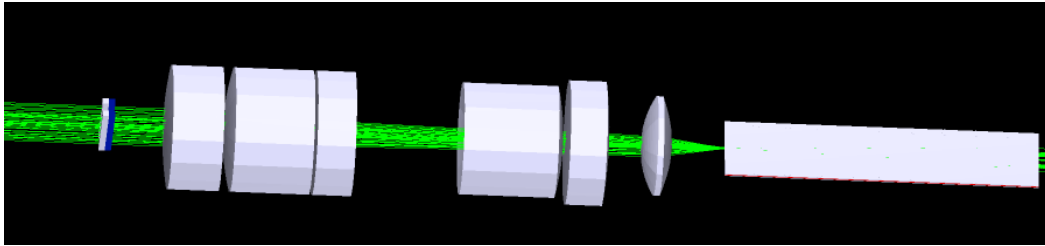


Figure 8.4: Coupling the output of the NECSEL directly into the waveguide by using optical lenses. The laser is emitting from the left and after passing through the various lenses is coupled into the waveguide which is the last object on the right. The waveguide width is 10 mm.

In this approach, a system must be designed consisting of lenses to focus the beam onto the waveguide input surface. The width of the beam has to be reduced to a maximum value of 100  $\mu\text{m}$  (this is the required width for the final output so the thickness of the waveguide can be maximum 100  $\mu\text{m}$ ) and the divergence should be less than the NA of the waveguide to achieve the maximum beam coupling efficiency.

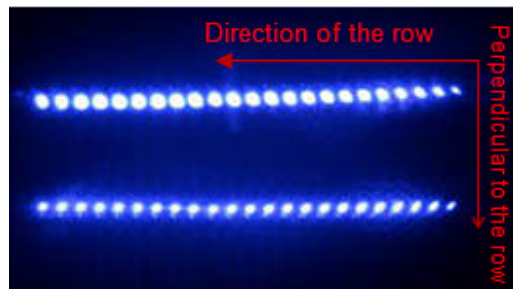


Figure 8.5: Configuration of the emitters of the NECSEL

The question here is whether it is possible to reduce the size of the laser beam into 100  $\mu\text{m}$  or not? To answer this question, the BPP of the laser beam and the waveguide are compared. The BPPs are calculated as:

*beam parameter product = laser's half angle divergence  $\times$  radius of the beam at the beam waist*

$$\text{BPP for one row in the perpendicular direction to the row} = 4.8 \times 0.04 = 0.192 \text{ mm} - \text{mrad}$$

$$\text{BPP for two rows in the perpendicular direction to the row} = 4.8 \times 1.1 = 5.28 \text{ mm} - \text{mrad}$$

$$\text{BPP for one row in the direction of the row} = 4.8 \times 3.8 = 18.24 \text{ mm} - \text{mrad}$$

*beam parameter product of optical waveguide = Numerical aperture  $\times$  radius of the waveguide*

## Chapter 8: Waveguides for Laser Beam Combining, Homogenisation, and Beam shaping for Display Backlighting

$$BPP \text{ for the waveguide } (NA = 0.22, \text{ diameter} = 100 \mu\text{m}) = 220 \times 0.05 = 11 \text{ mm} - \text{mrad}$$

$$BPP \text{ for the waveguide } (NA = 0.22, \text{ diameter} = 10000 \mu\text{m}) = 220 \times 5 = 1100 \text{ mm} - \text{mrad}$$

In the equation for calculating the BPP for one row of NECSEL the size of the beam in the direction of a row of emitters is the size at the beam waist which is 7.62 mm ( $3 \times 0.328 + 0.080 = 7.62$  mm). In the perpendicular direction to the rows of the emitters, the BPP for one row is about 0.192 mm-mrad and for two rows is 5.28 mm-mrad. On the other hand, the BPP for the 100  $\mu\text{m}$  waveguide is 11 mm-mrad. Therefore, it is possible to send the light into a 100  $\mu\text{m}$  waveguide. In the direction of the row of emitters, the laser beam has a BPP = 18.24 mm-mrad but as the waveguide has a larger width (10 mm) the laser can be coupled into the waveguide (BPP = 1100 mm-mrad).

The problem with using lens systems is that any misalignment of the focused laser beam and the waveguide will cause light loss of at the coupling section. However, the principal problem for using this approach is the coupling of three different lasers into one waveguide. Consider the size of the lasers and the waveguide in Figure 8.3 and required optical lens for each laser in Figure 8.4. The width of each NECSEL is 8 cm and the width of the red laser is 3 cm. Therefore, the lasers occupy at least 19 cm width ( $8+8+3$ ) when they are arranged as shown in Figure 8.3. The waveguide is 10 mm so, it can be realised that using the lens system approach requires sophisticated optical designs and components to send the three lasers into the waveguide which increases the cost of the system and in reality is not practical.

### 8.3.2 Coupling Laser Beams into a Waveguide Using Optical Fibre

Another option for coupling the laser output into the waveguide combiner is to use optical fibres. There are different options regarding the use of fibre as the mid-section for coupling the laser into the waveguide. However, it should be noted that there are two optical power coupling efficiencies that must be considered for each fibre; the coupling of the laser beam into the fibre and the coupling of the output of the fibre into the waveguide. For each of these couplings the BPP agreement should be checked.

#### 8.3.2.1 Fibre ribbon:

Fibre ribbons consist of a certain number of fibres arranged horizontally next to each other with a specific distance between the fibres. In fact, the fibres are glued inside a number (depends on

Chapter 8: Waveguides for Laser Beam Combining, Homogenisation, and Beam shaping for Display Backlighting

the design) of grooves with specific distance between the grooves. This arrangement of fibres is used in laser guiding and photonics [8.16-20]. The aim is to couple each laser emitter into a single fibre of the ribbon and at the other end the fibre ribbon is attached to the waveguide end facet. Figure 8.6 shows a schematic diagram from the method. Standard MT connectors can be used to connect the fibre ribbon into the waveguide. This method requires a design of lenses to focus the beam from each emitter into one fibre. The advantage of the fibre ribbon method is that the fibre ribbon can be easily handled, moved around and adjusted to the design of the system as it can be bent or twisted around any object as long as the bend radius is not smaller than the permitted radius for the fibre by the fibre manufacturing company. One issue to be still considered is the core diameter and the numerical aperture of the fibres which are used inside the ribbon. The larger the diameter of the fibre, the easier and more efficient the laser-fibre coupling will be as it increases the BPP of the fibre; however, the fibres with larger core diameter occupy a larger space when they are arranged next to each other at the other end of the ribbon where the ribbon is attached into the waveguide. It should be noted that the width of the waveguide is 10 mm. Each NECSEL will have two ribbons (one ribbon per row) with 24 fibres in each ribbon. The red laser will have one ribbon with 20 fibres inside. In total 5 ribbons will be used to couple the red, green and blue lasers into the waveguide.

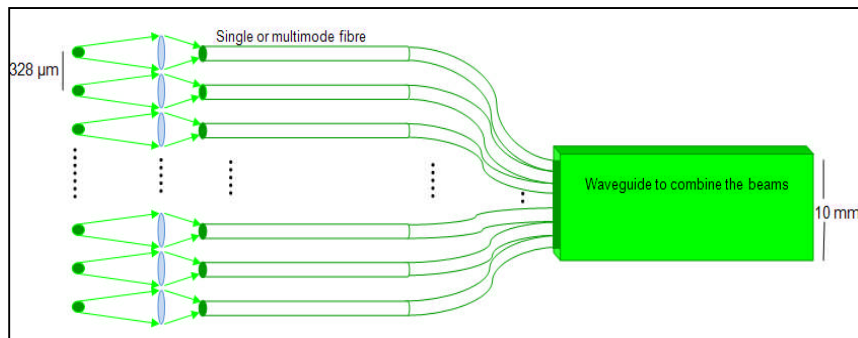


Figure 8.6: Schematic diagram showing using fibre ribbon for coupling laser beam into the waveguide.

As each emitter is coupled into a single fibre, it is possible to couple the emitters into single mode or multi-mode fibres due to the small value of the BPP of the emitters:

$$\text{beam parameter product} = \text{laser's half angle divergence} \times \text{radius of the beam at the beam waist}$$

$$\text{BPP for a single emitter} = 4.8 \times 0.04 = 0.192 \text{ mm} - \text{mrad}$$

Chapter 8: *Waveguides for Laser Beam Combining, Homogenisation, and Beam shaping for Display Backlighting*

To compare fibres with different diameter the BPP and the width of the ribbon at the waveguide are listed and compared in Table 8.1.

Table 8.1: Comparison of the possibilities of coupling laser emitters into different fibres. The NA for the fibre and the waveguide is considered to be 0.22.

Fibre core diameter ( $\mu\text{m}$ )	BPP (mm-mrad)	BPP of the waveguide (mm-mrad)	Width of the ribbon at the waveguide NECSEL/Red laser (mm)	Width of all of the ribbons (4 ribbons from NECSEL and one ribbon for the red laser) (mm)
9	0.99	11	0.216/ 0.180	1.044
50	5.5	11	1.20/ 1.00	5.8
62.5	6.88	11	1.50/ 1.25	7.25
100	11	11	2.40/ 2.00	11.60

Based on Table 8.1 and the BPP value of the emitters, it is possible to couple the emitters into either single mode or multi-mode fibres as the BPP of the emitters is less than that of the fibres. Another point to consider is that three lasers with 5 rows of emitters (2 rows of green, 2 rows of blue and one row of red emitters) must be coupled into the waveguide. Therefore, 5 ribbons must be used (2 for blue, 2 for green and one for red laser) with these ribbons placed next to each other and attached to the waveguide. The larger the fibre core diameter, the larger the emitter-fibre coupling efficiency and the misalignment tolerance. However, fibres with the larger core area will engage a larger area at the waveguide. For example, if fibres with 100  $\mu\text{m}$  diameter are used in the fibre ribbon then the width of the beam at the waveguide will be 11.6 mm which is larger than the waveguide (which is 10 mm). The solution could be a tapered waveguide which has a larger width at the fibre ribbon and smaller width at the output (Tapers cause more optical loss[8.21]). Another option to reduce the width of the ribbons at the input of the waveguide is to put them into a hexagonally close packed 2D array. But the maximum core diameter that can be used is 9  $\mu\text{m}$  as the thickness of the waveguide is 100  $\mu\text{m}$  and the thickness of the 2D arranged ribbons must be less than the waveguide thickness.

One should bear in mind that although using 100  $\mu\text{m}$  fibres will be more convenient and reliable for the laser emitter-fibre coupling, the other end of the system will be less tolerant for misalignment to the waveguide. The waveguide is also 100  $\mu\text{m}$  and any misalignment between the ribbon and waveguide will cause optical loss.

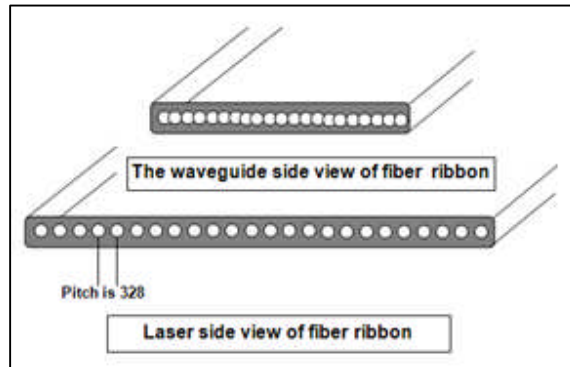


Figure 8.7: Schematic diagram of a fibre ribbon structure. Each emitter is to be coupled into a single fibre.

In total, reducing the core diameter of the fibres in the ribbon will make emitter-fibre coupling more difficult but the system will be more robust in terms of misalignment tolerances on the waveguide side. Therefore, there is a trade-off between the coupling difficulty and the misalignment tolerance.

### 8.3.2.2 Multi-mode Fibre:

Another option for coupling the laser beams into the waveguide is to send the beam of each laser (colour) in one multi-mode fibre and then attach the three fibres (one for each colour) into the waveguide. The coupling efficiency is challenging as the laser is multi-emitter with a low beam quality and a sophisticated lens design is required to send all the emitters into one single fibre. The advantage of this method is that the lasers can be placed away from the system and the optical power can be used easily anywhere away from the source. This advantage is achieved by using fibre ribbon but it is important that the fibre is a standard type as this significantly reduces the system cost (an optical fibre costs 100 pounds while fabrication of the fibre ribbon is at least 7000 pounds). The waveguide combiner system can be used for any type of laser provided the lasers are fibre pigtailed in case any of the lasers breaks down and needs to be replaced; this fact is very important and there is no need for another optical design when the laser is changed in the system. However, the challenge of the coupling efficiency between the laser and the fibre must be considered. The beam parameter product of the NECSEL beam and the laser are listed in Table 8.2.

Chapter 8: Waveguides for Laser Beam Combining, Homogenisation, and Beam shaping for Display Backlighting

Table 8.2: The Beam Parameter Product for different fibres to be used for laser beam coupling. The NA of 0.22 and 0.48 are standard numerical apertures.

<i>beam parameter product of a laser beam</i> = <i>laser's half angle divergence</i> × <i>radius of the beam at the beam waist</i>				
<i>beam parameter product of an optical waveguide = Numerical aperture</i> × <i>radius of the waveguide</i>				
Fibre core diameter (μm)	NA	BPP (mm-mrad)	BPP of the laser beam (mm-mrad)	Efficient coupling
200	0.22	22	18.24	✓
	0.48	48	18.24	✓
100	0.22	11	18.24	✗
	0.48	24	18.24	✓
50	0.22	5.5	18.24	✗
	0.48	12	18.24	✗
9	0.22	0.99	18.24	✗
	0.48	2.16	18.24	✗

The laser-fibre coupling efficiency is reduced when the BPP of the laser beam is larger than the BPP of the optical fibre. Table 8.2 indicates that the minimum fibre diameter can be 100 μm and the fibre has to have a large NA of 0.48. In this case, the high divergence of the light from the fibre output due to the high numerical aperture must be considered as it requires the waveguide to have at least the same NA to capture the output of the fibre. The BPP of a standard fibre with 100 μm core diameter and NA= 0.22 is 11 mm-mrad. Comparing the fibre beam parameter product and laser BPP (18.24 mm-mrad), indicates that the fibre coupling is not efficient as the fibre captures about half of the power emitted by the laser.

Chapter 8: *Waveguides for Laser Beam Combining, Homogenisation, and Beam shaping for Display Backlighting*

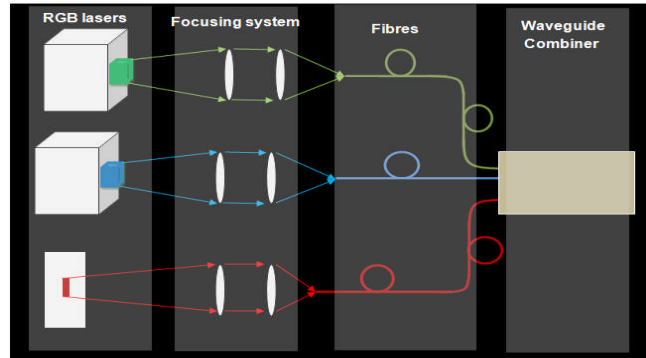


Figure 8.8: Schematic diagram for using fibre to couple the laser light into the waveguide.

To reduce the BPP of the laser beam and improve the beam quality we either need to increase the fill factor and reduce the divergence angle (fill factor is the ratio of the emitter size in near field to the distance between the emitters) or use other optical elements such as step mirror and optical lenses to increase the beam quality in one direction and reduce it in the other direction [8.22-26]. Step mirrors rearrange the position of the emitters and consequently the laser beam is more symmetric in  $x$  and  $y$  directions (the laser beam in the direction of the rows ( $x$ ) is about 8 mm and in the perpendicular direction to the rows of emitters ( $y$ ) is about 3 mm. The step mirrors rearrange the emitter's radiation to have the same size in the  $x$  and  $y$  direction) [8.22;26]. The fill factor method is applied to the laser diodes with one row of emitters. Using a step mirror for the NECSEL laser will require a complicated optical design and will not be tried in this project. Therefore, the second method to increase the beam quality factor of the NECSEL lasers is to reduce the divergence of the beam and increase the filling factor of the emitters at the same time.

The BPP of the NECSEL beam and an optical fibre with 100  $\mu\text{m}$  core diameter and  $\text{NA} = 0.22$  is 18.24 mm-mrad and 11 mm-mrad respectively. Consequently, the laser beam coupling will not be efficient as the fibre will not be able to capture all of the distributed optical energy of the laser. One way to solve this problem is to reduce the divergence of the laser and increase the filling factor, which is the ratio of the emitter size in near field to the distance between the emitters, at the same time (Figure 8.9). If we reduce the divergence to 4 mrad, the BPP of the laser is reduced to 8 mm-mrad which increases the coupling efficiency.



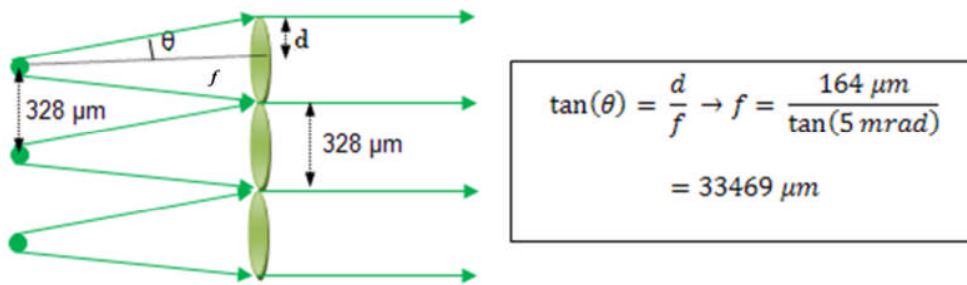


Figure 8.9: Calculation of the micro-lens for collimating the laser

Micro-lenses are to be used to increase the filling factor and reduce the divergence. For the NECSEL laser the filling factor is 24.3% (80 μm /328 μm). As shown in Figure 8.9, the effective focal length of the micro-lens should be 33.5 mm and the pitch between the lenslets must be 328 μm. The beam waist of each emitter is placed at the location of the focal point to achieve an effective collimation.

### 8.3.2.3 Fibre Bundle:

A fibre bundle is made of a large number of fibres (thousands of fibres, dependent on the application) which are placed together in a bundle and are used for various applications and can provide an easy way to bring the light from an inaccessible position. They are in two types of coherent and incoherent bundle. In the coherent fibre bundle, fibres are arranged in the same way at both ends.

In fibre bundle coupling, the laser light is coupled into a bundle of the fibres and guided to the location required. One advantage of the fibre bundle is that the fibres can be rearranged to be appropriate for the waveguide coupling. Another advantage is that the light can be carried out into an accessible position outside the NECSEL housing to which there is no access. Additionally, with a fibre bundle there is no need to use any micro-lens or any other optical elements to couple the laser light into the fibres which reduces the challenge of the alignment of the microlens and also cut the cost of the microlens fabrication (which is about 10000 \$). The bundle is attached into the output cap of the laser without requiring any adjustment or complicated aligning and the output power of the laser is shared between the fibres and guided to the other end of the fibre. In other words, the fibre bundle samples the optical output and delivers it at the other end of the bundle.

## Chapter 8: Waveguides for Laser Beam Combining, Homogenisation, and Beam shaping for Display Backlighting

The input of the fibre bundle can be attached to the NECSEL with the output rearranged into a line and attached into the waveguide; in this way the colours are mixed and the required column is formed.

When the fibres in the bundle are single mode with a diameter of 9  $\mu\text{m}$ , for each emitter we will have:

$$\text{Number of the fibres} = \frac{\text{Area of the emitter}}{\text{Area of the fibre}} = \frac{\pi \times (0.04)^2}{\pi \times (0.0045)^2} = 79$$

So for each emitter we will have 79 fibres and for all the emitters in a row:

$$\text{Total number of the fibres} = 24 \times 79 = 1896$$

The challenge in this case is to separate the 1896 fibres and rearrange them in order to couple the light into the waveguide. It is not practical to arrange them side by side as the length of the line would be large ( $1896 \times 9$  (diameter of each fibre) =  $17064 \mu\text{m} = 17.064 \text{ mm}$  for each row).

The fibres could be arranged in a different configuration to fill all the area of the waveguide core but a large amount of work is required which increases the cost of the system. Another point to mention is that the above calculation is valid if the fibre bundle is placed at the position of the beam waist as we have considered the beam diameter to be 80  $\mu\text{m}$ , however the beam waist is inside the laser housing and cannot be accessed. To apply this method the beam waist must be imaged somewhere outside the housing using a lens with a bundle placed in the position of the image. The bundle can be attached to the laser cap without any lens or imaging section but the size of the beam at the laser housing output was measured to be at least 140  $\mu\text{m}$  (chapter 6). This beam diameter increases the number of the illuminated fibres by 4 times.

Therefore, the use of a fibre bundle is not practical compared to the fibre ribbon and the multi-mode fibre but it can be used to bring the beam further away from the laser and then other methods applied. In this case, access to the beam will be easier but the divergence of the beam is larger as the NA of the fibres is larger than the laser divergence (for a fibre with NA=0.22 the half angle divergence is  $12.7^\circ$  and the half angle divergence of the laser beam is  $0.137^\circ$ ).

Fibre bundles have the problem of low efficiency due to the dead space between the fibres. Any optical power landing on the dead space is lost as it is not captured by any of the fibres. Fibre

bundles will, therefore, not be considered as a solution due to their low efficiency and the complexity that they add to the system which makes them impractical.

### 8.3.2.4 Multiple Fibres

Another option to consider for using optical fibres to couple the laser light into the waveguide is to focus the beam into several fibres and then connect them to the waveguide individually. In this method, the fibres at the waveguide will act as a fibre ribbon and they are placed next to each other side by side) but on the laser side, fibres are joined together in a circular or elliptical shape.

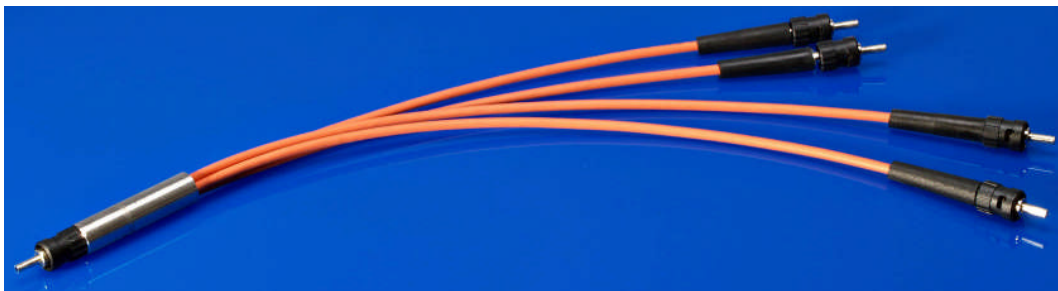


Figure 8.10: Fibre beam combiner made by EOC Company. The fibres are stripped and put together at the input. At one end the fibres are close together and the other they are totally separated [8.27].

Figure 8.10 shows a picture from one of the available fibre beam combiner. The laser beam from each laser is focused into a spot where the joined fibres are placed. Focusing the laser beam in this case does not require any special lens to increase the cost of the system.

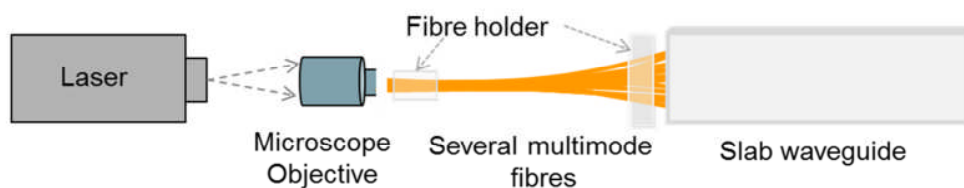


Figure 8.11: Schematic diagram for using several multimode fibres to couple the laser light into the waveguide.

The fibres which contain the red, green and blue laser beam can be merged (arranged) into each other to have a sequence of RGB colours to increase the colour homogenization at the end of the slab waveguides as the colours are mixed while the laser beams are propagating inside the waveguide (This method will be tried in chapter 10).

### 8.3.3 Coupling Laser Beams into the Waveguide using Flexible Waveguide

A flexible waveguide is another option as it enables us to bring the optical power of the three lasers together and combine them to achieve the required output for the light engine. This method is similar to the fibre ribbon but here we use a slab waveguide instead of using many fibres. There are two ways of using flexible waveguides. In the first method, one flexible waveguide can be used to couple each row of the emitters into a slab waveguide whose other end is connected to the waveguide combiner. Therefore, for each NECSEL two slab waveguides are used and in total there are 5 slab waveguides) which must be connected to the waveguide combiner (4 waveguides for the NECSEL lasers as each NECSEL has two rows of emitters and one waveguide needs to be dedicated to each row. Only one waveguide is necessary for the red laser. The width of each waveguide used for the NECSELs is 8 mm and for the red laser is 4 mm which makes 36 mm in total).

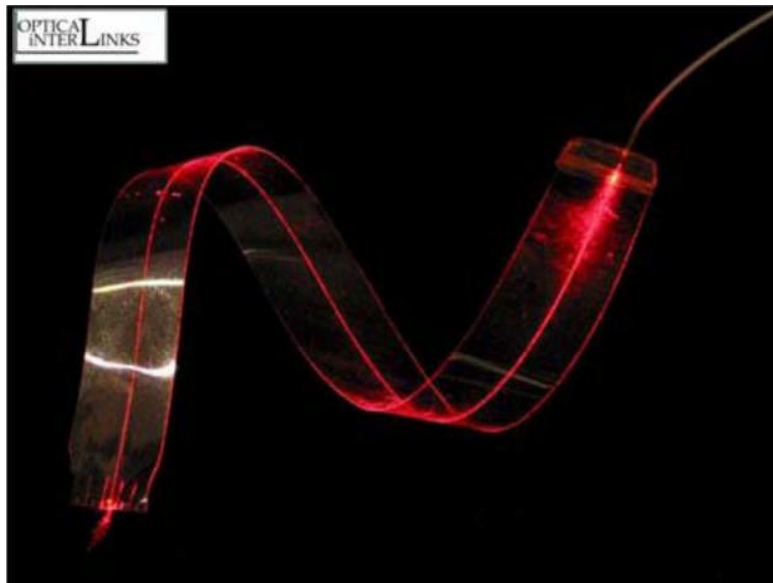


Figure 8.12: Flexible waveguide made by Optical InterLinks (With permission from L. Booth).

Waveguides with 36 mm wide input create a problem as the waveguide combiner must be tapered to achieve the 10 mm output line. An alternative solution is to use a flexible waveguide which is thinner, for example they can be 50  $\mu\text{m}$  thick. In this case, the total waveguide width will be 36 mm but this can be rearranged as two waveguides placed on top of each other (2 waveguides each having a thickness of 50  $\mu\text{m}$ ) at the location of the waveguide combiner. This arrangement reduces the width of the waveguide combiner to 20 mm which is still twice the

Chapter 8: *Waveguides for Laser Beam Combining, Homogenisation, and Beam shaping for Display Backlighting*

required output width. Thinner flexible waveguides can also be used to reduce the size of the beams at the location of the waveguide combiner, but reducing the thickness decreases the misalignment tolerance at the laser end.

In the second method one flexible waveguide is designed to gather the light from the lasers and then combine them together (Figure 8.13).

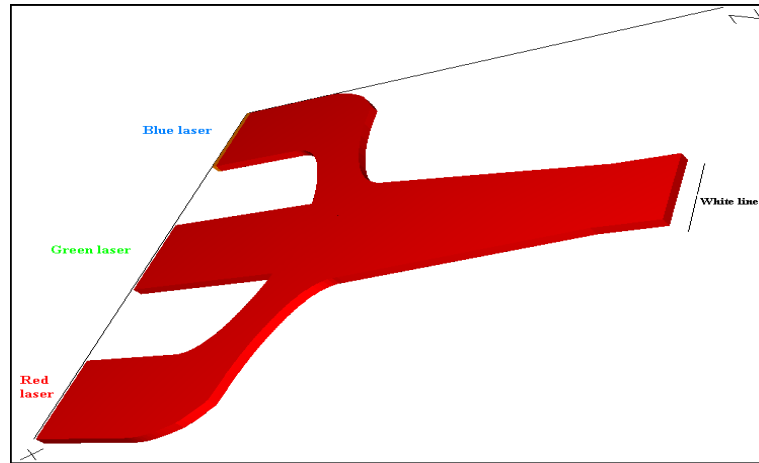


Figure 8.13: Alternative design for the waveguide combiner. Some calculation is required to find the optimum length for each section. The waveguide is flexible and can be bent or twisted if required.

In this design just one of the rows of the emitter is used and 50% of laser power is wasted which reduces the efficiency of the system. This loss of power can be tolerated provided the efficiency of the other parts of the system is high but it is risky as the waveguide absorbs light, particularly in the blue (for example Optical interlinks quoted the material absorption of their flexible waveguide to be 2-3 dB/cm at the time this research was performed in 2009). As shown in Figure 8.13, each laser beam will be coupled into a waveguide and they will be combined together by propagating inside the waveguides. However, the waveguide must be designed carefully for optimising the crossing and the taper angles. The use of the flexible slab waveguide requires one with low loss as the width and length of the waveguide must be large enough to couple three lasers. The idea of using a one-piece waveguide (as shown in Figure 8.13) to collect the laser beam from the NECSEL and red lasers and combine them together will not be particularly practical due to high light loss, manufacturing difficulties and more importantly, the design being very sensitive to misalignment at both the laser-flexible waveguide and flexible

waveguide-waveguide combiner. As they are one-piece, any dislocation, rotation or misalignment in one of the lasers will also affect coupling of the other lasers and the waveguide combiner. Moreover, just one row of the emitters of the NECSEL lasers can be used which loses half of the power for the green and the blue colours.

## 8.4 Summary of Methods

Several relevant methods that can be used for combining the laser beams chosen for the 3D auto stereoscopic system into the waveguide combiner were explained in section 8.3. In this section, the methods are summarised and compared with each other to find the best method to be used in the system.

Three approaches of free space, fibre combining, and waveguide combining were compared in section 8.2. Based on the explanation provided in this section and also the experiment results achieved by Koç University on using free space and microlens array for homogenizing, the fibre combining and waveguide combining method were chosen and will be designed and implemented in the system, which are explained in chapter 9.

One of the considerations connected with waveguide combiner application is the efficiency of fibre/waveguide coupling which fundamentally is related to the beam quality in terms of the beam quality factor  $M^2$ . In the table below, the requirements of beam quality for efficient coupling based on the laser beam parameter product (BPP) are listed. The BPP is defined for a fibre or waveguide as the product of the waveguide/fibre radius (which is half of the core diameter in millimetres) and the NA of the waveguide/fibre in milli-radians. The beam quality factor for the laser beam and fibre/waveguide are calculated using the equations below:

$$\frac{d}{2} \cdot NA = M^2 \frac{\lambda}{\pi} \text{ fiber}$$

$$w \cdot \theta = M^2 \frac{\lambda}{\pi} \text{ emitter}$$

Where  $d$  is the diameter of the fibre/waveguide,  $NA$  is the numerical aperture of the fibre/waveguide,  $w$  is the beam radius of the laser and  $\theta$  is the half angle divergence of the laser beam in mrad. In Table 8.3 the BPPs for the laser beams and individual emitters for each laser employed in the auto stereoscopic laser illuminated display (HELIUM3D) are listed.

Chapter 8: *Waveguides for Laser Beam Combining, Homogenisation, and Beam shaping for Display Backlighting*

Table 8.3: Beam propagation product of the emitters and lasers used in auto stereoscopic laser illuminated display project.

<b>Optical Component</b>	<b>Laser Half Angle Divergence (mrad)</b>	<b>Beam Diameter (mm)</b>	<b>BPP of the beam (mm-mrad)</b>
<b>NECSEL</b>	4.8	8 (row)	18.24
<b>One emitter</b>	4.8	0.080	0.192
<b>Red laser</b>	78.5 (Slow axis )	4	157
	9 (fast axis)	0.002	0.009
<b>Emitter of the red laser</b>	78.5 (Slow axis )	0.200	7.85
	9 (fast axis)	0.002	0.009

Based on the discussions of the different methods for coupling the laser beam into the waveguide combiner in this chapter, a summary of the advantages and disadvantages of each method is listed in Table 8.4.

The free space method is not applicable due to the increase of the cost, size and the complexity of the system. The fibre bundle method has not been tried due to the cost of the bundle and the amount of work required for the bundle-waveguide coupling which makes the method unsuitable for mass production (an off the shelf fibre bundle cost a few thousands pounds sterling). In addition, any misalignment and movement between the fibre bundle and the waveguide will cause coupling loss as the light will be coupled into the adjacent fibres which are not connected into the waveguide combiner.

There are various difficulties associated with the use of flexible slab waveguides. The thickness of the flexible waveguide should be considered. 5 slab waveguides are required (2 slab waveguides for green, 2 for blue, 1 for red laser) with a 20  $\mu\text{m}$  thick flexible waveguide that gives a total thickness of 100  $\mu\text{m}$  which is the same as the thickness of the waveguide combiner. However, it should be considered that coupling the emitter's output into a 20  $\mu\text{m}$  thick waveguide requires an extra microlens array for focusing the emitter's output. If the thickness is larger than 20  $\mu\text{m}$ , then the flexible waveguide cannot be coupled into the waveguide combiner as the thickness of the waveguides is larger than the thickness of the waveguide combiner.

*Chapter 8: Waveguides for Laser Beam Combining, Homogenisation, and Beam shaping for Display Backlighting*

The next methods for coupling the laser beam into the waveguide combiner are to use optical fibres. Fibres are flexible and the cost will be less than all other methods due to the low cost of the optical fibres.

For these reasons we investigated the use of fibre bundles and multi-mode fibres for laser beam-waveguide coupling.



Chapter 8: Waveguides for Laser Beam Combining, Homogenisation, and Beam shaping for Display Backlighting

Table 8.4: Comparison of various methods of laser beam coupling into the waveguide.

Method		
Free space with using optical lens	Advantages	The loss is less than the waveguide methods as we do not use any waveguide or fibre.
	Disadvantages	<ul style="list-style-type: none"> <li>– Optical system for focusing the laser beam.</li> <li>– Optical elements (mirrors or prism to bring the focused laser beam close together).</li> <li>– Very sensitive to misalignment.</li> <li>– The cost of the system is high due to the required specific optical elements to be custom made.</li> </ul>
	Comment	This method is not practical due to the difficulty of bringing three laser beams close together. In fact, using free space for combining and homogenizing will cost less and will be easier to align compared to using a waveguide for homogenisation. The light will be coupled in a 100 $\mu\text{m}$ thick waveguide so it is not reliable as any shaking or shock can decouple the lasers.
Fibre ribbon	Advantages	<ul style="list-style-type: none"> <li>– Laser can be separated from the rest of the system.</li> <li>– Just one micro-lens array is required for the coupling.</li> <li>– It is very rigid and so is a reliable system.</li> <li>– Easy to couple into the waveguide using a standard MT connector.</li> <li>– Low loss due to using standard fibres in the ribbon.</li> </ul>
	Disadvantages	<ul style="list-style-type: none"> <li>– Fibre ribbon requires a specific pitch which increases the cost of the system. A ribbon with 328 <math>\mu\text{m}</math> pitch costs 8000 dollar.</li> <li>– The cost of the system due to the custom designed micro-lens array and fibre ribbon. A custom made microlens array cost 10000 dollar.</li> </ul>
	Comment	The main problem with this method is the suitable fibre ribbon and the micro-lens alignment for coupling the laser into the ribbon. It is an efficient and safe method.
Multi-mode fibre	Advantages	<ul style="list-style-type: none"> <li>– Laser can be separated from the rest of the system.</li> <li>– It is a rigid and hence a reliable system.</li> <li>– Easy to couple into the waveguide using a standard MT connector.</li> </ul>
	Disadvantages	<ul style="list-style-type: none"> <li>– Optical elements required to couple the laser into a multi-mode fibre.</li> <li>– Sensitive to misalignment at the laser coupling into the fibre.</li> <li>Loss will occur in the fibre coupling process.</li> </ul>
	Comment	The fibre coupling and its efficiency are the main concerns.
Fibre bundle	Advantages	– Light can be carried away from the laser housing with the shape/position of the emitters retained.
	Disadvantages	<ul style="list-style-type: none"> <li>– Fibre bundle are very expensive (8000 dollar for a conventional bundle).</li> <li>– Very many fibres to be aligned, arranged, and be coupled into the waveguide.</li> </ul>
	Comment	A large number of the fibres (1896 fibres) must be aligned and attached into the waveguide. The system will be fragile as any change in the bundle position or any misalignment will cause loss.
flexible waveguide	Advantages	– The system will have all the advantages of the fibre ribbon.
	Disadvantages	<ul style="list-style-type: none"> <li>– The system will be lossy due to the bend and material absorption (3 dB/cm in blue). Also a tapering must be applied which increase the optical loss.</li> <li>– The cost of the system is high due to the cost of the material and manufacturing.</li> </ul>
	Comment	Coupling the laser light into the flexible waveguides and the reliability of the system is much less comparing to the other waveguide methods such as using multimode fibres.

## 8.5 Options for the Waveguide Combiner

After coupling the three laser beams into the waveguide, their outputs must be combined and homogenised to achieve a uniform white column of light. The waveguide combiner has to mix the three wavelengths (colours) together to achieve a uniform output. There are different options to be considered that are explained below:

### 8.5.1 Slab Waveguide:

The first option is a slab waveguide with an output of 10 mm (it can be varied dependent on the dimensions of the LCoS modulation device). The thickness of the waveguide determines the width of the output line, which is equal or less than 100  $\mu\text{m}$ .

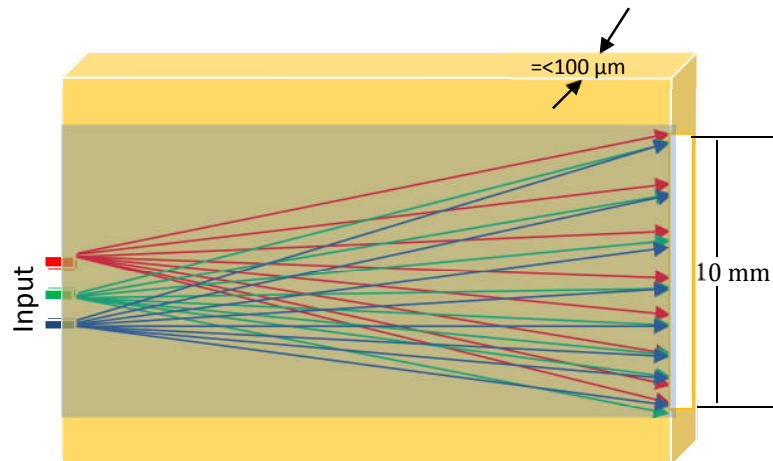


Figure 8.14: A schematic diagram from a slab waveguide without diffraction sites in which three lasers are combined by propagating inside the waveguide.

The thickness depends on the material and the waveguide fabrication method. If we use polymer the maximum possible thickness is 70  $\mu\text{m}$  due to manufacturing problems (multilayer waveguides can reach a suitable thickness but there is a concern about the adhesion of the different layers). Off-the-shelf 100  $\mu\text{m}$  thickness glass sheets are available [8.28]. In the simple design shown in Figure 8.14, each laser beam propagates inside the waveguide and is mixed with other lasers to provide a uniform line at the output. It is a simple design to manufacture but the length of the waveguide needs to be calculated carefully to ensure that the lasers are mixed and their outputs homogenised. It might be necessary to allow the beam to propagate and reflect side to side several times by increasing the length of the waveguide. The disadvantage of this is that increasing the length of the waveguide is not desirable due to the absorption loss of the

## Chapter 8: Waveguides for Laser Beam Combining, Homogenisation, and Beam shaping for Display Backlighting

waveguide material. Any scattering will cause more colour mixing (and exciting more modes) but will increase the loss (due to the material absorption as the beam propagates more inside the waveguide and also some of the beam can miss the total internal reflection condition and escape from the waveguide).

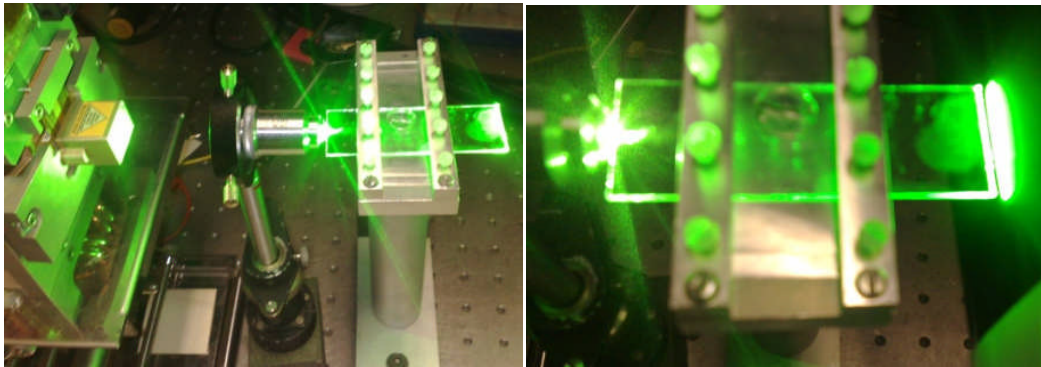


Figure 8.15: Experimental configuration to determine the performance of the glass slab waveguide. The 3 W green laser was focused on the waveguide facet using a microscope objective lens. The waveguide is 300  $\mu\text{m}$  thick and 10 mm wide.

To increase the scattering, the sidewalls can be made to have rough surfaces. In this case, the light will scatter in a Lambertian profile and the mixing will be more effective. However, there is also the problem of scattering out of the waveguide resulting in loss.

### 8.5.2 Channel Waveguides

Another design considered was to guide the laser beams onto an array of waveguides and to mix them together at the end of the waveguide assembly (Figure 8.16). The advantage of this method is that we have more control of the power of the laser inside the waveguide as we guide the light everywhere required inside the waveguide; however, we need to consider that the light is travelling a longer distance which raises absorption loss issues (about 2-3 dB/cm). Figure 8.16 shows two schematic designs which are different at the input of the waveguide. In both designs the optical power from the lasers is coupled into the waveguides and the waveguides mix the colours by crossing each other and deliver the laser beam at the end.

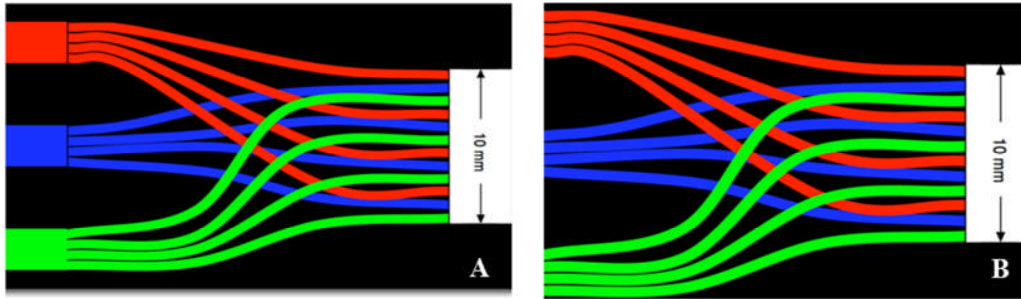


Figure 8.16: Schematic design of the waveguide combiner. Each emitter is coupled into one waveguide and the waveguides rearrange to provide a mixed output.

Designing, manufacturing, laser coupling, and the efficiency of a combiner such as Figure 8.16, is considerably more difficult than a slab waveguide while there is no significant advantage. Any bend or cross section causes optical loss in the waveguide. The manufacturing will limit the length and the thickness of the waveguide. There would be a problem of multi-spot formation at the waveguide output if another slab shaped part or diffuser is not designed at the end section of the waveguide combiner (white part in Figure 8.16). It should be noted that the end of the waveguide is to be imaged onto the LCoS device. In Figure 8.16 part A, the input can be single fibre or fibre ribbon and in part B the input is from fibre ribbons where each emitter is coupled into one waveguide. In both A and B only 4 waveguides are shown for each colour for the purposes of clarity but in practice there will be 24 or 48 waveguides.

## 8.6 Summary and Conclusion of the Options for Laser–Waveguide Coupling and Waveguide Combiner:

Based on the explanation of the different methods and approaches in section 8.4, using a multimode optical fibre for each laser (section 8.3.2.2) and using several multimode fibres together for each laser (section 8.3.2.4) appears to be the most suitable method for the laser-waveguide coupling. Fibre optics can be used in the form of; a fibre ribbon, a multi-mode fibre for each colour or one multi-mode input to several other multimode fibre outputs. For waveguides, the slab waveguide with scattering surfaces is the most relevant, efficient and cost-effective method. In Chapter 9, the design and the results of the experiments for each method is explained.

## **8.7 Polymer Micro-lens Array Material Aging Characteristics**

### **8.7.1 Introduction**

One of the most important concerns in this system is the stability and thermal tolerance of the materials which are exposed to high-power lasers. The transparency of the material from which the components are made might become degraded and the coatings and attaching materials such as polymer glue can be damaged. In some cases, impurities or any dust can absorb extra power and cause local damage to the surface. The power of each laser in the HELIUM3D system is 3 W and this power is focused down to a linewidth of one hundred microns and the combined focused beam from the red, green and blue lasers can attain the optical power density of  $9 \times 10^6$  W/m<sup>2</sup> ( $\frac{9 \text{ W}}{100 \times 10^{-6} \times 10 \times 10^{-3} \text{ m}^2}$ ). High laser power densities are not just used in the HELIUM3D system but also occur in other laser projection display systems. The materials used must be stable with this optical power density with no expansion or degradation taking place. The materials should be tested for the short-term and long-term effects.

Polymer and glass materials will be used for microlens arrays and waveguides and both must be tested before being used to manufacture components. Unfortunately, most of the companies for example Optical Interlinks, Microsharp, Exxelis and Dow Corning, who make waveguides from polymer do not have data sheets or experimental results for absorption of their material in the visible range of the spectrum; this is particularly important for blue wavelengths. This is understandable as this is a new area of development, however, this information is necessary and cannot be ignored as it is crucial in high power intensity environments. Some transmission stability and surface scattering experiments were carried out at UCL on PMMA (Poly methyl methacrylate) polymer material supplied from Microsharp that is suitable for micro-lens and superlens screen applications. Waveguides might also be made out of this material. The experiments described in this section clarify the effect of a photo-thermal mechanism due to vibration and rotational excitation of chromophores inside the polymer that affects the transmittance of the material and are based on the change of the surface profile and transmission coefficient of the material due to the exposure of high power density laser beam. Scanning by atomic force microscopy (AFM) to find the surface profile of the polymer and transmission

Chapter 8: Waveguides for Laser Beam Combining, Homogenisation, and Beam shaping for Display Backlighting

coefficient measurement using a spectrum analyser were used to test the material and the results are presented and discussed below.

The sample is made of three layers as shown in Figure 8.17. Microlens arrays were made the same as Figure 8.17 and the same PMMA material is used for the waveguide. A layer of PMMA material with a special formula confidential to Microsharp Company is glued to a Plexiglas® layer (which is PMMA with a different formula to Layer 1). Plexiglas® is an extruded PMMA product that has been developed for applications with the highest demands on optical and surface quality. In general, PMMA and Plexiglass are well known materials [8.29] and their transmission spectra, heat properties, and other physical and chemical properties have been investigated before[8.22;30]. However, the microlens fabricated by these materials contains a layer of adhesive. The three layers are explained in Figure 8.17 and we try to find if this assembly degraded due to the high intensity laser illumination.

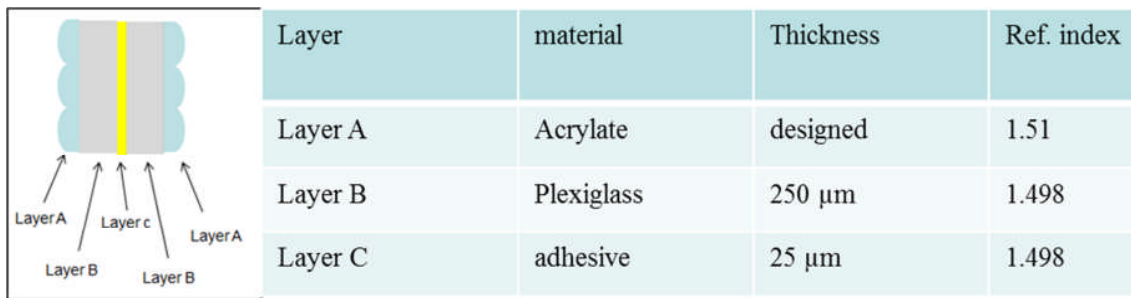
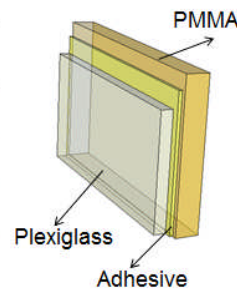


Figure 8.17: Schematic diagram of the sample made for the experiments.

The sample used for the test was made by Microsharp and was in three layers. Table 8.5 shows the materials used for the sample. The materials are exactly the same as the microlens material but in a plane cube shape. In this section, we refer to Plexiglas® as the substrate.

Table 8.5: The properties of the material used in the sample made by Microsharp

Layer	Thickness (μm)	Material	Refractive index
Layer 1	4000 ± 10	PMMA	1.51 ± 0.01
Layer 2	50 ± 5	Adhesive	1.49 ± 0.02
Layer 3	250 ± 10	Plexiglass	1.49 ± 0.01



Chapter 8: *Waveguides for Laser Beam Combining, Homogenisation, and Beam shaping for Display Backlighting*

Before exposure to the laser, the sample was scanned by AFM (Atomic Force Microscopy) to measure the surface for roughness and measured using a monochromator to find the optical transmission. The sample then was exposed for 25 minutes to a 532 nm 3.5 W NECSEL laser beam directly on to the polymer side; this gave a power density of  $0.7 \times 10^7 \text{ W/m}^2$  at the polymer surface. There was no heat sink or fan around the sample and it was in free air having a temperature of  $23.7^\circ\text{C}$  and humidity of 48%. The sample was scanned by AFM before and after exposure with the laser to investigate any changes to the surface.

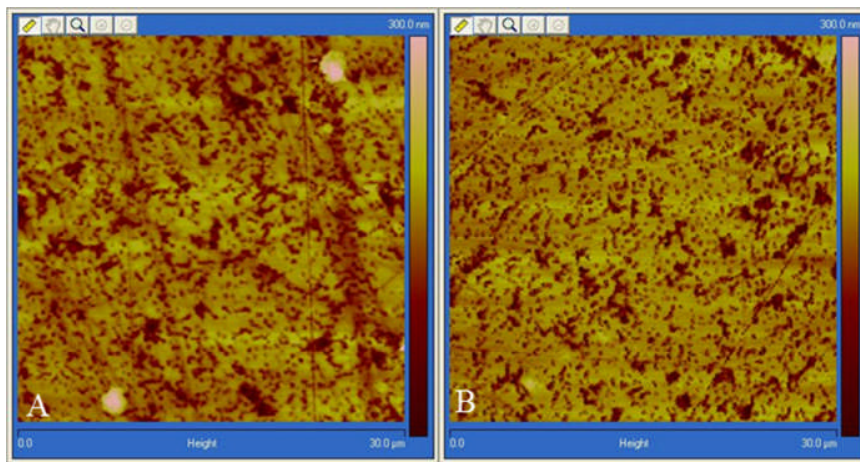


Figure 8.18: Surface profile of the substrate under the AFM (A) before exposure and (B) after exposure to the laser.

Figure 8.18 and Figure 8.20 show the roughness profile of the substrate and the polymer side respectively provided by AFM. No change was detected by AFM or optical microscopy on the substrate or polymer side after exposing the sample. Figure 8.19 shows a typical roughness profile of the substrate.

Chapter 8: *Waveguides for Laser Beam Combining, Homogenisation, and Beam shaping for Display Backlighting*

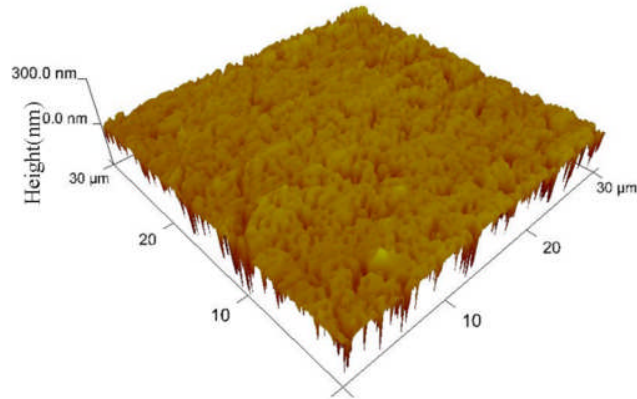


Figure 8.19: The 3D profile from the surface roughness of the substrate after exposure to the laser. The roughness value is the height of the surface roughness.

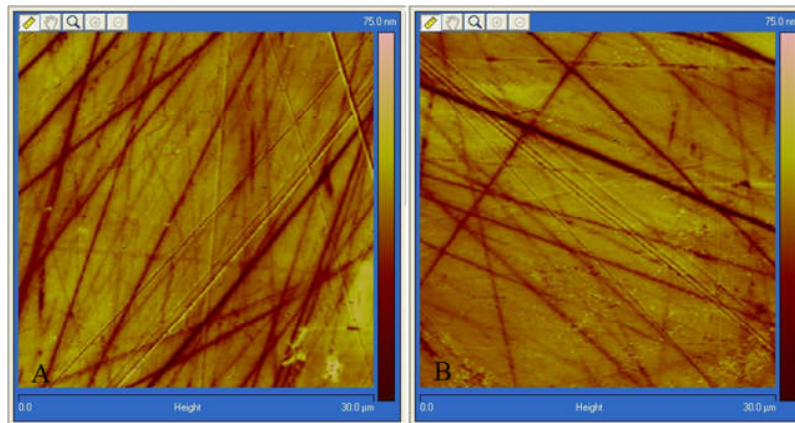


Figure 8.20: The roughness profile of the polymer under AFM (A) before and (B) after (B) exposure to the laser

Figure 8.21 is an AFM roughness measurement of the polymer side.

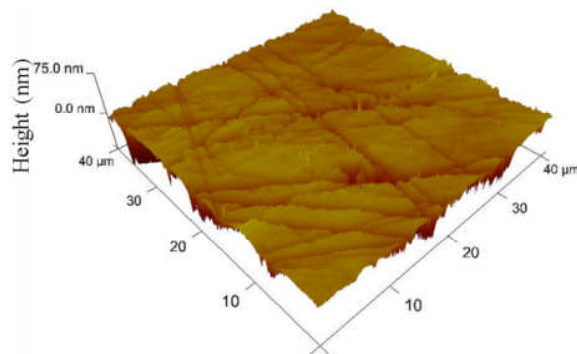


Figure 8.21: 3D profile sample of the polymer surface after exposure to the laser. The roughness value is the height of the surface roughness



Chapter 8: Waveguides for Laser Beam Combining, Homogenisation, and Beam shaping for Display Backlighting

The surface observed under an optical microscope shows no significant change in the surface colour or roughness. There was also no sign of cracking, burnt spots or melted points. Figure 8.22 and Figure 8.23 compare the statistical parameters of the surface roughness before and after exposure to the laser beam in order to show any differences in the parameters before and after the exposure.

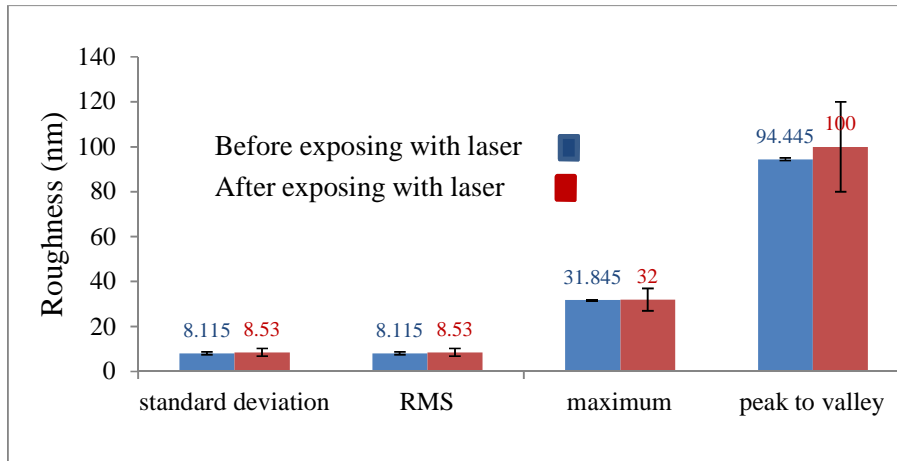


Figure 8.22: Comparison of the roughness for the polymer side before and after exposure to the laser.

As indicated in Figure 8.22 and Figure 8.23, the roughness components of standard deviation, RMS, maximum and peak-to-valley are substantially the same before and after exposure to the laser.

On the polymer side of the sample there was no obvious change and the roughness data Figure 8.23, indicates that the surface properties of the sample have not been affected by the laser.

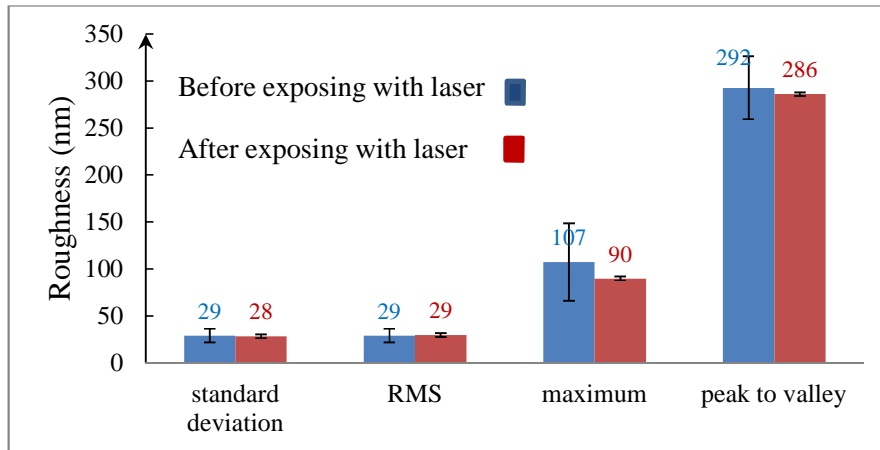


Figure 8.23: Comparison of the roughness for the substrate side before and after exposure to the laser.

### 8.7.2 Spectroscopy:

In addition to the surface roughness, the effect of exposure to high-power laser illumination on the spectral characteristics of the light absorption of the material used for the micro-lens was also measured in the experiment described below. As shown in Figure 8.24 a white light source illuminates the sample and the spectrum is analysed with a monochromator after passing the light through the sample and an iris is used to ensure that only light passing through the sample area is measured. The monochromator functions by rotating a grating to scan the spectrum and detect the power at each wavelength. A slit with diameter of 1 mm was used in the monochromator which gives us 1 nm resolution.

Firstly, the spectrum was analysed to find the power at each wavelength without any sample in the way. The sample was placed into the experimental configuration and its spectrum scanned. The sample was then removed and exposed to the laser. It was scanned again by the monochromator in order to determine the new transmission spectrum. At each particular wavelength, the power with the sample was divided by the power without the sample in order to determine the absorption.

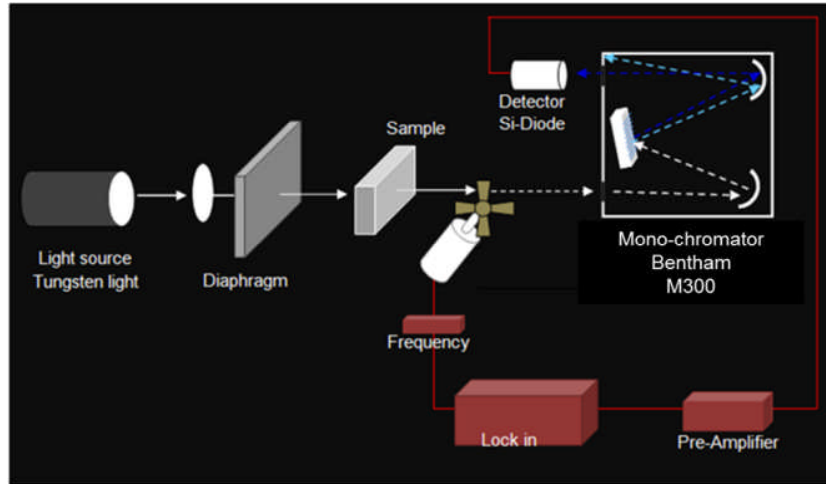


Figure 8.24: Schematic diagram of the experiment using the monochromator to measure the absorption of the material at different wavelengths.

All the measurements were applied to the raw sample, which is the sample before exposure, and the exposed sample which is the sample after the exposure. The region between 380 and 700 nanometres was covered and the results are shown in Figure 8.25 and Figure 8.26

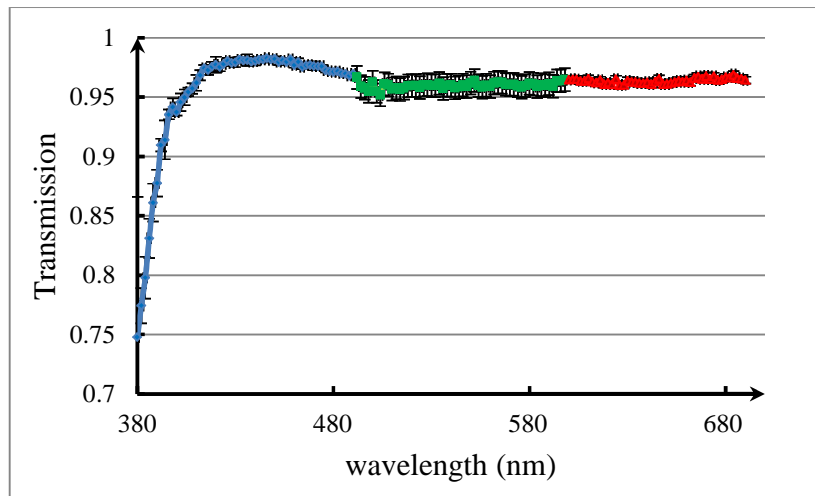


Figure 8.25: Transmission of the sample at different wavelengths before exposure to the laser.

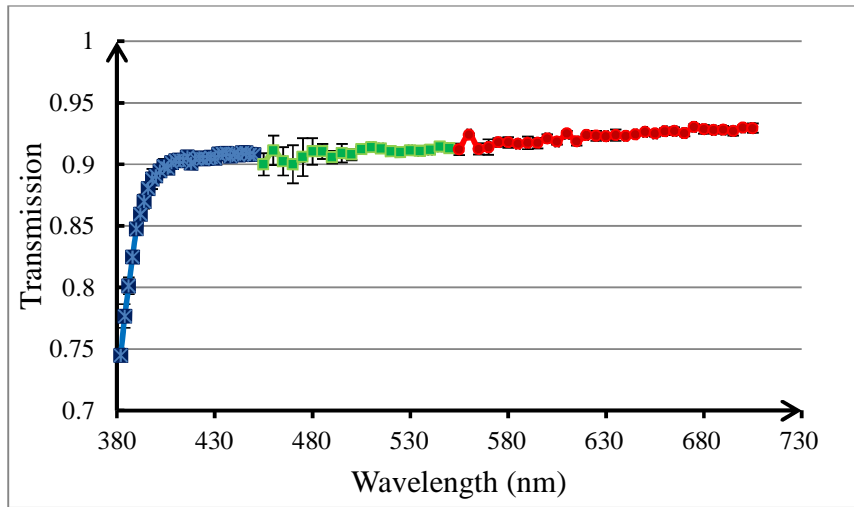


Figure 8.26: Transmission of the sample at the different wavelengths after exposure to the laser. As shown in Figure 8.25 and Figure 8.26, the transmittance has been degraded after the exposure. The difference on the transmittance is shown in Figure 8.27.

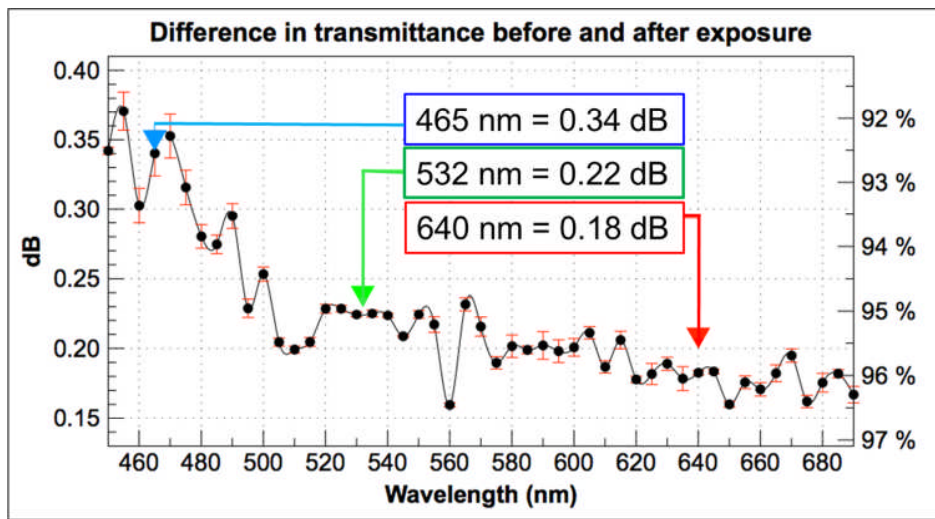


Figure 8.27: Difference in transmittance before and after the sample was exposed to the 3 W laser. The experiments show that there is degradation due to the exposure. This degradation could be due to one layer or to all of them and it could be a one-off effect where the material had reached a stable condition or it could be part of an on going process. The other material to be considered for the waveguide and microlens array is glass which is available in various thicknesses and with different properties and has been used for a long time.

## **8.8 Conclusions:**

In this chapter, a new means of laser beam combining, beam homogenizing and beam shaping in display application was introduced. Our idea was to design a system to use multimode waveguides to combine, homogenise and shape the output of three red, green, and blue lasers for a 3D autostereoscopic display system, called HELIUM3D, and at the same time reduce the speckle contrast, which is a major problem in laser illuminated displays. A newly developed multi-emitter laser, called NECSEL, was chosen as the light source.

Several different designs for using optical waveguides in the light engine of the HELIUM3D system were considered for the first time and compared based on cost, safety, optical loss and efficiency.

The comparison was carried out on two sections 1: To couple the laser light from the NECSEL into a 100  $\mu\text{m}$  thick waveguide that acts as the colour combiner and colour homogeniser 2: The design of the waveguide combiner.

For section 1, two methods of using multimode optical fibre for each laser and using a bundle of fibres which are glued in one end were chosen to couple the laser light into the waveguide combiner. For section 2, a slab waveguide was chosen to be the best option for the waveguide combiner.

An investigation of the stability and aging properties of a newly developed polymer (by Micro Sharp) was carried out. The material was to be used for micro lens manufacturing and waveguide combiners. The effect of a 3 W laser on the material was measured by measuring the change in the surface profile and transmission properties of the material before and after exposure. The results showed no change in the surface profile after exposing the sample for two and half hours. However, in the transmission graph there was a shift in the transmission spectrum. We detected a difference of 0.18 dB at 640 nm, 0.22 dB at 532 nm and 0.34 dB at 465 nm, which means there has been a degradation of the transmission in the material.

## References

- [8.1] Kishore V.Chellappan, Erdem Erden, and Hakan Urey, "Laser Based Display," *Applied Optics*, vol. 49, no. 25, p. f 79-f 98, Mar. 2010.
- [8.2] H.Baghsiahi, D.R.Selviah, E.Willman, Anibal Fernández, and Saly E.Day, " Beam Forming for a Laser Based Auto-stereoscopic Multi-Viewer Display," *SID Symposium Digest of Technical Papers*, vol. 42, no. 1, pp. 702-705, June 2011.
- [8.3] Kishore V.Chellappan, Erdem Erden, and Hakan Urey, "Lasr Based Display," *Applied Optics*, vol. 49, no. 25, p. f 79-f 98, Mar. 2010.
- [8.4] SIFAM Fiber Optics, "Multimode power combiner," [http://www.sifamfo.com/data\\_pdfs/multimode\\_power\\_combiner.pdf](http://www.sifamfo.com/data_pdfs/multimode_power_combiner.pdf), April 2008.
- [8.5] Art Berman, "HDI develops 3D LCOS laser projector," <http://displaydaily.com/2009/04/08/hdi-develops-3d-lcos-laser-projector/>, June 2009.
- [8.6] V. Jolivet, P. Bourdon, B. Bennai, L. Lombard, D. Goular, E. Pourtal, G. Canat, Y. Jaouen, B. Moreau, and O. Vasseur, "Beam Shaping of Single-Mode and Multimode Fiber Amplifier Arrays for Propagation Through Atmospheric Turbulence," *IEEE Journal of Selected Topics in Quantum Electronics*, vol. 15, no. 2, pp. 257-268, 2009.
- [8.7] N. Lichtenstein, Y. Manz, P. Mauron, A. Fily, B. Schmidt, J. Muller, S. Pawlik, B. Sverdlov, S. Weiss, A. Thies, and C. Harder, "High-brightness 9xx and 14xx single-mode emitter array laser bars," *High-Power Diode Laser Technology and Applications III*, vol. 5711, pp. 101-108, 2005.
- [8.8] A. von Pfeil and T. von Freyhold, "Beam shaping of broad area diode lasers: Principles and benefits," *Test and Measurement Applications of Optoelectronic Devices*, vol. 4648, pp. 82-90, 2002.
- [8.9] Rüdiger Paschotta, "Beam Parameter Product," Laser Physics and Technology, [http://www.rp-photonics.com/beam\\_parameter\\_product.html](http://www.rp-photonics.com/beam_parameter_product.html), February 2010.
- [8.10] P. Poon and D. R. Selviah, "Astigmatism in ellipsoidal and spherical photoresist microlenses used at oblique incidence," *IOP Second International Conference on Microlens Arrays*, pp. 65-71, 1995.

Chapter 8: *Waveguides for Laser Beam Combining, Homogenisation, and Beam shaping for Display Backlighting*

- [8.11] A. F. Kurtz, "Design of a laser printer using a laser array and beam homogenizer," *Laser Beam Shaping*, vol. 4095, pp. 147-153, 2000.
- [8.12] T. Sales, "Structured microlens arrays for beam shaping," *Optical engineering*, vol. 42, pp. 3084-3085, 2003.
- [8.13] K. J. W. Reinhard Voelkel, "Laser Beam Homogenizing: Limitations and Constraints," *SPIE Europe, Glasgow, Scotland, UK*, vol. 5456 Sept. 2008.
- [8.14] J. Masson, R. Bitterli, W. Noell, N. F. de Rooij, A. Bich, K. Weible, and R. Voelkel, "Dynamically deformable micromirror array for defined laser beam shaping and homogenizing," *IEEE, Optical MEMS and Nanophotonics (OMN)*, pp. 3-4, 2011.
- [8.15] Hadi Baghsiahi, David Selviah, Eero Willman, Anibal Fernández, and Sally Day, "Beam Forming for a Laser Based Auto-stereoscopic Multi-Viewer Display," *SID Symposium Digest of Technical Papers.*, vol. 42, no. 1, pp. 702-705, June 2010.
- [8.16] A. Poudoulec, J. Caulet, C. Vaudry, and N. Devoldere, "Fibre ribbon positioning in silicon dry etched U-grooves for collective optoelectronic hybridization," *Ecio'99: 9Th European Conference on Integrated Optics and Technical Exhibition*, pp. 417-420, 1999.
- [8.17] M. Hoffmann, S. Dickhut, and E. Voges, "Silicon fibre ribbon pigtailed with rhombus-shaped fibre channels and integrated photodiodes," *3Rd International Conference on Micro Opto Electro Mechanical Systems (Optical MEMS), Proceedings*, pp. 206-209, 1999.
- [8.18] T. Coosemans, A. Van Hove, R. Bockstaele, K. Vandeputte, L. Vanwassenhove, B. Dhoedt, R. Baets, P. Van Daele, and J. Van Koetsem, "MT (TM)-compatible connectorisation of VCSEL and RCLED arrays to plastic optical fibre ribbon for low cost parallel datalinks," *Materials Science in Semiconductor Processing*, vol. 3, no. 5-6, pp. 475-480, 2000.
- [8.19] F. Zhang, N. Collings, W. A. Crossland, T. D. Wilkinson, P. L. Neo, M. R. Taghizadeh, and A. Waddie, "Free-space optical fibre ribbon switch for use in storage area networks," *Iee Proceedings-Optoelectronics*, vol. 152, no. 6, pp. 285-291, 2005.
- [8.20] F. Zhang, N. Collings, and B. Crossland, "Fibre-ribbon switching for application in core-edge storage area networks," *ICTON 2006: 8th International Conference on Transparent Optical Networks, Vol 4, Proceedings*, pp. 48-51, 2006.
- [8.21] I. Papakonstantinou, D. R. Selviah, and F. A. Fernandez, "Multimode polymer bent tapered waveguide modeling," *Conference Proceedings - Lasers and Electro-Optics Society Annual Meeting-LEOS*, vol. 2, pp. 983-984, 2004.
- [8.22] H. G. Treusch, K. Du, M. Baumann, V. Sturm, B. Ehlers, and P. Loosen, "Fiber-coupling technique for high-power diode laser arrays," *Proc. SPIE, Condeferne of Laser Resonators*, vol. 3267, pp. 98-106, 1998.

Chapter 8: *Waveguides for Laser Beam Combining, Homogenisation, and Beam shaping for Display Backlighting*

- [8.23] Y. Liao, K. Du, S. Falter, J. Zhang, M. Quade, P. Loosen, and R. Poprawe, "Highly efficient diode-stack, end-pumped Nd: YAG slab laser with symmetrized beam quality," *Applied Optics*, vol. 36, no. 24, pp. 5872-5875, 1997.
- [8.24] P. Wang, "Beam-shaping optics deliver high-power beams," *Laser Focus World*, vol. 37, no. 12, pp. 115-120, 2001.
- [8.25] K. Du, Y. Liao, and P. Loosen, "Nd: YAG slab laser end-pumped by laser-diode stacks and its beam shaping," *Optics communications*, vol. 140, no. 1-3, pp. 53-56, 1997.
- [8.26] K. Du, M. Baumann, B. Ehlers, H. G. Treusch, and P. Loosen, "Fiber-coupling technique with micro step-mirrors for high-power diode laser bars," *Advanced Solid State Lasers*, 1997.
- [8.27] ELECTRO OPTICAL COMPONENTS, "Fiber Combiner," [http://www.eoc-inc.com/imm/imm\\_fiber\\_combiner\\_testing.htm](http://www.eoc-inc.com/imm/imm_fiber_combiner_testing.htm), Aug. 2010.
- [8.28] TED PELLA Inc., "Microscope Coverslip Technical Data," [http://www.tedpella.com/histo\\_html/coverslip-info.htm](http://www.tedpella.com/histo_html/coverslip-info.htm), Aug. 2010.
- [8.29] P. Duelli and R. Wehner, "The spectral sensitivity of polarized light orientation in *Cataglyphis bicolor* (Formicidae, Hymenoptera)," *Journal of Comparative Physiology A: Neuroethology, Sensory, Neural, and Behavioral Physiology*, vol. 86, no. 1, pp. 37-53, 1973.
- [8.30] Koji Minami, "Optical plastic," Zeon Corporation ,Kawasaki, Japan, pp. 112-132, 2010.



## **Chapter 9: Design, Simulation, and Experimental Results for a Laser Beam Combining, homogenising and Shaping Waveguide**

### **9.1 Introduction**

In this chapter, the design of a light engine using optical waveguides for a High Efficiency Laser-Based Multi-user Multi-modal 3D Display (HELIUM3D) system is described, simulated, constructed and tested experimentally. Two designs using either optical fibre or a slab waveguide for colour combining and homogenisation are also presented.

In chapter 8, several designs for light engines using optical waveguides for a 3D autostereoscopic display system were considered and compared. Two methods, namely using a multimode optical fibre for each colour of red, green, and blue, and using several multimode fibres attached together at one end in a circular shape, were chosen to be incorporated into the High Efficiency Laser-Based Multi-user Multi-modal 3D Display (HELIUM3D) system. These two methods were chosen to couple the light from lasers into the waveguide combiner. A slab waveguide was chosen as the best option for laser beam combining and power homogenisation.

The optical design description is presented in two parts. In the first part, the components required to couple the lasers into a fibre or fibre ribbon are described. In the second part the design of a waveguide combiner is described. This chapter starts with the design of a focusing lens system to couple NECSEL multiemitter laser beams into an optical fibre. The results of the simulation and experiment are explained and then the fibre is implemented in the HELIUM3D system. Then, a simulation of the waveguide combiner and the experimental results of using a slab waveguide are presented.

#### **9.1.1 Design of a lens system to couple the beams from NECSEL multiemitter lasers into an Optical Multimode Fibre**

Two of the options for colour combining and homogenising are to use a fibre combiner or to use a waveguide. In both methods, the laser light needs to be coupled into a single multimode optical fibre. The size of the output beam from each NECSEL laser is about 3 mm × 8 mm and the

multimode fibre has a diameter of 100  $\mu\text{m}$  and an  $\text{NA} = 0.22$ . Therefore, the aim of the designs in this section, is to focus each laser beam to a spot with a maximum width of 100  $\mu\text{m}$ , while ensuring that the divergence is less than the light acceptance cone of the fibre.

Commercially available Zemax software is used for either sequential or non-sequential ray tracing simulation. In sequential ray tracing, light travels from one surface to another in a pre-defined order with the surfaces being numbered sequentially. All of the surfaces are located between the object (which is the source) and the image (which is the final result). In sequential ray tracing the rays start from the surface 0 (object), and are then traced to surface 1, then surface 2 and so on; no ray is traced from surface 3 to surface 2. Therefore, the rays do not reflect back and each ray strikes a surface just once. The sequential method simplifies ray tracing but it is not applicable to every optical design, especially when there is a waveguide in the design as the rays might impinge on a surface several times. In non-sequential ray tracing there is no predefined path for any ray and rays are traced only along a physically realisable path until they intercept an object. A ray is traced and strikes any object in its path. The ray may reflect, refract, scatter or split after striking an object depending upon its structure. Non-sequential is more general than sequential ray tracing. Rays in this method may strike a group of objects in any order or may strike the same object repeatedly.

#### **9.1.1.1 Sequential Ray Tracing for Designing a Focusing Lens System**

For the first design, we used sequential ray tracing with a source comprising 12 point sources each having a half angle divergence of 4.8 mrad. Sequential ray tracing in Zemax can simulate a maximum of 12 sources. These sources simulate the NECSEL emitters. The wavelength of the beam was 532 nm (green NECSEL) and the positions of the emitters are shown in Figure 9.1. As discussed in Chapter 8, the beam quality of the laser must be improved in order to couple the laser beam into the fibre with 100  $\mu\text{m}$  core and  $\text{NA} = 0.22$ . To achieve a laser beam with a better beam quality a microlens array is used to decrease the divergence of the laser and increase the filling factor.

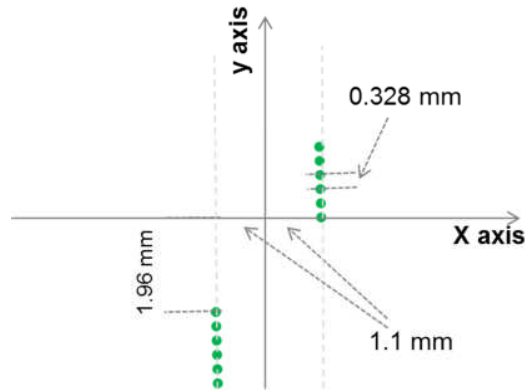


Figure 9.1: Position of the 12 sources for the sequential mode ray tracing simulation. 6 emitters from the centre of one of the rows and 6 emitters from the end of the other row were chosen.

Table 9.1 and Figure 9.2 show the design and the lens parameters which were used in the lens system simulation.

Table 9.1: System designed to focus the NECSEL beam into a small spot size. The spot radius is 5 microns. There is just one set of micro-lenses in this design and just one of the surfaces is aspherical.

Object type	Radius (mm)	Thickness (mm)	Semi-Diameter (mm)	Glass
Standard	Infinity	25.24	4.92	-
Lens let array	-20.60	10	4.92	-
Standard lens	30	5	5	BK7
Standard lens	-50	20	5	-
Standard lens	50	3	5	BK7
Standard lens	5.630	2	5	-
Standard lens	5	5	5	BK7
Standard lens	-5	3.77	5	-
Image	Infinity	-	5.528E-003	BK7

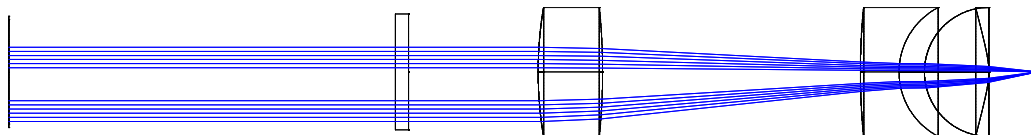


Figure 9.2: Optical design for focusing the NECSEL beam into a multimode fibre

Figure 9.3 shows the spot diagram for the designed system. The spot diagram shows how the optical power of the traced beams is distributed at the focusing point. In other words, it shows

Chapter 9: Design, Simulation, and Experimental Results for Laser Beam combining, homogenising, and shaping Waveguide

the size of the focusing spot. The results show that by using a microlens array and reducing the divergence angle we are able to reduce a spot size to 75  $\mu\text{m}$  diameter. This is the size of the beam determined from the Airy disk (the black circle on the diagram). The spot size cannot be smaller than the size of the Airy disk which is the smallest point to which a laser beam can be focused due to diffraction. About 84% of energy is confined in the Airy disk area and 91% within the outside diameter of the first ring of the Airy function[9.1;2]. The Airy disk of a lens system depends on the wavelength of the light, lens aperture and focal length. The focal lens of the system is the distance from the image space to the output aperture when a parallel beam is sent through the lens system.

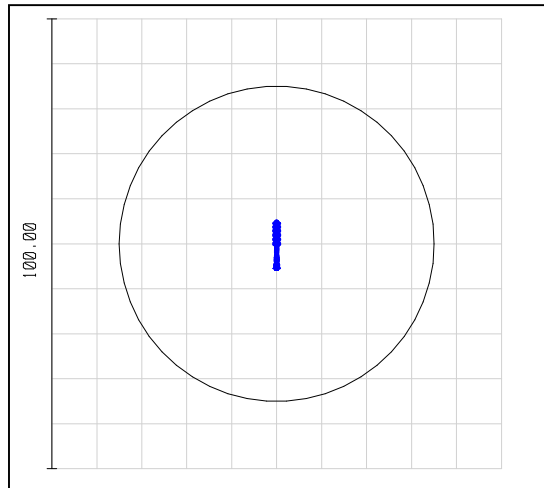


Figure 9.3: Final spot diagram and the size of the Airy disk of the design whose parameters are given in Table 9.1. The Airy disk radius is 35.04  $\mu\text{m}$ . the blue part in the middle of the circle is the focused NECSEL beam. The scale is in  $\mu\text{m}$ .

To calculate the fibre coupling efficiency with the microscope objective, ray tracing and beam propagation method (BPM) were used. Zemax has a tool called physical optics propagation (POP) which can be employed to find the amplitude and the phase of the wavefront at the end surface by tracing beams along the optical system. This information can be imported into BPM to calculate the efficiency of the coupling between the shaped beam and the waveguide. POP works in a way that Zemax stores the complex amplitude of the electric field at each point in a plane, while the beam propagates through the optical objects. The phase of these complex values determines the phase of the wavefront relative to a reference surface and the amplitude of the values can be used to determine the power of the beam. The fibre coupling efficiency was

Chapter 9: Design, Simulation, and Experimental Results for Laser Beam combining, homogenising, and shaping Waveguide

calculated first by Zemax and gave the results shown in Figure 9.4; this shows 73% coupling efficiency for coupling into a 100  $\mu\text{m}$  step index core multimode fibre with  $\text{NA} = 0.22$ .

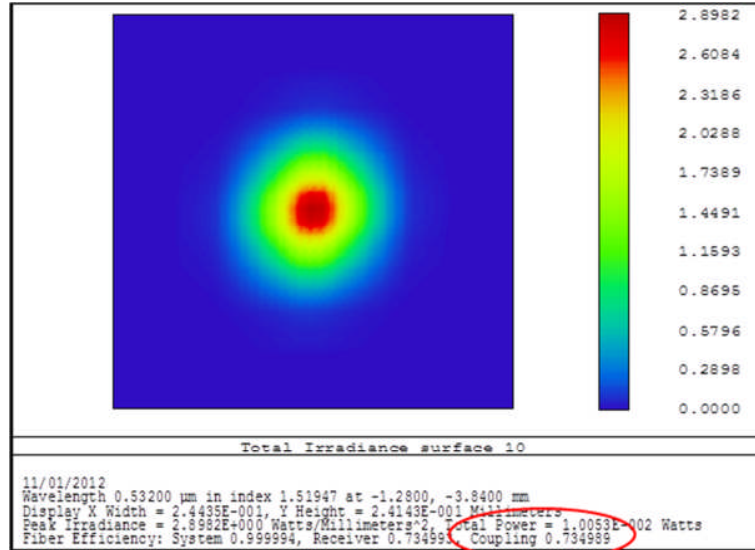


Figure 9.4: Amplitude of one of the emitters after propagating and focusing by the lens system. The calculated fibre coupling efficiency by ZEMAX is 73%.

The output of the ZEMAX simulation was also launched into a fibre and the coupling efficiency calculated using BPM method.

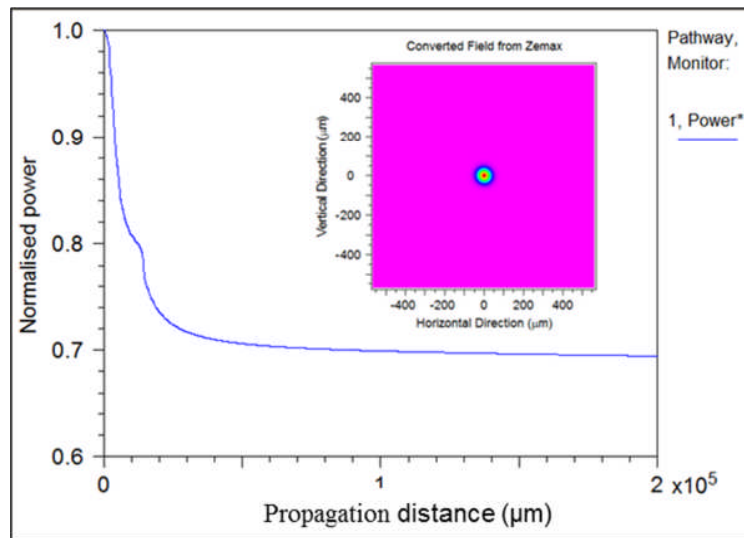


Figure 9.5: Calculating the fibre coupling efficiency using Beam PROP. The core diameter of the fibre is 100  $\mu\text{m}$  with  $\text{NA} = 0.22$

Figure 9.5 shows the simulation result and layout of the fibre. The graph shows how the input power is lost until it reaches a stable region and propagates through the fibre. The optical loss at the beginning of the fibre is due to the radiation mode excitation at its input. As can be seen from the blue plot, the efficiency is about 72 % which is in good agreement with the ZEMAX simulation.

### 9.1.1.2 The use of Non Sequential Ray Tracing for Designing a Focusing Lens System

There are some limitations in using sequential ray tracing in ZEMAX; for example the number of the sources (emitters) is limited to a maximum of 12. To obtain a more general and complete design for the fibre coupling system, the non-sequential (NS) ray tracing was applied and several designs were tested. There is no limit for emitter numbers in NS ray tracing. Figure 9.6 shows a design using a cylindrical lens to reduce the size of the beam in the slow-axis direction in which both NECSEL and red lasers have a wide beam. After the beam size is reduced to the size of the fast-axis direction (which is about 4 mm), spherical lenses are used to focus the beam into a 100  $\mu\text{m}$  diameter. A micro-lens array is used to collimate the laser beam.

Table 9.2: The properties of the lenses used in the design shown in Figure 9.6

Object type	Position (mm)	Front Radius (mm)	Back Radius (mm)	Thickness (mm)	Material
Source diode	0				
Rectangular volume	32	Infinity			BK7 (n=1.52)
Lens let array	32	Infinity	40		BK7
Toroidal lens	40	20	-20		BK7
Toroidal lens	50	-12	12		BK7
Standard lens	53	8	-8	2	BK7
Standard lens	57	-5	5	1	BK7
Standard lens	60	5	-5	1	BK7
Standard lens	63	-2.50	2.5	1	BK7
Standard lens	66	2	-2		BK7

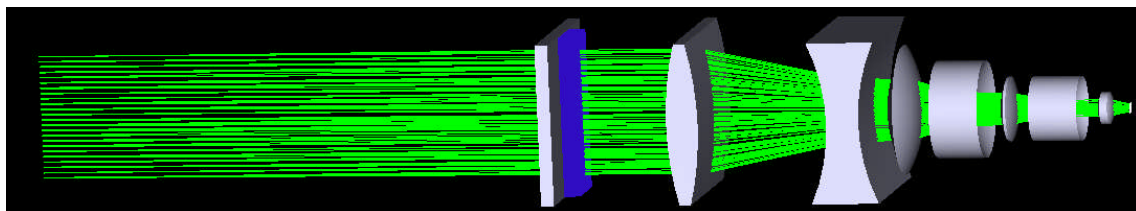


Figure 9.6: The design for focusing NECSEL laser beam into 100 microns diameter using cylindrical lenses. The size of the laser beam is reduced in one dimension (in the direction of the row in the NECSEL and in the slow axis direction for the red laser) using cylindrical lens and spherical lenses are used at the second stage to focus the light in both fast and slow axis.

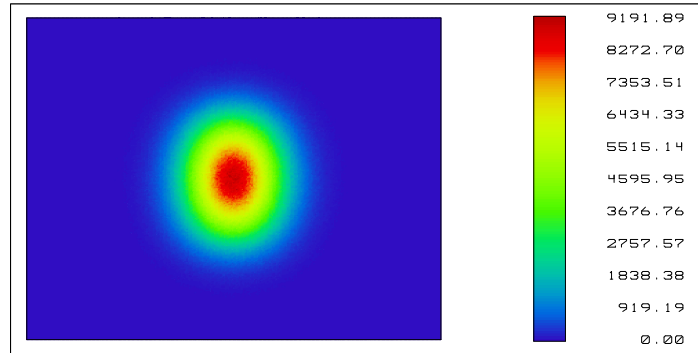


Figure 9.7: Spot size of the NECSEL beam after passing through the design shown in Figure 9.6. The beam is 8 mm × 3 mm at the input.

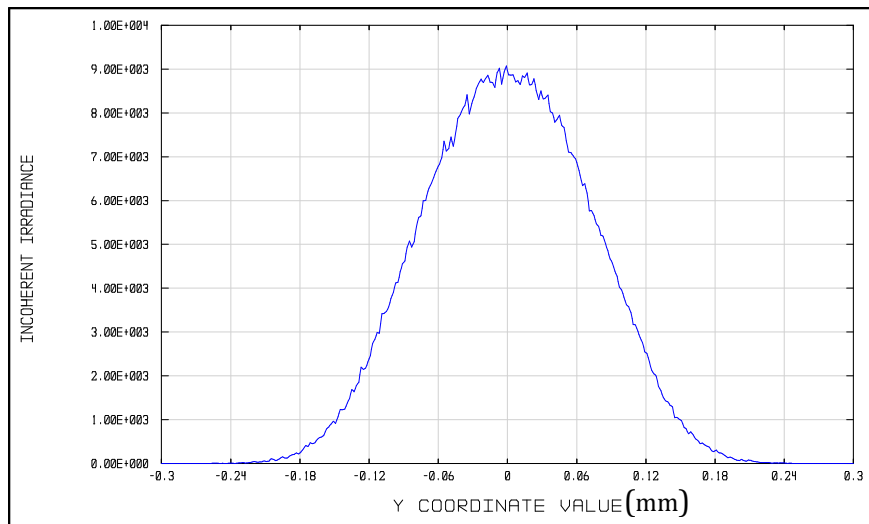


Figure 9.8: Size of the NECSEL beam at the detector (output) in the direction of the row of emitters. The width of the laser beam is 240 μm where the power drops to  $1/e^2$  of the maximum value.

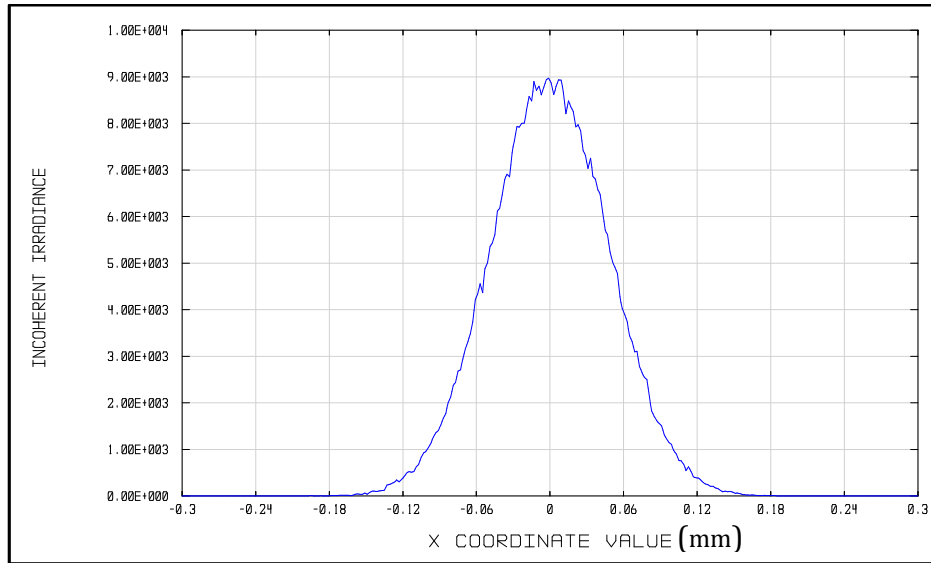


Figure 9.9: The size of the NECSEL beam at the detector in the normal direction to the row of emitters (fast axis). The width of the laser beam is 120  $\mu\text{m}$  where the power drops to  $1/e^2$  of the maximum value.

As shown in Figure 9.8 and Figure 9.9 the width of the laser has been reduced from 8 mm to 240  $\mu\text{m}$  in the slow axis and from 2.2 mm to 120  $\mu\text{m}$  in the fast axis. These results need to be improved to decrease the spot size of the beam and improve the fibre coupling efficiency. The maximum spot size must be 100  $\mu\text{m}$  and the divergence angle from the focusing point should be less than 25 degrees.

$$\text{fibre's numerical aperture} = 0.22$$

$$NA = n \times \sin(\theta) = 0.22$$

$$\theta = \text{Arcsin}(0.22) = 12.7 \text{ degrees}$$

Where  $n$  is the refractive index of the air and  $\theta$  is the half divergence angle. The point about this approach is that the lenses are designed specifically for this application (NECSEL lasers) and must be manufactured to order, which increases the cost of the system. Also, the lenses must be maintained accurately in position and a casing and lens holder must be designed and manufactured which adds to the cost of the system.

To avoid the cost of lens manufacturing, another idea of using off-the-shelf microscope objective lenses was considered. In this case the object is to locate an objective lens that is suitable for



Chapter 9: Design, Simulation, and Experimental Results for Laser Beam combining, homogenising, and shaping Waveguide

focusing the NECSEL and red lasers. The microscope objective requires collimated input beams so micro-lenses must be used to reduce the divergence of the beams before feeding into it.

To pursue the microscope objective approach for focusing the beam, different designs of microscope objective have been considered and simulated to achieve a small laser beam spot size (maximum 100  $\mu\text{m}$ ). The design below produces a spot size of 90  $\mu\text{m}$ .

Object type	Position (mm)	Front Radius (mm)	Back Radius (mm)	Thickness (mm)	Material	Refractive index
Source diode	0					
Rectangular volume	30			1	BK7	1.52
Lens let array	31	Infinity	-40	1	BK7	1.52
Rectangular volume	30			1	BK7	1.52
Lens let array	31	Infinity	-40	1	BK7	1.52
Standard lens	40	54.153	152.522	8.747	SK2	1.61
Standard lens	49	35.951	0.00	14.00	SH16	1.62
Standard lens	64	0.000	22.270	3.777	F5	1.60
Standard lens	89	-25.685	0.00	3.777	F5	1.60
Standard lens	92	0/	-36.980	10.834	SK16	1.62
Standard lens	104	196.417	-670	6.858	SK16	1.62
Standard lens	116	15/	-15	5.000	SK16	1.62

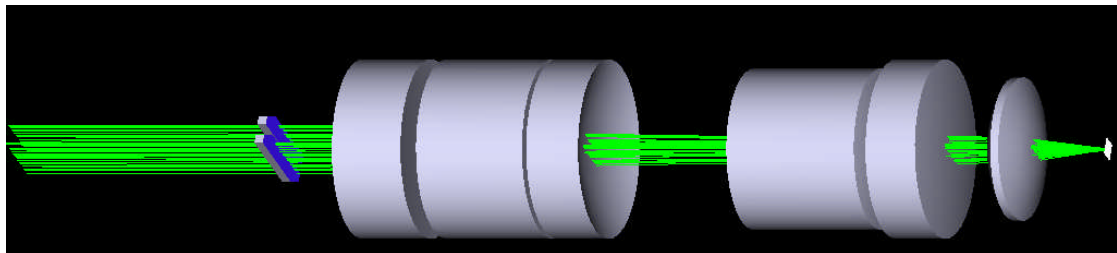


Figure 9.10: Microscope objective design used for focusing the laser beam into a small spot.

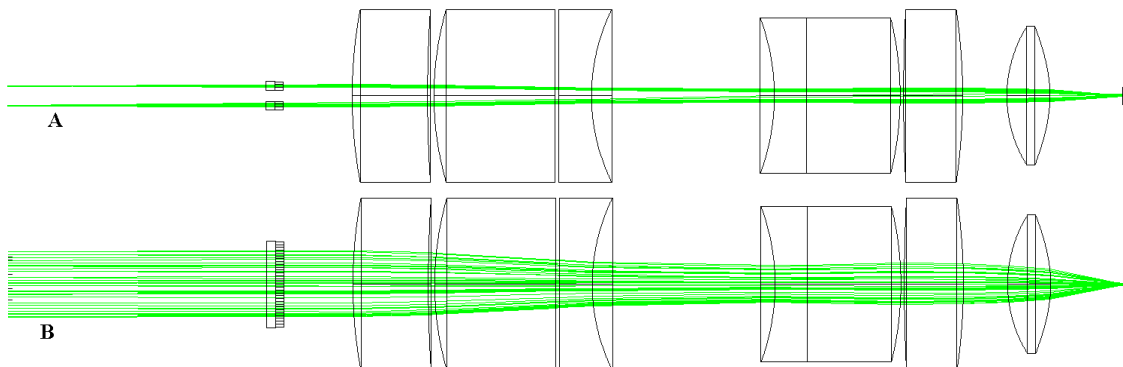


Figure 9.11: Side view (A) and top view (B) for the microscope objective design used for focusing the NECSEL into 100  $\mu\text{m}$  diameter.

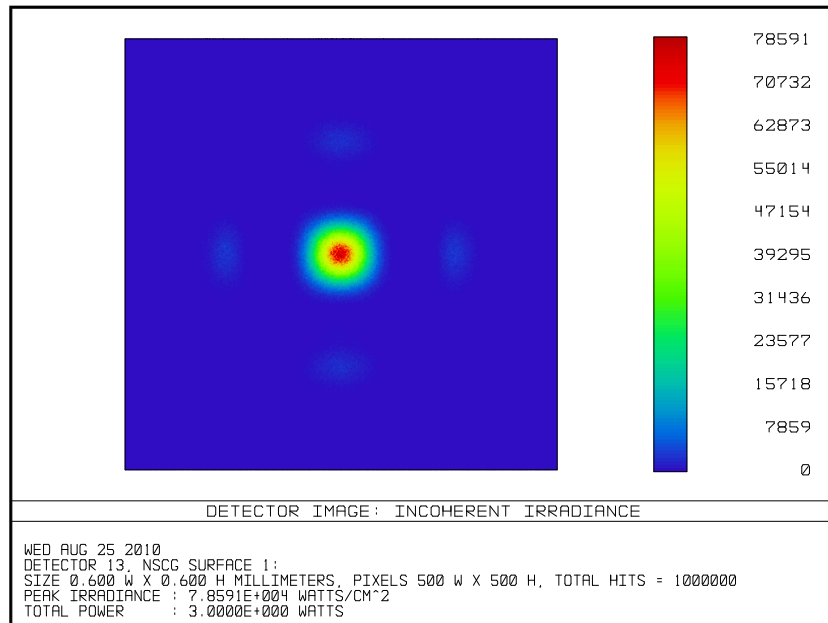


Figure 9.12: The spot size of the NECSEL beam after passing through the design shown in Figure 9.10. The beam is about 8 mm × 3 mm at the input.

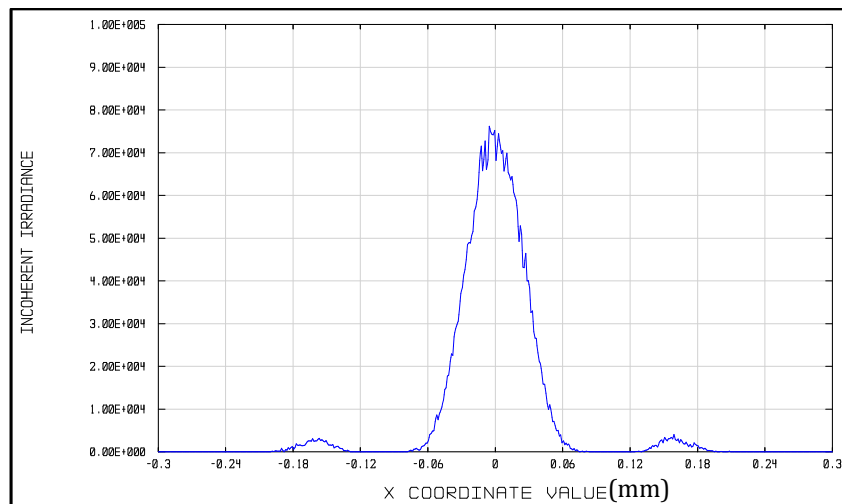


Figure 9.13: The spot size of the NECSEL beam at the detector. The diameter of the laser beam is 90 μm where the power drops to  $1/e^2$  of the maximum value.

Figure 9.13 shows the spot diameter of the beam has been reduced to 90 μm, which is less than the diameter of the fibre.

Chapter 9: Design, Simulation, and Experimental Results for Laser Beam combining, homogenising, and shaping Waveguide

Microscope objective lenses with larger magnification have a smaller Airy disc focus but a larger NA;  $NA = n \times \sin(\theta)$  where  $n$  is the refractive index of the medium and  $\theta$  is the maximum angle that rays can be angled away from the central ray to be captured by the lens system. The formula for NA does not depend on the magnification; however, the focused point of the lens system is closer to the output aperture of an objective lens with higher magnification. This fact increases the acceptance angle of the light; this is the angle through which the light will diverge after the focusing point and it is important that it is comparable to the NA of the fibre to achieve an efficient coupling.

The design was shared with different microscope objective manufacturing companies to find the best match for the system. A focusing objective designed to transmit the high power of  $500 \text{ MW/cm}^2$  for  $532 \text{ nm}$  wavelength was sourced from Thorlabs. The lens is designed to focus the light into a diffraction-limited spot and the spectral transmission window of the objective extends from  $250 \text{ nm}$  to  $1.6 \mu\text{m}$  therefore making the objective suitable for visible wavelengths. Figure 9.14 shows the simulation of the fibre coupling using the lens design of the Thorlabs. They were not permitted to provide the complete design of the objective and, hence, a black box was used for the simulation. The parameters of this were as follows; working distance for the  $20\times$  objective is  $6 \text{ mm}$ , EFL (effective focal length) =  $10 \text{ mm}$ , NA =  $0.40$  and EA (entrance aperture) =  $8 \text{ mm}$ .

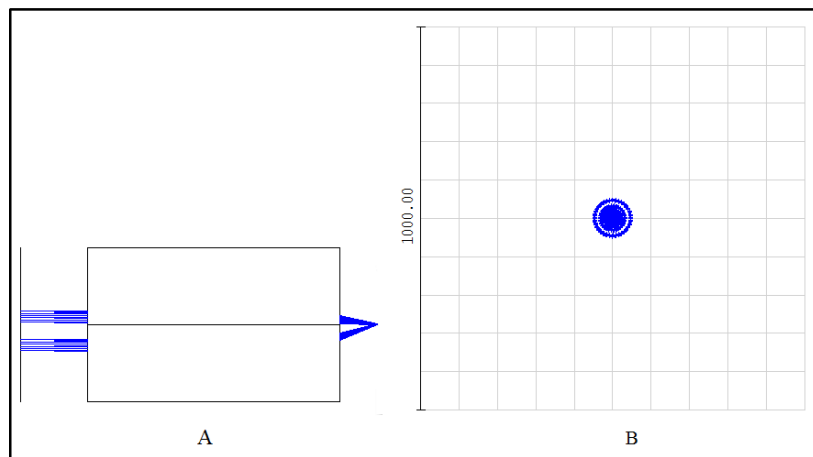


Figure 9.14: Simulation results for using the black box of the microscope objective from Thorlabs. The unit for the 1000 dimension on the figure is  $\mu\text{m}$ .

The root mean square (RMS) of the spot size radius in Figure 9.14 is  $31.7 \mu\text{m}$  which is the diameter of a circle containing approximately 68% of the energy. The experimental results of using this microscope objective are explained in the next section.

## 9.2 Optical Fibre for Colour and Power Homogenisation

In this section, the experimental results for using a multimode optical fibre and waveguide for laser-waveguide coupling, beam homogenising and beam shaping are explained. The experiments are in three parts; laser - fibre coupling, using fibre in the HELIUM3D system for power and colour homogenizing, and using the waveguide combiner.

To check the microscope objective, the experiment shown in Figure 9.15 and Figure 9.16 was arranged. The high-power microscope objective (from Thorlabs Ltd.) was used to focus the light into an optical fibre. Due to financial constraints we did not manufacture the microlens arrays for collimation (the cost of the microlens array was 10000 Euro and is made by Ingeneric Company in Germany). Therefore, the laser-fibre coupling efficiency is reduced compared to simulation if a fibre with  $100 \mu\text{m}$  core diameter is used.

Two optical fibres with  $100 \mu\text{m}$  core diameter ( $\text{NA} = 0.22$ ) and  $200 \mu\text{m}$  core diameter ( $\text{NA} = 0.39$ ) were tried and the coupling efficiency using a blue NECSEL was measured to be  $55\% \pm 10$  and  $80\% \pm 5\%$  for  $100 \mu\text{m}$  and  $200 \mu\text{m}$  respectively.

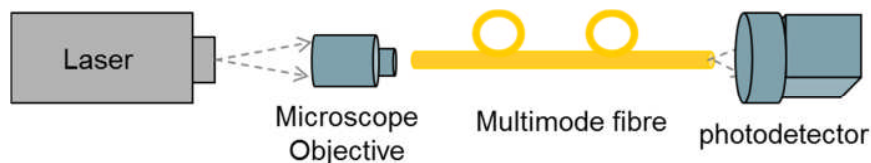


Figure 9.15: Schematic diagram for testing a microscope objective used for fibre coupling.

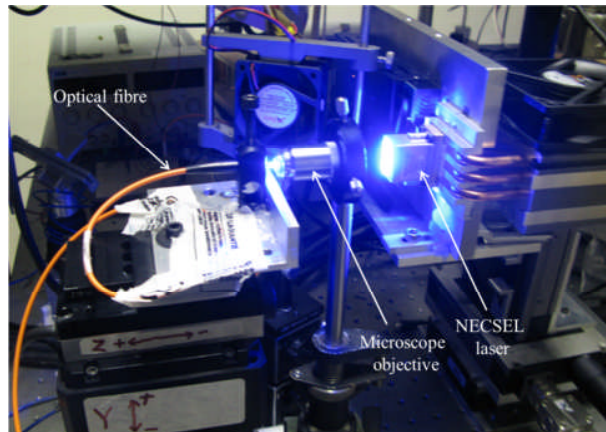


Figure 9.16: Experiment configuration for testing the microscope objective used for fibre coupling.

After designing the system and achieving a good fibre coupling efficiency in the experimental test, the fibre was incorporated into the HELIUM3D display system (Figure 9.17). To incorporate the optical fibre into the system shown in Figure 9.17, a step-index optical fibre with 200  $\mu\text{m}$  core diameter and an  $\text{NA} = 0.39$  was used for fibre coupling. The coupling efficiency was measured to be  $75\% \pm 5\%$  (this experiment was carried out in Koç University in Turkey with different alignment equipment which is the source of the difference between this efficiency and that mentioned before in this section). In Figure 9.17, the output of the fibre must be shaped into a line to be scanned across the LCoS modulation device. A spherical lens (25 mm focal lens) was used to collimate the output of the fibre and a cylindrical lens (100 mm focal length) employed to shape the line. The output profile of the light coming out of the fibre is not top hat and is close to a Gaussian profile [9.3]. To achieve more homogenisation across the light line, two identical off-the-shelf microlens arrays were used to homogenize the intensity across the line as first demonstrated by David R. Selviah in 1995 [9.4].

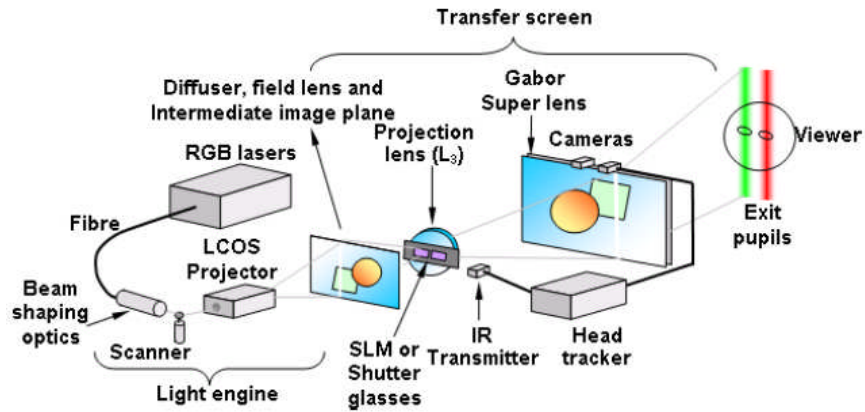


Figure 9.17: Schematic diagram for the HELIUM3D system that incorporates the fibre used for colour and power homogenization (this picture was drawn by Phil Surman from DMU University).

A ray tracing approach was used to simulate the beam shaping and beam homogenisation after the optical fibre in Koç University by Kaan Aksit and was improved by the author. Figure 9.18 shows the ZEMAX simulation results and the different components used in the process are listed in Table 9.3.

Table 9.3: Lens specification used for the beam shaping after optical fibre

Object type	Position (mm)	Front Radius (mm)	Back Radius (mm)	Thickness (mm)	Material
Source fibre	0				
Standard lens	5	0	-13.1	11.7	N-BK7
Standard lens	35	0	-25.8	5.3	N-BK7
Lenslet array	60	0	-0.5	2	PMMA
Lenslet array	65	0.5	0	2	PMMA
Toroidal lens	67	0	-51.7	5.2	N-BK7
Toroidal lens	177	51.7	0	5.2	N-BK7
Toroidal lens	187	0	-51.7	5.2	N-BK7

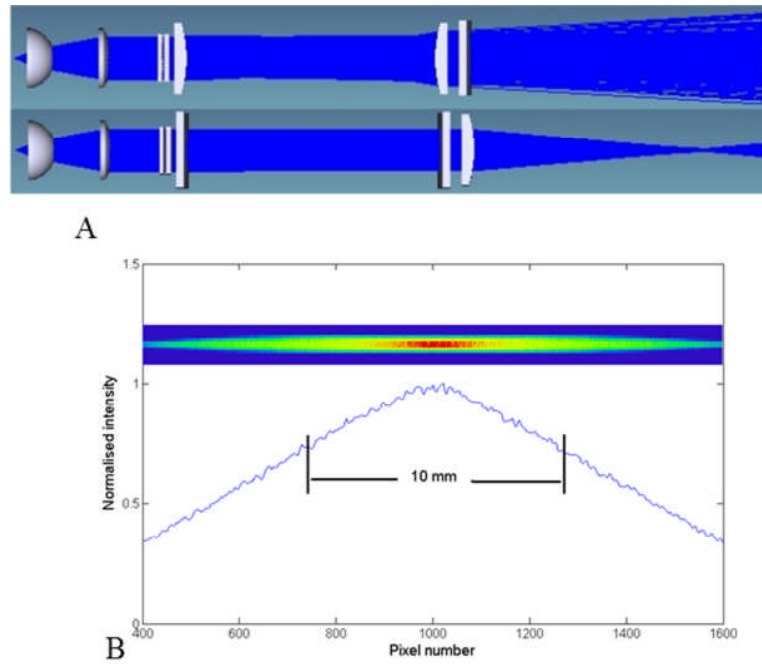


Figure 9.18: Top and side view of the ZEMAX simulation for beam shaping after optical fibre. Table 9.3 shows the lens specification used in the design.

Figure 9.18 shows the simulation and Figure 9.19 illustrates the experimental results for the light engine to create the line at the LCoS device.

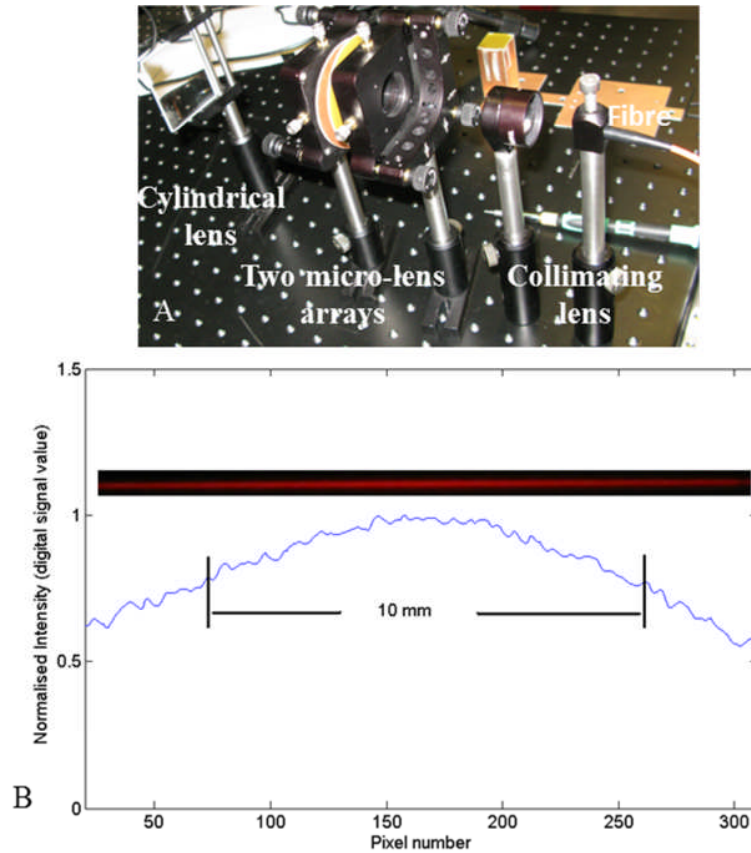


Figure 9.19: Experimental results of the intensity profile of the light line after homogenizing and shaping by using an optical fibre and 2 microlens arrays.

Figure 9.18 and Figure 9.19 show the uniformity of the illumination across the light line when the fibre is used. As opposed to the free space method, there is no sign of stripes in the scanned image or periodic fluctuation across the line (compare with Figure 9.32 part A). Figure 9.19 shows the results after generating the line at the LCoS modulation device. As indicated in the graph, there is no sign of non-uniformity in the form of multi-spot intensity or periodic stripes as in the free space approach. Although the line is not completely top hat shaped, the statistic parameter (Figure 9.19) shows that the intensity fluctuation across the line is small. Figure 9.20 shows the scanned line on the LCoS modulator device. To take this picture the line was scanned with a frequency of 60 Hz using a galvanometer scanner. The results show 85% uniformity (minimum value of the digital signal after the camera divided by the maximum value) along the laser line. The standard deviation of the intensity fluctuation is 5.4, mean value= 151, maximum value =160, and minimum value =137[9.5].



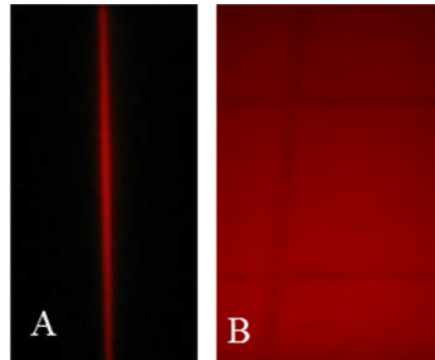


Figure 9.20: The shape of the beam A: at the LCoS and B: the scanned line on the LCoS.

### 9.3 Waveguide Combiner Simulation

Three lasers with different wavelengths must be combined after coupling the laser beams into the waveguide combiner. In this section, we simulate the waveguide and investigate the output shape and uniformity of the power intensity. In the waveguides investigated in this section, the thickness of the core material is 100  $\mu\text{m}$  and the width of the waveguide is 10 mm.

A slab waveguide consists of a core surrounded with a cladding material. The difference between the refractive index of the core and the cladding material defines the NA of the waveguide and so the divergence of the beam at its output.

$$NA = \sqrt{n_{cor}^2 - n_{clad}^2}$$

The waveguide can be considered to be without cladding (air as the cladding) and the resultant NA will be larger which is beneficial for the fibre coupling (due to the larger light acceptance angle of the waveguide). However, the combined light emerging from the waveguide will diverge into a larger angle as well. The waveguides simulated in this section were slab waveguides without any wall roughness or scattering sites inside the waveguide. The refractive index of the material was 1.52 for  $\lambda = 546.1$  nm. This number was chosen for two reasons: firstly there is a company that can provide glass sheets with this refractive index, and secondly, it is close ( $n_{core} = 1.556$ ) to the refractive index of the polymer we used for waveguide manufacturing (chapter 4, 6, and 7).

### 9.3.1 Simulation of a Slab Waveguide with Three Fibre Inputs:

For the first simulation, the input is three fibres with  $NA = 0.22$  and diameter of  $100\ \mu\text{m}$ . These fibres are represented by the three colours as shown below.

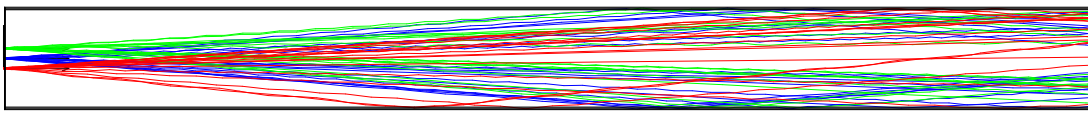


Figure 9.21: Slab waveguide and one multi-mode fibre for each colour. The width of the waveguide is 10 mm, the thickness is  $100\ \mu\text{m}$ . The length is calculated to provide uniform output intensity.

In the design shown in Figure 9.21, the optical fibre core diameter is  $100\ \mu\text{m}$  to achieve a light line with  $100\ \mu\text{m}$ . Figure 9.22 shows the output profile of the slab waveguide. One million rays were used for ray tracing each colour in the simulation.

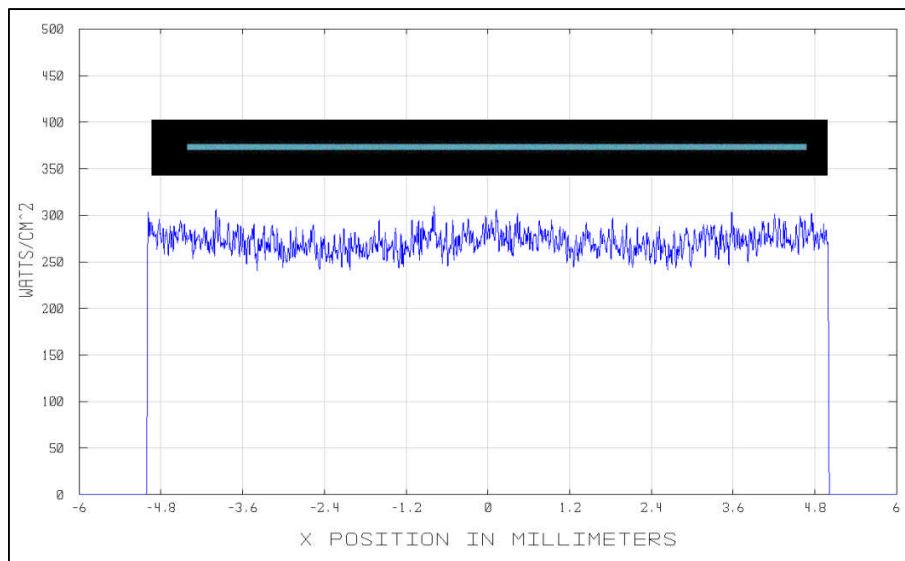


Figure 9.22: The output of the waveguide after combining the three lasers together. The line at the top of the graph shows the actual colour after emerging from the waveguide at the output. The length of the waveguide was calculated to be  $75\pm 5$  mm to achieve this output.

The laser beams are combined as they propagate in the waveguide. The three colours have the same power weight and the efficiency of this design was calculated to be 92%; this is calculated by dividing the number of the rays that arrive at the detector, placed at the output of the waveguide by the number of rays launched into the waveguide. The actual efficiency will be less

than this as the material absorption and the loss due to the end facet roughness has not been taken into account.

Figure 9.22 shows the output of the slab waveguide after the three colours have propagated through it. The length of the waveguide is 75 mm and the uniformity for one colour is 60 %. The uniformity is defined as the minimum value divided by the maximum value. Uniformity more than 90% is aimed for in our simulation and experiments. What is shown in Figure 9.22 is the overlapping of the three colours at the output. To find the optimum length of the waveguide to achieve the required homogenization of more than 90%, several slab waveguides with different length were simulated and the results are shown in Figure 9.23. These show that the length of the slab waveguide needs to be larger than 210 mm to achieve a uniform output for the three colours. In fact, after 210 mm, the irradiance is distributed uniformly across the waveguide.

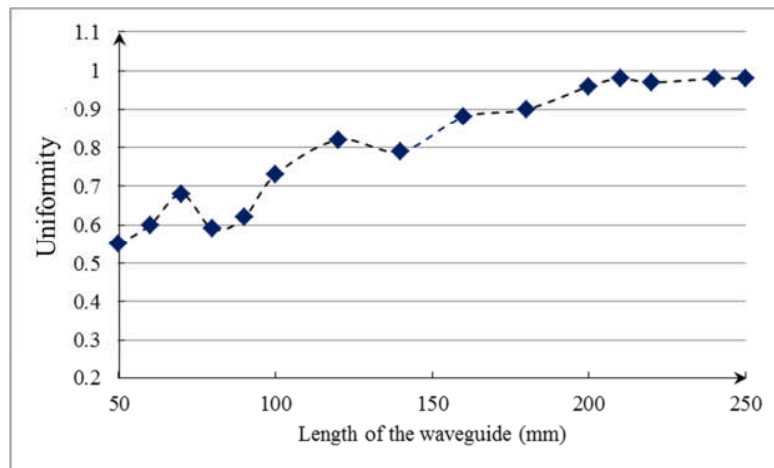


Figure 9.23: Uniformity of the irradiance at the output of the slab waveguide for different waveguide lengths.

Figure 9.24 shows the output of a waveguide with 210 mm length and Figure 9.25 shows the linear best fit line with the residual compared to a linear fit line. The residual is the difference between the actual result and the best fit straight line. The line was fitted to find the non-uniformity by calculating the angle between the line and horizontal direction and also by determining the residual. Higher uniformities correspond to smaller gradients of the fit line and also smaller magnitudes for the residual.

Chapter 9: Design, Simulation, and Experimental Results for Laser Beam combining, homogenising, and shaping Waveguide

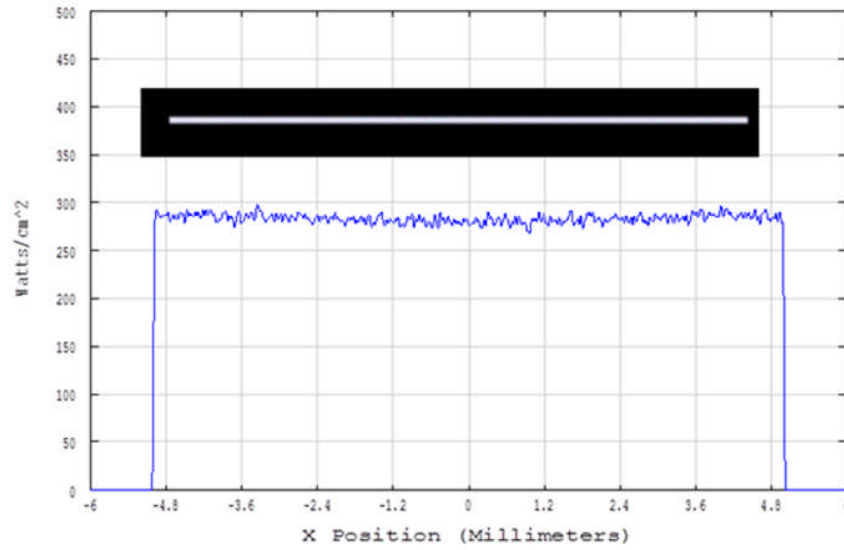


Figure 9.24: Output of the waveguide after combining the laser beams. The line at the top of the graph shows the actual colour after emerging from the waveguide. The waveguide length is 210 mm. The colour ratio is R=1, G= 0.50, B= 0.54

Figure 9.24 shows a white colour achieved at the output of the waveguide. More investigation into colour balancing is required to achieve a true white colour for 6500 K. However, in experimental tests it must be borne in mind that the material absorption is larger at blue wavelengths and this will affect the colour adjustment.

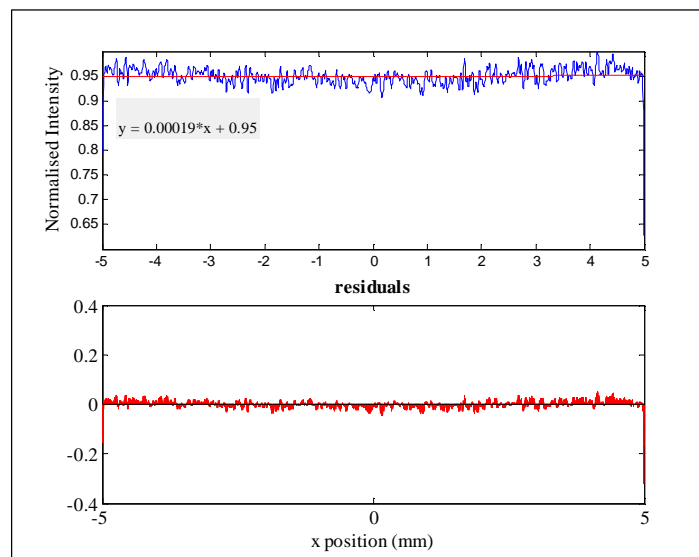


Figure 9.25: The output irradiance from the waveguide with a straight line fitted to the profile. The residual diagram also indicates the difference between the output profile and the fitted line.

Figure 9.25 shows the output and a linear line fitted to the graph. The gradient of the fitted line is  $1.9 \times 10^{-4}$  which gives a slope of  $8 \times 10^{-3}$  degrees to the line, which is negligible.

Table 9.4: Statistical parameters of output profile of the light emerging from the waveguide beam combiner.

Gradient (Degree)	Maximum (W/m <sup>2</sup> )	Minimum (W/m <sup>2</sup> )	Standard deviation (W/m <sup>2</sup> )	Average (W/m <sup>2</sup> )	uniformity
0.008	300	294	2.75	295.3	97%

In Table 9.4 the statistical parameters of the output profile of the 210 mm slab waveguide is listed. The output of the waveguide is 97% uniform. The standard deviation of the output profile is 2.74 W/m<sup>2</sup>. The low value of the standard deviation indicated here shows a good degree of uniformity of the line.

### 9.3.2 Simulation of the use of a Fibre Ribbon for Laser-Waveguide Coupling:

The second option for the NECSEL beam-waveguide coupling is to use fibre ribbon. The fibre ribbon is connected to the waveguide with four ribbons each with 24 fibres connected to each row of the blue and green NECSELs and one ribbon with 20 fibres is connected to the red laser array. This gives a total of 5 ribbons delivering the laser beams; 2 ribbons for blue, 2 ribbons for green and one ribbon for red. The ribbons can be attached in an optimum configuration to achieve the best colour balance and combination.

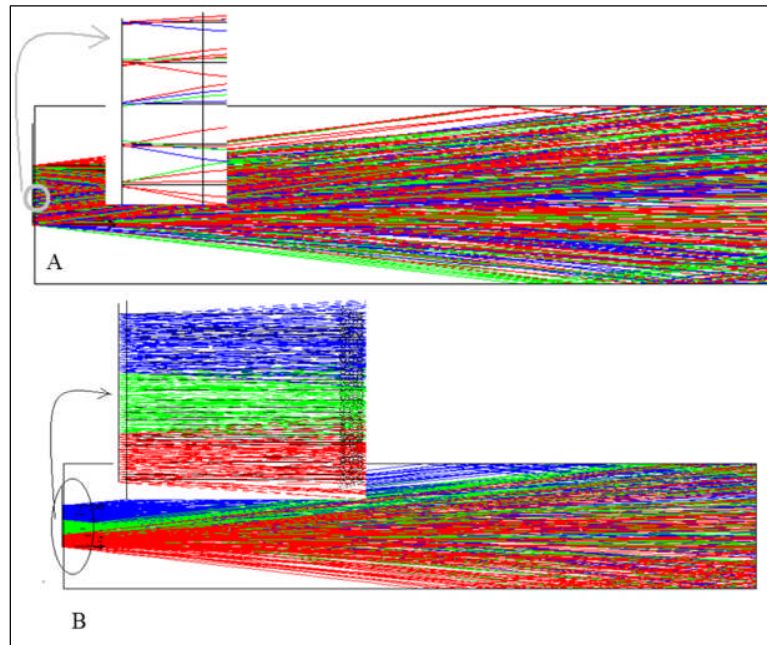


Figure 9.26: Fibre ribbon attached into the waveguide. The fibres in the ribbons can be arranged in different ways. A: fibres are arranged to have a sequential of red, green, and blue mixed with each other. B: fibres for each colour are placed next to each other.

Figure 9.26 shows two different arrangements for coupling the fibre ribbons into the waveguide. The fibres of the ribbons in option A, are arranged to have a sequence of red, blue and green colour so the fibres with different colours are mixed at the input and in option B, the ribbons for each colour are beside one another at the entrance to the waveguide.

Below the result of the simulation in arrangement A is explained. The waveguide is  $100\ \mu\text{m}$  thick and  $10\ \text{mm}$  wide. The inputs are multimode fibres with  $100\ \mu\text{m}$  core diameter and  $\text{NA}=0.22$ .

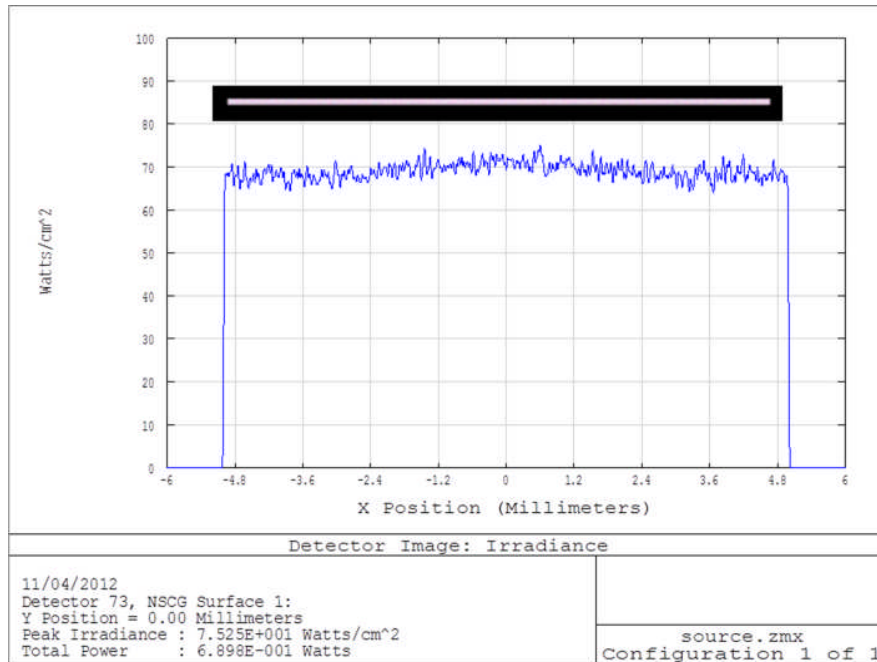


Figure 9.27: The output of the waveguide after combining the lasers together using fibre ribbon for laser coupling (situation A in Figure 9.26). The line at the top of the graph shows the true colour after emerging from the waveguide.

Figure 9.27 shows the output profile and a true colour graph for the output of the waveguide with the input being several fibre ribbons. The fibres are aligned next to each other as it is shown in Figure 9.26 part B. The length of the waveguide was reduced to 150 mm and a uniformity of 92% was achieved. Therefore redistributing the power across the input can help to reduce the length of the waveguide. The input ratio of the red, green, and blue colours is 1:1:1 and the colour at the output of the waveguide is more towards the red which can be improved by changing the input weight of the colours. In the experiment, the colour is adjusted by balancing the output of the lasers.

## 9.4 Colour Balancing and Homogenising in a Slab Waveguide

Colour balancing is applied by changing the ratio of the different input wavelengths. The output of the waveguide also must have a uniform power density along the column. As shown in Figure 9.22, Figure 9.24 and Figure 9.27 the output power fluctuates across the waveguide unless the length of the waveguide is sufficiently long (210 mm) to achieve an acceptable uniformity (>90 %). Increasing the length of the waveguide is not a very viable solution for two reasons. Firstly, handling a long waveguide is a challenge. The waveguide thickness is only 100  $\mu\text{m}$  and a glass

## *Chapter 9: Design, Simulation, and Experimental Results for Laser Beam combining, homogenising, and shaping Waveguide*

sheet with this thickness breaks easily and must be protected properly. The optical loss due to the material absorption increases with increasing waveguide length. This is important for safety concerns, particularly as high power lasers are used to compensate the power lost and also heat is generated inside the waveguide as a result of absorption. Secondly, implementing a long waveguide in display systems increases the size of the display. Moreover, the waveguide combiner will not be suitable for microdisplay systems such as microprojectors.

To obtain a homogenised output at a shorter length of waveguide, the light needs to be scattered inside the waveguide and mixed. What we simulated in the previous section was a slab waveguide without any wall roughness or scattering sites inside the waveguide. In an actual waveguide, there is always wall roughness which is a source of light scattering. There might also exist other factors including; impurities, microbends, and non-uniformity at the microscopic level in the refractive index of the material. However, scattering spots and the wall roughness are not entirely beneficial as they can also cause light to be scattered into an angle greater than the critical angle and consequently increase the optical loss. Therefore, there is a trade-off between the optical loss and achieving uniform output using roughness and impurities.

We tried to use both the wall roughness and also some designed scattering sites which can be implemented inside the slab waveguide to diverge the light up to the critical angle. Therefore, we use both the scattering of the wall roughness and also try to use all the space in the waveguide more efficiently for beam combining and homogenising. In the design shown in Figure 9.28, two objects with a triangular cross section have been implemented inside the waveguide to scatter the light. The position and the angle of the scattering sites were optimised to give the shortest length waveguide with the best uniformity. The scattering sites are 1 mm away from the input facet of the waveguide and there is no material in their location (refractive index of one). The use of the scattering sites is more efficient where the NA of the waveguide is larger than the NA of the fibre. In this case, light is coupled into the waveguide with a small angle and can be scattered more without reaching the critical angle. In other words, the larger the refractive index difference between core and cladding of the waveguide, the larger the scattering angle that can be achieved and, hence, the smaller the waveguide length will be so glass waveguides with air cladding are very suitable.



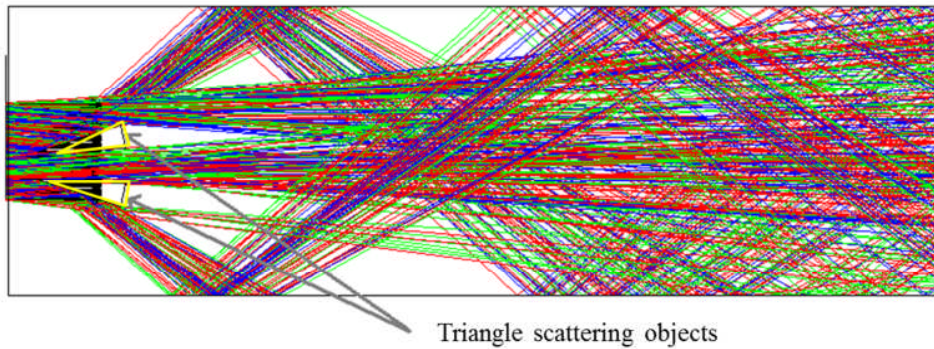


Figure 9.28: Slab waveguide with some scattering sites. The scattering sites are triangular regions which have been removed from the waveguide so their refractive index is 1.0. The length of the waveguide has been truncated to be able to show the scattering sites.

Figure Figure 9.28 shows an example of scattering sites with a triangular cross section shape removed from the waveguide. Although the length of the waveguide was reduced to 85 mm with implementing of the scattering sites, the simulation results show that efficiency has been decreased. The efficiency of the waveguide combiner without the scattering site is 92% whereas with the scattering site it is reduced to 69% for the same waveguides. As defined previously, the efficiency has been calculated by dividing the number of the rays arriving at the detector by the number of rays launched into the waveguide.

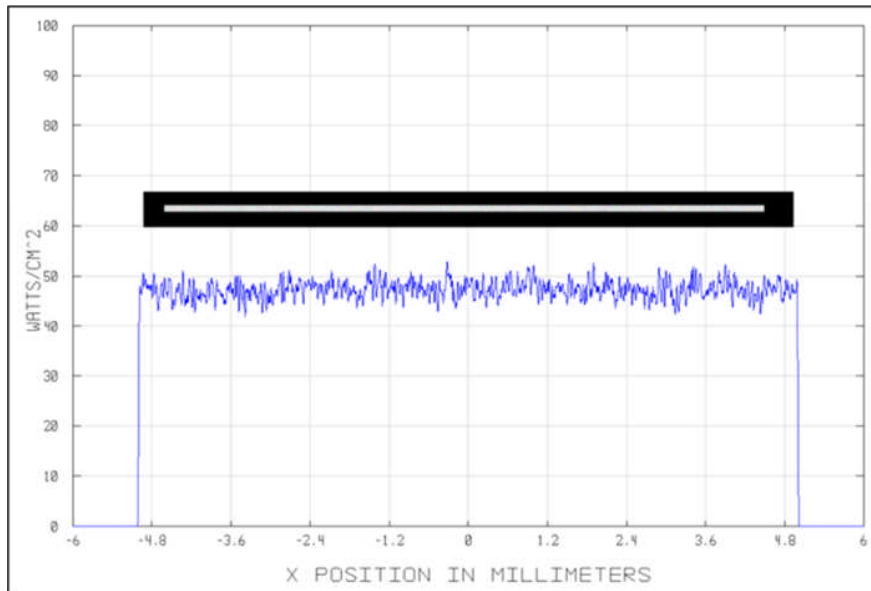


Figure 9.29: The output of the waveguide after implementing the scattering site inside the slab waveguide. The uniformity is 93%.

The efficiency of the waveguide with scattering sites can be improved by improving the scattering site shapes, angles and positions and by increasing the NA of the waveguide (which means using a different core material with larger refractive index). The loss is due to the rays which are scattered away from the waveguide at larger than the critical angle.

## 9.5 Experiment Results using Slab Waveguides:

Several experiments were carried out to analyse the performance of a slab waveguide in the display system. Different slab waveguides with different lengths were used and the light from the lasers was coupled into the slab waveguide using an optical fibre or several multimode fibres in a ribbon. The experimental configurations are shown in Figure 9.30. As shown in this figure part A, the output of the high power laser is coupled into a multimode optical fibre (100  $\mu\text{m}$  core diameter) and the optical fibre is connected to the slab waveguide. The slab waveguide is made of glass with a refractive index of 1.523. It should be mentioned that in the experiments explained in this section, we try to prove the concept and find the difference between our method of using waveguides and the conventional free space approach. Therefore, the optical loss is not very crucial at this stage. The slab waveguide used was 1 mm thick and the results presented below were achieved for a length of 75 mm. The width of the slab waveguide was 20 mm. The difference between the waveguide used for the experiments and the simulations is mainly the thickness. An off the shelf glass waveguide with 100  $\mu\text{m}$  thickness was also tried but the length of the waveguide was just 30 mm and it was too short to achieve a good homogenisation at the end.

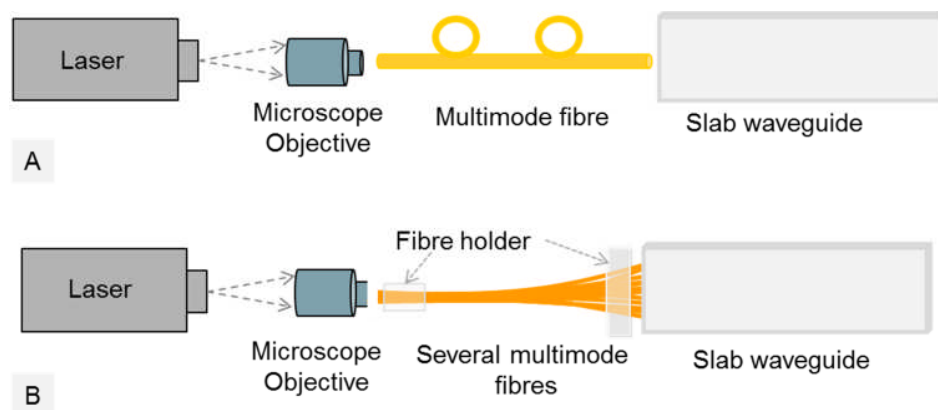


Figure 9.30: Schematic diagram of using slab waveguide for beam homogenization and de-speckling.

Chapter 9: *Design, Simulation, and Experimental Results for Laser Beam combining, homogenising, and shaping Waveguide*

In the display system, three fibres one for each of the RGB lasers is connected to the slab waveguide and the power and colour are mixed, homogenised, and shaped by propagating inside the waveguide.

Figure 9.30(B) shows a different situation where instead of having one single fibre, several fibres are used in the form of a ribbon. 40 step index fibres with core diameters of 50  $\mu\text{m}$  were used. The fibres were placed inside a glass cylindrical tube having an inner diameter of 4 mm and were glued together and the output of the laser was focused on the input of the fibres. At the other end of the ribbon the fibres were placed next to each other and sandwiched between two glass sheets and glued. The outputs of the fibres were then coupled into the slab waveguide. Figure 9.31 shows the experimental configuration. In the display system, the fibres for three RGB colours are mixed and then sandwiched between the glass sheets as it helps a better colour mixing.

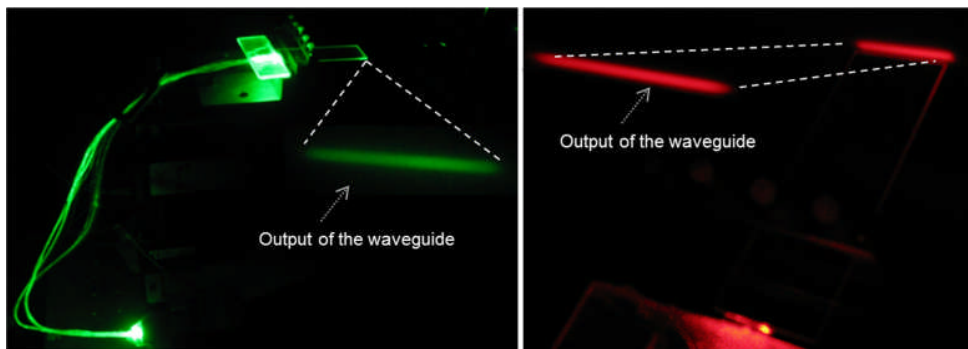


Figure 9.31: Fibre ribbon connected to the slab waveguide for the green and red laser.

Figure 9.32 shows the output of the waveguide scanned on the SLM with a frequency of 60 Hz. The results shown in this figure, which is compared with the free space approach, shows a significant difference. There is no sign of the multiple stripes or multi-emitter interference that can be seen in the free space system using microlens arrays. The uniformity across the photograph in Figure 9.32 for part A and B is 48% and 87% respectively.

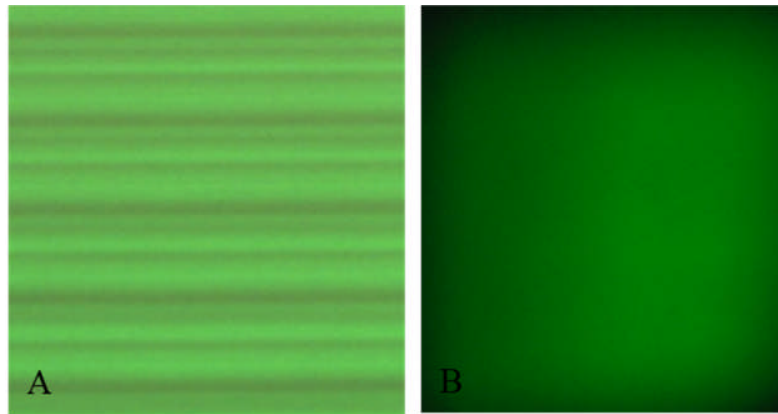


Figure 9.32: A: Scanned output of the free space approach. B: Scanned output of the slab waveguide.

## 9.6 Conclusions:

Two different lens systems were designed and simulated using ray tracing to focus the output of the NECSEL beam into an optical fibre with 100  $\mu\text{m}$  diameter and NA of 0.22. The coupling efficiency was calculated to be 73%.

As the manufacturing of a custom lens system increases the cost of the display system, the use of a microscope objective for focusing the NECSEL beam was considered and a new microscope design was developed and designed for NECSEL laser focusing. The NECSEL beam was reduced from 3 mm  $\times$  8 mm to a spot with 90  $\mu\text{m}$  diameter, which is less than the diameter of the fibre.

The microscope objective was tested by experiment and 75% NECSEL-fibre efficiency was achieved for a 200  $\mu\text{m}$  core diameter fibre with NA of 0.39.

The optical fibre was implemented in the light engine of the HELIUM3D system. We achieved 85% uniformity across the light line. Moreover, there was no sign of any multiple spots on the line, which was seen in the free space homogenisation approach due to the multiple beams emitted from the NECSEL laser.

A slab waveguide was simulated to be used for beam shaping and beam combining for the first time and was used in the HELIUM3D system. Two options of 1) three optical fibres for red, green, and blue colours and 2) three fibre ribbons each for one colour, were used for the input of

## *Chapter 9: Design, Simulation, and Experimental Results for Laser Beam combining, homogenising, and shaping Waveguide*

the waveguide combiner. The results show that for a glass slab waveguide which is 10 mm wide and 100  $\mu\text{m}$  thick, the required length is 210 mm to achieve 90% uniformity at the output of the waveguide and have a good uniformity. (These results were achieved with three optical fibres as the input. The length of the waveguide was reduced to 150 mm with a uniformity of 92% at the output of the fibre combiner when the input was three fibre ribbons).

The simulation results indicate the requirement for a long waveguide. The waveguide thickness is only 100  $\mu\text{m}$  and a glass sheet with this thickness breaks easily and must be protected properly. The optical loss due to the material absorption increases with increasing waveguide length. This is important for safety particularly as high power lasers are used to compensate for the power lost, and heat is created inside the waveguide. Moreover, implementing a large waveguide in display systems increases the size of the display and the waveguide combiner will not be suitable for the micro display system such as micro projectors.

The simulation results explained above are for a waveguide without wall roughness or any scattering site to scatter the light inside the waveguide. A low-cost scattering site with a triangle shape was suggested and simulated. Implementing this scatter-site decreased the waveguide length to 85 mm. Although the length of the waveguide was reduced to 85 mm with implementing of the scattering sites, the simulation results show that efficiency has been decreased. The efficiency of the waveguide combiner without the scattering site is 92% whereas with scattering site it is reduced to 69% for the same waveguides.

The use of a slab waveguide as the power homogeniser was experimentally tested by using a glass slab waveguide with a thickness of 1 mm. Increasing the thickness of the waveguide and so the output light line does not degrade the performance of the HELIUM3D system seriously. The results for a slab waveguide with a length of 75 mm show a uniformity of 85% at the output of the waveguide. Moreover, there was a significant reduction of the speckle pattern, which is concluded in the next chapter.

## References

- [9.1] Eugene Hecht and Alfred Zajac, *Optics*, 4 ed Addison Wesley, San Frnsisco, CA, 1999.
- [9.2] "Light and its detection," <http://www.astro.ljmu.ac.uk/courses/phys134/scopes.html>, July 2009.
- [9.3] T. Cizmar and K. Dholakia, "Shaping the light transmission through a multimode optical fibre: complex transformation analysis and applications in biophotonics," *Optics Express*, vol. 19, no. 20, pp. 18871-18884, 2011.
- [9.4] P. Poon and D. R. Selviah, "Astigmatism in ellipsoidal and spherical photoresist microlenses used at oblique incidence," *IOP Second International Conference on Microlens Arrays*, pp. 65-71, 1995.
- [9.5] Hadi Baghsiahi, David Selviah, Eero Willman, Anibal Fernández, and Sally Day, " Beam Forming for a Laser Based Auto-stereoscopic Multi-Viewer Display," *SID Symposium Digest of Technical Papers.*, vol. 42, no. 1, pp. 702-705, June 2010.

## **Chapter 10: Laser Speckle Analysis Techniques**

### **10.1: Introduction**

In this chapter a new method of speckle investigation based on the speckle spot size is introduced. A new computer program (with a CCD camera) was developed to record the speckle pattern and analyse it in real time to calculate the speckle contrast, speckle spot radius, uniformity of the pattern and analyse the speckle pattern using image processing techniques. The benefit of this software is demonstrated by using it to monitor the speckle contrast, diameter and uniformity at various positions along the optical path after each optical component in an autostereoscopic display system (explained in chapter 6). The speckle contrast is also mapped at the viewer's position. Such results have never been shown for any system before and have the advantage of showing the fluctuation of speckle contrast across the display system and the effect of each optical component in the system on the speckle pattern. In the second part of this chapter, the results of new research on the effect of the diameter of an optical fibre on the speckle contrast are presented by experiment. Finally, speckle patterns recorded in light emerging from a slab waveguide used for beam combining, beam shaping and homogenization in the autostereoscopic display system (chapter 9) are shown and compared with those from other waveguides with different size.

In chapter 3, the speckle phenomenon was explained where coherent light is reflected from (or transmitted through) an optically rough surface. The scattered/transmitted light beams interfere with each other at the detector surface (camera or human eye) and present a fine granular structure in the intensity distribution called speckle. The origin of the speckle is due to the random roughness of the surface from which the light is reflected/transmitted as it gives a phase shift to the reflected/transmitted light [10.1]. Speckle has a profound effect on the information that can be extracted from an image produced by a coherent light source as it reduces the quality of the pictures.

Speckle patterns are random distributions of dark and bright spots and the size of the speckle is related to the coherency of the illumination source. A light source with a higher spatial coherence produces larger speckle contrast. The coherence of the light source, and so the speckle contrast, can be determined by the auto-correlation function of the speckle pattern. A larger spatial coherence will result in a slow de-correlation and therefore, causes larger speckle contrast. The half-width at half maximum of the auto-correlation function defines the speckle contrast[10.2;3]. The speckle contrast should be reduced and there are several methods for reducing this parameter which were reviewed in chapter 3. The amount of reduction is given by the fundamental results of probability theory for adding  $N$  independent, identically distributed, uncorrelated real-valued patterns. Based on this theory, if  $N$  independent speckle patterns are added the contrast of the resultant speckle pattern is reduced by  $\frac{1}{\sqrt{N}}$  [10.3]. Therefore, the result of each method that is used to reduce the speckle contrast depends on how many independent speckle patterns are created by that particular method. The speckle situation on a picture is presented by calculating the speckle contrast numerically. The contrast ratio of a random intensity fluctuation is defined by:

$$\text{Contrast Ratio} = \frac{\sqrt{\langle P_i^2 \rangle - \langle P_i \rangle^2}}{\langle P_i \rangle}$$

Where the  $P_i$  is the grey scale value detected by the  $i^{th}$  pixel of a CCD (charge coupled device) camera and the brackets  $\langle \rangle$  express the expected value[10.2;3]. The above equation is equivalent to dividing the standard deviation ( $\sigma$ ) by the mean value ( $\mu$ ) of the pixels' value and the result lies between 0 to 1. If the contrast of the speckle is below the threshold of the human eye perception, then the speckle pattern cannot be resolved by human eye and it will not affect the image quality. The speckle pattern is not perceived by human eyes if the speckle contrast is equal or less than 0.04 [10.4;5]. However other researchers have reported that the speckle contrast should be less than 0.01 to be below the threshold of the human perception[10.2].

## **10.2: Speckle Contrast Measurements and Characterization**

To measure the speckle pattern, two experimental configurations shown in Figure 10.1 and Figure 10.2 were used. In these experiments, the speckle patterns are recorded by a black and white CCD camera with the pixel size of  $4.5 \mu\text{m} \times 4.5 \mu\text{m}$ . The camera had a controllable exposure time, aperture and sensitivity.



In Figure 10.1, the speckle pattern is recorded by a CCD camera without any lens or aperture system. In this case, the light scattered/transmitted from the optical elements reaches the CCD chip and the interference pattern on the surface of the chip is recorded as the speckle pattern.

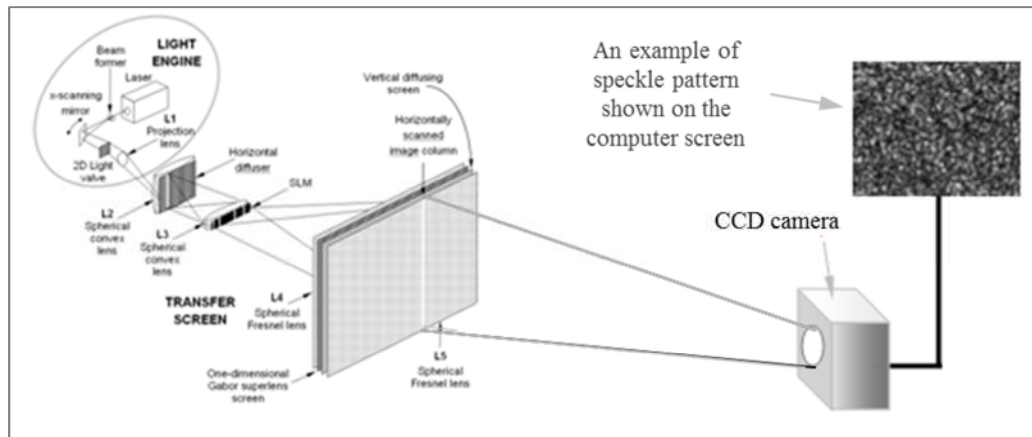


Figure 10.1: Schematic of the system illumination and measurement setup. The HELIUM3D system is explained in chapter 5 in detail. In this figure the focus is on the speckle measurement configuration.

In Figure 10.2, a spherical lens with an aperture was used to measure the speckle contrast as it is seen by the viewer. A spherical lens with an aperture was added to the CCD chip to measure the speckle contrast as it is seen by the human eye. In this configuration the CCD chip simulates the retina of the eye and the spherical lens with a focal length of 25 mm, was used to image the speckle pattern on the CCD chip, and mimics the lens. A manually adjustable aperture was also placed in front of the lens to simulate the iris in the human eye (Figure 10.2).

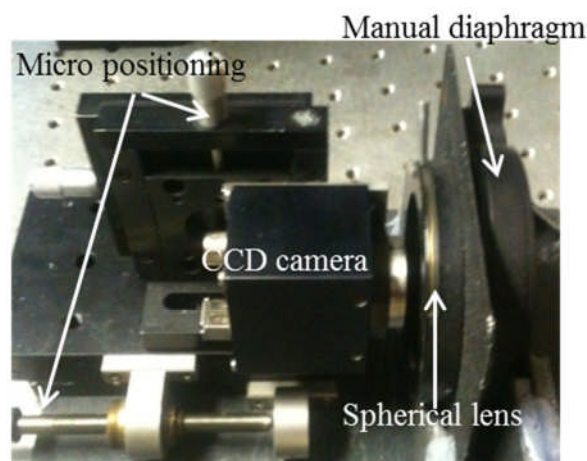


Figure 10.2: Optical arrangement for recording speckle pattern as it is seen by the human eye

A completely accurate model of the human eye would be much more complicated than this but the comparison of the CCD images with actual observations showed a high level of similarity.

The plan is to have the camera fixed in the position first and then add the optical elements one after another and measure the difference on the speckle contrast after adding each part such as L2, diffuser, L3, SLM, etc. This gives us an idea of the effect of each optical component on the speckle configuration which is helpful in the next stage for reducing the speckle contrast.

Another important issue to be considered is the movement of the viewer. If the position of the viewer changes, will the perceived speckle be different? When the viewer changes his/her position, he/she receives a different wave front emitted from different angles and different parts of the super lens screen which could have different roughness. Therefore, the received wave fronts have different phase properties and produce a different interference pattern, which is the speckle pattern in that position. Therefore, the movement of the viewer needs to be investigated to find if the perceived speckle is different in different positions. A manual rail was used and the camera was attached to the stage and can be displaced in two horizontal and vertical directions. This system enables us to carry out the experiment and investigate the change in the position of the viewer's eye.

The speckle pattern captured by the CCD camera needs to be processed to determine the speckle contrast. Although all the calculations are based on the intensity value detected by the CCD camera, not all of the captured data contributes to the speckle as there are some non-speckle phenomena to be separated such as fringing pattern, edge scattering or any other regular pattern that might be added due to the design of the optical system and using multilayer components. Apart from the edge effect, the other artifact can be regarded as the low frequency pattern such as the effect of non-uniform illumination. The non-speckle effects are removed by using image processing and filtering. The speckle patterns are recorded in different experiments and analysed in Matlab. However, it was found that sometimes analysing the speckle pattern suggests some change in the system to see the change in the speckle. To be able to perform this action, new Matlab based software was developed to analyse the speckle pattern in real time. This is very useful and applicable to any speckle pattern. The software is explained in the next section.

### **10.2.1: Real Time Speckle Analysis Software**

To analyse the speckle pattern, a graphical user interface (GUI) was written in Matlab which captures the data and enables the user to calculate the histogram of the intensities captured by the camera, autocorrelation function, speckle contrast, uniformity and Fast Fourier transform (FFT) in real time.

The software output shows several graphs and can be used to compare the speckle pattern in various situations. It can also calculate the 2D FFT and apply different filters to the data in the frequency domain. Another option has also been implemented in the software, which calculates the speckle size; this is a very useful feature for the speckle analysis. Figure 10.3 is an example of the appearance of the software output and shows how graphs and options are arranged.

The software can be used for either real-time calculation or for any saved pattern. It is most useful where the user makes a change to the system such as adjusting the alignment of components in  $x$ ,  $y$ ,  $z$  or in 3 angles and wants to see the resulting change in the speckle contrast immediately. So, for example, the alignment giving the least speckle contrast can be chosen by real time optimisation. The software can also be used to calculate the illumination uniformity across the pattern or any selected part of the recorded pattern.

Another aspect of the software is that the user can choose any part of the speckle pattern and analyse the selected part by cropping the image and analysing a different part of the speckle pattern in real time. The uniformity is determined by dividing the minimum value of the data by the maximum value. The software shows the speckle and non-uniformity in a bar graph at the right hand side in the middle of the image (Figure 10.3).

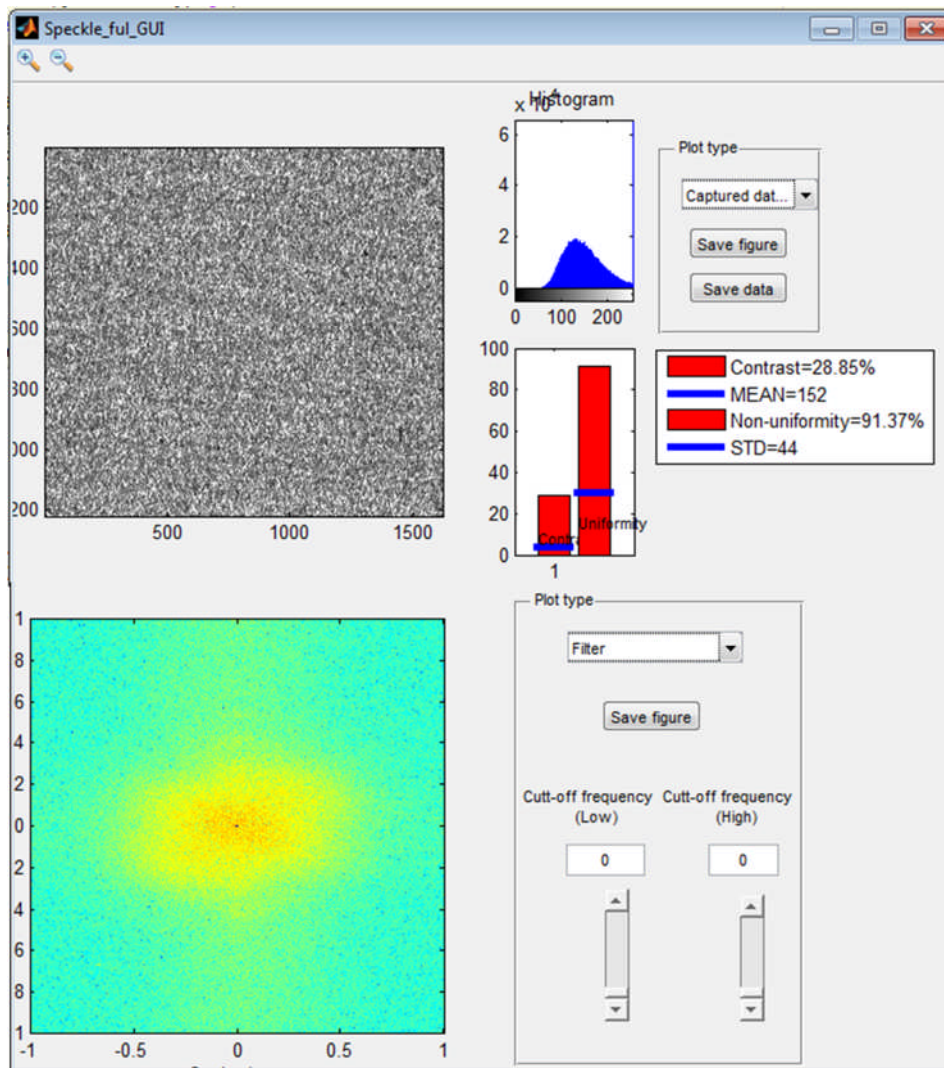


Figure 10.3: A sample of the speckle analysing software.

Figure 10.3 shows a snap shot of the output of the program. The user can choose different modes from the drop down window. The software can be used for real time processing or can save the current speckle and the viewer can apply some measurements and analyses quickly. Figure 10.4 shows the available option for the speckle pattern shown on the axes and the analysis to be applied.

To apply analysis such as FFT and speckle spot diameter, the captured mode or crop mode should be chosen and, then, the relevant option from the analysis window applied as due to the memory limitation and time consumed for the analysis, it will not be applicable to the real time measurements.

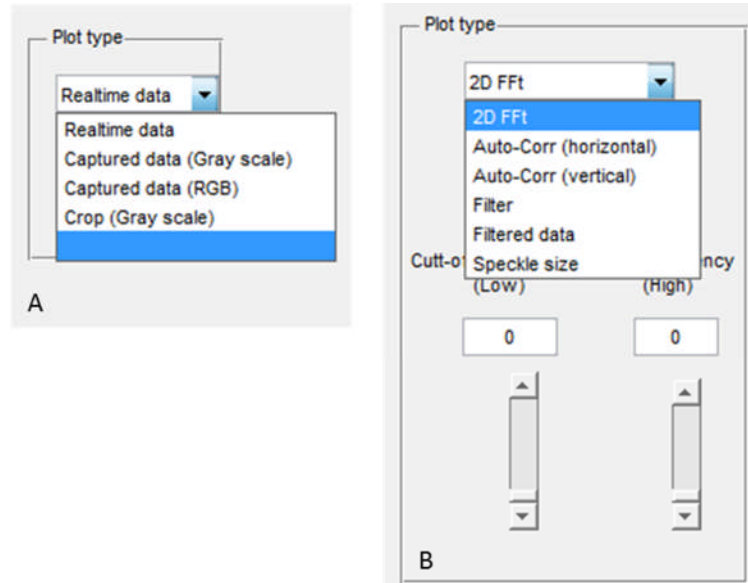


Figure 10.4: A: Different available option for the speckle analysis software to be chosen by the user. B: the analysis option available for the user after choosing the speckle pattern to be analysed.

The program can calculate the auto-correlation function which is useful for calculating the speckle diameter. Moreover, it is very helpful to find if there is any repeated pattern in the picture which is not due to the speckle but illumination non-uniformity or optical design.

Speckle spot diameter is also a very useful option to find the diameter of the bright and dark spots. The speckle size detection uses the Granulometry technique which is explained in Appendix 1.

### 10.2.2: Speckle Spot Diameter Measurements

Speckle spot diameter has been considered in different systems and speckle pattern by theory and experiments. However, in display systems the speckle contrast is the main parameter which is reported by different researchers and companies as it is explained in Chapter 3. Image processing and statistical theory have been used to calculate the speckle spot diameter. Fourier transform, autocorrelation function and spectral density are the main parameters that have been used for calculating the speckle spot diameter[10.6;7].

The first research into calculation of this parameter was carried out by Goldfischer where he used the autocorrelation function and derived the power density of a speckle pattern. He showed that this function is proportional to the autocorrelation of the effective scattering area[10.6]. The speckle size in three dimensions has also been considered by using autocorrelation function of the intensity[10.8].

It was found that the distance between the source and the scattering surface has nothing to do with the speckle size but the distance between the viewer and the scattering site effects the observed speckle size. In general all the published research indicates that the autocorrelation function of the random irradiance determines the speckle spot distribution. The average speckle size is determined from the first minimum of the autocorrelation function[10.9].

The speckle size and the calculation of the speckle size is not easy in general especially in a speckle pattern. The reason is that firstly there is not a very clear boundary for the black and white spots and they merge together. Secondly, they do not have a particular shape and as several different spots merge together they produce random spot shapes. Another issue to mention is that the size of the black and white spots are not the same and there are small and large spots in the speckle pattern. These points make the speckle calculation in a real speckle pattern difficult. In this thesis we use a new method for calculation the speckle spot diameter which is Granulometry. In fact apart from the nature of the speckle and what causes the speckle, the focus is on the speckle pattern recorded by a camera or perceived by human eye. Granulometry is the process to measure different grain size in a granular material. In this process, the size of the objects is estimated based on the size in a photograph. This is a well-known process and is used extensively in different industries such as mining[10.10].

This method is used in this thesis to calculate the intensity surface area distribution of the bright spot as a function of size. The method we used in this research is based on the Granulometry algorithm from Matlab software. The method is explained in Appendix 2.

Granulometry was implemented to calculate the speckle size in the developed software for speckle analysis (Figure 10.4). However, the software provides the option to calculate the autocorrelation function and can be used for comparing the speckle size obtained from different methods.

To see the difference between the autocorrelation and Granulometry method, the speckle spot diameter calculated by these methods are compared with each other for some designed patterns (Figure 10.5) and real speckle patterns. Figure 10.5 contains circles with a range of diameters, and autocorrelation and Granulometry are used to calculate the diameter of the circles. These circles simulate the speckle bright spots and are drawn manually and distributed randomly. The exact diameter of the circles is also determined by manually counting the number of pixels in each circle.

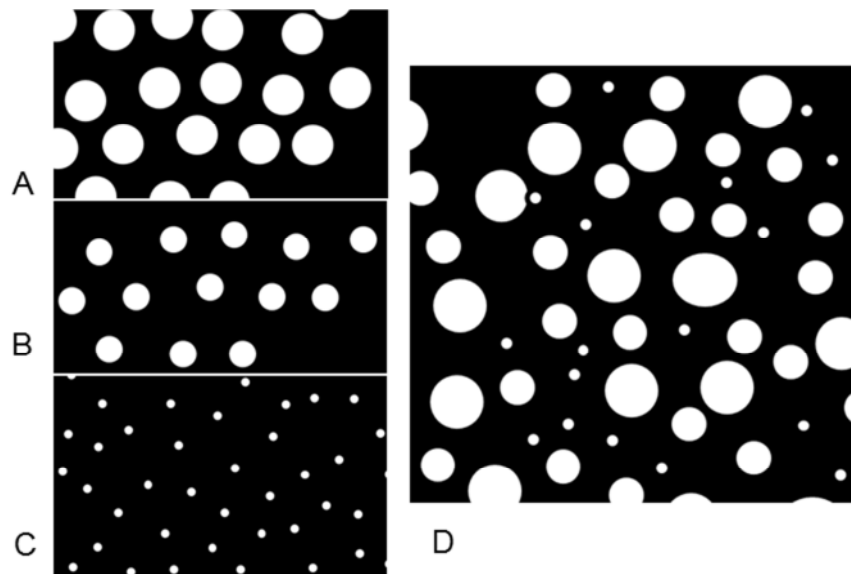


Figure 10.5: designed pattern for comparing the speckle size calculation method. The diameter of the circles in part A, B, and C is 52, 34, and 11 pixels respectively.

In Figure 10.6 the autocorrelation function and in Figure 10.7 Granulometry is used to calculate the diameter of the circles shown in part A, B, and C in Figure 10.5. In these patterns the circles have the same size and as the figures below show, both methods calculate the size of the circles with a small error.

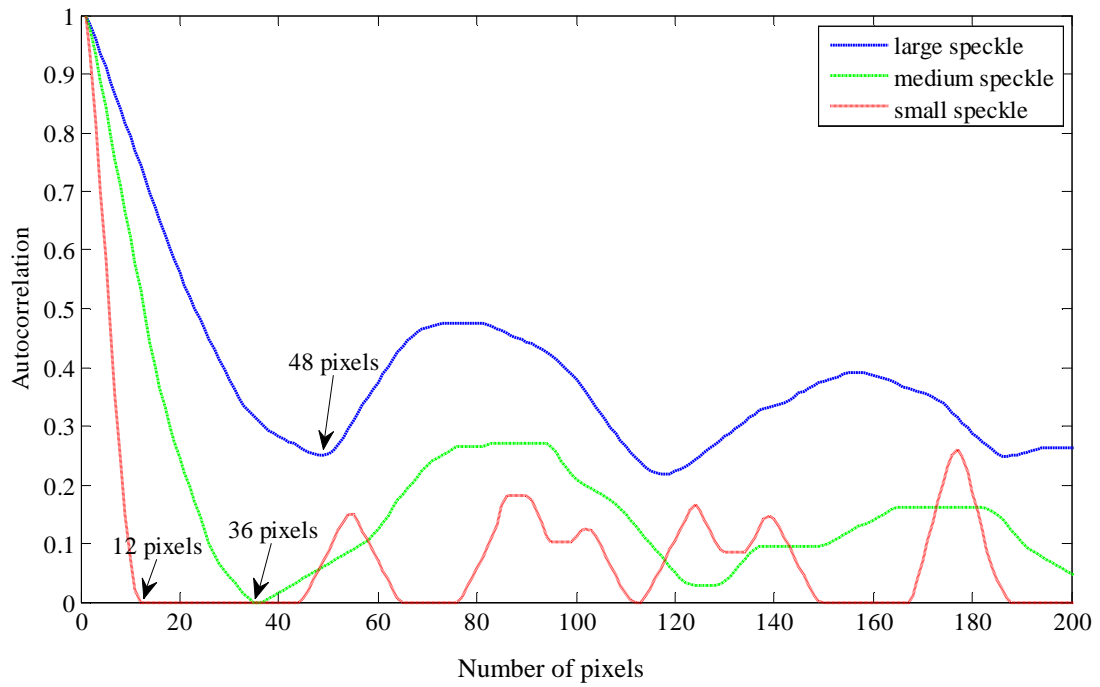


Figure 10.6: Autocorrelation function of the pattern in Figure 10.5.

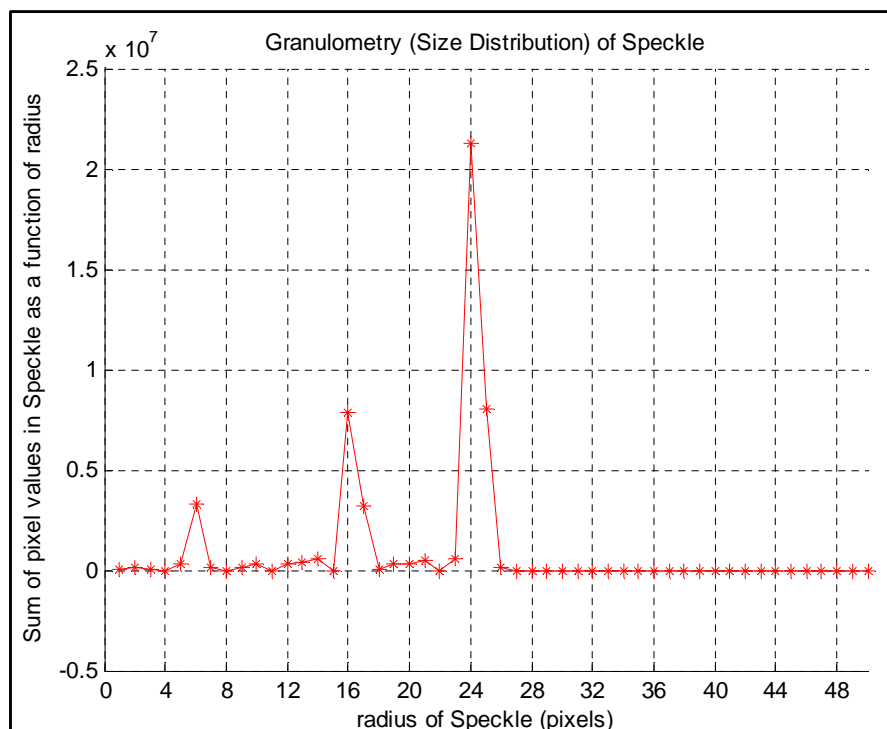


Figure 10.7: The radius of the circles in part A, B, and C in patterns shown in Figure 10.5 calculated by Granulometry. Three peaks in the graph show the radius of each circle.



Both autocorrelation and Granulometry methods determine the size of the circle very accurately in Figure 10.6 and Figure 10.7. But this is a very ideal situation where all the circles or speckles are neat and of the same size. In real speckle patterns, there are several bright and dark spots with different diameters which must be considered. To compare the functionality of the methods in such a situation, the circles are mixed and randomly distributed and the size of the circles is calculated again (Figure 10.5 pattern D). The results are shown in Figure 10.8 and Figure 10.9. The results show that the autocorrelation function in this case, which is more realistic, cannot provide accurate information as it shows an average distribution of the speckle sizes. In contrast, there is no difference for the Granulometry and the circles with different size are recognised despite the distribution or number of them. Comparing Figure 10.7 and Figure 10.9 can prove this matter as in both figures; the speckle size has been calculated to be exactly the same.

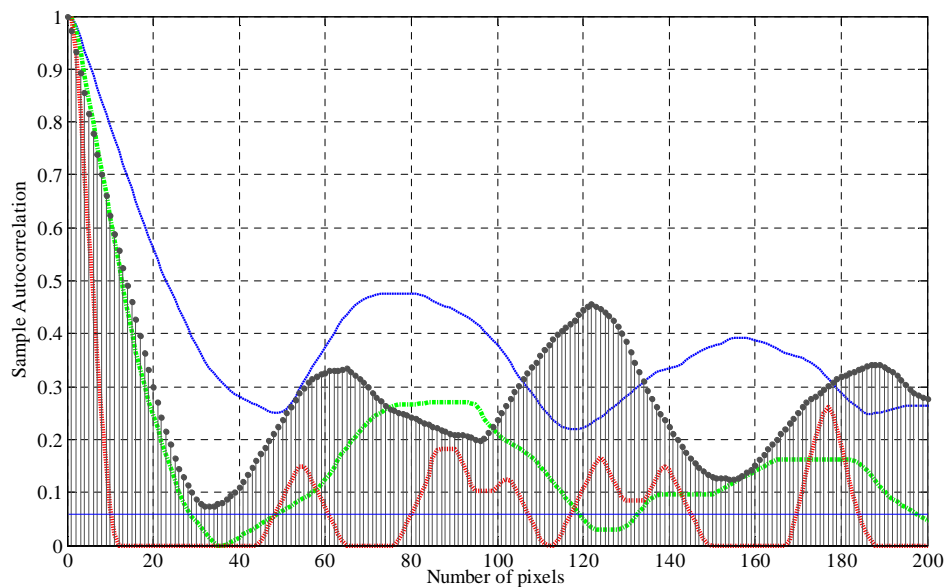


Figure 10.8: Autocorrelation of the pattern shown in Figure 10.5 part D. the red, green and blue graphs are the autocorrelation for the patterns A, B, and C.

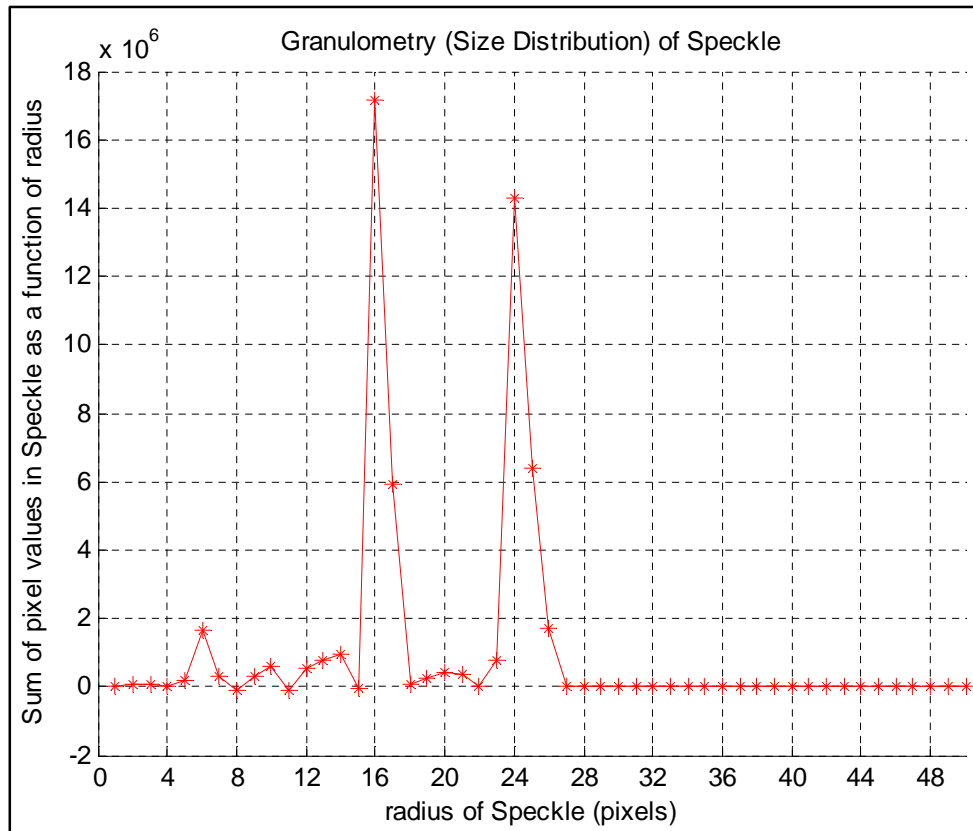


Figure 10.9: The size of the circles in part D shown in Figure 10.5 calculated by Granulometry. Three picks in the graph show the radius of each circle.

The problem in a real speckle pattern obtained from a rough surface or diffuser is different. The fact is that normally speckle patterns do not have a sharp edge and the contrast can change across the pattern. There are several bright and dark spots overlapping each other and make the spots have different shapes to one another. Speckle size is the radius or the diameter of the bright or black spots but due to the overlap of the speckle spots and the shape of the speckle spots the size may be different in different directions. The autocorrelation function will again provide an average size of the speckle and the Granulometry method should be considered with more caution. To finish this section the speckle size for a real speckle pattern is calculated by both autocorrelation and Granulometry methods for two different speckle patterns shown in Figure 10.10.

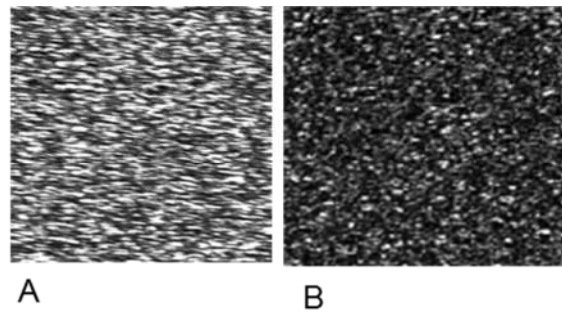


Figure 10.10: Two different speckle patterns. A: after a diffuser; the speckle size is  $5 \times 40$  pixels. B: speckle size is  $5 \times 4$  pixels.

The speckle size calculations using the autocorrelation method and Granulometry are shown in the next three figures.

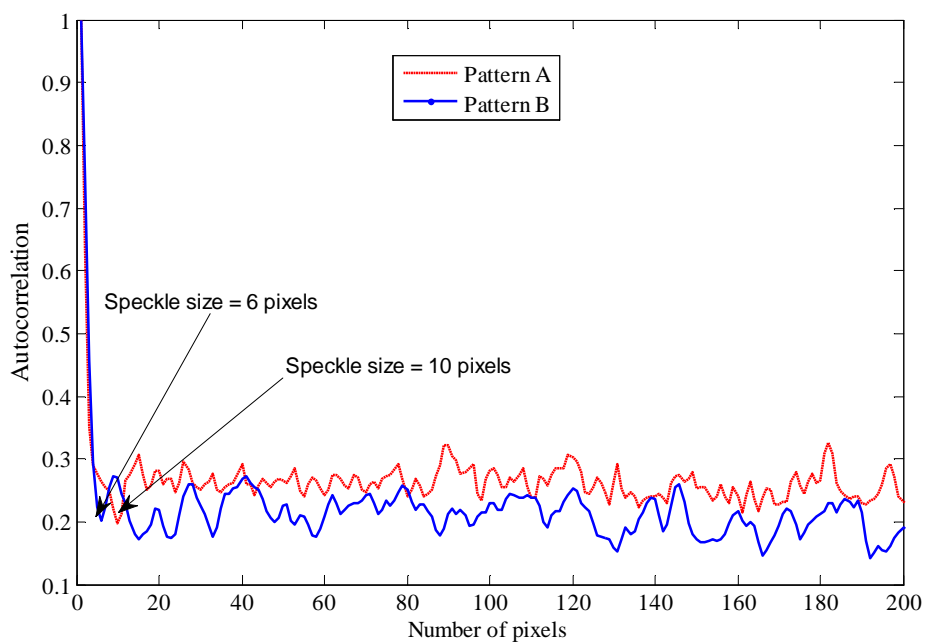


Figure 10.11: Speckle size calculation using autocorrelation function for speckle patterns in Figure 10.10 in the vertical direction.

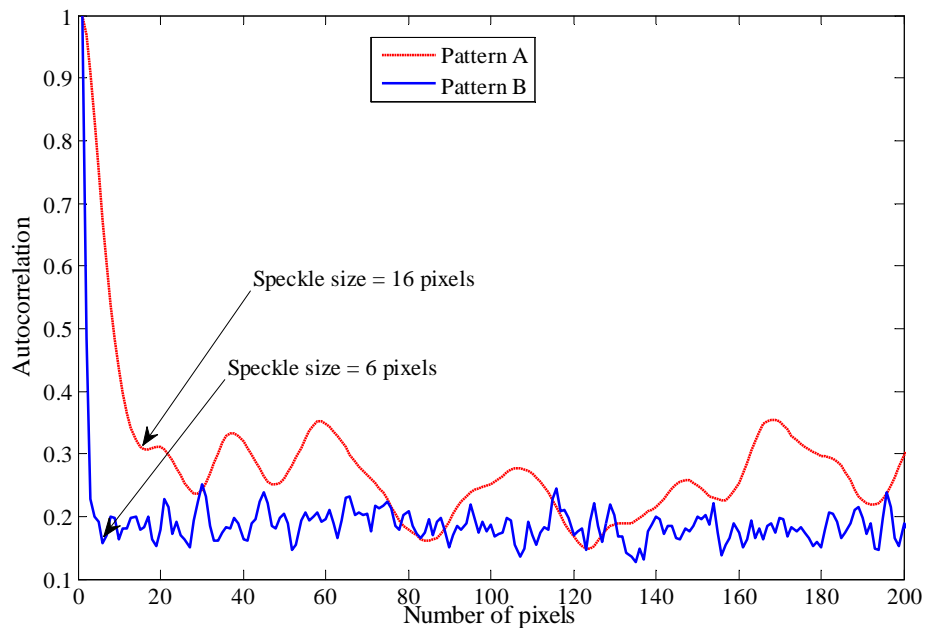


Figure 10.12: Speckle size calculation using autocorrelation function for speckle patterns in Figure 10.10 in the horizontal direction

Figure 10.11 and Figure 10.12 show the results for using autocorrelation in the horizontal and vertical direction for the middle row and column of the speckle pattern in Figure 10.10. The speckle pattern A was recorded after a horizontal diffuser so the speckles are longer in one direction. It was chosen deliberately to show which method works better for the speckle size calculations. Comparing the results in Figure 10.11 and Figure 10.12 with Figure 10.13 shows that Granulometry gives better results when the speckle spots are symmetric, or in other words have a more circular shape. The size of the grains in the pattern A is 4-6 pixels in one direction and about 30-40 pixels in the other direction and it is 4-5 pixels for most of the speckle spots in pattern B.

For pattern B the autocorrelation function gives a size of 6 pixels and Granulometry 4 pixels. But for pattern A, Granulometry in fact does not work as the speckle grains are in an elliptical shape. The results are not even close to the 40 pixels size as it is shown in Figure 10.13. The autocorrelation function calculates more accurate results especially if the second minimum is considered as the speckle size in Figure 10.12.

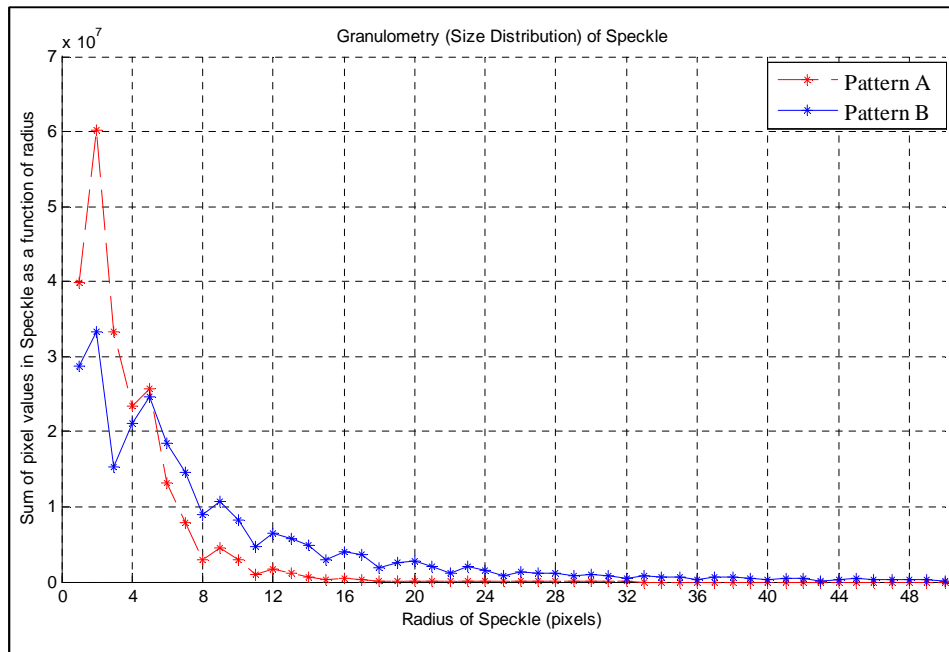


Figure 10.13: Speckle size calculation using Granulometry for speckle patterns in Figure 10.10.

Therefore, based on the results shown in this section Granulometry and autocorrelation should both be used on the results to achieve a reliable result. In most of the speckle patterns where the black and white spots are symmetric the Granulometry provides better results for the grain size. The important fact is that it can calculate the size of different spots in the pattern. It should be mentioned that the limitation on the Granulometry algorithm should be considered and improved with different image processing implementation methods.

### 10.3: Speckle contrast measurements and results

In this section different speckle measurements are presented. The measurements are based on the optical components used in the HELIUM3D system. Lasers, optical diffusers and all of the elements were chosen to reduce the speckle, as speckle was noted at first due to using coherent laser beams for the light source. Therefore, a comprehensive investigation of the speckle pattern is presented in this section.

### **10.3.1: Speckle Contrast Measurement using NECSEL Laser as the Light Source**

Speckle contrast can be reduced either by reducing the laser coherency or statistical addition of different diffraction patterns[10.3]. Integration of different speckle pattern is the most applicable method reported and employed in the laser display system. The HELIUM3D system is a laser display system, which uses three lasers as the light source. Therefore, the speckle problem reduces the image quality. However, the lasers were chosen to be multiple emitter, which can reduce the speckle contrast by adding different speckle patterns created by each emitter if the emitters are coherently independent.

#### **10.3.1.1: Reducing the Speckle Contrast by Increasing the Bandwidth of the Laser**

Semiconductor lasers are used as the light sources and laser feedback or thermal effects shift the central frequency of the laser or widens the spectrum which results in speckle reduction[10.1]. We measured the spectrum of the laser and measured the speckle pattern to detect the change in the line width by changing the driving parameter of the NECSEL lasers. We tried to displace the central frequency and widen the laser beam bandwidth to reduce the coherency of the laser beam. Increasing the bandwidth, which is comparable to chirp in digital electronics[10.11], can be imposed by changing the drive current. NECSEL lasers provide access to the frequency and the duty cycle of the driving signal, which are used to tune the output power of the laser. To take advantage of broadening the line width of the NECSEL beam, the duty cycle and frequency of the laser pulses were changed and for each duty cycle the speckle contrast and the spectrum was measured. Figure 10.14 and Figure 10.15 shows the results of the NECSEL spectrum and the speckle contrast recorded by the CCD camera. The spectrum was measured by a spectrum analyser (PMA-12 from HAMAMATSU Company).

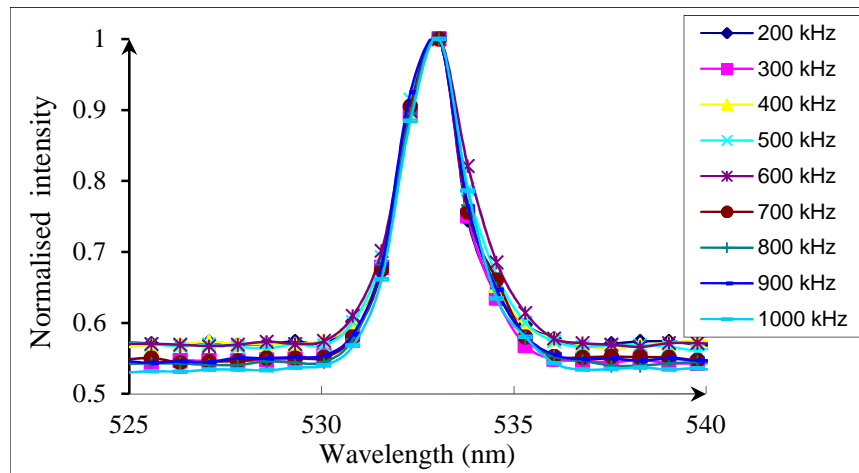


Figure 10.14: Spectrum of the green NECSEL for different driving frequencies. . A Hamamatsu spectrum analyzer (PMA-12) was used for the measurement.

The results show there is no detectable change in the spectrum or speckle pattern and changing frequency of the drive current does not provide any speckle reduction.

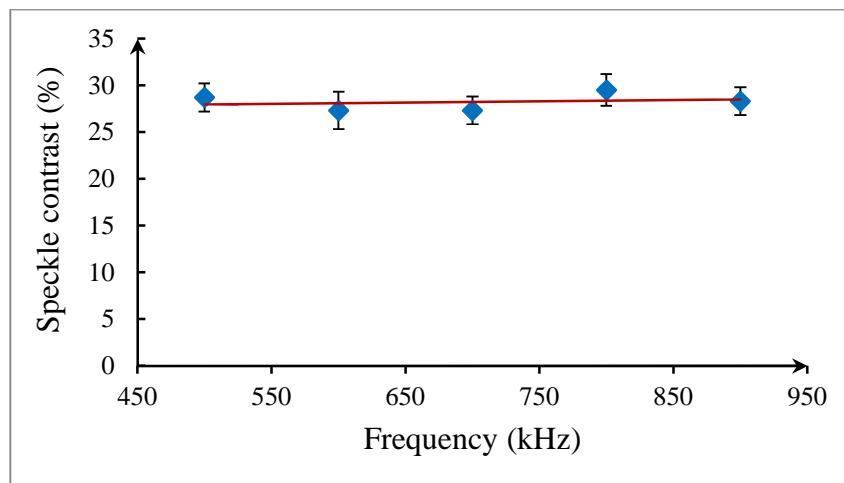


Figure 10.15: Speckle contrast of the green NECSEL output in different frequencies of the drive current.

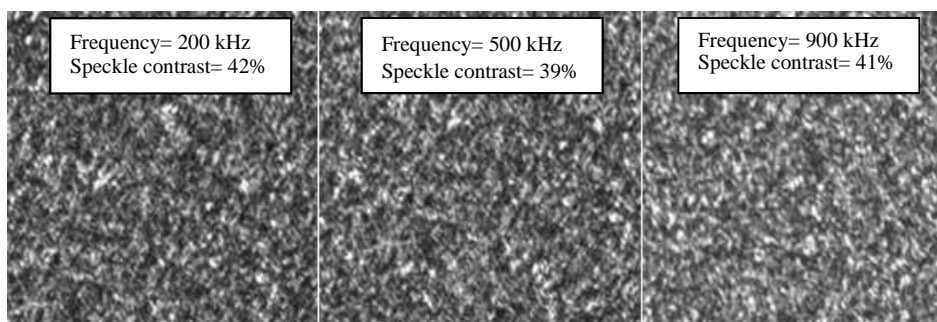


Figure 10.16: the speckle pattern recorded by CCD camera for different laser driving frequencies. The recording camera was 20 cm away from a print quality paper and recorded the speckle pattern reflected from the paper.

The laser beam bandwidth in different frequencies shows that there is no change in the frequency of the laser when the driving parameter changes. The speckle pattern and speckle contrast also show no significant changes (Figure 10.15 and Figure 10.16). The results in Figure 10.15 and Figure 10.16 can be explained by considering the NECSEL structure. NECSELs are doubled frequency diode lasers with Volume Bragg Gratings (VBG) implemented inside the casing to stabilize the wavelength of the laser (Figure 10.17).

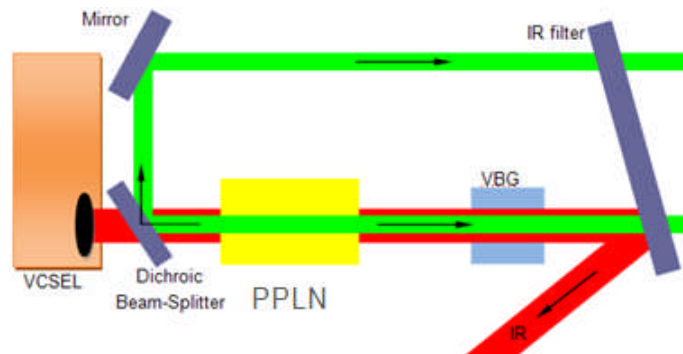


Figure 10.17: Schematic graph for the NECSEL laser. The graph shows a side view, which is the beam formation of one single emitter. There are 24 emitters in each row.

The VBG makes the laser output temperature independent and no other wavelength is allowed to radiate from the laser other than the designed wavelength. Therefore, although wavelength diversity decreases the speckle contrast however, it cannot be used in this case. Therefore, HELIUM3D cannot benefit from wavelength diversity for green and blue colours.

### 10.3.1.2: Speckle Pattern of the Laser as a Function of the Number of Emitters and Diffusers

The transfer screen section of the HELIUM3D display system uses two horizontal and vertical diffusers and 48 laser sources of each of the blue and green lasers and 20 emitters of the red laser in the multi-emitter lasers as the light source. Theoretically, when all sources are of equal brightness; the speckle contrast should be reduced by a factor of  $N^{-1/2}$  where  $N$  is the number of emitters. We measured the speckle pattern resulting from various numbers of emitters and various numbers and orientations of diffusers. Figure 10.18 shows a schematic diagram of the experiment.



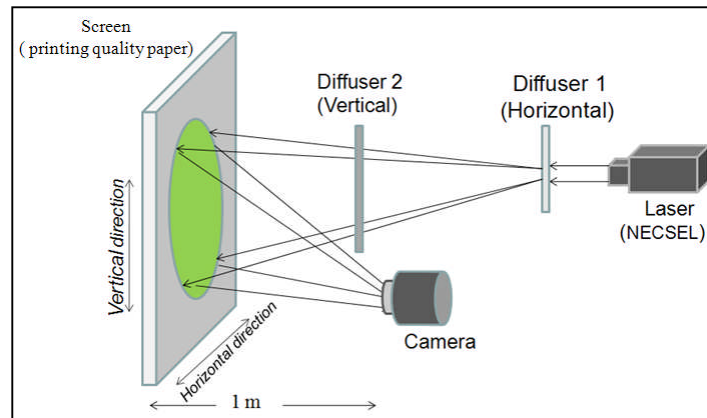


Figure 10.18. Schematic diagram of the configuration of the experiment to measure the speckle pattern.

For the measurement, the CCD camera was used without any lens. The laser source was 2 m away from the reflecting surface and the distance between the camera and the surface was 1 m. Different numbers of the emitters were in operation and the speckle pattern was recorded after reflecting from a print quality paper. The position of the camera and lasers and the reflecting surface were constant during the experiment.

#### 10.3.1.2.1: The Speckle Contrast as a Function of the Number of Emitters

The experiment in Figure 10.18 without having the diffusers in the system was arranged and the speckle patterns which different numbers of emitters were recorded. Figure 10.19 shows the recorded speckle pattern for different number of emitters. The results show a significant change in the speckle pattern.

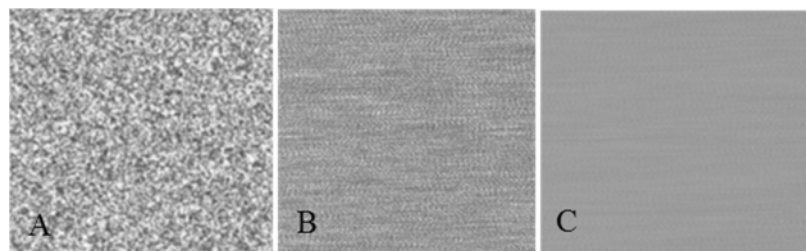


Figure 10.19: The speckle pattern of the NECSEL beam. A: 2 emitters B: 16 emitters, C: 48 emitters are switched on.

The speckle contrast as a function of the number of emitters is plotted in Figure 10.20 with a plot for statistical theory of the reduction of  $N^{-1/2}$  for  $N$  number of emitters. The yellow area under the horizontal straight red line in the graph shows the 4% contrast limit of perceptibility for human eyes. Any speckle contrast below this graph will not be detected by the human eye.

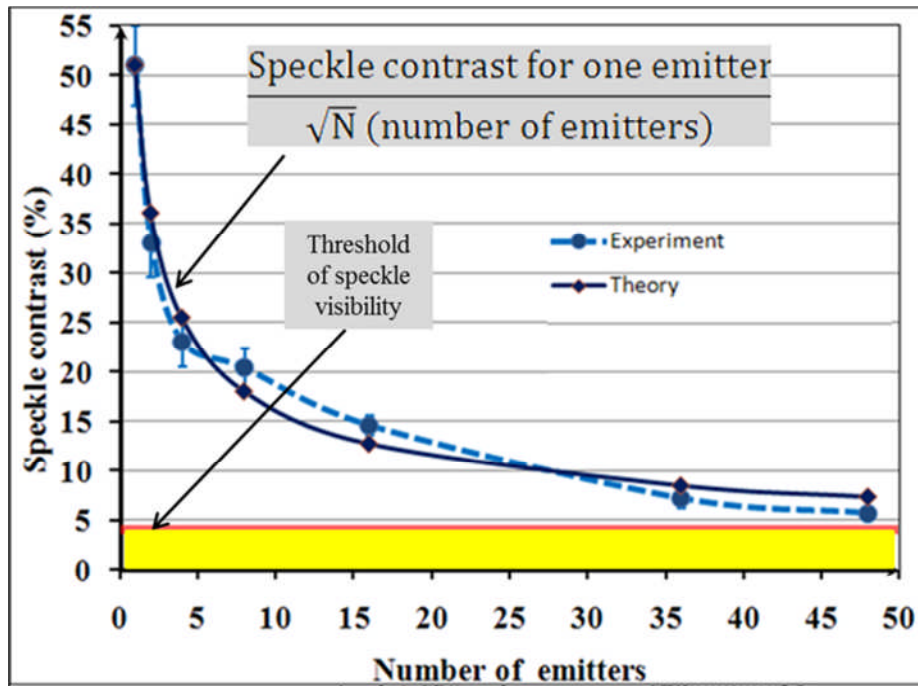


Figure 10.20. Speckle contrast obtained as a function of number of independent emitters. Any speckle pattern with a contrast below the red line (<4%) is imperceptible.

The black solid curve in Figure 10.20 indicates the maximum suppression of the speckle contrast due to the combination of  $N$  independent speckle patterns ( $N^{-1/2}$ ) and the dotted graph shows the experimental results. On the viewing plane, which is the CCD camera array, the speckle contrast will be influenced by the angle subtended by all the emitters. The subtended angle is different for the horizontal and vertical emitters. The theory and experiment agree to within experimental error.

### 10.3.1.2.2: Speckle Pattern with Various Numbers of Diffusers in the System

Figure 10.20 indicates that the chosen lasers will bring the speckle contrast very close to the region where it cannot be observed when all of the emitters are operating. To examine the effect of the diffusers, we recorded the speckle pattern in the presence of different numbers and orientations of diffuser. The experimental arrangement and the position of the diffusers are shown in Figure 10.18. (In the 3D system one horizontal and one vertical diffuser are used in the same order). The diffusers were arrays of polymer cylindrical microlenses and only 10 emitters were used to avoid damaging the diffusers. Figure 10.21 shows the speckle pattern after using different numbers of diffusers.

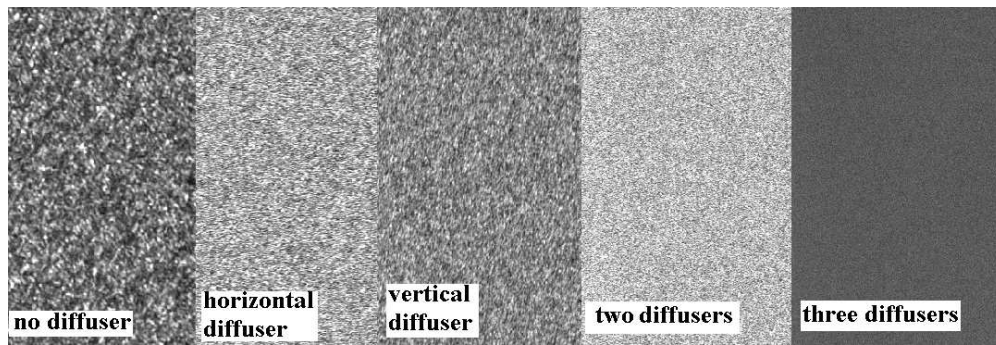


Figure 10.21: The speckle patterns of the laser beam with different number of diffusers in the system. Speckle contrasts from left to right are 30.2%, 13.3%, 10.9%, 5.7% and 1.8% respectively.

The speckle contrast due to different diffusers is shown in Figure 10.22 as a function of the number of horizontal and vertical diffusers. Each diffuser diverges the light by an additional  $30 \pm 5$  degree.

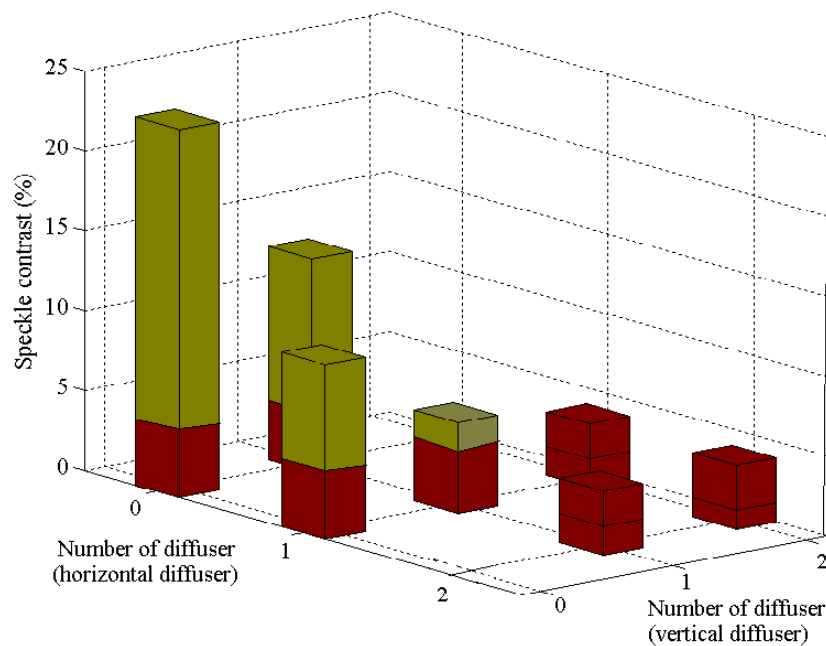


Figure 10.22. Speckle contrast for various numbers and orientations of diffusers. Each diffuser diverges the light by  $30 \pm 5$  degrees ( $523 \text{ mrad}$ ). 10 NECSEL emitters are operating.

The red surface in Figure 10.22 indicates the 4% contrast limit and the green bars show the measured speckle contrast. The contrast is below the visible limit when there are three diffusers in the system. The speckle contrast is 5.7% with two horizontal and vertical diffusers and 10 emitters. It should be noted that in this experiment the speckle contrast was reduced from 22.3% to 5.7% with two diffusers.

Therefore, from this measurement and Figure 10.20, we can infer that the speckle contrast will be below the quoted sensitivity in the 3D system if we use all 48 emitters and two diffusers. However, it must be mentioned that the effects of additional system lenses, the SLM, diffraction due to the micro lenses, and surface scattering must also be taken into account to find the final degree of speckle contrast. Another issue to keep in mind is that the experiment results are based on the reflective speckle as we use a white print quality paper in the experimental configuration (Figure 10.18). The HELIUM3D system is not a reflective projection system and the viewer essentially looks directly at the screen which receives the transmission speckle pattern. Therefore, further measurements have been done on a system which simulated the HELIUM3D system. In the experiment, we try to measure the speckle as it is seen by the viewer so we use a combination of lens and iris in front of the CCD sensor to record the speckle pattern.

### **10.3.2: Characterization of Speckle in the HELIUM3D System**

We explained the system and also the measurement equipment and software in the previous chapters and sections. In the next part of this chapter, the speckle is monitored at several points through the system in different places and speckle contrast changes along the system after each component is reported for the first time. This shows the effect of each part of the system on the speckle which is helpful at the next stage for reducing the speckle contrast. All of the lenses and other components are arranged as they are in the HELIUM3D system with the same specification. In the experimental configuration used for speckle characterisation a static aperture was used (Figure 10.23) instead of the real dynamic SLM of the final display. To investigate the speckle contrast the experiment was arranged as shown in Figure 10.23. To investigate the speckle situation in the HELIUM3D system several experiments were carried out to compare the effect of beam shaping and line scanning compared to the static image system. To find the effect of the optical components in the system on the speckle contrast a single green laser was used.

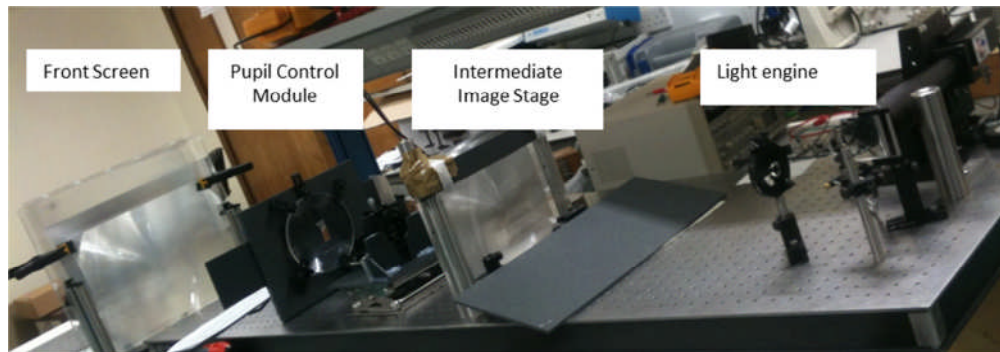


Figure 10.23: The experimental configuration for speckle and uniformity measurement.

The laser source was a 300 mW, DPSS (Diode-Pumped Solid-State) model from Laser 2000 ltd. with a measured wavelength of 532 nm. Free-space beam-shaping optics is used to shape the output of the laser into a line after expansion using a 5× beam expander. To shape the expanded beam into a line a cylindrical lens was used to focus the light in the horizontal direction. The shaped beam then was scanned on a spherical lens which was used as the projection lens.

### 10.3.2.1: Effect of the Scanning Image on the Speckle Pattern

In the HELIUM3D system the image is formed by scanning a line of light on the LCoS (liquid crystal on silicon) intensity modulator. To find the effect of the scanning line, the speckle patterns after the horizontal diffuser and at the viewer position are investigated and compared. A simple beam shaping optic element (a cylindrical lens) is used to shape the output of the laser into a line after expansion using 5× beam expander. Figure 10.24 shows the result, which is the light line at the position of L2 (the horizontal diffuser).

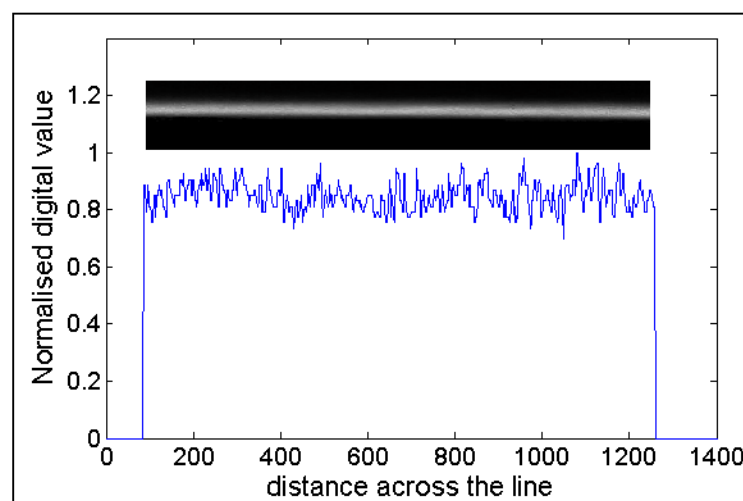


Figure 10.24: Light line at the horizontal diffuser. The line is 260  $\mu\text{m}$  wide. The speckle pattern is  $11.5\% \pm 2.5\%$  across the line.

Figure 10.25 shows the speckle contrast at the viewer position for different output of the light engine. The output of the light engine was the expanded laser beam without the beam shaping part (The cylindrical lens was removed not to shape the beam into a line), just a static line (light column without scanning), and a scanning line (real system).

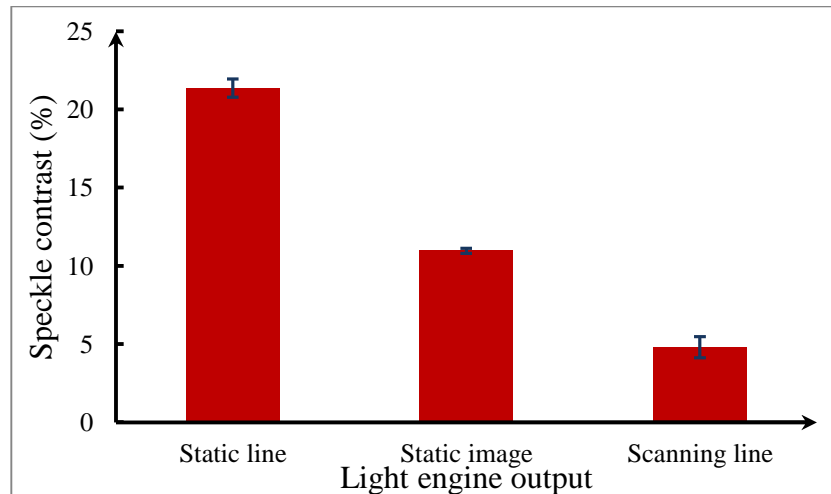


Figure 10.25: Speckle contrast at the viewer point for different output at the light engine.

The speckle pattern was also recorded at different distances from the horizontal diffuser (Figure 10.23). Figure 10.25 shows that the speckle contrast at the viewer strongly depends on the configuration of the illumination. Moreover, Figure 10.26 shows that the speckle contrast varies considerably throughout the system. For example, the speckle contrast at the position of the SLM (500 mm away from the horizontal diffuser) is even less than the speckle pattern at the viewer position (2.5% at the SLM and 4.9 % at the viewer).

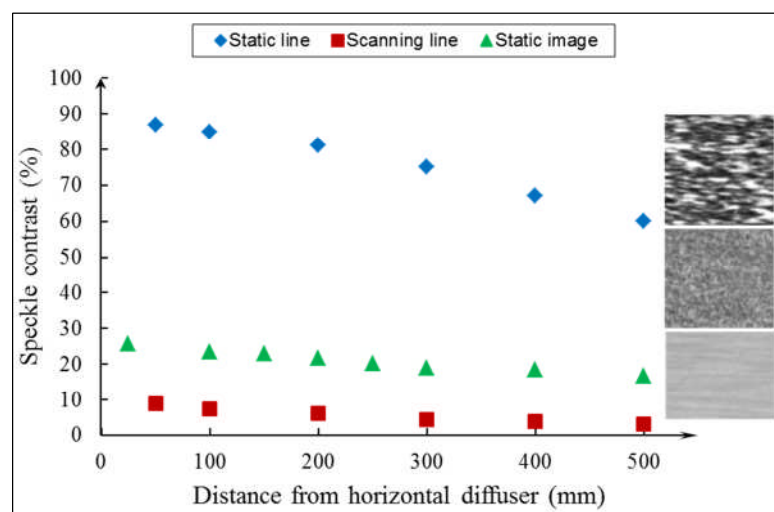


Figure 10.26: The speckle contrast for different types of image at the position of the horizontal diffuser.

The results in Figure 10.25 and Figure 10.26 show a difference in the speckle contrast values with different output of the light engine while the same laser source is used for all the experiments. Each particular recorded speckle pattern is due to the interference of several beams at the detector. The laser beams come from different parts of the system with random roughness and angle of emission, therefore, the speckle pattern is due to the overlapping of several speckle patterns created by the laser beam passing from the different parts of the system. Several speckle patterns overlap and the overall speckle contrast is the result of the combination of the integrated patterns. Figure 10.25 shows that the speckle contrast increases considerably when an image is formed in the shape of a line. This is expected as the detector is illuminated by a small part of the lens. However, scanning the line solves the problem as it is scanned with a frequency of at least 60 Hz which allows the scanning time to be sufficiently small for the human eye to integrate the speckle patterns. The exposure time of the camera in the scanning line case was set to be one scan period. The speckle pattern was checked by looking at it and making sure that the recorded pattern was similar to the one observed. Figure 10.27 shows the speckle pattern contrast as a function of scanner frequency.

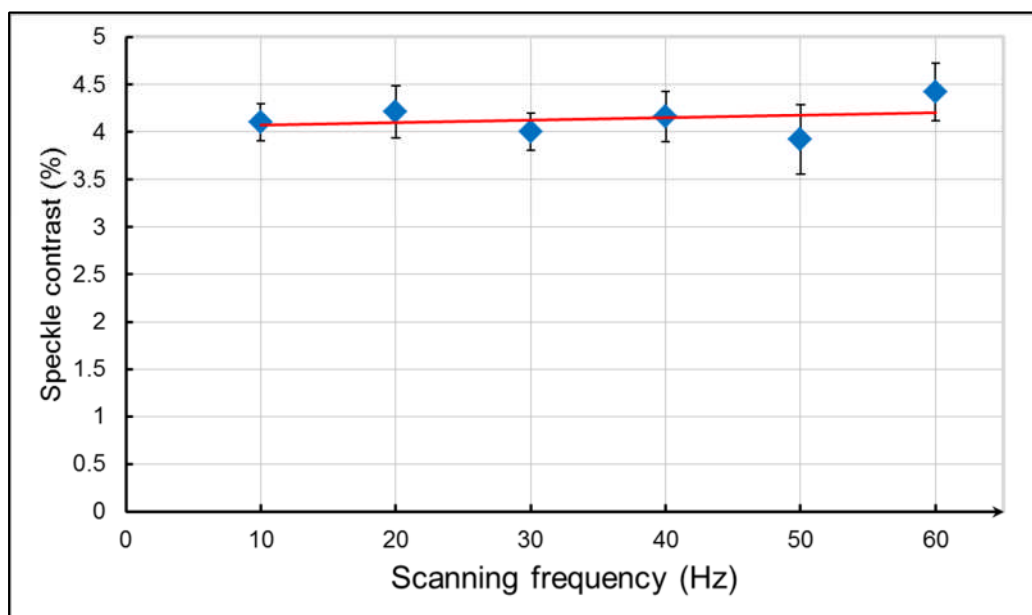


Figure 10.27: Speckle contrast at different scanning frequencies. The speckle is recorded 300 mm away from horizontal diffuser. The exposure time is one scan period.

As can be seen in Figure 10.27 the scanning frequency does not alter the speckle contrast as long as the exposure time is one period. Having determined that the scanning frequency does not change the speckle pattern, the effect of the width of the scanned area was investigated; this can be altered by changing the projection lens or the distances between lenses [10.12]. To test the effect of the scan-width on the speckle the speckle contrast for different scan-widths was measured. Figure 10.28 shows the results

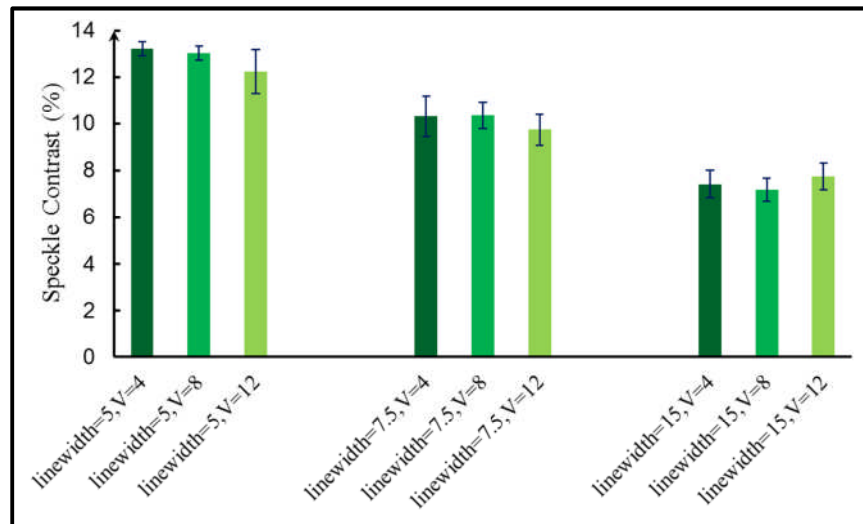


Figure 10.28: Speckle contrast 300 mm away from horizontal diffuser. The frequency is 60 Hz and the speckle contrast is measured for different scanning amplitudes. Line width is in cm and V is pick to pick scanning voltage.

The results in Figure 10.28 show that the speckle contrast reduces with increasing the size of the scanning area. It is understandable as the speckle pattern is formed as the results of the light beams coming from different parts of the screen. Increasing the size of the screen produces more light beams with different phase as they pass through different parts of the screen, which can have different roughness profile, and also their path to the camera is different to each other so they arrive with altered phase shift.



### 10.3.2.2: Speckle Contrast through the System

The speckle pattern variation with scanner parameters which was investigated in the previous section shows that the speckle contrast varies through the system due to the effect of optical components and the divergence and convergence they cause to the beam passing through the system. To find the speckle variation in different parts of the system the speckle contrast was recorded in several places and the results are shown in Figure 10.29. The results show how the speckle pattern contrast changes from the horizontal diffuser to the superlens screen, where the incidence angle of the light onto the screen is determined by the SLM aperture. The results show the speckle contrast reduces after the horizontal diffuser and increases after the SLM.

This is due to the convergence of the light after the horizontal diffuser and divergence of the light after the SLM. The SLM blocks some of the light and just the illumination which hits the aperture area can pass through the aperture; this is why the speckle contrast increases more rapidly after SLM. Figure 10.29 also illustrates how the speckle contrast changes by moving the camera from the viewer position. The graph shows that the speckle changes by only a small amount when the camera moves away from the viewer position.

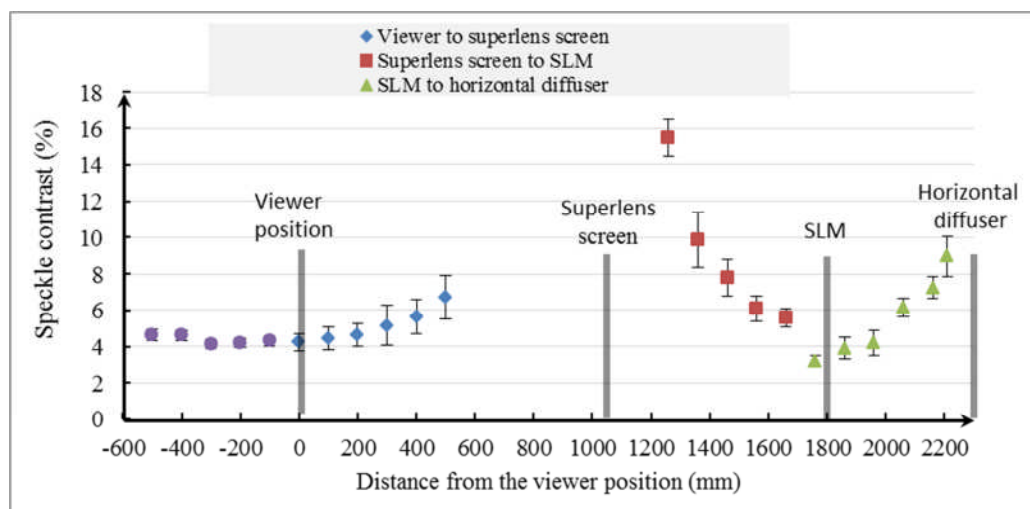


Figure 10.29: Change of the speckle contrast as the camera is moved from the position of the viewer with a static SLM aperture. The positive distance is moving towards the screen and the negative value indicates moving away.

In Figure 10.29 the viewer position is defined as the real image of the aperture that is formed in the viewing field. The real image of the SLM in the viewing field is referred to as the conjugate plane and a viewer position in this plane does not require the position of the aperture to move over the duration of a scan. In the HELIUM3D dynamic system if the viewer changes position in the  $z$  direction the SLM aperture changes position throughout the scan. This is achieved with the use of a fast ferroelectric liquid crystal (FLC) linear array[10.12].

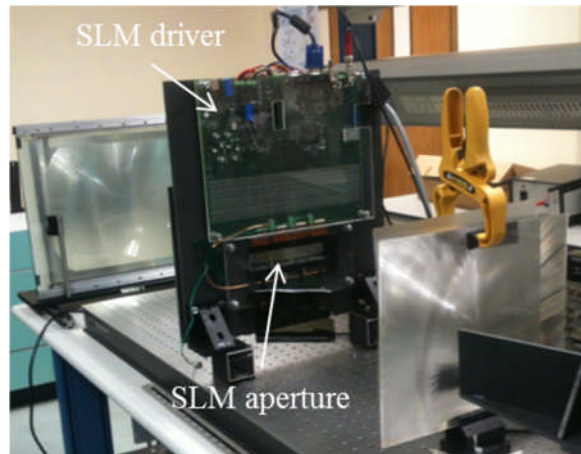


Figure 10.30: Real SLM functioning with the head tracker in HELIUM3D system.

Figure 10.31 shows the speckle contrast results with the SLM implemented in the system for the dynamic aperture measurements. The aperture in the SLM is moving over the time of the scan in order to accommodate the range of  $z$  coordinate values.

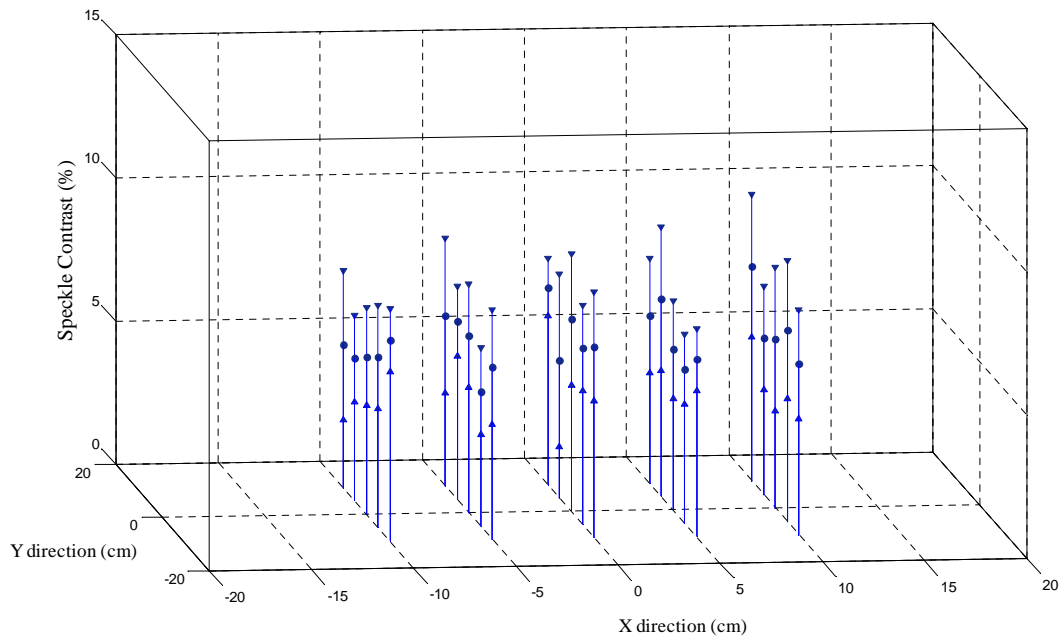


Figure 10.31: Speckle contrast variation with viewer position. The information of the position of the viewer is fed back to the SLM to adjust the conjugate plane.

The results in Figure 10.31 do not show any significant change in the speckle pattern in different positions of the viewer after experimental error has been accounted for.

The results in Figure 10.31 are expected as the dynamic aperture refocuses the light into the new position of the viewer. Moreover, there is no change on the illuminated area in the transfer screen system and of the rays from all of the surfaces of the transfer screen contribute into the speckle pattern at the viewer position. One aspect which is recognisable though is that the speckle contrast is larger compared to the situation in Figure 10.29 where the aperture is a slit. The speckle contrast is on average 4% higher with the dynamic aperture which could be due to the structure of the SLM and the effect of the liquid crystal cells. Several cells filled with liquid crystal are joined together to form the aperture. The increase of the speckle pattern must be due to the cells as everything in the experiment configuration is exactly the same.

### 10.3.2.3: Speckle Pattern using Simulated eye

Figure 10.32 shows the recorded picture at the viewer position when the dynamic SLM is in operation. Speckle analysis in this case, requires some image processing.

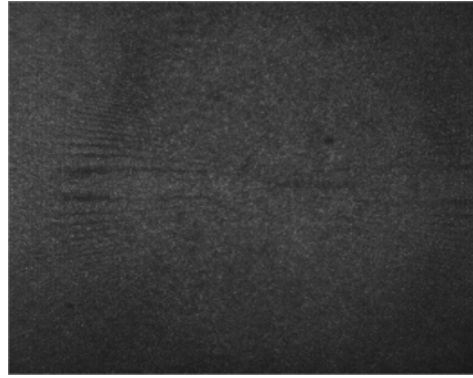


Figure 10.32: The detected picture at the viewer position

The most obvious features are that it contains some Moiré patterns which are due to the overlap between the linear pattern of the superlens screen and the circular pattern of the Fresnel lens. This Moiré patterns can be reduced by choosing an optical component with high quality and design the periodic structures to match and reduce the interface pattern. This will imply redesigning the system and increasing the cost. The other solution is to remove the pattern by using image processing methods such as Gaussian blurring that reduces the sharpness by blurring the image. However, it reduces fine features and speckle data and cannot eliminate the Moiré pattern completely. Therefore, analysing the speckle required three different analysis techniques, namely:

1. A low frequency cut filter needs to be applied to reduce the effect of the non-uniformity
2. The fringes must be separated from the image; however, sometimes the fringes are high frequency so that removing the fringes removes the speckle data too. Different filter and blurring technique were used to reduce the effect of the fringes.

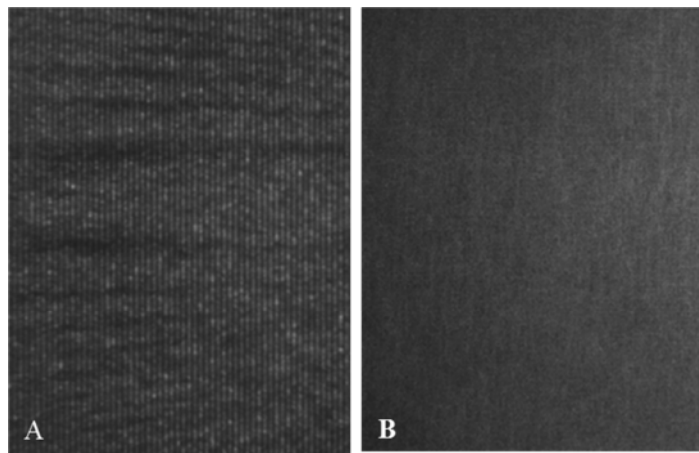


Figure 10.33: Applying filter and blurring to reduce the effect of fringing. A: recorded picture, B= processed image

Figure 10.33 shows the results of the speckle measurement and the processed image. To calculate the speckle contrast, first a 2-D median filtering and blurring technique were applied to erase the effect of high frequency components created by the micro lens and Moiré fringes. The speckle software was also used to process the data and the best result for the speckle contrast was calculated to be  $9.3 \pm 2\%$  at the viewer position. These results were obtained with the use of a single emitter laser.

### 10.3.3: Speckle in Light Emitted from Optical Waveguides

For the measurement of the speckle pattern of light emitted from a waveguide, several optical fibres with the same length (2 m) and the same numerical aperture (NA=0.39) and different core diameter were chosen. The fibres have different core diameter therefore, the number of modes in the fibre with the larger diameters is greater. The speckle pattern from different fibres was recorded and compared.

What we are trying to investigate is the effect of the modes on the speckle pattern. A commercial camera was used to look at the end of the fibres. Figure 10.34 shows the speckle pattern at the end of the fibres with different core diameters. The USB FibreVu Probe made by Digital Lightwave Company, is specially designed to look at the end of the fibres in telecommunication applications to observe the end of the fibre after cleaning or cleaving.

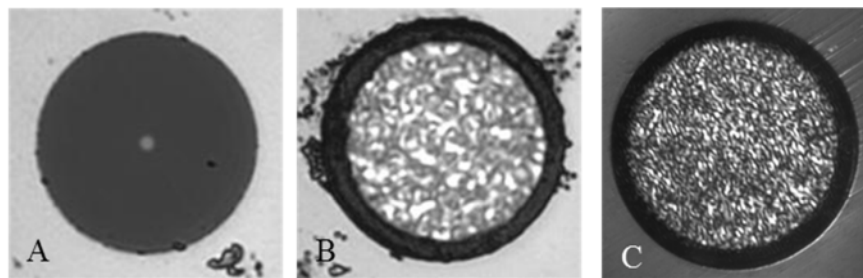


Figure 10.34: Speckle pattern at the output of optical fibre. A: 9  $\mu\text{m}$  core diameter, B: 100  $\mu\text{m}$  core diameter, C: 200  $\mu\text{m}$  core diameter

The output of a 640 nm diode laser was coupled into the fibres and the speckle pattern at the end of the fibre was recorded. The pattern is due to the interference of different modes on the surface of the camera sensor. Figure 10.34 shows that, in the case of single mode fibre (A) there is no speckle pattern as there is just one mode propagating inside the fibre. Part B and C in this figure show interesting patterns though. The speckle size, which is the size of the dark and white spots, is different and smaller for the 200  $\mu\text{m}$  core fibre.

To investigate this effect more and to find the diameter of the speckle spots, another experiment was arranged. The speckle pattern for fibres with different core diameters was recorded and the results are presented in Figure 10.36 and Figure 10.37. The experimental configuration is shown in Figure 10.35. The speckle pattern was derived from sending the output of a DPSS green laser (532 nm) into the fibre. The fibres were coiled around a cylindrical column to make sure that all the modes were excited inside the fibre. A CCD camera was placed 50 cm away from the output of the fibre and the intensity fluctuation due to the speckle phenomena was recorded by the CCD camera.

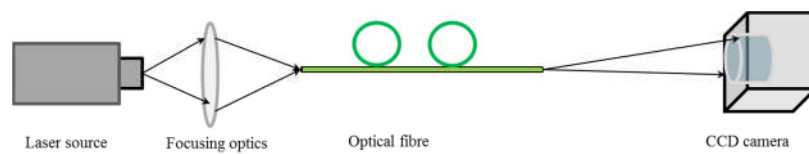


Figure 10.35: Schematic diagram for the speckle pattern recording from an optical fibre.

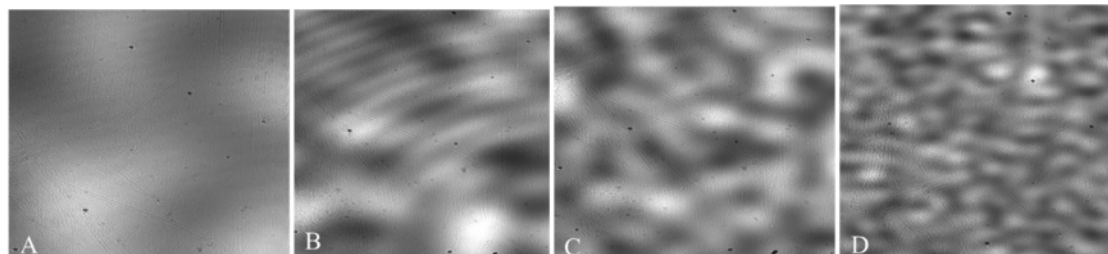


Figure 10.36: A sample of the Speckle pattern 50 cm from the output of the fibres with NA= 0.39 and core diameter of A: 200  $\mu\text{m}$ , B: 400  $\mu\text{m}$ , C: 600  $\mu\text{m}$ , and D: 1000  $\mu\text{m}$ .

The speckle size was calculated by counting the number of pixels in each of several bright and dark spots and was compared with the speckle spot diameter calculated with image processing using the first minimum of the 1D autocorrelation function. The new speckle program introduced in section 9.4.1 was used for calculation.

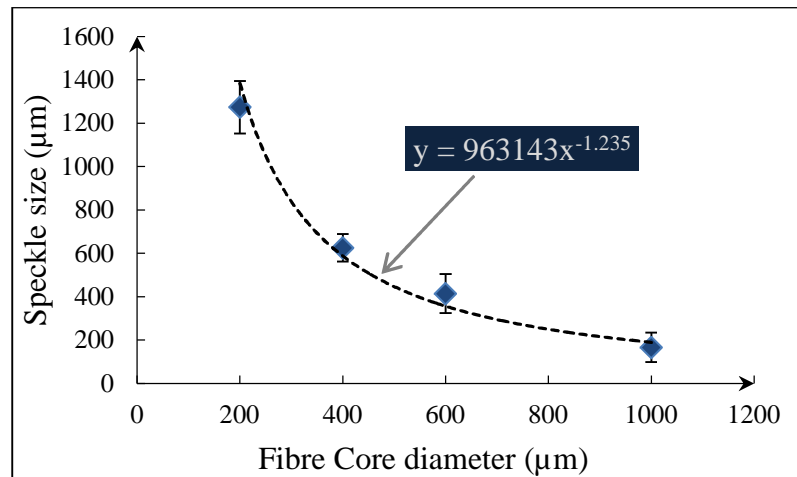


Figure 10.37: Speckle size versus the core diameter of the fibre. The NA of the fibres are the same and the speckle contrast is  $21 \pm 5\%$ .

Figure 10.37 shows the results for the speckle size for fibres with different core diameters. It should be mentioned here that the size of the speckle depends on the recording configuration[10.13] but the interesting point is the reduction of the size of the speckle. Speckle is normally judged based on the speckle contrast in the display systems[10.14]. In Figure 10.36 the speckle contrast for all of the patterns is the same ( $21 \pm 5\%$ ) but there is a difference in the speckle size. There are two important issues to be considered which has not been investigated by researchers: first of all the speckle contrast and speckle perception is different. Speckle contrast is due to the fluctuation of the intensity across the pattern and could be the same for fluctuation with different frequency. This can be understood by considering the definition of the speckle contrast which is the standard deviation of the intensity fluctuation normalised by the average of the fluctuations.

However if the fluctuations are at a very high frequency then the human eye will not be able to resolve it and will, therefore, not see it.

The second issue is about speckle reduction. Optical fibres have been used in the display system and the speckle contrast has been reduced by vibrating the fibre. Vibrating the fibre changes the distribution of the energy inside the modes and therefore, the phase shift between different modes varies and as a result the speckle pattern will be different. So the speckle contrast is reduced if the vibration is fast enough and phase change is sufficient to shift the speckle patterns in time and integrate them to cover each other. This is where the size of the speckle is important.

Producing enough phase shift and as a result enough shift in the speckle patterns to cover the dark spots depends on the size of the dark spots. Figure 10.38 can clarify this claim.

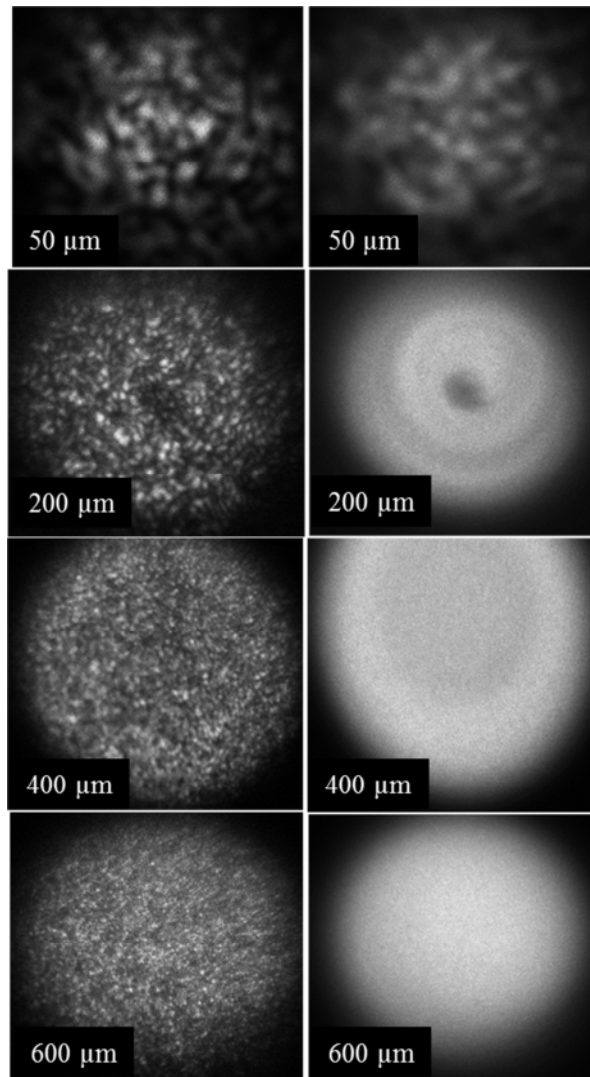


Figure 10.38: Far field speckle pattern (30 cm from the output of the fibre) without (left) and with (right) vibration of the fibre. Fibres have different core diameters written on each speckle pattern photograph.

In Figure 10.38 the speckle pattern from fibres with different core diameters are shown. The patterns were recorded using the configuration in Figure 10.39.



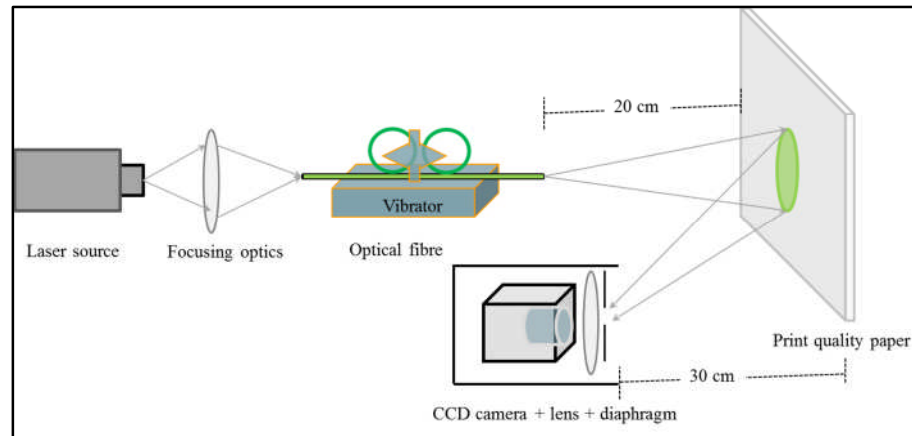


Figure 10.39: Schematic diagram for the experiment of reducing speckle contrast by vibration optical fibre.

The recording camera shown in Figure 10.39 is the same as Figure 10.30. The speckle pattern was recorded before and after vibrating the fibres with different core diameter. The vibrating frequency was 50 Hz and the amplitude was 0.5 cm for all fibres. Results in Figure 10.38 show that vibrating the fibre with the 50  $\mu\text{m}$  core area reduces the speckle contrast but does not remove the non-uniformity due to the speckle completely, whereas the same vibration removes the speckle pattern completely in the fibre with core diameter of 600  $\mu\text{m}$ . This effect happens not because the speckle contrast in the fibre with 50  $\mu\text{m}$  core is higher than the 600  $\mu\text{m}$  fibre, but because the speckle size in the fibre with larger core diameters is smaller. Therefore, a small change in the position of the speckle patterns can cover the small dark spots and so the result of integrating the speckle patterns removes all of the non-uniformity.

### 10.3.3.1: Speckle Contrast Reduction using Multimode Waveguides

For the last part of this chapter, the information on the previous chapter is combined with the idea in chapter 8, for using a waveguide for beam shaping and beam homogenising. It was proved that using optical fibres with higher core diameter helps to reduce the speckle contrast more easily and effectively. Also the advantage of larger core was producing a larger number of modes and as a result higher phase shift. Therefore, if we produce even higher modes then the phase shift between modes can even reduce the coherency of the laser beam and as a result there will not be any speckle problem. Optical waveguides were used in chapter 9 for preparing the beam for a 3D display system.

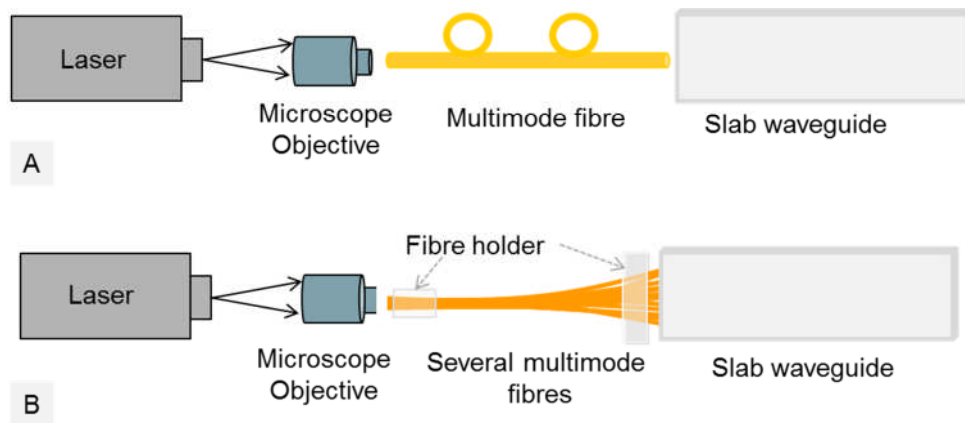


Figure 10.40: Schematic diagram of the use of a slab waveguide for beam homogenization and de-speckling.

To investigate the effect of the waveguide on the speckle pattern the same waveguide is used here and the speckle pattern at the output of a slab waveguide is compared with that from a 100  $\mu\text{m}$  fibre in Figure 10.42. The experimental set-up is shown in Figure 10.41.

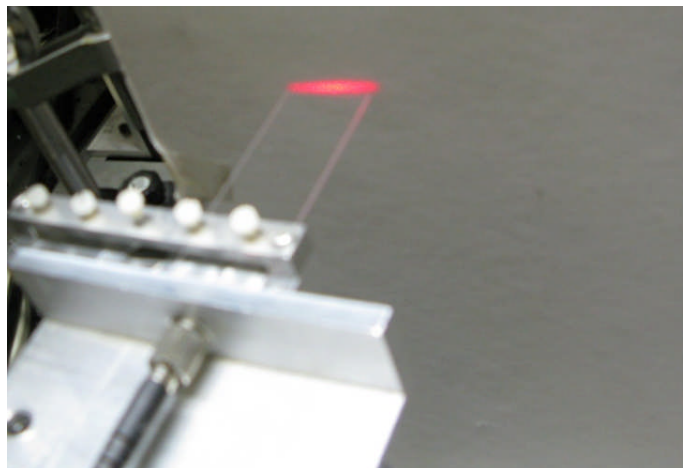


Figure 10.41: waveguide speckle investigation. Low power red laser is used for the alignment

The output of a green laser was coupled into a 100  $\mu\text{m}$  core fibre and the fibre was aligned with a slab waveguide. The waveguide is made of glass ( $n=1.34$ ) with a size of 15 mm  $\times$  70 mm  $\times$  1 mm. The speckle recording camera was the same as shown in Figure 10.39.

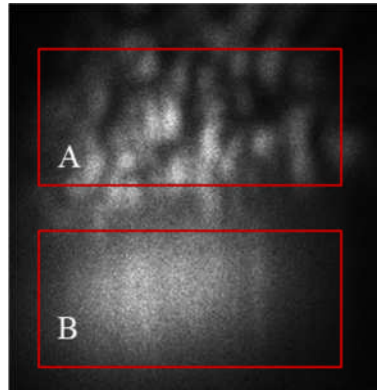


Figure 10.42: Speckle pattern at the output of 100  $\mu\text{m}$  fibre (A) and a slab waveguide (B). speckle pattern shown in Figure 10.42 indicates a very interesting difference between the output of the optical fibre and the waveguides. In fact, there is no visible speckle in the waveguide output as the speckle contrast in part B Figure 10.42 was measured to be 2.9%. Figure 10.43 shows the scanned output of the slab waveguide that was used for laser beam homogenization in chapter 9. The output the waveguide was scanned with a frequency of 60 Hz. The speckle pattern has been removed completely.

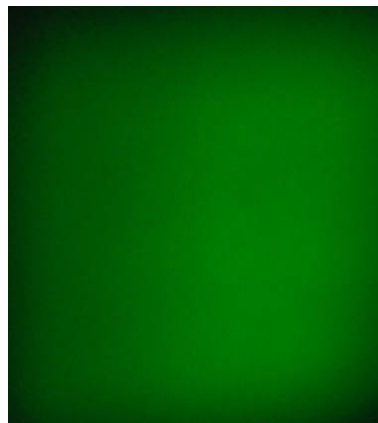


Figure 10.43: Scanned output of the slab waveguide (shown in Figure 10.42 part B) the speckle contrast is one percent. In fact there is no speckle pattern

The reason for the speckle contrast reduction can be explained based on what we mentioned for the optical fibres. The number of modes in the waveguide is much greater here and the phase shift causes the speckle size to be small and not resolved by the human eye. In other words, the phase shift between the modes at the output of the waveguide removes the coherency of the light therefore there is no speckle pattern. The speckle contrast in Figure 10.43 is  $1.25\% \pm 0.83\%$ .

## 10.4: Speckle Pattern and Human Perception of Speckle

In chapter 3, several methods for reducing the speckle contrast in display systems were reviewed. It was mentioned that the speckle contrast should be reduced to less than 4% and in some work it has been reported that it should be less than 1%. In this section, the speckle pattern is considered and investigated from a different point of view where the speckle visibility is considered with the human ability to detect and to resolve an object. The human ability to perceive the details of an object is determined by the size and the contrast of the object. Therefore, by considering only the speckle contrast (as has previously been considered by companies) and not the speckle size, or the integration time of the eye, an important part of the speckle information is ignored, which can affect the speckle visibility. The human eye is a very powerful and complicated system; however, there are limitations on the image size that can be resolved and the contrast discrimination which must be considered. In Table 10.1, some of the limitations of a human eye are listed.

Table 10.1: Some of the limitations of Human eye in perception [10.15].

Normal viewing distance	250 mm
Angular resolution	1'
Spatial resolution	80 $\mu\text{m}$
Average cell distance on retina	1.5 $\mu\text{m}$
Spectral range	400 nm - 800 nm
Contrast perception	4%
Focal length	10

In human eyes, the optical receptors lie on the retina and like any other optical detectors if the size of the image of an object is large with respect to the size of the retinal receptors then the image will be recognised with the general shape of the object[10.15].

There is an issue here that no matter if the image on the retina is sharp (high contrast) or blurred (low contrast), if the size of the image on the retina is less than the visual resolution of the eye, the object will no longer be visible. On the other hand, no matter what the size of an object is and how large it is respect to the receptors size, if the difference between the illumination of the object and the background does not exceed the luminance threshold of the eye in that level of illumination, the object will not be recognised.

A dark object can be perceived based on the luminance difference threshold which is known as the Weber-Fechner fraction[10.15]. Based on this fraction, a line subtending as little as 0.5 seconds of arc may be seen if the contrast is about 2%[10.15]. The function of perception is very complicated and depends on several different optical and biological parameters and in fact, it changes from one person to another. Considering all the aspects of the speckle perception by human eye is out of the scope of this research as the biological information must be taken into account. However, in this research the contrast sensitivity of the human eye for different spatial frequencies is considered for the recorded speckle patterns. In this case, both contrast and speckle size are considered at the same time. The idea is to find the spatial frequency of the speckle pattern (which depends on the speckle size in a way that smaller speckle size is related to the higher spatial frequency). As the contrast sensitivity of the human eye changes for different spatial frequencies, relating speckle size and contrast will determine if the speckle is perceivable for the human eye.

#### **10.4.1: Contrast sensitivity of human eye**

The human ability to perceive the details of a scene depends on the size and the contrast of the object presented. There are several factors that can affect the perception ability, which is called visual acuity[10.15], such as size of the pupil, illumination, time of the exposure of the target, area of the retina which is simulated, adaption of the eye and the eye movement. Considering all these parameters increases the complexity of the investigation however, research has been performed to understand the human perception criteria[10.15-17]. One of the results of the research that is used in this chapter is the relationship between the contrast sensitivity of a human eye and the spatial frequency of the object. This is called the contrast sensitivity function (CSF) which determines the maximum resolution of the human eye[10.17].

The CSF determines the required contrast for a particular spatial frequency to be seen by the viewer. In fact, each individual person has his/her specific CSF as it depends on several personal parameters but as an average study, CSF has been determined for different groups of humans based on different parameters such as age and object illumination[10.18]. Most of these experiments are based on using gratings and altering the spatial frequency and the contrast of the bars in a grating[10.19]. A grating pattern was used by Campbell and Green to determine the maximum resolution of the human eye by finding the Contrast Sensitivity Function (CSF)[10.19].

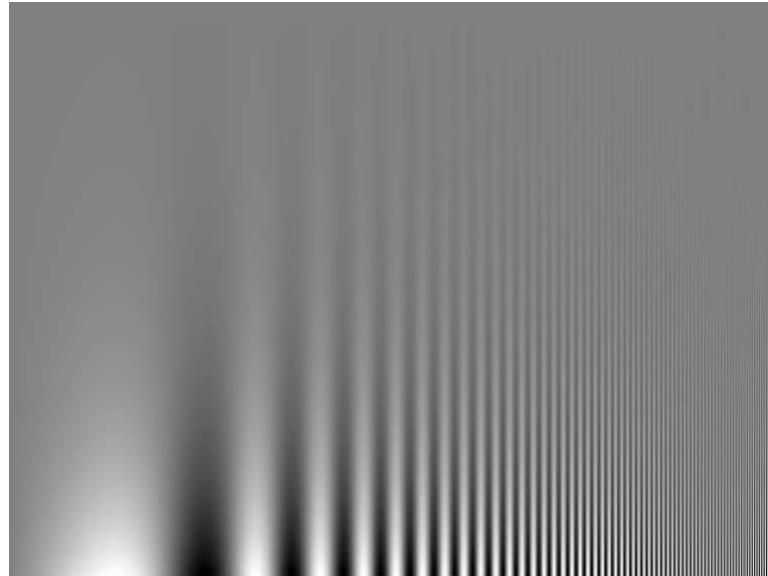


Figure 10.44: A sample of the patterns which shows gratings with different grating spacing and contrasts used to find the contrast sensitivity function of human eye.

In these experiments, the contrast threshold for several grating patterns with different spatial frequencies were measured and from the results of these experiments the CSF was derived. The luminance profile of the grating patterns was chosen to be either sinusoidal or square wave shape and the necessary contrast for the sinusoidal pattern to be perceived by a human over a range of spatial frequencies was determined by experiment [10.19]. A sample of the gratings with various profiles are shown in Figure 10.45 where the amplitude of the sine/square wave determines the contrast and the frequency of the pattern is the spatial frequency.

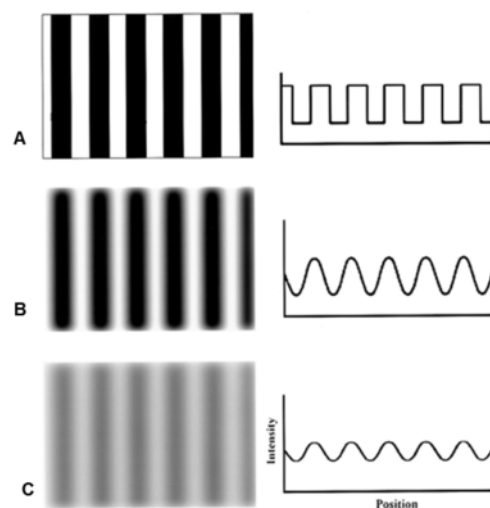


Figure 10.45: Examples of a sinusoidal and square grating pattern. A: square shape, B: sinusoidal shape, C: sinusoidal with lower contrast compared to part B.

The results of the experiment and the CSF are shown in Figure 10.46. In this figure, the horizontal axis is in cycle/degree which shows the spatial frequency of the grating.

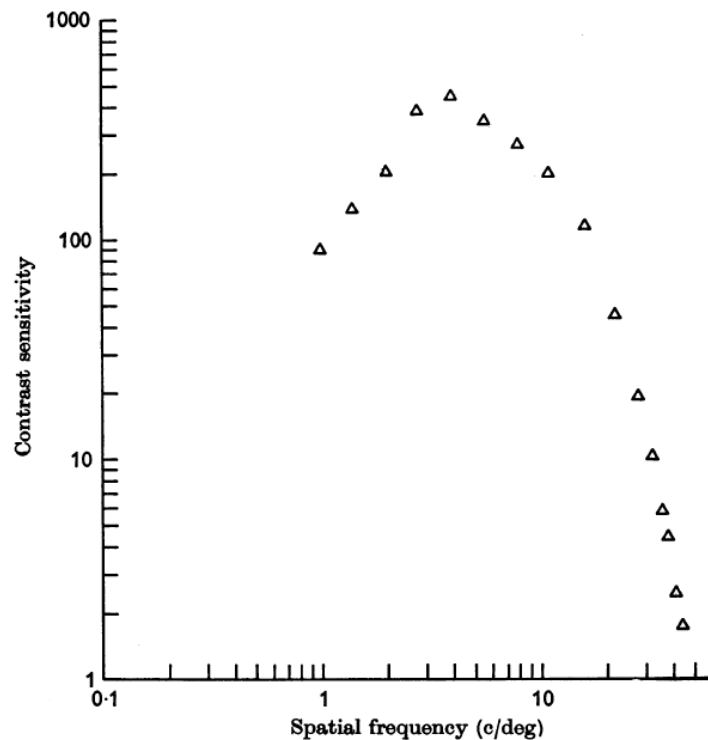


Figure 10.46: Contrast sensitivity for sine wave grating derived by CAMPBELL [10.19]. The frequency in the horizontal axis is in cycle/degree.

In Figure 10.46, the axes are logarithmic and the graph shows the contrast sensitivity for different spatial frequency for viewer distances of 285 cm. As shown in the graph, the maximum sensitivity took place around a spatial frequency of 4 cycles/degree and the sensitivity is reduced for higher and lower frequencies. This means that the human eye (of the participating viewer in the experiment) will be able to detect the features with spatial frequency of 4 c/degree in the lowest perceivable contrast.

The information in Figure 10.46 is used to relate the speckle perception with the speckle size and contrast for the display. If we determine the spatial frequencies in a speckle pattern, the CSF can determine the required contrast for each particular frequency component for it to be observed by the viewer. The frequency components of the speckle pattern depend on the speckle sizes existing in the pattern. Therefore, the speckle perception is tested not only based on the contrast of the speckle pattern but also on the speckle spot diameter.

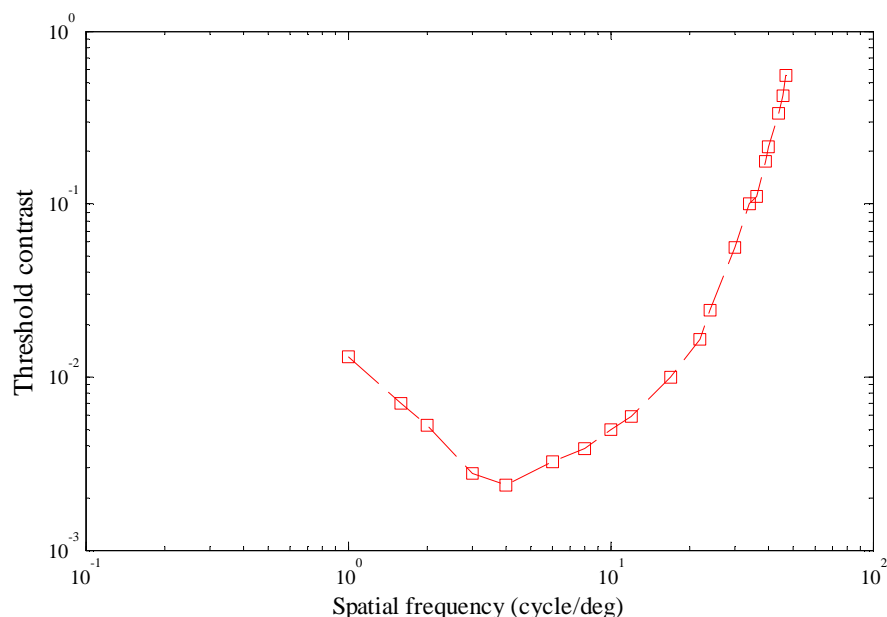


Figure 10.47: The contrast sensitivity function of the human eye. These data were extracted from the graph in Figure 10.46 as the original data is not available.

We propose to do the calculation cycle: We assume that the response in Figure 10.47 is independent of angle of the periodic lines (this assumption can be avoided by recalculation of the special frequency based on the distance of the viewer to the screen and the size of the speckle diameter). Now we carry out a 2D FFT of the speckle pattern to obtain a plot of all of the spatial frequencies present in the speckle. Then we filter this pattern using the graph of Figure 10.47.

Firstly we must convert the graph to the threshold of contrast that can be perceived; Then we rotate the graph in around the vertical axis assuming that the same graph applies independent of rotation in the field of view. Then we use this as a threshold so we subtract all contrasts or amplitudes of the Fourier components which are less than this curve. Finally we inverse Fourier Transform to obtain the remaining speckle pattern that the human observer can perceive. The amount of speckle remaining can be quantified by integrating either in the real domain or in the Fourier domain after thresholding.

This is the first time anyone has proposed or demonstrated this new technique and means that laser displays become more of a reality as although the speckle is present we can arrange it to below the level of human perception. Unfortunately due to the short of time, we were not able to characterise the method and test it with a real speckle pattern. This is considered as future research.



## **10.5: Conclusions:**

In this chapter, speckle pattern as a source of non-uniformity in the image in laser illuminated display systems were investigated. The Granulometry method was used to find the speckle spot diameter. This method was compared with the conventional method of using an autocorrelation function. It can be concluded from the results that in most of the speckle patterns where the black and white spots are symmetric Granulometry provides better results for the grain size. However, if the spots are not circular, autocorrelation has more accuracy. These two methods should be joined together for calculating the speckle size.

The speckle contrast was mapped at the viewer's position. Such results have never been shown for any system before and have the advantage of showing the fluctuation of speckle contrast across the display system and the effect of each optical component in the system on the speckle pattern.

For the measurement of the speckle pattern of light emitted from a waveguide, several optical fibres with the same length (2 m) and the same numerical aperture (NA=0.39) and different core diameter were chosen. The speckle pattern for fibres with different core diameters was recorded and the speckle spot diameter was calculated. It was shown that the speckle size reduces as the diameter of the fibre increases. However, the speckle contrast is constant. Two interesting results can be concluded from this experiment: Speckle is normally judged based on the speckle contrast in the display systems. The speckle contrast for all of the recorded patterns was the same ( $21 \pm 5\%$ ) but there was a difference in the speckle size. There are two important issues to be considered which have not been investigated by researchers: first of all the speckle contrast and speckle perception is different. Speckle contrast is due to the fluctuation of the intensity across the pattern and could be the same for fluctuations with different frequencies. However if the fluctuations are at a very high frequency (which means the speckle spots are small) the human eye will not be able to resolve it and will, therefore, not see it.

The second issue is about speckle reduction. Optical fibres have been used in the display system and the speckle contrast has been reduced by vibrating the fibre. Vibrating the fibre changes the distribution of the energy inside the modes and, therefore, the phase shift between different modes varies and, as a result, the speckle pattern will be different. Therefore, the speckle contrast is reduced if the vibration is fast enough and phase change is sufficient to shift the speckle patterns in time and integrate them to cover each other. This is where the size of the speckle is important. Producing enough phase shift, and in result, enough shift in the speckle patterns to cover the dark spots depends on the size of the dark spots. The smaller the speckle size, the smaller the movement (less mode scrambling) required to remove the speckle. We used a vibrator and show that speckle contrast in a 50  $\mu\text{m}$  core fibre is higher than that in a 600  $\mu\text{m}$  fibre core when both of the fibres are subjected to the same vibration. Therefore, if we want to remove the speckle by vibrating an optical fibre, the fibre core diameter should be as large as possible to have more effective speckle reduction results.

This suggests that, if the size of a waveguide/fibre is large enough, the speckle pattern should not be observed and there is no need for fibre vibration. The output from a 15 mm  $\times$  70 mm  $\times$  1 mm slab waveguide was considered. This is the slab waveguide used for the laser beam combining and homogenising in chapter 9. There was no detectable speckle pattern on the scanned output of the waveguide.

This proves that a waveguide can be designed and used in a display system to combine, homogenise, shape laser beams and more importantly de-speckle the output image.

## References

- [10.1] Joseph W. Goodman, *Speckle Phenomena in Optics*, 1 ed Roberts and company, New York city, 2008.
- [10.2] K. K. A. R. R. Martinsen, "Speckle in laser imagery: efficient methods of quantification and minimization," *Annual meeting of the lasers and electrooptics society*, vol. 1, pp. 354-355, 1999.
- [10.3] J. W. Goodman, "Some Fundamental Properties of Speckle," *Journal of the Optical Society of America*, vol. 66, no. 11, pp. 1145-1150, 1976.
- [10.4] K. V. Chellappan, E. Erden, and H. Urey, "Laser-based displays: a review," *Applied Optics*, vol. 49, no. 25, p. F79-F98, 2010.
- [10.5] L. L. Wang, T. Tschudi, T. Halldorsson, and P. R. Petursson, "Speckle reduction in laser projection systems by diffractive optical elements," *Applied Optics*, vol. 37, no. 10, pp. 1770-1775, 1998.
- [10.6] L. I. Goldfischer, "Autocorrelation function and power spectral density of laser-produced speckle patterns," *JOSA*, vol. 55, no. 3, pp. 247-252, 1965.
- [10.7] T. Iwai, N. Takai, and T. Asakura, "The Auto-Correlation Function of the Speckle Intensity Fluctuation Integrated Spatially by A Detecting Aperture of Finite Size," *Optica Acta*, vol. 28, no. 10, pp. 1425-1437, 1981.
- [10.8] Q. B. Li and F. P. Chiang, "Three-dimensional dimension of laser speckle," *Applied Optics*, vol. 31, no. 29, pp. 6287-6291, 1992.
- [10.9] B. Eliasson and F. M. Mottier, "Determination of the granular radiance distribution of a diffuser and its use for vibration analysis," *JOSA*, vol. 61, no. 5, pp. 559-565, 1971.
- [10.10] N. H. Maerz, T. C. Palangio, and J. A. Franklin, "WipFrag image based granulometry system," *Measurement of Blast Fragmentation*, pp. 91-99, 1996.
- [10.11] R. A. Saunders, J. P. King, and I. Hardcastle, "Wideband chirp measurement technique for high bit rate sources," *Electronics Letters*, vol. 30, no. 16, pp. 1336-1338, 1994.
- [10.12] P. Surman, R. S. Brar, I. Sexton, and K. Hopf, *Muted and Helium3D Autostereoscopic Displays* IEEE International Conference on Multimedia and Expo, pp. 194-199, 2010.
- [10.13] Petre Janssens, "Laser projector speckle measurements," *29th International Display Research Conference (EURODISPLAY-2009)*, pp. 191-193, Sept. 2009.

- [10.14] Kishore V.Chellappan, Erdem Erden, and Hakan Urey, "Laser Based Display," *Applied Optics*, vol. 49, no. 25, p. f 79-f 98, Mar. 2010.
- [10.15] Arthur Bennett and Ronald Rabbetts, *Clinical Visual Optics*, 2 ed Butterworths, 1989, pp. 23-85.
- [10.16] K. K. De Valois, "Spatial frequency adaptation can enhance contrast sensitivity," *Vision research*, vol. 17, no. 9, pp. 1057-1065, 1977.
- [10.17] C. Owsley, R. Sekuler, and D. Siemsen, "Contrast sensitivity throughout adulthood," *Vision research*, vol. 23, no. 7, pp. 689-699, 1983.
- [10.18] R. F. Hess and E. R. Howell, "The threshold contrast sensitivity function in strabismic amblyopia: evidence for a two type classification," *Vision research*, vol. 17, no. 9, pp. 1049-1055, 1977.
- [10.19] F. W. Campbell and J. G. Robson, "Application of Fourier analysis to the visibility of gratings," *The Journal of Physiology*, vol. 197, no. 3, p. 551, 1968.

## **Chapter 11 Conclusions and Future Work**

### **11.1 Introduction**

This chapter contains a discussion of the results and the conclusion, benefits and the impact of the new research, which was described in chapters 6 -10. This chapter is divided into three sections. Firstly, the results of the research on the multimode waveguide for optical printed circuit boards (OPCB) are discussed which is the findings for the optical coupling loss due to the end facet waveguides caused in the fabrication process; and the optical loss in the crossing waveguides.

In the next section the results of using multimode optical waveguide in laser-illuminated display and the speckle contrast reduction by using waveguide is discussed. At the end, the speckle contrast and speckle measurements for the display systems is reconsidered with the aid of the research results on the speckle contrast sensitivity and the speckle size.

### **11.2 Multimode Optical Waveguide in High Data Rate Optical Interconnections**

In chapter 4 the OPCB system developed at University College London (UCL) was explained. The aim of the research was to design and manufacture an OPCB for high data rate interconnections. Several waveguides were designed at UCL, fabricated by other partners (Exxelis, Loughborough University and Heriot Watt University) and then tested at UCL to derive the design rules for optical engineers who aim to design the future boards. The waveguides were in various sizes, shapes and configurations such as bend, crossing and straight waveguide. The author of this thesis was involved in all the design and testing process. However, the concentration was mainly on the optical coupling loss due to the end facet roughness, and optical loss due to waveguide crossing which was investigated by simulation and experiments. In this section the new work on optical coupling loss and waveguide crossing are summarised and discussed.

#### **11.2.1 Optical Coupling Loss due to the Waveguide End Facet Roughness**

The results from end facet roughness due to different fabrication processes and the effect of the end facet roughness on the optical loss were presented in chapter 6. In this chapter, the end facet

## Chapter 11: *Conclusions and Future work*

roughness due to the use of dicing saw and flute router for cutting waveguide was investigated. It was found that the surface of the waveguide cut by a dicing saw is smoother than a flute router as the average roughness after using dicing saw was 61 nm (cutting with 30,000 rpm, cutting speed = 0.6 m/min, diamond particle size on the resin blade 30  $\mu$ m) while the lowest RMS roughness achieved for milling router was  $183 \pm 13$  nm. However, flute routers are a more suitable tools than dicing saws for OPCB fabrication as they can be controlled with a CNC machine to cut in any required shape. Besides, all PCB manufacturers have, and use, a CNC milling machine and there is no extra cost for fabrication. Apart from cutting OPCBs, milling routers are also used for making 45° mirrors and the surface quality after the milling process affects the results.

To find the relation between the waveguide surface quality and the router parameters for optimization using a milling router to cut optical polymer waveguides, several routers with different numbers of cutting edges (flutes) were used to cut the waveguide and the resultant surface roughness was measured by AFM. The results from using routers with one, two and three flutes show that one flute router provides a better surface quality in terms of the roughness magnitude. The three-flute router cutter leaves a very rough surface (standard deviation of  $911 \pm 285$  nm). Some groove or gouge-shape structures could be observed on the surface cut by a three-flute cutter. The one-flute cutter gives a better and smoother surface (standard deviation of  $183 \pm 13$  nm).

After choosing the one flute router, to optimise the parameters for this router, several samples were cut with different rpm and cutting speed and were tested to find the best cutting parameters. The best surface quality in terms of low magnitude of the roughness was achieved with 15000 rpm, and 0.25 m/min cutting speed.

Another issue to consider happened at higher rpm (between 34000- 70000 rpm). The end facet of the waveguides cut within this range of rotation speed appeared to be covered with another layer of material and the waveguide source (core material) was not clear under the microscope even with back illuminating of the waveguide. The layer might be due to the heat created on the surface of the waveguide.

We also found that the best experimental results were achieved when the rotation and translation speed are increased or decreased in step with each other. In other words, high rotation speed

should be used with high translation speed and vice versa. This is an interesting result, as in the case of a high rpm with a low translation speed the cutter touches the surface more and heat produced causing polymer melting. In addition, a low rotation speed with a high translation speed applies a translational force to the cutter. In this case the cutter might be tilted, which affects the end facet quality. More research should be undertaken in this area to clarify the results.

We calculated the chip load for each case of rotation speed and translation speed. The recommended chip load from the router manufacturer for incurring the least damage to the router and giving the smoothest surface is 8  $\mu\text{m}/\text{revolution}$ , which gives us a rotation and translation speed of 60,510 rpm and 0.484 m/min respectively. Although the plot of roughness against the chip load had a minimum at this number, the results indicate that a much smaller roughness is obtained at a chip load of 16  $\mu\text{m}/\text{revolution}$ . It is interesting that this is 2 times the recommended chip load. The problem that occurred with 60,510 rpm and 0.484 m/min, which gives a chip load of 8  $\mu\text{m}/\text{revolution}$ , was the blurred core surface of the waveguide. This aspect of the cutting has not been considered before.

The speed of the edge of the router cutter at the surface of the waveguide was calculated based on the rotation and the translation speed. It was found that the lowest roughness occurred at a speed of 150 m/min, increasing more quickly towards lower speeds and also increasing, although less quickly, towards higher speeds.

Another result that was derived for the first time to the best of our knowledge is the experimental relationship between the end facet roughness and the optical coupling loss. Optical coupling loss for samples cut with different end facet roughness was measured. The results indicate that increasing the roughness increases the coupling loss but not in a linear fashion. The optical loss was increased from 4.8 dB for a sample with 61 nm roughness to 6.8 dB for a sample with 183 nm roughness. However, for the sample with 340 nm roughness the coupling loss was increased to 7.8 dB.

Two methods of hand polishing and using a polishing router were tried to reduce the end facet roughness. We found that the problem with the hand polishing is the inconsistency of the results. The waveguide facet was tilted after polishing and the samples polished by different persons had

different surface profile. As we used a milling router to cut the waveguides, a polishing router was used to polish the end of the waveguide after cutting. Unfortunately, due to the shortage of time and budget, we were not able to find the best polishing router with optimised parameters and this is suggested as very useful work for future research.

To decrease the end facet waveguide roughness a new method of curing a layer of core material on the waveguide roughness was invented and successfully tested. The results of this research show an average improvement of  $2.23 \pm 1.2$  dB in the coupling loss after applying index matching fluid, and  $2.60 \pm 1.3$  dB after applying a layer of Truemode.

As future research, the effect of heat on the end facet roughness of the polymer waveguide should be examined. Considering manufacturing the waveguides under pressure and in a clean room can be further research to carry out.

### **11.2.2 Optical Loss due to the Waveguide Crossings**

In chapter 7, the optical loss due to crossing waveguides was calculated for different crossing angles. For the first time the results from two different simulation approaches, beam propagation and ray tracing were used and the simulation results were compared with the experiment results. Most of the previous research on crossing is for different material, such as silicon waveguides, or just for 90° crossings.

The results showed that the beam propagation method estimates a lower loss than the experiments, especially for sharper angles. For example, the optical loss due to a crossing angle of 10° was estimated by the BPM to be 0.078 dB while it was measured to be 0.159 dB. To investigate the source of the difference, and as the difference in the results was larger for the smaller crossing angles, the measured waveguide was studied and it was found that there is some core material left at the corners of the crossing waveguides, which makes the width of the crossed waveguide larger. This is due to the residue remaining during the waveguide fabrication. This can be improved by either bringing the mask more close to the core material during the curing or by using more collimated light during the curing process. It cannot be removed completely due to the diffraction of the UV curing light at the edge of the mask.

To find the estimated increase in the waveguide width due to the residue, crossing waveguides with different width on the crossed waveguide were simulated and it was found that if the



increase of the waveguide width is  $20\% \pm 5\%$ , the experimental results agree with the simulation. On the waveguide sample, the residue was measured to increase the waveguide width for  $15\% \pm 3\%$ , which is a good agreement with the simulation.

The next part of research in this chapter was to use ray tracing methods for the waveguide simulations, as the BPM algorithm can simulate the crossing angles only up to  $20^\circ$ . The results from ray tracing were opposite to the BPM results as they showed 10 times higher optical loss. To find the source of this error, the process of optical loss at the crossing was reconsidered. The optical source for the simulation was an optical fibre with NA of 0.22 and the waveguide NA is 0.3. The critical angle of the waveguide is  $78^\circ$  so that any ray which enters the waveguide will be propagated within the waveguide. In an actual waveguide wall roughness causes beams with sharper angles (high order modes) to radiate away from the waveguide. Therefore, only rays with a shallow angle (low order modes) are propagated in the waveguide. To determine the range of angles that propagate inside the waveguide, the NA of the source was reduced to find the smallest NA which shows optical loss comparable to the experiments. The best results were achieved where the  $NA = 0.05$ . This NA corresponds to an angle of 6 degrees. The interesting result is that the output angle of the waveguide was measured in our group by Kai Wang to be  $7^\circ \pm 2^\circ$ .

As future work, the optical loss in different crossings with various distances between the crossing waveguides should be considered. Waveguides with taper crossing, bent waveguide crossing, and a mixture of bend-straight and bend-taper should be investigated.

### **11.3 Multimode Optical Waveguide/Light guides in Laser Illuminated Display Systems**

In chapter 8, a new means of laser beam combining, beam homogenizing and beam shaping in display application was introduced. Our idea was to design a system to use multimode waveguides to combine, homogenise and shape the output of three red, green, and blue lasers for a 3D autostereoscopic display system, called HELIUM3D, and at the same time reduce the speckle contrast, which is a major problem in laser illuminated displays. A newly developed multi-emitter laser, called NECSEL, was chosen as the light source. The laser beam is formed from 48 emitters in two rows of 24 emitters. The waveguide was to be designed to have an

output light line with a dimension of  $10 \text{ mm} \times 100 \text{ }\mu\text{m}$  (A thickness of up to 1 mm was also acceptable).

### **11.3.1 Various Options for Laser-Waveguide Coupling and Waveguide Combiner**

The chosen laser source was a newly developed laser, and there was not much information about the laser beam and laser emitter properties except the data sheet from the company. Several experiments were carried out to characterise the laser and find the beam divergence, emitter spacing, and the positions of the beam waists of the emitters. The measured data was shared with the company and they changed their data sheet, as there was some difference between the measurement results and their quoted data.

Several different designs for using optical waveguides in the light engine of the HELIUM3D system were considered for the first time and compared based on cost, safety, optical loss and efficiency.

The comparison was carried out on two sections 1: To couple the laser light from the NECSEL into a  $100 \text{ }\mu\text{m}$  thick waveguide that acts as the colour combiner and colour homogeniser 2: The design of the waveguide combiner.

For section 1, two methods of using multimode optical fibre for each laser and using a bundle of fibres which are glued in one end were chosen to couple the laser light into the waveguide combiner. For section 2, a slab waveguide was chosen to be the best option for the waveguide combiner.

An investigation of the stability and aging properties of a newly developed polymer (by Micro Sharp) was carried out. The material was to be used for micro lens manufacturing and waveguide combiners. The effect of a 3 W laser on the material was measured by measuring the change in the surface profile and transmission properties of the material before and after exposure. The results showed no change in the surface profile after exposing the sample for two and half hours. However, in the transmission graph there was a shift in the transmission spectrum. We detected a difference of 0.18 dB at 640 nm, 0.22 dB at 532 nm and 0.34 dB at 465 nm, which means there has been a degradation of the transmission in the material. The sample was made of three layers of PMMA, Plexiglas and a glue layer and more investigation is needed to find the cause of the

change in the transmission spectrum. Based on this experiment, we decided to use a glass waveguide and microlens in the light engine of the HELIUM3D system.

The waveguide designed and introduced in chapter 8 and the discussion of the waveguide combining can be used for any other laser with any beam shape with a few adjustments.

### **11.3.2 Design and Experiment of using Waveguide in the HELIUM3D System**

Two different lens systems were designed and simulated using ray tracing to focus the output of the NECSEL beam into an optical fibre with 100  $\mu\text{m}$  diameter and NA of 0.22. The coupling efficiency was calculated to be 73%.

As the manufacturing of a custom lens system increases the cost of the display system, the use of a microscope objective for focusing the NECSEL beam was considered and a new microscope design was developed and designed for NECSEL laser focusing. The NECSEL beam was reduced from 3 mm  $\times$  8 mm to a spot with 90  $\mu\text{m}$  diameter, which is less than the diameter of the fibre.

The microscope objective was tested by experiment and 75% NECSEL-fibre efficiency was achieved for a 200  $\mu\text{m}$  core diameter fibre with NA of 0.39.

The optical fibre was implemented in the light engine of the HELIUM3D system and the output of the fibre was shaped using a cylindrical lens. We achieved 85% uniformity across the light line. Moreover, there was no sign of any multiple spots on the line, which was seen in the free space homogenisation approach due to the multiple beams emitted from the NECSEL laser. It was shown that using a multimode fibre helps to solve the problem of interference between the laser emitters by coupling their outputs into the fibre modes which results in multiple spots on the line. This multiple spot pattern reduces the uniformity of the image after the line is scanned on the LCoS modulation device.

A slab waveguide was simulated to be used for beam shaping and beam combining for the first time and was used in the HELIUM3D system. Two options of 1) three optical fibres for red, green, and blue colours and 2) three fibre ribbons each for one colour, were used for the input of the waveguide combiner. The results show that for a glass slab waveguide which is 10 mm wide and 100  $\mu\text{m}$  thick, the required length is 210 mm to achieve 90% uniformity at the output of the

waveguide and have a good uniformity. (These results were achieved with three optical fibres as the input. The length of the waveguide was reduced to 150 mm with a uniformity of 92% at the output of the fibre combiner when the input was three fibre ribbons).

The simulation results indicate the requirement for a long waveguide. The waveguide thickness is only 100  $\mu\text{m}$  and a glass sheet with this thickness breaks easily and must be protected properly. The optical loss due to the material absorption increases with increasing waveguide length. This is important for safety particularly as high power lasers are used to compensate for the power lost, and heat is created inside the waveguide. Moreover, implementing a large waveguide in display systems increases the size of the display and the waveguide combiner will not be suitable for the micro display system such as micro projectors.

The simulation results explained above are for a waveguide without wall roughness or any scattering site to scatter the light inside the waveguide. A low-cost scattering site with a triangle shape was suggested and simulated. Implementing this scatter-site decreased the waveguide length to 85 mm. Although the length of the waveguide was reduced to 85 mm with implementing of the scattering sites, the simulation results show that efficiency has been decreased. The efficiency of the waveguide combiner without the scattering site is 92% whereas with scattering site it is reduced to 69% for the same waveguides.

The use of a slab waveguide as the power homogeniser was experimentally tested by using a glass slab waveguide with a thickness of 1 mm. Increasing the thickness of the waveguide and so the output light line does not degrade the performance of the HELIUM3D system seriously. The results for a slab waveguide with a length of 75 mm show a uniformity of 85% at the output of the waveguide. Moreover, there was a significant reduction of the speckle pattern, which is concluded in the next section.

## **11.4 Speckle Analysis and Measurements**

Speckle pattern as a source of non-uniformity in the image in laser illuminated display systems were investigated in chapter 10.

A new computer program (with a CCD camera) was developed to record the speckle pattern and analyse it in real time to calculate the speckle contrast, speckle spot radius, uniformity of the

## Chapter 11: *Conclusions and Future work*

pattern and analyse the speckle pattern using image processing techniques. The benefit of this software was demonstrated by using it to monitor the speckle contrast, diameter and uniformity at various positions along the optical path after each optical component in an autostereoscopic display system.

The Granulometry method was used to find the speckle spot diameter. This method was compared with the conventional method of using an autocorrelation function.

It can be concluded from the results that in most of the speckle patterns where the black and white spots are symmetric Granulometry provides better results for the grain size. However, if the spots are not circular, autocorrelation has more accuracy. These two methods should be joined together for calculating the speckle size.

The speckle contrast was mapped at the viewer's position. Such results have never been shown for any system before and have the advantage of showing the fluctuation of speckle contrast across the display system and the effect of each optical component in the system on the speckle pattern.

Speckle contrast was not reduced by changing the modulation frequency and the duty cycle of the NECSEL laser. NECSELS are frequency doubled diode lasers with Volume Bragg Gratings (VBG) implemented inside the casing to stabilize the wavelength of the laser. Therefore, even though changing the modulation frequency and duty cycle to broaden the laser emission bandwidth, the output bandwidth will be constant. This was shown by a spectrometer.

NECSEL lasers were chosen for the HELIUM3D system, as they are multi emitter lasers. In addition, there is one horizontal and one vertical diffuser in the HELIUM3D system. The effect of the diffusers and multi-emitter lasers on the speckle contrast was investigated. In the diffuser experiment, the speckle contrast was reduced from 22.3% to 5.7% with two diffusers. By using a multiemitter NECSEL (without diffuser), the speckle was reduced from 56% to 6.2%. A speckle contrast below 4% is acceptable and cannot be perceived by human eye. Although the speckle contrast was not reduced to below the threshold of human perception, however, using both methods of multiemitter laser and diffusers can provide an acceptable level of speckle contrast.

#### **11.4.1 Speckle Reduction using Optical Waveguides**

For the measurement of the speckle pattern of light emitted from a waveguide, several optical fibres with the same length (2 m) and the same numerical aperture (NA=0.39) and different core diameter were chosen. The speckle pattern for fibres with different core diameters was recorded and the speckle spot diameter was calculated using the software detailed in the previous section. It was shown that the speckle size reduces as the diameter of the fibre increases. However, the speckle contrast is constant. Two interesting results can be concluded from this experiment: Speckle is normally judged based on the speckle contrast in the display systems. The speckle contrast for all of the recorded patterns was the same ( $21 \pm 5\%$ ) but there was a difference in the speckle size. There are two important issues to be considered which have not been investigated by researchers: first of all the speckle contrast and speckle perception is different. Speckle contrast is due to the fluctuation of the intensity across the pattern and could be the same for fluctuations with different frequencies. However if the fluctuations are at a very high frequency (which means the speckle spots are small) the human eye will not be able to resolve it and will, therefore, not see it.

The second issue is about speckle reduction. Optical fibres have been used in the display system and the speckle contrast has been reduced by vibrating the fibre. Vibrating the fibre changes the distribution of the energy inside the modes and, therefore, the phase shift between different modes varies and, as a result, the speckle pattern will be different. Therefore, the speckle contrast is reduced if the vibration is fast enough and phase change is sufficient to shift the speckle patterns in time and integrate them to cover each other. This is where the size of the speckle is important. Producing enough phase shift, and in result, enough shift in the speckle patterns to cover the dark spots depends on the size of the dark spots. The smaller the speckle size, the smaller the movement (less mode scrambling) required to remove the speckle. We used a vibrator and show that speckle contrast in a 50  $\mu\text{m}$  core fibre is higher than that in a 600  $\mu\text{m}$  fibre core when both of the fibres are subjected to the same vibration. Therefore, if we want to remove the speckle by vibrating an optical fibre, the fibre core diameter should be as large as possible to have more effective speckle reduction results.

This suggests that, if the size of a waveguide/fibre is large enough, the speckle pattern should not be observed and there is no need for fibre vibration. The output from a 15 mm  $\times$  70 mm  $\times$  1 mm

## Chapter 11: *Conclusions and Future work*

slab waveguide was considered. This is the slab waveguide used for the laser beam combining and homogenising in chapter 9. There was no detectable speckle pattern on the scanned output of the waveguide.

This proves that a waveguide can be designed and used in a display system to combine, homogenise, shape laser beams and more importantly de-speckle the output image.

As future work in this section, speckle analysis considering the speckle size and contrast is a very interesting area. At the end of chapter 10, the Contrast Sensitivity Function was explained and a new idea was suggested to implement speckle measurements with human ability for perception of objects with different size in different contrast level. More theoretical analysis and experiments should be carried out to find a mathematical relationship for the characterisation of speckle patterns in display systems.

## Appendix 1: The use of Granulometry for Speckle Spot Size Detection

Speckle pattern is a granular structure that consisting of bright and dark spots where the size of the spots determines the non-uniformity of the observed image due to the coherent nature of laser light. In this section, we try to determine the size of the speckle and relate the speckle size with the speckle contrast. Our goal is to calculate the size distribution of the bright spots in the image captured by the detector/camera containing the speckle pattern of a NECSEL laser. Nevertheless, the method can be applied to any other speckle pattern generated with another coherent source.

Granulometry is the process used to measure different grain sizes in a granular material. In this process, the size of the objects is estimated based on the size in a photograph. This is a well-known process and is used widely in different industries such as mining[47]. We try to use this method to estimate the intensity surface area distribution of the bright spots as a function of size. Granulometry likens image objects to stones whose sizes can be determined by sifting them through screens of increasing size and collecting what remains after each pass. Image objects are sifted by opening the image with a structuring element of increasing size and counting the remaining intensity surface area (summation of pixel values in the image) after each opening.

To find the size distribution, first we use contrast-limited adaptive histogram equalization (CLAHE) to increase the intensity contrast in the greyscale image. CLAHE divides the image into several small sections, called *tiles* and then enhances each tile's contrast so that the histogram of the output section approximately matches the histogram specified by the distribution parameter (the distribution function specifies the desired histogram shape for the image tiles. It can be chosen to be Uniform for flat histogram, Rayleigh for a bell-shaped histogram or exponential for a curved histogram). The neighbouring sections are then combined using bilinear interpolation to eliminate artificially induced boundaries. The contrast, especially in homogeneous areas, can be limited to avoid amplifying any noise that might be present in the image. We choose a counter limit so that the intensity surface area goes to zero as we increase the size of the structuring element.



## The use of Granulometry for Speckle Spot size Detection

Now we apply the program to two samples of fine and coarse speckle patterns. These speckle patterns were recorded with a green NECSEL laser. First, we increase the contrast in the pictures:

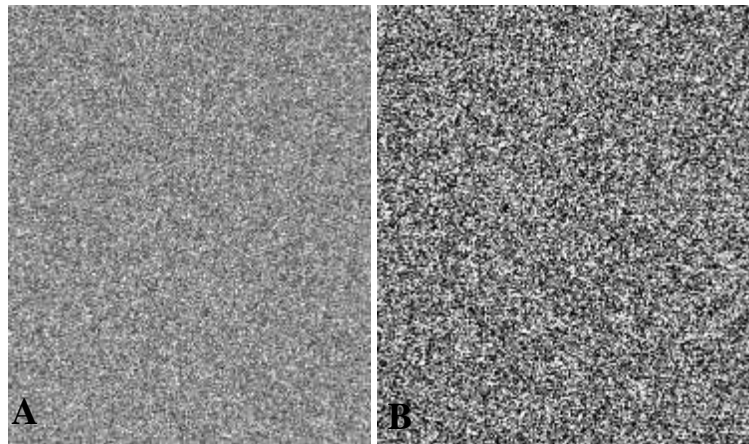


Figure 1: Fine speckle pattern A: before and B: after applying the contrast-limited adaptive histogram equalization. The tile was chosen to be  $10 \times 10$  pixels.

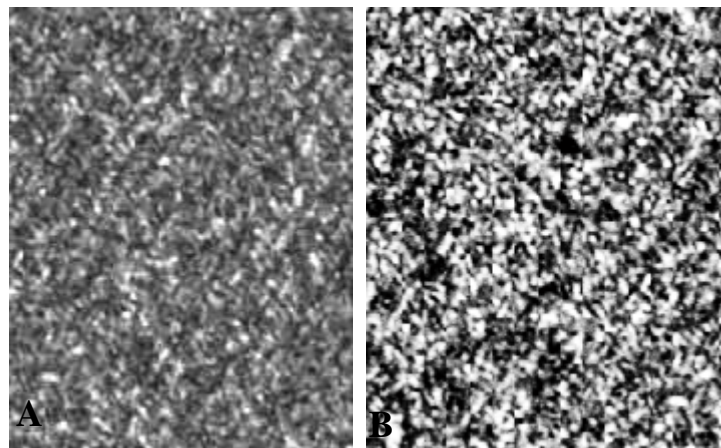


Figure 2: A coarse speckle pattern A: before and B: after applying the contrast-limited adaptive histogram equalization. The tile was chosen to be  $10 \times 10$  pixels.

Then we create a disk-shape structure and change the radius of the disk. For each disk with particular radius all the objects with a smaller radius are separated and calculate the intensity of the separated objects then we increase the disk's radius and apply sifting. For each disk radius we calculate the covered area by that particular disk radius. In Figure 3 the sum of the pixel values for different disk's radius is shown.

## The use of Granulometry for Speckle Spot size Detection

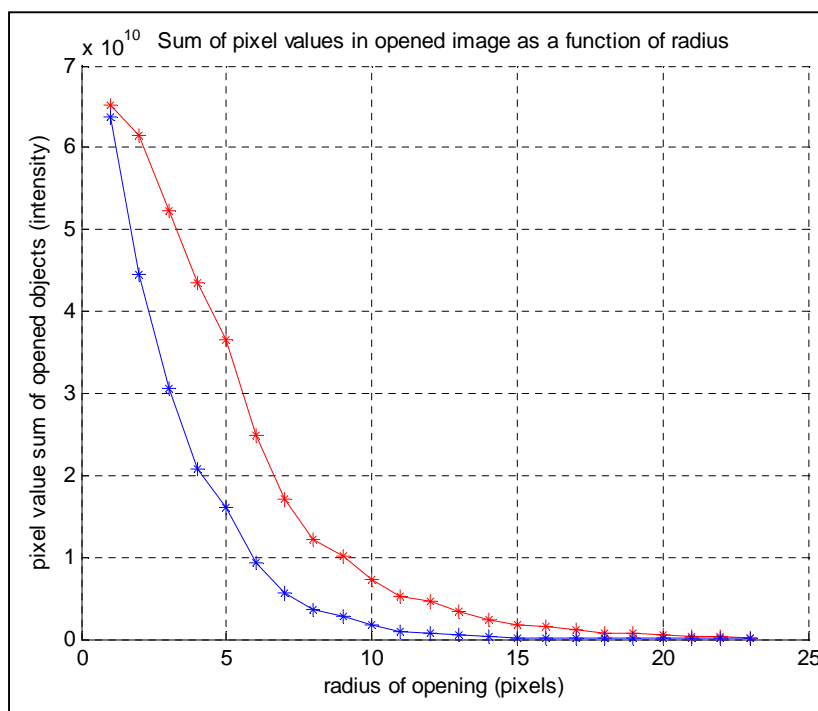


Figure 3: The blue line is for fine speckle and the red line is for coarse speckle pattern.

A significant drop in intensity surface area between two consecutive openings indicates that the image contains objects of comparable size to the smaller opening. This is equivalent to the first derivative of the intensity surface area array, which contains the size distribution of the bright spots in the image. We then calculate the first derivative with a simple difference operation. Figure 4 shows the size distribution of the speckle pattern.

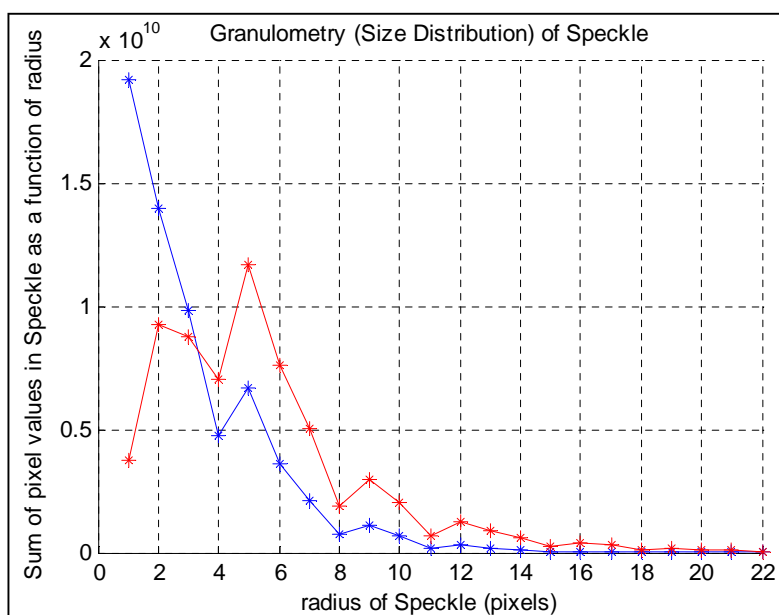


Figure 4: The blue line is for fine speckle and the red line is for coarse speckle pattern.

## The use of Granulometry for Speckle Spot size Detection

As is shown in Figure 4, the maximum number of disks happens with a radius of an order of a pixel area for the fine speckle whereas the disk size is about 4 pixels for the coarse speckle pattern. This number indicates the radius of each bright spot in the fine speckle pattern is about 5  $\mu\text{m}$  (speckle size) and about 25  $\mu\text{m}$  for the coarse speckle pattern (this is an average size as the speckle pattern is a random distribution of the spots).

In Figure 5, the spots with one pixel radius for fine speckle pattern and 5 pixels radius for the coarse speckle pattern have been extracted.

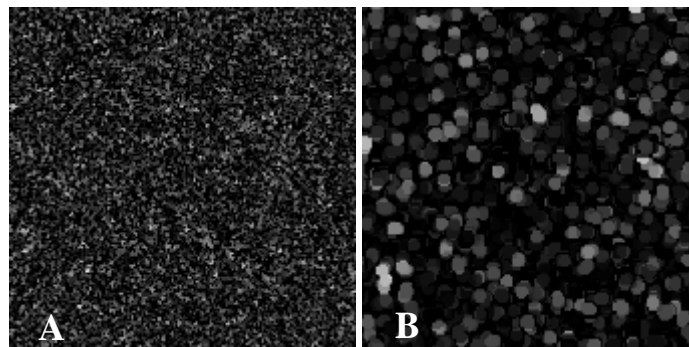


Figure 5: speckles with a particular radius. A: the speckle size is about one pixel and B: the speckle size is 5 pixels.

The two speckle patterns shown in this section were recorded in the lab from a NECSEL laser. For the measurement, a CCD camera with a  $4.5 \mu\text{m} \times 4.5 \mu\text{m}$  pixel area was used without any lens to record the speckle pattern. The laser source was 2 m away from the reflecting surface and the distance between camera and the surface was 1 m.

## List of Publications:

- H. Baghsiahi, E. Willman, F. A. Fernández, David R. Selviah, S. E. Day, K. Aksit, S. Ölçer, A. Mostafazadeh, E. Erden, VC Kishore, H. Urey, P. A. Surman, Micro-optics for a Laser Based Auto-stereoscopic Multi-Viewer Display, Society for Information Display International Symposium Digest of Technical Papers, Paper 48.4, 2011.
- Baghsiahi, H. and Selviah, D.R. and Yu, G. and Wang, K. and Yau, M. and Anibal Fernández. Photolithographically manufactured acrylate multimode optical waveguide translation and rotation misalignment tolerances. Presented at: 2nd Electronics System-Integration Technology Conference, ESTC 2008, Greenwich University, London, UK. 2008.
- K. Aksit, S. Olcer, E. Erden, VC Kishore, H. Urey, E. Willman, H. Baghsiahi, S.E. Day, D.R. Selviah, F. Anibal Fernández, “Light engine and optics for helium3d auto-stereoscopic laser scanning display”. In 3DTV Conference: The True Vision-Capture, Transmission and Display of 3D Video (3DTV-CON), pages 1–4. IEEE, 2011.
- K. V. Chellappan, E. Erden, H. Ürey, H. Baghsiahi, E. Willman, S. E. Day, D. R. Selviah, F. A. Fernandez, P. Surman, "Laser Scanning 3D Display with Dynamic Exit Pupil", Eurodisplay 2009, Rome, Italy, pp. 492-495, September 2009.
- E. Erden, K. V. Chellappan, H. Ürey, H. Baghsiahi, E. Willman, S. E. Day, D. R. Selviah, F. A. Fernández, P. Surman, "Laser Scanning Based Autostereoscopic 3D Display with Pupil Tracking", IEEE LEOS Annual Meeting Proc. Vol. I and II, Antalya, Turkey, pp. 10-11, Oct 2009.
- E. Willman, H. Baghsiahi, F. A. Fernández, D. R. Selviah, S. E. Day, V. C. Kishore, E. Erden, H. Urey, and P. A. Surman, “The Optics of an Autostereoscopic Multiview Display,” Digest of SID Annual Meeting, Paper: 16.4, pp. 222-225, Seattle, USA, May 2010.

## Chapter 11: *List of Publications*

- Pitwon, R.C.A. and Hopkins, K. and Wang, K. and Selviah, D.R. and Baghsiahi, H. and Offrein, B.J. and Dangel, R. and Horst, F. and Halter, M. and Gmür, M. Design and implementation of an electro-optical backplane with pluggable in-plane connectors. In: Glebov, A. L. and Chen, R.T., (eds.) *Optoelectronic Interconnects and Component Integration IX*. International Society for Optical Engineering: Bellingham, US.
- Selviah, D. R and Walker, A. C and Hutt, D. A and Wang, K and McCarthy, A and Fernández, A and Papakonstantinou, I and Baghsiahi, H and Suyal, H and Taghizadeh, M and Conway, P and Chappell, J and Zakariyah, SS and Milward, D and Pitwon, R and Hopkins, K and Muggeridge, M and Rygate, J and Calver, J and Kandulski, W and Deshazer, DJ and Hueston, K and Ives, DJ and Ferguson, R and Harris, S and Hinde, G and Cole, M and White, H and Suyal, N and Rehman, HU and Bryson, C (2010) Integrated optical and electronic interconnect PCB manufacturing research. *Circuit World*, 36 (2) 5 - 19. 10.1108/03056121011041654.
- Wang, K. and Selviah, D.R. and Baghsiahi, H. and Anibal Fernández. and Papakonstantinou, I. and Yu, G. Design rules for polymer waveguides and measurement techniques. Presented at: 2nd International IEEE Symposium on Photonic Packaging Electrical Optical Circuit Board and Optical Backplane, Messe München, Munich, Germany, June 2008.
- Zakariyah, S.S., Conway, P.P., Hutt, D.A., Selviah, D.R., Wang, K., Baghsiahi, H., Rygate, J., Calver, J., Kandulski, W. ‘‘Polymer Optical Waveguide Fabrication using Laser Ablation’’. *G4 - LED and Optoelectronic Packaging Session, 11th Electronics Packaging Technology Conference EPTC, Singapore, Friday, 11 December 2009*.

## Chapter 11: *List of Publications*

- Selviah, D.R. and Hutt, D.A. and Walker, A.C. and Wang, K. and Fernández, A. and Conway, P.P. and Milward, D. and Papakonstantinou, I. and Baghsiahi, H. and Chappell, J. and Zakariyah, S.S. and McCarthy, A. and Suyal, H. , Innovative optical and electronic interconnect printed circuit board manufacturing research. Presented at: 2nd Electronics System-Integration Technology Conference, ESTC 2008, Greenwich, London, UK. 2008.
- Wang, K. and Selviah, D. R. and Papakonstantinou, I. and Yu, G. and Baghsiahi, H. and Fernández, F. A., Photolithographically manufactured acrylate multimode optical waveguide loss design rules. Presented at: 2nd Electronics System-Integration Technology Conference, ESTC 2008, Greenwich, London, UK.
- Selviah, D.R. and Anibal Fernández, and Papakonstantinou, I. and Wang, K. and Baghsiahi, H. and Walker, A.C. and McCarthy, A. and Suyal, H. and Hutt, D.A. and Conway, P.P. and Chappell, J. and Zakariyah, S.S. and Milward, D. (2008) Integrated optical and electronic interconnect printed circuit board manufacturing. *Circuit World* , 34 (2) pp. 21-26. 10.1108/03056120810874546.
- Selviah, D.R. and Hutt, D.A. and Walker, A.C. and Wang, K. and Anibal Fernández, F. and Conway, P.P. and Milward, D. and Papakonstantinou, I. and Baghsiahi, H. and Chappell, J. and Zakariyah, S.S. and McCarthy, A. and Suyal, H. (2008) Innovative optical and electronic interconnect printed circuit board manufacturing research. In: *Proceedings 2008 2nd Electronics System-Integration Technology Conference Greenwich, UK: Vol 1.* (pp. 867-872). IEEE: Piscataway, US.
- Wang, K and Selviah, D. R and Papakonstantinou, I and Fernández, FA and Baghsiahi, H (2008) Optical Waveguide Modelling, Measurement and Design for Optical Printed Circuit Board. In: (Proceedings) *IEEE Workshop on Interconnections within High Speed Digital Systems, HSDS, Santa Fe, USA, 18-21 May 2008.*
- Baghsiahi, SH Photolithographically manufactured acrylate polymer multimode optical waveguide loss design rules. In: *Proceedings - 2008 2nd Electronics Systemintegration Technology Conference, ESTC.*

## Chapter 11: *List of Publications*

- R. C. A. Pitwon, K. Wang, J. Graham-Jones, I. Papakonstantinou, H. Baghsiahi, B. Offrein, R. Dangel, D. Milward, D. R. Selviah, ‘FirstLight: Pluggable Optical Interconnect Technologies for Polymeric Electro-Optical Printed Circuit Boards in Data Centers’, (submitted and revised, ready to be published).
- K. Aksit, H. Baghsiahi, E. Erden, VC Kishore, D. R. Selviah, P. Surman, H. Urey “Laser scanning based light engine for auto-stereoscopic display system”, in preparation for Optics Express.
- Baghsiahi, H, Wang, Kai, Pitwon, R, Selviah, D. R,’ Polymer waveguide end facet cutting and smoothing: roughness and optical Input/Output coupling loss’ (under preparation for Optics express).
- Baghsiahi, H, Wang, Kai, Selviah, D. R, ‘Optical loss and Crosstalk in optical polymer crossing waveguides’, (under preparation for Optics express).
- Baghsiahi, H and Selviah, D. R, ‘Speckle contrast Perception in Laser Based Display System’. Nature Photonics (under preparation).
- Hadi Baghsiahi, David R. Selviah, Sally Day, Anibal Fernandez, ‘Effect of Optical waveguide in Laser Based Display system on the reduction of the speckle contrast’ (under preparation for Optics Express).
- Hadi Baghsiahi, Phil Surman, David R. Selviah, Sally Day, Anibal Fernandez, ‘Speckle contrast measurement techniques in laser based display systems’(under preparation).